Melt Growth and Microstructural Control of Single Crystal YBCO High Temperature Superconducting Materials

by

Karina E. A. Rigby

B.S., Materials Science and Engineering
Massachusetts Institute of Technology, 1992

Submitted to the Department of Materials Science and Engineering
in Partial Fulfillment of the Requirements for the Degree of

DOCTOR OF PHILOSOPHY
in Ceramics

at the
MASSACHUSETTS INSTITUTE OF TECHNOLOGY

June, 1997

Signature of Author: _____
Department of Materials Science and Engineering
May 2, 1997

Certified by: _____
Professor Michael J. Cima
Norton Professor of Ceramics
Thesis Supervisor

Accepted by: _____
Professor Linn W. Hobbs
John F. Elliott Professor of Materials
Chairman, Departmental Committee on Graduate Students

Melt Growth and Microstructural Control of Single Crystal YBCO High Temperature Superconducting Materials

by

Karina E. A. Rigby

Submitted to the Department of Materials Science and Engineering
on May 2, 1997 in Partial Fulfillment of the Requirements
for the Degree of Doctor of Philosophy in Ceramics

Abstract

Two types of processing methods were used to gain knowledge about single crystal growth of YBCO materials. Laser Heated Floating Zone (LHFZ) growth was used to prepare directionally solidified YBCO single crystals. Seeded growth was used to prepare YBCO single crystals solidified in both the ab- and c-directions. Crystals produced using these growth methods were used to study relationships between processing, microstructure and superconducting properties of YBCO materials.

The LHFZ precursor fiber production and growth processes were optimized in an effort to produce longer single crystals of high quality YBCO materials. Limitations to the production of long single crystals were examined. A model was proposed to explain secondary grain nucleation during LHFZ growth. The effect of flux pinning sites in the form of stacking faults introduced in YBCO materials during oxygen annealing was examined and related to changes in $YBa_2Cu_3O_{7-\delta}$ (123) crystal structure and improved critical current densities in the YBCO material. Critical current densities of $2x10^5$ A/cm^2 were obtained for 123 single crystals produced by LHFZ growth. This value is near the current observed maximum critical current density obtained in non-irradiated bulk YBCO single crystal materials.

123 single crystal growth rates for samples produced by seeded growth were related to processing parameters such as undercooling and Y_2BaCuO_5 (211) particle characteristics. 123 single crystal habit was shown to be similar to the crystal habit predicted by periodic bond chain (PBC) analysis. 123 growth rate and interface structure was shown to vary according to crystal face. The presence of spiral growth and hopper growth microstructures were observed on 123 crystals produced by seeded growth. It was shown that differences in the relationship between growth rate, R, and undercooling, ΔT, for the different growth mechanisms of 123 single crystals can account for the fact that the c-face

is the fast growth face at low undercoolings while the ab-face is the fast growth face at high undercoolings.

211 segregation in stoichiometric 123 and excess 211 YBCO materials was investigated and quantified. It was shown that 211 segregation in both types of samples was due to variations in 211 particle dissolution rates in the barium cuprate liquid in front of the 123 crystal. The driving force for the differences in dissolution rates in stoichiometric YBCO materials was found to be due to differences in the yttrium concentration profile in front of the faces, edges and corners of the 123 crystal. The driving force for the differences in dissolution rates in excess 211 YBCO materials was found to be due to barium cuprate liquid entrapment within the platelet structure of the 123 crystals.

211 particles were shown to coarsen during their residence time in the barium cuprate liquid formed during melt growth of YBCO materials. Experiments were performed to examine the coarsening process of the 211 particles and to quantitatively describe their coarsening behavior above the peritectic temperature by evaluating k, the coarsening constant, and by determining the 211 particle size distribution vs. coarsening time. The effectiveness of platinum as a dopant to reduce 211 particle coarsening was also evaluated.

Thesis Supervisor: Professor Michael J. Cima
Title: Norton Professor of Ceramics

To my Mom and Dad

Acknowledgments

Cambridge, April 8th, 1997

I would like to thank my advisor, Professor Michael Cima, for inspiring me to go into the field of ceramics processing and for his guidance and support during my graduate studies. I feel privileged to have had the chance to experience the many different sides of ceramics processing and materials engineering at the Ceramics Processing Research Laboratory (CPRL). Many thanks also to Professor Merton Flemings and Professor John Vander Sande for being on my thesis committee. It was an honor to have had the opportunity to work with and to discuss my research with such authorities in the fields of solidification and superconductivity. I greatly appreciate the contributions of Dr. John Haggerty in the area of Laser Heated Floating Zone (LHFZ) growth. Special thanks also to Professor Regis Pelloux who believed in me as an undergraduate and inspired me to go on to graduate school.

I would like to express my appreciation to the Tokyo Electric Power Company for providing the funding for this research. I also greatly appreciate the contributions of my colleagues and friends in the TEPCO group. Thanks to Anacleto Figueredo for being a great officemate and for showing me the ropes in the areas of precursor preparation and laser processing. Special thanks also to Tae-Hyun Sung for his TEM work, Shoichi Honjo for his work in the area of seeded growth, and Hua Shen for his useful polishing tips.

Much of my graduate life was spent at the CPRL and wouldn't have been the same without the friendship and support of its staff. I would especially like to thank Lenny Rigione for his round-the-clock assistance with SEM and EDX questions as well as for all of the fun lunchroom discussions. I'm sure that all of the other members of the CPRL will agree with me when I say that Barbara Layne is a truly invaluable member of the group, who keeps the administrative side of the lab running smoothly and has the amazing ability to deal with dozens of stressed researchers and never lose her patience. Thanks for everything, Barbara! I would also like to thank Neville Sonnenberg for his helpful comments on my research, for constructing and maintaining our computer network and for keeping me entertained with all of the cute stories about his kids. John Centorino also provided valuable technical assistance whenever any equipment needed fixing.

A number of other people who were part of my life during graduate school deserve extra special thanks. Lynne, your friendship and support really helped preserve my sanity while I was writing my thesis. Thanks so much for keeping me company during breaks and listening to each and every one of my theories in detail. I'm sure you could write an entire book on 211 particles by now! Special thanks also to Cesare, who made me smile and laugh no matter how tired or discouraged I was. I feel lucky to count you among my

friends. I also want to thank Kamala, a great friend and wonderful officemate with whom I could talk about anything. I'm really going to miss you! Special thanks also to Satbir and Jack for providing advice on all sorts of subjects and to Felix for stopping by and making me laugh during those long hours in front of the laser. Thanks also to Susi, Jae, Todd, Kevin, Ken, Bill, Jason, Matt, Ben, Man-Fai, Bugra, John S. and all of the other great people at the CPRL.

I couldn't have gotten this far without the lifelong love and support of my parents. Mom, you were there the day I discovered my love of research and you have encouraged me every step of the way. You showed me that I could do anything I set my mind to and instilled in me the love of learning. Thanks for always being there when I need you. Danke! Dad, you showed me that science and engineering can be fun, even before I was old enough to walk. Thanks for letting me pull the scrap metal out of your workshop cabinets and for always taking me with you to Radio Shack. I'm proud to follow in your footsteps and become the second Dr. Rigby. Thanks for everything! Thanks also to Kar for being a cool brother. I also want to thank my Größi, who has been a real role model of female strength in my life.

Finally, I thank my boyfriend, Olaf, who gave me a reason to finish my thesis so that we could start our life together. Looking forward to life in Germany with you after graduate school really kept me going. Thank you for all of your love and support!

Table of contents

List of figures

Chapter 1

Chapter 2

Chapter 3

Chapter 4

Chapter 5

Chapter 6

Chapter 7

Chapter 8

List of tables

Chapter 4

Chapter 5

Chapter 8

Chapter 1

Introduction

1.1. History of high T_c superconducting materials

Superconductivity, the decrease of electrical resistivity to zero below a certain temperature, was discovered in 1911 by the Dutch physicist Kammerlingh Onnes in the course of his experiments on the electrical conductivity of metals in liquid helium. The idea of carrying current through zero-resistance material was promising, although the temperatures at which these materials remained superconducting were extremely low. Superconductivity remained mainly a laboratory phenomenon, except for a very few specialized applications, until the mid 1900s. In the 1940s and 1970s, niobium alloys, which superconduct at temperatures up to 23 K, were discovered. These temperatures were still well within the liquid helium range and no new progress was made on superconducting materials for many years.[1-2]

In mid-1986 J. G. Bednorz and K. A. Müller reported transition temperatures in the 30 K range for metallic, oxygen deficient compounds in the barium, lanthanum, copper oxide system and the search for a room-temperature superconductor began in earnest. Other HTSC materials, also known as type II superconductors, which superconducted close to 40 K, were discovered by the end of 1986 and the beginning of 1987. In the last decade, superconductivity has been observed in ceramic copper oxide materials containing lanthanum, strontium, bismuth, calcium, tantalum and many other elements.[3] Wu et al. discovered superconductivity around 90 K in the yttrium, barium, copper oxide (YBCO) system in 1987.[4] Materials in this system are of significant technological interest

because of their high critical temperatures, high critical current densities, high field tolerance and low toxicity. The significant knowledge base established by the large number of researchers working on this material has made the goal of using HTSC superconductors in commercial applications a reality. A number of significant problems related to the properties, processing and performance of these materials must still be overcome, however, before large scale commercial or non-commercial use will be feasible.

1.2. Technological importance of bulk HTSC materials

HTSC materials have already been used in a number of applications within the power industry. Many more applications are planned for the future when greater knowledge of the processing-properties-performance relationships in HTSC superconductors enable the mass production of high quality materials. The two main classes of applications for which HTSC materials are being used or considered are new applications which take advantage of the special properties exhibited solely by superconductors and traditional applications whose performance is enhanced through the replacement of standard materials with HTSC materials.[5]

Two main electrical properties exhibited solely by superconducting materials are zero electrical resistance and the Meissner effect. Both of these materials characteristics are important for magnetic energy storage and levitation applications. Current transport with zero electrical resistance enables superconducting materials to be used for magnetic energy storage. Energy is stored via current carried in magnetic coils without loss. Energy stored in superconducting coils can be released to rapidly supply electric power for short times in cases where main electric power is interrupted. Energy can also be stored at times of low demand and discharged in periods of high use. Magnetic energy

storage is also important for applications which require high power for short times such as applications using large lasers.[6] Superconductors also exhibit the unique phenomenon known as the Meissner effect. Magnetic flux is expelled by a superconductor in a field below H_c, the critical field. This effect can be utilized for many magnetic levitation (maglev) applications. Extensive research has been performed in the area of levitating bearings and flywheels which can function without friction.[6] High-speed maglev trains have been developed to take advantage of the Meissner effect as well. Maglev trains use superconducting coils in the vehicle which interact with guideway conductors to provide suspension, guidance and propulsion (see figure 1.1).[5,7]

HTSC materials also have the characteristic that they can support high critical current densities. HTSC materials revert to their normal nonsuperconducting state above a certain critical current density, J_c. This process is known as quenching. This characteristic provides an additional unique use for HTSC materials as fault current limiters. A fault current limiter using HTSC materials designed by the Tokyo Electric Power Company (TEPCO) can carry currents up to 2756 A for a specific diameter. If a fault current above this value occurs, the HTSC material exceeds its critical current density and quenches. HTSC materials can quench much faster than an ordinary fuse, which allows fault currents to be limited much more effectively.[5,7]

The fact that HTSC materials can support high critical current densities with zero resistance also makes them attractive for use in traditional current carrying applications. Generators can be made much more efficient by replacing standard magnetic coils with superconducting materials. Nuclear magnetic resonance (NMR) and magnetic resonance imaging (MRI) are two further applications which take advantage of zero electrical resistance and high critical current density of HTSC materials. Both of these applications rely on high magnetic fields which can be produced much more easily with superconducting materials than with standard materials.[7] AC power transmission can also be significantly enhanced through the replacement of standard conductors. Although

HTSC materials do exhibit losses and do not have completely zero resistance under AC conditions, the advantages gained through the use of superconducting materials outweighs the small losses incurred.[7] A study performed by TEPCO has shown that HTSC materials can be fitted into existing ducts for standard conductors (150 mm in diameter) if the critical current density of the superconducting materials is above $1x10^6$ A/cm^2 at 0.15 T and $2x10^5$ A/cm^2 at 0.9 T. A schematic of the superconducting cable design is shown in figure 1.2.[8] A cost reduction of approximately 15% per year can be achieved through the replacement of standard conductors with such an HTSC material. These calculations take into account not only the power transmission savings, but also the cost of construction, refrigeration systems, and operation power and power loss of the refrigeration system. The fact that primary substations can be eliminated because of uniform voltages in the HTSC cables increased the overall cost savings to 21% per year.[8]

1.3. Motivation for work

All of the applications listed above require the production of high quality HTSC materials with excellent properties. YBCO materials have a critical temperature of above 90 K and, therefore, fulfill the temperature requirement for use with liquid nitrogen cooling systems which can cool materials to 77 K. One of the most significant barriers to the use of YBCO materials in power industry applications is the fact that critical current densities are below the required value. YBCO materials in thin film form have been prepared with critical current densities greater than 10^6 A/cm^2 in 0 field.[9] This value is much lower for bulk YBCO materials, however.[10-14] It has been shown that critical current densities in YBCO materials are significantly degraded by the presence of high angle grain boundaries (see section 2.2.3).[15-19] Any materials produced for use in most of the above applications must, therefore, have an aligned microstructure or be in single crystal form.

Critical current densities greater than $1x10^5$ A/cm^2 have been achieved in single crystal YBCO bulk materials[11-12,20] but even this value is not high enough for some applications. Other methods used to produce YBCO materials with aligned microstructures result in lower critical current densities.[14,21-24] Extensive research has shown that the inclusion of flux pinning centers in YBCO materials can significantly increase critical current densities and lower their field dependence.[25-32] Understanding the relationship between materials processing, microstructure and critical current densities in bulk YBCO materials is, therefore, an important step toward being able to produce HTSC materials with the required properties.

All of the applications listed above also require the production of large quantities of HTSC materials. As mentioned above, most applications require critical current densities which can only be achieved in single crystal form. Growth of YBCO materials is limited, however, by the incongruent melting of the superconducting phase and the highly faceted nature of the material. The maximum growth rate of single crystal YBCO materials is currently limited to a few cm per hour.[11,33] This value is much to low for mass production of HTSC materials for use on an industrial scale. Single crystals produced for commercial applications must also exhibit uniform properties. Many researchers have found that some types of single crystal growth methods produce nonuniform microstructures.[15,34-43] Such microstructural inhomogeneity can cause significant variations in the superconducting properties within the single crystal. Significant research must, therefore, be conducted to understand how processing parameters affect the microstructure and growth rate of YBCO single crystals.

The research presented here is concerned with understanding the relationship between processing parameters, growth rate, microstructure and properties of single crystal YBCO superconducting materials.

1.4 Thesis organization

The first two chapters of this thesis give an introduction and background to YBCO materials. Chapter 1 gives a short history of the discovery of YBCO and describes its many commercial applications. The required improvements in HTSC materials which are needed for industrial use are presented as motivation for this work and a short overview of thesis organization and terminology is given. Chapter 2 presents the necessary background knowledge on the thermodynamics and kinetics of crystal growth in the YBCO system, the structure of the main materials used in this research, the theory of superconductivity in the YBCO system and an overview of various solidification methods for the production of YBCO single crystals. Chapter 2 also describes the importance of 211 particles in YBCO single crystal growth and property enhancement. Chapter 3 presents a study on the coarsening of 211 particles in the semi-solid melt produced via the peritectic decomposition of the 123 phase. Chapter 4 details the sample preparation and growth methods of bulk YBCO single crystal fibers by laser heated floating zone (LHFZ) growth. Improvements in precursor production and growth methods, designed to produce longer single crystals, are discussed. A secondary grain nucleation model is introduced to explain limitations in YBCO single crystal growth using LHFZ processing. Chapter 5 details the sample preparation and growth methods of bulk YBCO single crystals produced by seeded growth. Results on single crystal growth rate, 211 particle dissolution, crystal habit and interface morphology are presented. Chapter 6 discusses the effect of 211 dissolution rate on the microstructure of stoichiometric YBCO single crystals produced by seeded growth. Finite element modeling is used to confirm a new theory describing the cause of inhomogeneous 211 particle entrapment during growth of stoichiometric 123 crystals. Chapter 7 discusses the effect of excess 211 particles on the microstructure of YBCO single crystals produced by seeded growth. Massive 211 particle segregation during growth of excess 211 crystals is demonstrated and analyzed according to current theories. A new theory based on 211 particle dissolution is

proposed. Chapter 8 discusses the effects of oxygen annealing on the critical current density and structure of bulk YBCO single crystals. Chapter 9 presents conclusions on the relationship between processing parameters, growth rate, microstructure, and properties of bulk YBCO single crystals. The role of 211 particles in single crystal production and properties is summarized and future work is suggested.

1.5. Terminology

The yttrium-barium-copper-oxide system is denoted as YBCO. The two main YBCO phases discussed in this work are $YBa_2Cu_3O_{7-\delta}$ and Y_2BaCuO_5. The $YBa_2Cu_3O_{7-\delta}$ phase is denoted as 123 and the Y_2BaCuO_5 phase is denoted as 211 or Y-211 throughout this work. The $YBa_2Cu_4O_8$ phase is denoted as 124. Samples containing neodymium and erbium were also produced as part of the research presented here. The $NdBa_2Cu_3O_{7-\delta}$ phase is denoted as Nd-123. The $Nd_4Ba_2Cu_2O_{10}$ phase is denoted as Nd-211. The Er_2BaCuO_5 phase is denoted as Er-211. Solid solutions of Er-211 and Y-211 are denoted as (Er,Y)-211.

Nearly all 123 crystals produced for this work contain some amount of the 211 phase in particle form. The 211 particles are contained within a single crystal 123 matrix. Such a crystal is not a single crystal in the standard sense, since it contains many second phase particles. These quasi single crystals act as single crystals from the standpoint of superconducting properties as well as crystal growth theory, however. The crystals grown in this work are, therefore, denoted as single crystals if there are no 123 / 123 grain boundaries within the material.

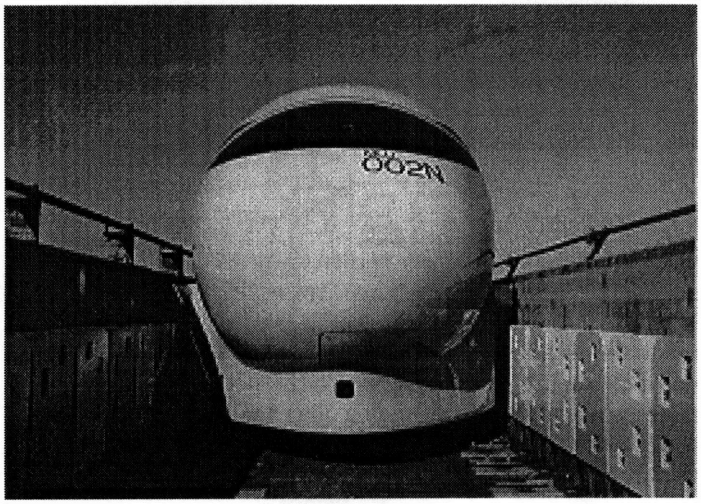

Figure 1.1. Maglev train and track produced by Miyazaki.[7]

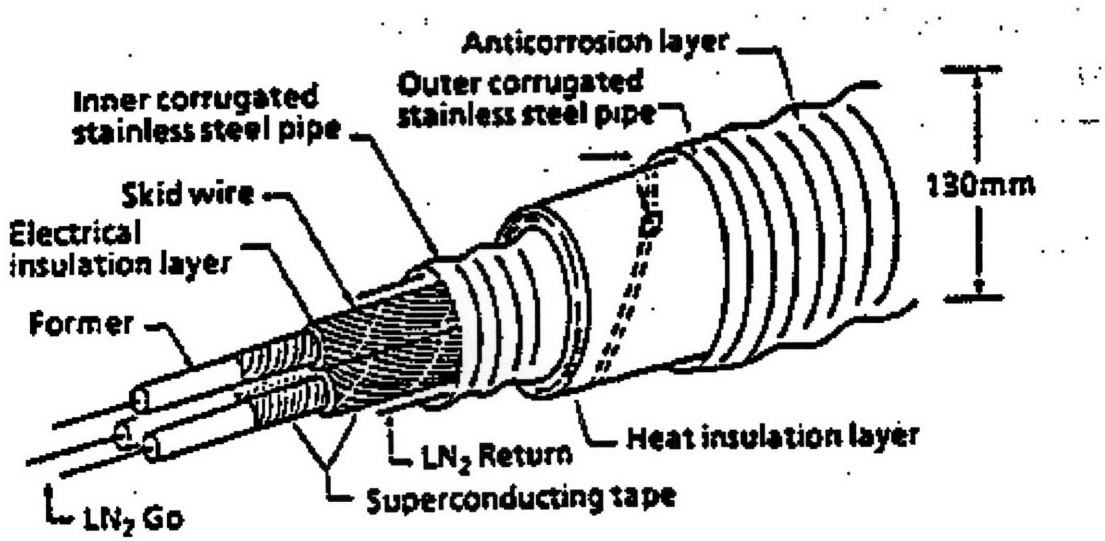

Figure 1.2. Schematic of AC high temperature superconducting cable designed by the Tokyo Electric Power Company.[8]

Chapter 2

Background

2.1. Phase equilibria in the Y-Ba-Cu-O and Nd-Ba-Cu-O systems

Figure 2.1 shows the ternary phase diagram of the YBCO system at approximately 850 °C in air.[45-46] The two main phases pertinent to this work are the 211 phase (labeled as 1:2:1 in figure 2.1) and the 123 phase (labeled as 2:1:3 in figure 2.1). Figure 2.2 shows the BaO:5/2(Y_2O_3) - 3BaO:5CuO binary phase diagram along the section a_1-a_2 in figure 2.1.[45-46] Most of the experiments conducted for this work had initial compositions either on the 123 composition line or in the 211+123 phase field. It can be seen from figure 2.2 that the 123 phase undergoes a peritectic reaction to from the 211 phase plus barium cuprate liquid around 1000 ± 2 °C. Nearly all types of melt processing methods used to produce YBCO superconductors are based on this peritectic reaction. The 123 phase also undergoes a phase transformation from a tetragonal structure to an orthorhombic structure around 500 °C. The orthorhombic phase is the superconducting 123 phase with the highest T_c.

The Nd-211 phase was used in a number of LHFZ growth experiments. Nd-123 single crystal seeds were also used in seeded growth experiments. Figure 2.3 shows the 1/6($NdBa_2Cu_3O_{7-\delta}$) - 1/8(3BaO:5CuO) binary phase diagram.[46-48] It can be seen that the Nd-123 phase forms Nd-211 plus liquid at 1090 ± 10 °C. Knowledge of this peritectic reaction was used to produce large Nd-123 crystals for use as seeds (see section 5.2.1).

2.2. Crystal structure of the 123 phase

The most technologically important superconducting phase in the YBCO system is the 123 phase. A schematic of the 123 crystal structure is shown in figure 2.4.[49] The structure of the 123 phase resembles three perovskite cells stacked on top of each other. The lattice parameters of the oxygenated orthorhombic phase are a = 3.820 Å, b = 3.885 Å and c = 11.683 Å for $YBa_2Cu_3O_{6.91}$.[50] The tetragonal 123 phase forms as a result of oxygen loss and has lattice parameters of a = b = 3.86 Å and c = 11.82 Å for the $YBa_2Cu_3O_{6.06}$ composition.[51] The high T_c superconducting orthorhombic phase can be obtained at room temperature by annealing the tetragonal phase in oxygen at a temperature slightly below 500 °C.

It can be seen from figure 2.4 that copper oxide planes run through the crystal perpendicular to the c-axis. It has been proposed that the interactions between the copper and oxygen ions in this layer form positively charged holes. These holes may reside on a Cu site in the form of Cu^{3+}, on an oxygen site in the form of O^- or between the Cu-O bond in the form of a $[Cu\text{-}O]^+$ cluster. It is theorized that current is carried without resistance by the holes in this layer, causing superconductivity.[52]

2.3. Summary of superconductivity theory

The concepts of critical temperature, critical field and critical current density are important aspects of superconductivity theory. These superconducting characteristics are all interrelated and can be affected by processing parameters used to produce the HTSC material. The elimination of weak links and the introduction of flux pinning sites can significantly enhance the superconducting properties of the material.

2.3.1. The relationship between T_c, J_c and H_c

The critical temperature, T_c, of a superconductor is the temperature at which the resistance of the material begins to drop rapidly while $T_{c,0}$ is the temperature at which the resistance actually reaches zero. Pure materials will have a T_c and $T_{c,0}$ which are approximately equal while impure materials will exhibit a resistance curve which progresses from T_c to $T_{c,0}$ more gradually. The critical current density, J_c, of a superconductor is the maximum current density which a material can carry and remain superconducting. If this critical current density is surpassed, the material will revert to a non-superconducting state, even below T_c. Superconductivity is also dependent on the magnetic field surrounding the material. Below a certain critical field, H_c, type II superconducting materials completely expel magnetic flux. This phenomenon is known as the Meissner effect. As the field is raised above H_c, magnetic flux lines penetrate the superconductor and the material reverts to its normal state if a strong enough magnetic field, H_{c2}, is applied. The material is said to be in a mixed state between H_c and H_{c2}.[53-54] Figure 2.5 shows the relationship between T_c, J_c and H_c.[53]

Material in the mixed state contains cylindrical regions of normal material of radius ξ, the coherence length of the material, surrounded by superconducting material extended to a distance λ, called the penetration depth. This basic unit of the mixed state is known as a vortex or fluxoid. A supercurrent flows in the superconducting region to generate one quantum of flux. This is shown in figure 2.6.[55] The equilibrium vortex density in the material increases as the magnetic field is increased between H_c and H_{c2} and the number of flux lines penetrating the material increases. Superconductivity disappears above H_{c2} when the normal cores of the fluxoids overlap.

A Lorenz force given by equation 2.1 results when an electric current is applied to HTSC materials in the mixed state:

$$f = J_s \times \frac{\Phi_0}{c} \tag{2.1}$$

where Φ_0 is the direction parallel to the flux density, J_s is the supercurrent flux density and f is the resulting Lorenz force. This force tends to move the vortices in a direction perpendicular to the applied field, resulting in an electric field, E, parallel to the current. This results in a resistive dissipation of energy.[54] The material will become normal unless the motion of the fluxoids is prevented by some mechanism.

2.3.2. Flux pinning

Critical current density has been shown to be dependent on defects in the HTSC materials. Research suggests that imperfections in the superconducting lattice which are similar in size to the vortices (i.e. on the order of the coherence length of the superconducting material) act as flux pinning centers to pin magnetic flux lines and prevent movement of the vortices. The presence of these flux pinning centers increases the critical field which the material can withstand and remain superconducting. The critical current density will also increase for a given T_c if the critical field is increased by the presence of flux pinning centers. The characteristic dimension for such a site in YBCO materials is on the order of 2 to 4 Å for the c-axis and 10 to 20 Å for the ab-axis.[27,54] Many researchers have found that the critical current density is highest in the ab-direction and decreases as the angle between the applied field and the c-axis of the crystal is increased.[11-12,25-27,56-58] The similarity between the c-axis coherence length and the separation between the copper-oxygen planes in the 123 crystal structure suggests that the basic structure of the crystal is responsible for intrinsic flux pinning when the magnetic field is applied perpendicular to the c-axis of the crystal.[25-27] Tachiki et al.[25-26] have supported this theory through calculations of the necessary pinning force.

Tachiki et al.[25] also theorized that critical current densities in YBCO materials can be enhanced by the presence of additional flux pinning sites in the form of microstructural defects. Gerber et al.[28] found that the density of screw dislocations in thin films of YBCO was extremely high (10^9 cm^{-2}) and theorized that the high critical current densities in thin film materials were a result of high flux pinning by these defects. Jin et al.[29] found through TEM analysis that melt textured samples have more than 2 orders of magnitude more screw dislocations than sintered bulk YBCO samples. They attributed the fact that thin films have higher J_c values to this phenomenon. Mannhart et al.[32] have also reported the improvement in critical current densities with the increase of screw dislocation density in bulk YBCO materials. Other researchers have suggested that flux pinning takes place due to twin boundaries which form in the 123 crystal when it undergoes the tetragonal to orthorhombic phase transformation.[44,59] Many researchers have also speculated that flux pinning takes place via stacking faults and dislocations in the 123 crystal.[31,44]

It has also been shown that J_c is increased by the presence of 211 particles in YBCO materials. The 211 particles themselves are much larger than the coherence length of YBCO materials and can, therefore, not act as pinning centers directly. The relationship between 211 particles and enhanced flux pinning is discussed in section 2.7. Although many theories have been presented, the exact mechanism by which flux pinning occurs in the YBCO system has yet to be identified. It is, therefore, crucial to investigate methods of introducing effective pinning centers in order to further enhance the J_c of bulk YBCO materials.

2.3.3. Weak links

Critical current densities in polycrystalline YBCO materials have been found to be 2 to 4 orders of magnitude lower than bulk single crystals or thin film materials.[60] This

decrease in J_c values for polycrystalline materials is due to the presence of high angle grain boundaries which act as weak links between the grains. Researchers believe that high structural disorder at the grain boundaries acts as a barrier to current flow or as an easy path for flux flow.[15-17] The J_c decreases as the misorientation between the copper-oxygen planes on each side of the grain boundary increases.[15] J_c values were found to decrease by almost 2 orders of magnitude for grain boundary misalignment values from 0° to 20°. The dislocation arrangement at the grain boundaries was shown to be the most important factor in the determination of the critical current densities across the grain boundaries in these materials.[16] Dimos et al.[16] suggested that the superconducting order parameter is depressed in the region of the grain boundary. They theorized that this was due to structural disorder at dislocation cores and from distortions caused by the strain field of the grain boundary. The grain boundary area through which superconducting current flow can occur will be less than the actual area of the boundary if the superconducting order parameter is depressed at each dislocation core. The functional area of the grain boundary depends on the spacing between the dislocations. The decrease in J_c with misorientation angle saturates at angles above approximately 20°, when the dislocation cores at the grain boundary begin to overlap.[16]

The problem of high angle grain boundaries acting as weak links is less significant in materials based on thallium and bismuth, two families of superconducting materials which have also been researched extensively. Current flows preferentially in the c-direction across the generally only slightly mis-aligned (001) twist boundaries, which are the most common grain boundaries in the main superconducting materials in these families of compounds.[154] The dissipation characteristics of polycrystalline materials of these compounds is dominated by flux motion within the grains, rather than weak-links between the grains. The fact that these materials exhibit poor intrinsic flux pinning results in extensive flux motion at temperatures above 30 K.[61] The problems of weak links in YBCO materials and low intrinsic flux pinning in bismuth- and thallium-based superconductors must be minimized in order to use these materials in tapes and wires

composed of polycrystalline materials. The requirements of many bulk HTSC applications requiring high J_c values can be met by components with length scales on the order of those of single crystal HTSC materials, however. The production of single crystals of YBCO materials eliminates the problem of grain boundaries, thereby making YBCO materials good candidates for these bulk HTSC applications.

Research has also shown that melt-growth of YBCO materials produces materials with special high-angle grain boundaries which do not act as weak links. It was found that melt growth allows the YBCO crystals to adopt low-energy orientations between crystals sharing a grain boundary.[15] Zhu et al.[62] showed that such boundaries can be described through a constrained coincident-site lattice (CCSL). Both grains on this type of grain boundary share many lattice sites at the boundary.[15,62] These types of high angle grain boundaries within melt-grown materials can therefore carry relatively high critical currents. A great deal of research has therefore been directed toward processing methods involving melt-growth of YBCO materials.

Barium cuprate phases have also been found to wet grain boundaries and form nonsuperconducting layers between grains in polycrystalline materials.[19] The presence of nonsuperconducting phases at the grain boundaries can adversely affect critical current densities because of the low coherence length of YBCO materials relative to the width of the grain boundaries.[15] The fact that critical current densities are anisotropic in YBCO materials, as discussed in the previous section, is an additional reason for the overall decrease in J_c in polycrystalline materials. Some grains in a polycrystalline sample will be oriented in high J_c directions relative to current flow, while other grains will be oriented in directions of lower J_c. The overall J_c of the polycrystalline sample will, therefore, be lower than that of a textured or single crystal material. This factor in the reduction of J_c values in polycrystalline materials is heavily outweighed by the problem of high angle grain boundaries, however.

Melt-texturing and single crystal growth of 123 materials have been investigated by many researchers in an effort to eliminate weak links and increase critical current densities.[10-13,14,21-24,33,35,43,63-72] Figure 2.7 shows the various J_c values presently obtained for different types of YBCO materials based on processing methods.[60] It can be seen that materials with less weak links and more flux pinning centers exhibit higher J_c values. It can also be seen from figure 2.7 that single crystal materials have the highest reported J_c values of the bulk materials due to the fact that all of the problems associated with the presence of high angle grain boundaries are eliminated. The work presented here was performed on melt-grown single crystal YBCO materials for this reason.

2.4. Growth mechanism of YBCO crystals

Melt processing of YBCO materials begins by heating the 123 phase above the peritectic temperature to form 211 and barium cuprate liquid by reaction 2.2:

$$2YBa_2Cu_3O_{6.5}\ (s) = Y_2BaCuO_5\ (s) + [3BaCuO_2 + 2CuO]\ (liq) \qquad (2.2)$$

123 material nucleates as the temperature is brought below the peritectic temperature. Growth of the 123 phase occurs via the dissolution of 211 particles in the barium cuprate liquid near the 123 growth interface. This has been shown very clearly using high temperature imaging and hot stage X-ray diffraction by Rodriquez et al.[73] The solubility of yttrium in the barium cuprate liquid is approximately 2%.[74-75] 211 particles dissolving in the barium cuprate liquid, therefore, supply nearly all of the yttrium required for the formation of the 123 phase. An yttrium concentration gradient in the liquid at the 123 interface relative to the liquid far away from the interface is the driving force for the dissolution of the 211 particles and the diffusion of yttrium from the dissolving particles

to the 123 growth interface. Two basic theories have been developed to explain the formation of this yttrium concentration gradient near the 123 growth interface.[10,33]

Cima et al.[33] proposed that the compositional driving force for 211 particle dissolution and yttrium diffusion is a result of constitutional supercooling in front of the 123 interface. Figures 2.8 and 2.9 illustrate the solidification model proposed by Cima et al.[33] Figure 2.8 a) illustrates the 211 particles (α phase) in the barium cuprate liquid in front of the 123 (γ phase) growth interface. The 211 particles are separated by a distance $2l$. Diffusion of yttrium from the dissolving 211 particles to the 123 interface takes place over a distance l. Cima et al. assumed that the 211 particles are in interfacial equilibrium with their surrounding liquid and are large enough that the effect of radius of curvature on melting point is negligible. Figure 2.9 shows an expanded section of the peritectic region of the YBCO phase diagram.[33] The dashed line is the metastable extension of the 211 (α phase) liquidus. The temperature at the 123 (γ phase) interface is given by:

$$\Delta T_p = \Delta T_G + \Delta T_S + \Delta T_C \tag{2.3}$$

where ΔT_P is the undercooling below the peritectic temperature, ΔT_G is the depression of the integrated temperature resulting from the temperature gradient, ΔT_S is the maximum "constitutional supercooling" ahead of the 123 interface and ΔT_C is the temperature depression resulting from the deviation in solute concentration at the 211 interface from that of the peritectic liquid composition. These quantities are shown in figure 2.8 c). The resulting yttrium concentration gradient in front of the 123 interface is shown in figure 2.8 b) where C_{LP} is the yttrium content of the peritectic liquid, $C'_{L\alpha}$ is the yttrium content of the liquid in contact with the 211 particles and $C^0_{L\gamma}$ is the yttrium content of the liquid in equilibrium with the 123 interface. Cima et al. developed the following equation for maximum growth rate of a planar interface by equating the solute rejected from the growing 123 interface with that diffusing into the liquid:

$$R_{max} = \frac{D_L}{l\left(C_{S\gamma} - C_{LP}\right)}\left[\frac{\left(\Delta T_s\right)_{max} + Gl}{m_{L\gamma}}\right] \tag{2.4}$$

where R_{max} is the maximum growth rate of a planar 123 interface, l is half the distance between the 211 particles in the barium cuprate liquid, D_L is the diffusion coefficient of yttrium in the liquid, $C_{S\gamma}$ is the yttrium content of the 123 phase, C_{LP} is the yttrium content of the liquid, G is the temperature gradient, $(\Delta T_S)_{max}$ is the maximum constitutional supercooling ahead of the 123 interface and $m_{L\gamma}$ is the slope of the equilibrium 123 liquidus (assumed to be constant). Cima et al. assumed that any perturbations in the 123 growth interface resulting from the presence of a supercooled region in front of it will be limited by the high surface energy of the faceted YBCO faces.[33]

An alternative solidification model explaining the formation of an yttrium concentration gradient near the 123 growth interface was proposed by Izumi et al.[10] This model also assumed that the rate limiting step for crystal growth is the diffusion of yttrium from dissolving 211 particles. Izumi et al. suggest, however, that the yttrium concentration gradient in front of the 123 interface results from a change in the chemical potential at the 211 / liquid interface caused by the curvature of the 211 particles.[10,15] The change in chemical potential is related to the undercooling by the Gibbs-Thomas equation:

$$\Delta T_r = \frac{2\Gamma}{r} \tag{2.5}$$

where ΔT_r is the undercooling, r is the radius of the 211 particle and Γ is the Gibbs-Thomas coefficient given by:

$$\Gamma = \frac{\sigma}{\Delta E_F} \tag{2.6}$$

where σ is the interfacial energy between the 211 particles and liquid and ΔE_F is the volumetric energy of fusion. The resulting yttrium concentration gradient at the 123 interface can then be determined from the phase diagram by:

$$\Delta C = C_L^r - C_L^\infty = \frac{2\Gamma}{rm_L} \tag{2.7}$$

where ΔC is the difference between the yttrium concentration in the liquid at the 211 particles and that at the 123 interface, C_L^r is the yttrium concentration at the 211 particle, C_L^∞ is the yttrium concentration in the liquid in contact with the 123 interface and m_L is the 211 liquidus slope. The velocity of the 123 interface can be calculated from the initial size distribution of the 211 particles, the initial volume fraction of the 211 phase, the diffusivity of yttrium in the liquid, the Gibbs-Thomas coefficient, the maximum 211 dissolution rate, and a number of other variables.[10,15]

Both solidification models suggest that maximum growth rate is dependent on the size of the 211 particles, either directly or by the spacing between the 211 particles which is proportional to the size of the particles. Both theories suggest that growth rate increases with decreasing 211 particle size. Both theories also calculate maximum growth rates for planar interfaces of 123 crystals of a few millimeters to a few cm per hour.[10,33]

2.5. Solidification processing of YBCO single crystals

High angle grain boundaries in YBCO materials act as weak links and degrade the superconducting properties of the material, as described in section 2.3.3. Salama et al.[76] introduced the concept of melt growth to produce larger 123 crystals. Jin et al.[21] developed a new melt texturing process in an effort to produce an aligned microstructure in YBCO materials. Much research since then has been directed toward the development of melt growth processing methods which result in textured or single crystal materials.[10-13,14,21-24,33,35,43,63-72,78] This work focuses on single crystal growth methods in order to maximize the J_c values of the bulk HTSC materials produced. The two single crystal growth methods explored in this work are seeded growth and laser heated floating zone (LHFZ) growth. Background information on these and other single crystal growth techniques is, therefore, provided in the following sections. Information on melt texturing methods which do not produce single crystal materials, such as melt-textured-growth (MTG),[14,21] quench-melt-growth (QMG),[22] melt-powder-melt-growth (MPMG)[23] and powder-melting-process (PMP),[24] can be found elsewhere.

A number of techniques have been developed to grow YBCO single crystals. These include Bridgeman growth,[78] floating zone growth,[10-12,33,63-65] solute rich liquid crystal pulling (SRL-CP),[79-81] seeded growth,[35] flux growth[66-67,69-72] and infusion growth[13,43]. All of these processes rely on growth from a melt. Single crystal materials can be produced by either directional or non-directional solidification. Some of the most commonly used growth methods are discussed in the following sections.

2.5.1. Directional solidification

Floating zone growth and Bridgeman growth are directional solidification processes which grow single crystals along only their fast growth axes. The ab-axis has been shown to be the fast growing axis at high undercoolings.[11,33,63] Bridgeman growth is a simple directional solidification method performed in a furnace. A bulk YBCO rod or bar is pressed and solidified in a temperature gradient by pulling it horizontally through the furnace. The temperature gradient within the furnace is produced by locating heating coils next to a water cooled quench tank. The YBCO precursor is melted in a crucible within the furnace. The 123 phase then nucleates and grows as the material is pulled under the quench tank and the sample temperature falls below the peritectic temperature. Growth rate can be controlled by the pulling speed and temperature gradient can be controlled by the relative temperatures of the furnace and quench tank. One major disadvantage of this method is that most of the sample is molten during its residence time in the furnace and contamination due to interaction with the crucible material can take place.[78]

Floating zone growth in general involves passing a sintered YBCO fiber vertically through a smaller hot zone. The hot zone can be produced using a number of heat sources. Laser heated floating zone (LHFZ) growth was used to produce YBCO single crystals for this study and is described in chapter 4. Other floating zone growth methods include electrically heated floating zone growth and floating zone growth using halogen or infrared lamps. Some methods of floating zone growth involve moving the precursor fiber through the zone while others involve moving the hot zone past the rigidly mounted fiber. The section of the polycrystalline fiber within the hot zone melts to form barium cuprate liquid and 211 phase. 123 phase nucleates as the fiber moves through the zone and cools below the peritectic temperature. Single crystal fibers can be produced by controlling the temperature gradient within the zone and the pulling rate of the fiber.

Figueredo et al.[11,33] found that growth front microstructure is dependent on pulling rate of the fiber as well as the temperature gradient within the zone, with pulling rate being the more dominant factor. Figure 2.9 shows the dependence of interface microstructure on growth rate and temperature gradient.[11,33] Figure 2.10 shows a schematic of the different interface structures.[11,33] It can be seen that YBCO single crystal fibers can be produced at a growth rate of up to approximately 3 μm/s in a temperature gradient of $1x10^6$ K/m. This is near the current maximum achievable growth rate for YBCO single crystals since LHFZ growth is able to produce the highest temperature gradient of all growth methods discussed here.[11-12] J_c values of more than $1x10^5$ A/cm^2 at 77 K were achieved for samples produced by LHFZ growth (see figure 2.7).[11-12] Other floating zone techniques produce YBCO materials with lower critical current densities.[10]

The solute rich liquid crystal pulling (SRL-CP), developed by Yamada et al.,[79] is a directional solidification method used to produce large YBCO single crystals.[79-81] 211 material in a copper rich melt is placed in a crucible and heated from the bottom. The temperature at the surface of the melt is controlled to be near the peritectic temperature of the YBCO material. The material at the bottom of the crucible is at a higher temperature than the material at the top, which produces a temperature gradient within the melt. The yttrium solute is transported from the higher temperature region at the bottom of the melt to the surface of the melt through natural and forced convection. A thin film of YBCO is used as a seed crystal to solidify YBCO at the surface of the melt. The seed is rotated rapidly and pulled from the melt to produce a semi-continuous single crystal.[79-81] The advantage of this growth method is that large single crystals can be produced. The disadvantage is that no 211 particles are incorporated into the YBCO material. This may degrade the properties of the 123 crystal, based on a number of factors discussed in section 2.7. Grain boundaries have also been observed in crystals produced by SRL-CP, which may degrade the properties of the crystals produced by this method.

2.5.2. Nondirectional solidification of YBCO single crystals

Seeded growth, flux growth and infusion growth are all non-directional solidification methods. These solidification processes grow crystals along three axes. The shape and orientation of the single crystal depend on the attachment kinetics at the various interfaces and the process parameters used during growth. Seeded growth was one of the techniques used to produce YBCO single crystals for this study and is described in chapter 5.

Flux growth[66-67,69,71-72] involves heating a YBCO material above the peritectic temperature to form a melt. The melt is then slowly cooled below the peritectic temperature, at which point 123 crystals begin to nucleate. Further slow cooling or soaking at a particular undercooling results in three dimensional growth of 123 single crystals. Much research has been performed on growth of YBCO materials from different melt compositions.[66-67,69-70,72] Researchers found that single crystals can be obtained through use of a flux composed of excess barium and copper.[66-67,69-72] Flux growth has the disadvantage that nucleation of 123 crystals cannot be controlled well. Many 123 crystals usually nucleate within the melt, producing large numbers of single crystals which are extremely small. It is also difficult to remove the crystals from the solidified flux and separate them from each other after processing. Boutellier et al.[66] have minimized the problem of flux separation by developing a process where a porous ceramic is immersed in the liquid flux at the end of growth. The porous material wicks the flux away from the YBCO crystals. This method works better than standard flux growth, although the problems of small crystal size and difficulties in crystal separation are still present. Although flux growth of single crystals is not a method which can produce crystals of the size necessary for industrial use, it is a simple method to produce single crystals of YBCO which can be studied to examine the relationships between processing and microstructure.

Infusion growth, also known as the isothermal peritectic reaction (IPR) process[13,43] is performed by producing a sintered mass of 211 phase containing interconnected pores. The 211 mass is then infused with a Ba-Cu-O glass melt. The sintered 211 particles react with the barium cuprate liquid to form 123 crystals. This process has similar drawbacks to standard flux growth in that the number and size of the resulting 123 crystals cannot be controlled. The infusion growth process is of scientific interest, however, because it uses a sintered mass of 211 particles. Sintering the 211 particles together renders them immobile except directly in front of the 123 interface where they dissolve to form the 123 phase. As will be discussed in chapter 7, the immobility of the 211 particles makes the infusion growth process an ideal method for testing the validity of 211 particle segregation via particle pushing during melt growth.

2.6. 123 platelet formation

It has been found that 123 single crystals produced by melt growth from excess 211 materials are actually composed of 123 platelets oriented perpendicular to the c-axis of the 123 crystal. These platelets are interconnected and oriented parallel to each other such that the overall material is considered a single crystal. YBCO single crystals made up of this platelet structure will act as a single crystal to current traveling through the superconducting material, since the current can travel around the platelet gaps to find a single crystal path through the entire crystal.[15,68,82]

Platelet formation has been studied extensively by Schmitz et al.[68] and Goyal et al.[82] It was theorized that the platelet structure results from 211 particles intersecting the 123 interface, resulting in localized impediments to uniform growth of the 123 crystal. Figure 2.12 shows how platelets are nucleated by 123 material growing around a 211 particle at the interface.[82] Figure 2.12 a) shows how a 211 particle intersects the 123 interface in

the semi-solid melt. 211 particles generally intersect the 123 interface asymmetrically, resulting in unequal growth rates around the 211 particle due to anisotropy in the growth rates parallel and perpendicular to the 123 platelet growth face, as shown in figure 2.12 b). The result is a new platelet gap, shown in figure 2.12 c), which separates two parallel platelets. The connection between this type of platelet structure and 211 particle segregation in YBCO materials containing excess 211 particles will be discussed in chapter 7.

2.7. Role of 211 particles

211 particles have been found to play many roles in the processing, properties and performance of YBCO superconducting materials. As discussed in section 2.4, 211 particles act as a yttrium source during melt growth of YBCO materials. 211 particles dissolve in the yttrium concentration gradient in front of the 123 crystal interface. Changes in 211 particle characteristics can significantly affect the growth rate of YBCO materials. Knowledge of 211 volume fraction, particle size and distribution are, therefore, important in order to predict the growth characteristics of YBCO materials. The presence of 211 particles within the semi-solid zone in floating zone growth methods, as well as other melt growth processes not involving crucibles, prevents the flow of liquid out of the semi-solid zone. Capillary forces produced by the presence of 211 particles within the melt increase the semi-solid zone stability.[11,63]

It has been found that 211 particles coarsen as they sit in the semi-solid melt produced via the peritectic decomposition of the 123 phase, described by equation 2.2. 211 particle coarsening during 123 crystal growth processes can effect the size and distribution of the 211 particles within the semi-solid melt. 211 particle coarsening will, therefore, affect the growth characteristics and properties of the 123 crystals. The addition of various

dopants materials has been shown to decrease the coarsening rate of 211 particles in the semi-solid melt.[36,83-93] Knowledge of 211 particle coarsening and the effect of dopants on this process are essential in order to predict the solidification characteristics and properties of YBCO materials. This will be discussed further in chapter 3.

The presence of 211 particles within solidified YBCO materials has also been linked to the superconducting properties of the material. A number of researchers have reported an increase in J_c with the incorporation of 211 particles into the 123 matrix during peritectic solidification. Murakami and others used the uniform distribution of very fine 211 particles to significantly enhance J_c values in YBCO materials.[23,94-95] The results of this work triggered many other researchers to investigate the effectiveness of 211 particles as pinning centers in the YBCO system.[88,96-99] These studies reveal the important role of 211 inclusions in pinning flux in 123 materials prepared using melt-texturing. 211 particles are too large to act as flux pinning centers directly, as described in section 2.3.2. Mechanisms explaining the correlation between 211 inclusions and flux pinning have been proposed by a number of investigators. Murakami et al. proposed that the interface between the 211 particles and the 123 matrix acts as a pinning center.[94] Wang et al.[100] and Yamaguchi et al.[101] suggested that the stacking faults around the 211 inclusions act as pinning centers. Murakami et al.[22] have also speculated that flux pinning takes place via dislocations which form around 211 particles due to stresses. 211 particles have also been linked to the theory that twin structures in YBCO materials contribute to flux pinning.[59] Research has shown a relationship between twin spacing and 211 particle distribution within the 123 crystal.[18,44]

211 particles have also been linked to platelet formation during melt growth of 123 single crystals, as described in section 2.6 and shown in figure 2.12. Jin et al. have shown that platelet spacing correlates with 211 particle spacing and scales almost linearly with 211 particle size.[29,89] It has also been shown that the platelet boundaries become cleaner as the 211 particle size is reduced to below 1 micron.[29,102] As discussed in section 2.3.3,

critical current densities are severely reduced by the presence of second phase layers which act as weak links in YBCO materials.

The presence of 211 particles within solidified YBCO materials has also been related to the reduction of crack formation. Murakami et al. suggested that 211 particles suppress crack formation by accommodating strain along the c-axis of the crystal during the tetragonal to orthorhombic phase transition.[95] Similar results were found by Jin et al.[102]

Significant 211 segregation within 123 crystals produced by non-directional melt growth processes has been observed.[34-43] Variations in 211 particle distribution with superconducting materials can significantly impact superconducting properties as well as crack formation in YBCO materials. This phenomenon is examined in chapter 6 and 7.

Research on the effects of 211 particles on the solidification and properties of YBCO is important for all of the reasons listed above. A significant part of the work presented here is, therefore, related to examining the role of 211 particles in melt processing of YBCO single crystal materials.

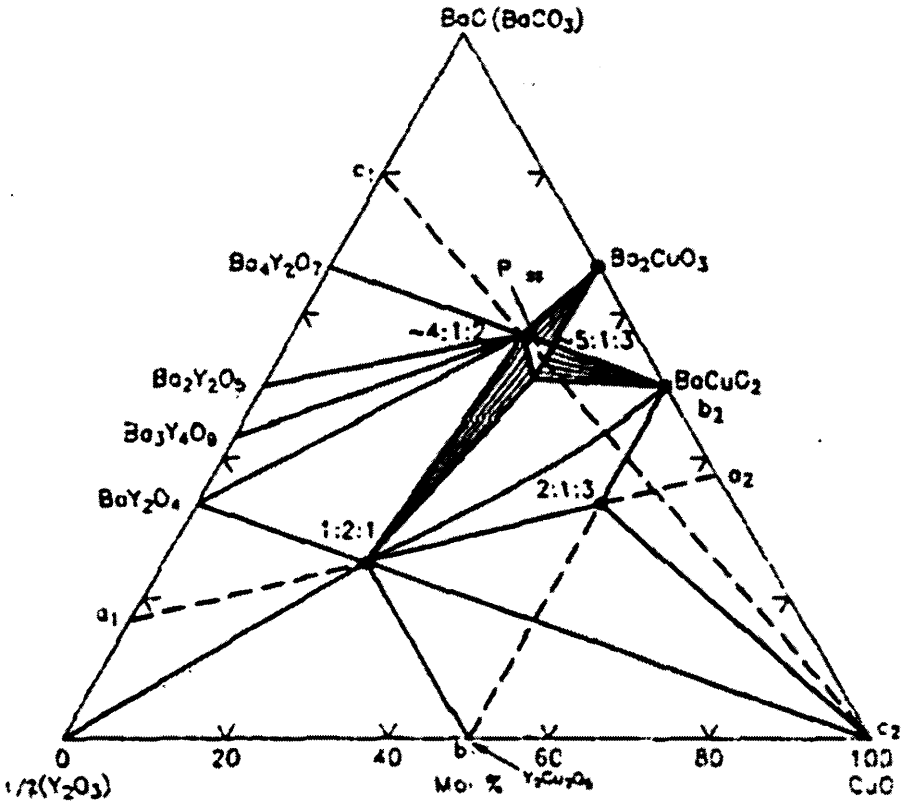

Figure 2.1. Ternary phase diagram of the YBCO system at approximately 850 °C in air.[45-46]

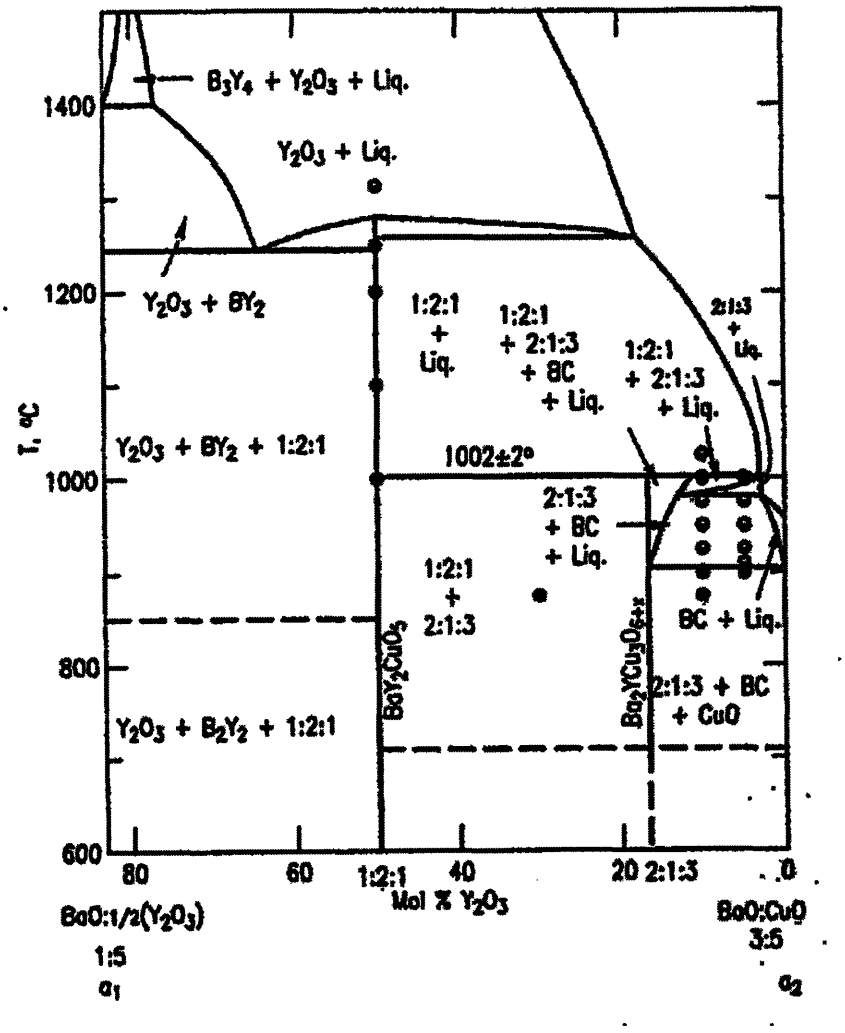

Figure 2.2. BaO:5/2(Y_2O_3) - 3BaO:5CuO binary phase diagram along the section a_1-a_2 in figure 2.1.[45-46]

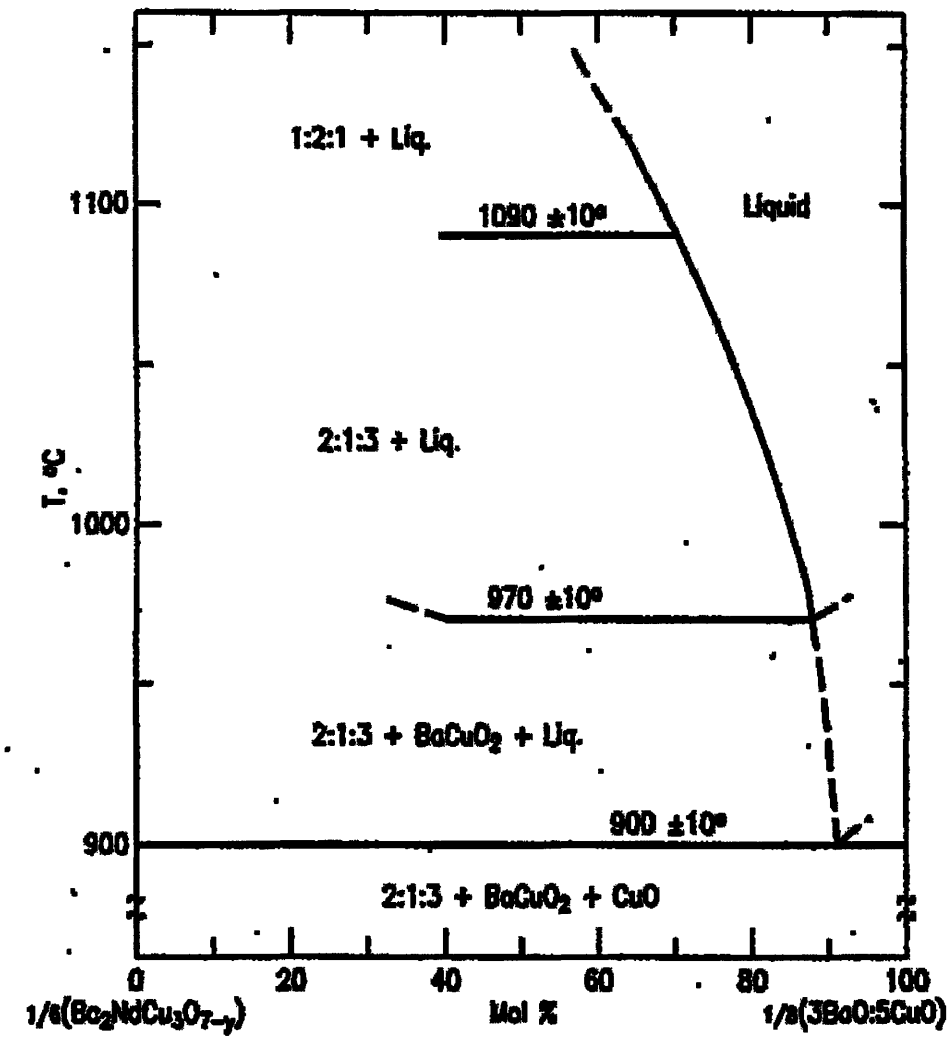

Figure 2.3. $1/6(NdBa_2Cu_3O_{7-\delta})$ - 1/8(3BaO:5CuO) binary phase diagram.[46-48]

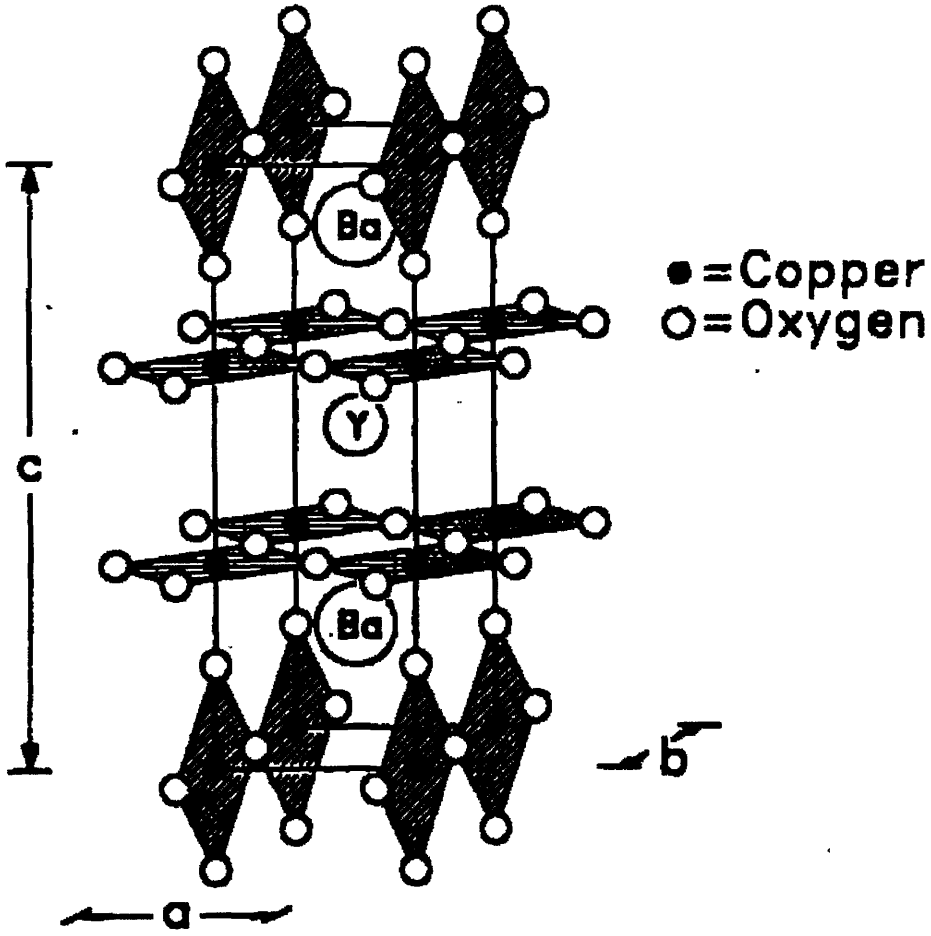

Figure 2.4. Schematic of the 123 crystal structure.[49]

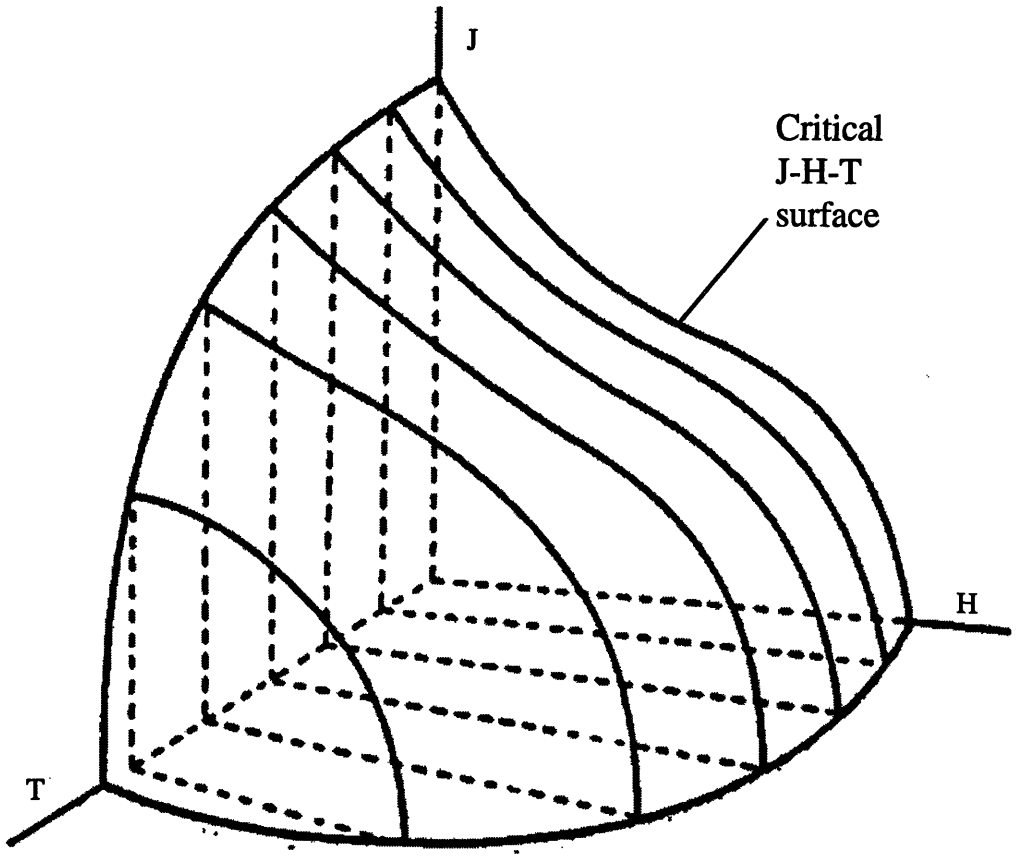

Figure 2.5. Relationship between T_c, J_c and H_c in HTSC materials.[53]

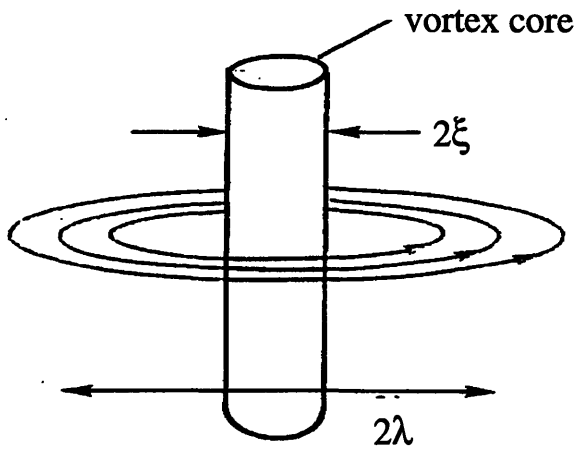

Figure 2.6. Schematic of a fluxoid produced by magnetic flux penetration in the mixed state of HTSC materials. The fluxoid consists of a vortex core surrounded by a supercurrent.[55]

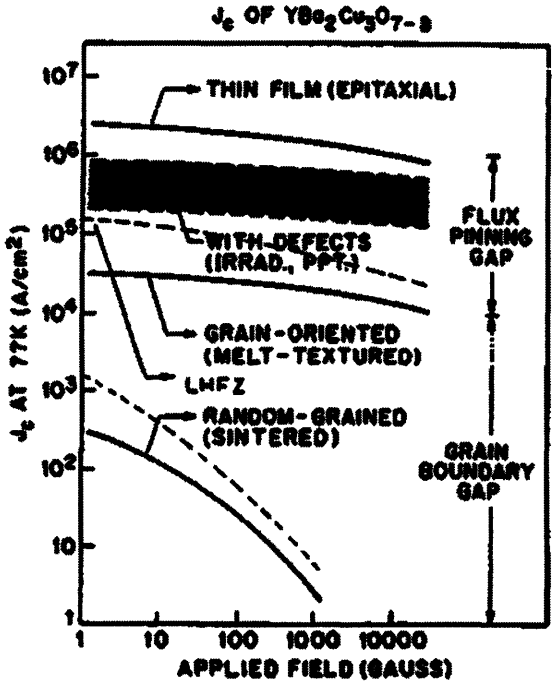

Figure 2.7. Transport current density vs. applied field for various types of YBCO materials.[60]

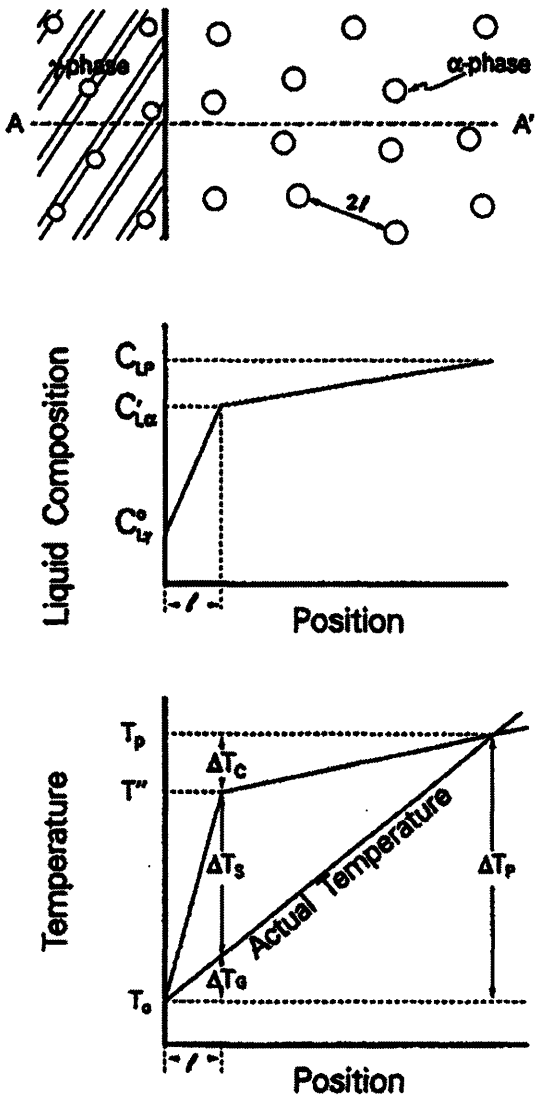

Figure 2.8. a) Schematic of the 211 particles (α phase) in the barium cuprate liquid in front of the 123 (γ phase) growth interface. The resulting yttrium concentration gradient in front of the 123 interface is shown in figure b). Figure c) shows the resulting temperature profile at the 123 interface.[33]

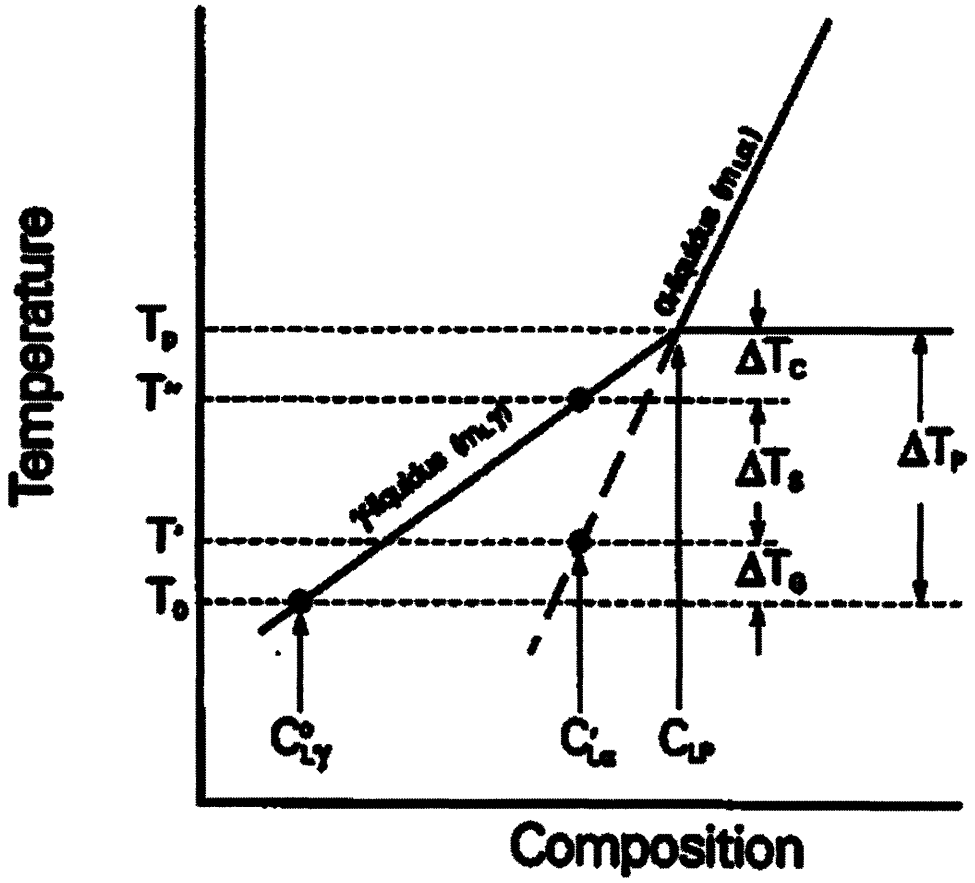

Figure 2.9. Expanded section of the peritectic region of the YBCO phase diagram.[33]

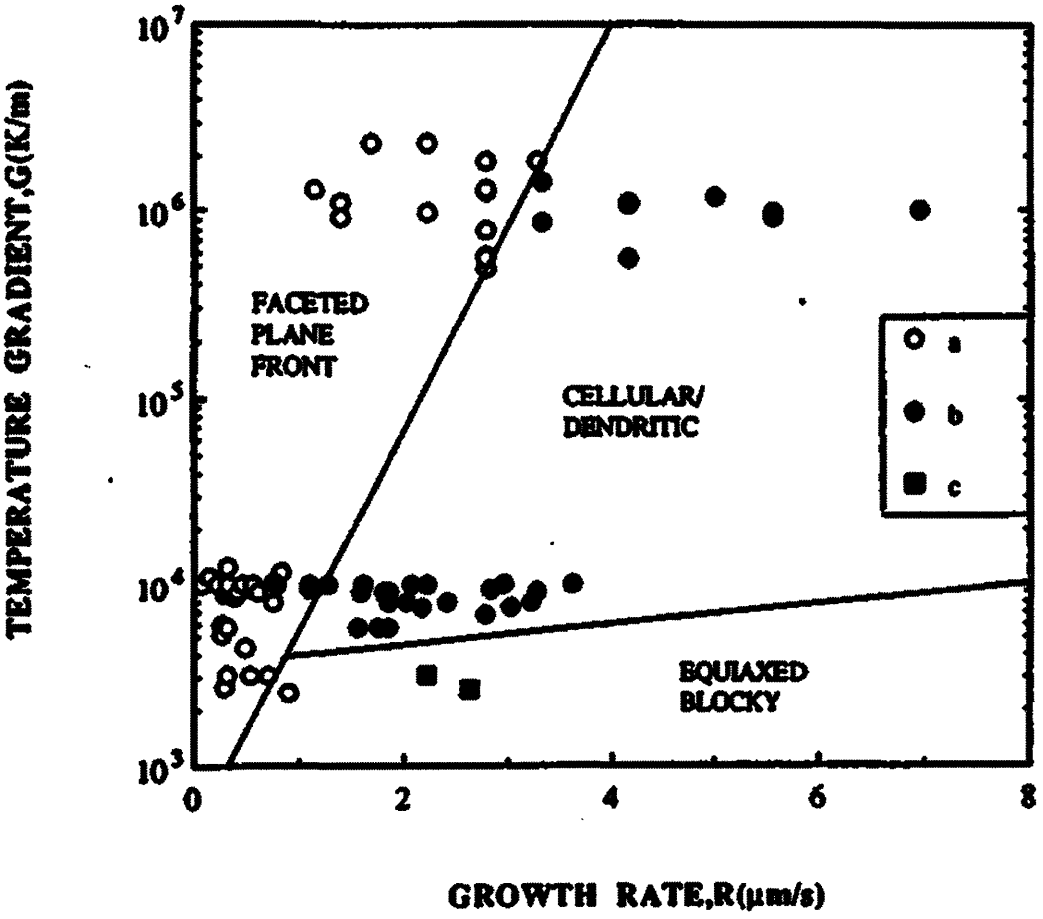

Figure 2.10. Dependence of interface microstructure on growth rate and temperature gradient for LHFZ growth of YBCO materials.[11,33]

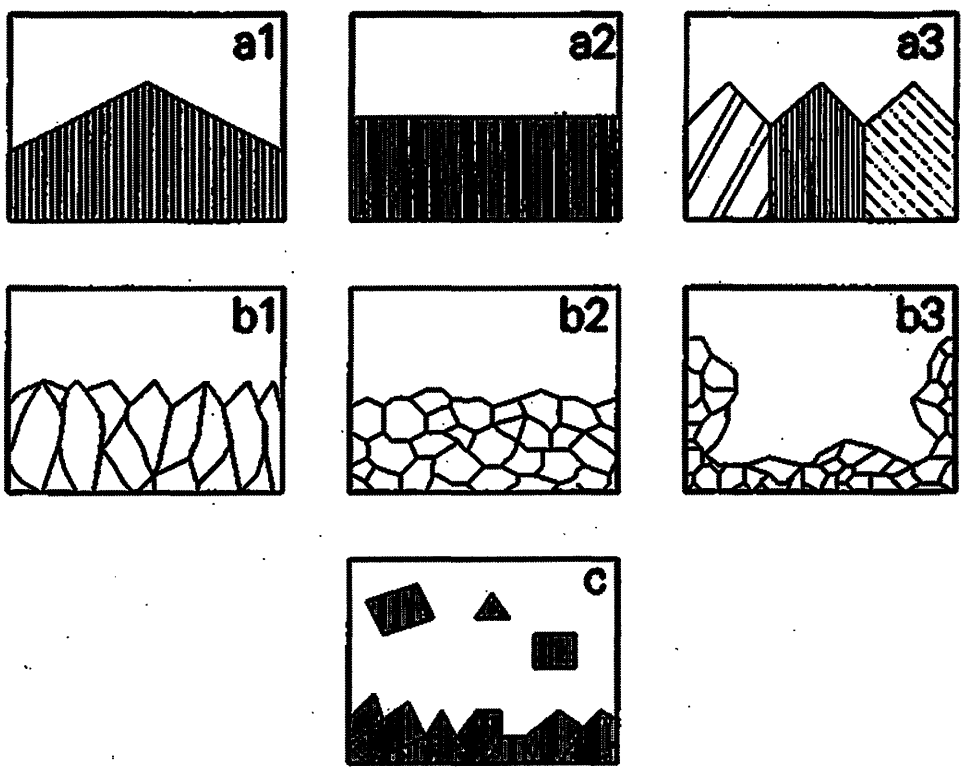

Figure 2.11. Schematic of the different interface structures found during LHFZ growth of YBCO materials.[11,33]

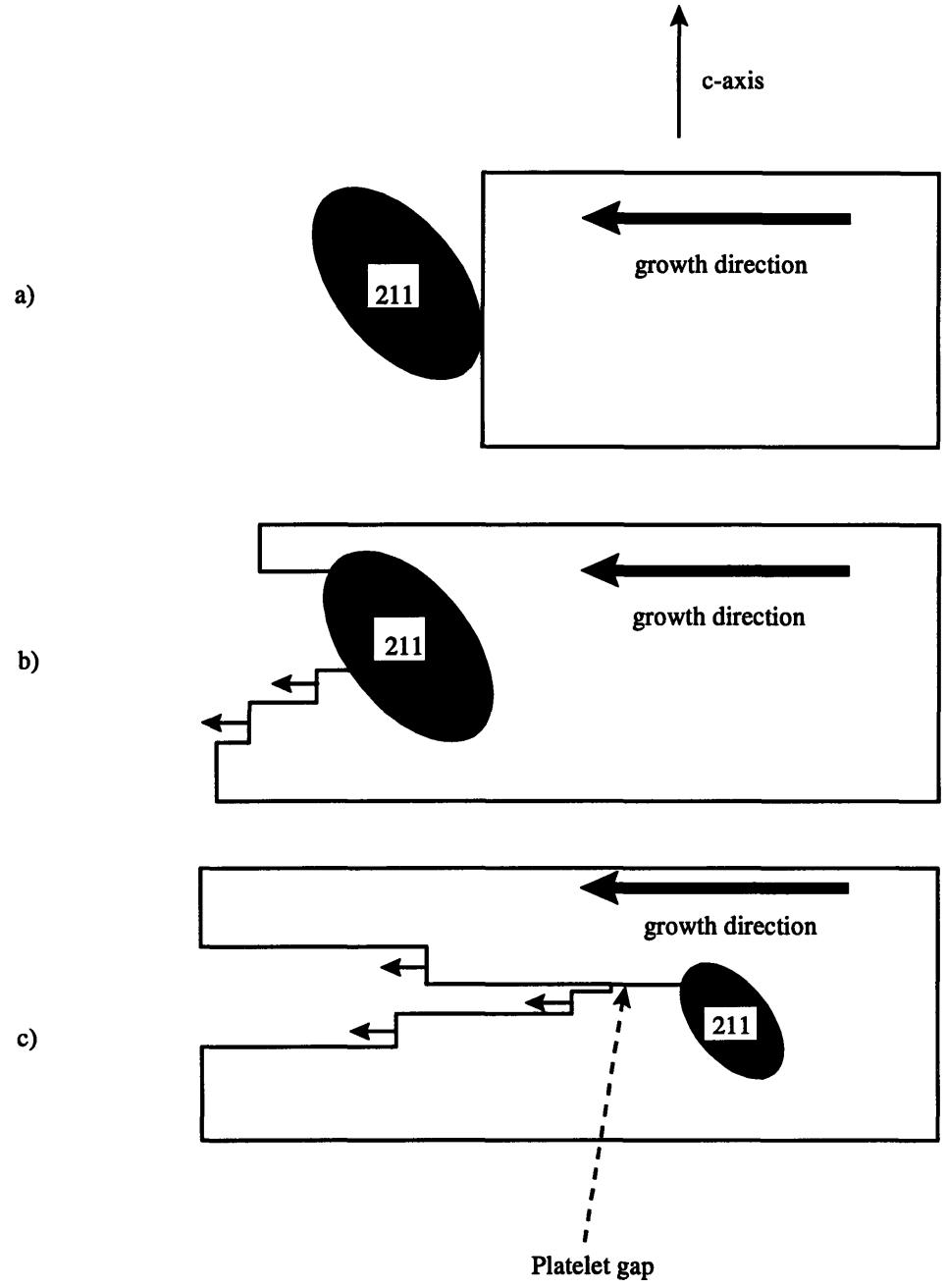

Figure 2.12. a) Schematic of a 123 platelet intersecting a 211 particle in the semi-solid melt. b) 211 particles generally intersect the 123 interface asymmetrically, resulting in unequal growth rates around the 211 particle due to anisotropy in the growth rates parallel and perpendicular to the 123 platelet growth face. The result is a new platelet gap, shown in figure c).[82]

Chapter 3

Coarsening of 211 particles in the semi-solid melt

3.1. Introduction

It is known that 211 particle size plays an important role in microstructural development, growth rate, and superconducting properties of YBCO single crystals. Knowledge of the formation of 211 particles, as well as their coarsening behavior, is important for understanding and controlling 211 particle size. Experiments were carried out to understand 211 particle formation and coarsening. It is known that the 211 phase within the semisolid melt of 211 plus barium cuprate liquid, formed during melt processing of YBCO materials, has two main points of origin. The original 211 particles mixed with the 123 phase remain in the semi-solid melt after heating above the peritectic temperature. Additional 211 phase is produced by the peritectic melting of the 123 phase described by equation 2.2. 211 material from both of these sources combine to form particles within the semi-solid melt. These particles, in turn, undergo ostwald ripening during their residence in the melt.

Many researchers have found that the addition of other compounds to YBCO samples keeps the 211 particle size relatively small. Work in this area includes research on the addition of $BaTiO_3$,[83-84] $BaSnO_3$,[85-88,103] Ag,[89-91] $BaCeO_3$[92] and CeO_2.[92] Platinum additions have been found to be particularly effective in reducing coarsening of 211 particles.[38,85,92,104-106] A number of different theories have been suggested to explain the influence of platinum doping on decreased 211 particle coarsening. Izumi et al. suggested that the chemical potential gradient in the liquid changes as a result of Pt

additions.[93,107] Izumi et al.[93] also suggested that platinum additions increase the viscosity of the barium cuprate liquid, thereby decreasing D, the diffusivity of solute in the liquid. Varanasi et al.[85] believed that platinum additions reduced the diffusivity of solute in the liquid, as well. Other researchers suggested that the interfacial energy of 211 particles in the liquid is reduced through the addition of platinum.[104,108] Ogawa et al.[106] and Durand et al.[40] theorized that platinum additions act as nucleation sites for the formation of 211 particles produced via peritectic decomposition of the 123 phase.

211 coarsening rate in undoped and Pt-doped samples was, therefore, studied as part of the research presented here. Microstructural changes in 211 particles due to the addition of platinum and the effectiveness of platinum as a dopant to reduce 211 particle coarsening were also evaluated. Experiments were also carried out to determine which theory is the cause of decreased 211 coarsening in Pt-doped samples.

3.2. Coarsening theory

Coarsening, also known as Ostwald ripening, is the process of large particles or crystals growing at the expense of small particles or crystals in order to minimize the surface energy of the system. This process can take place in a solid, liquid or gaseous medium, so long as the diffusing species has an appreciable solubility or vapor pressure in that medium. Small particles in a system of multi-sized particles residing in a liquid medium have a larger surface area per unit volume and, therefore, an increased solubility compared to larger particles in the system. The increased solubility, c_a, of a small particle is given by the Thompson-Freundlich equation:[109-110]

$$c_a = c_o \exp\left[\frac{\gamma M 2}{\rho RTa}\right] \tag{3.1}$$

where c_o is the equilibrium solubility of a planar interface, a is the particle radius, γ is the interfacial energy (ergs/cm^2), M is the molecular weight, ρ is the density of the particle, R is the gas constant and T is the temperature. Diffusion of solute from the small particles to the large particles, shown in figure 3.1 a), takes place in a diffusion field of a given radius, r, around the particles, as shown in figure 3.1 b).[109-110]

The radii of the particles in the system change according the coarsening theory (also known as the LSW theory) developed by Lifshitz and Slyozov,[111] Wagner[112] and Greenwood.[113] The change in particle radii is given by:

$$\bar{a}^3 - \bar{a}_0^3 = k \cdot t \tag{3.2}$$

where $\bar{a}$ is the average particle radius at time t, $\bar{a}_0$ is the initial average particle radius and k, the coarsening constant, is given by:

$$k = \frac{\alpha(\phi) D c_o \gamma M}{\rho R T} \tag{3.3}$$

where $\alpha(\phi)$ is a parameter which depends on the volume fraction of the coarsening phase and D is the diffusion coefficient.[111-113] It can be seen from equation 3.2 that the particle size in a coarsening system is dependent on $t^{1/3}$ and that k, the coarsening constant, can be obtained by plotting the cube of the relative particle size vs. time and measuring the slope. Equation 3.3 shows that the coarsening rate of the particles in a system with a given volume fraction of particles can be affected by changes in T, γ and D.

3.3. Experimental procedure and analysis

Sintered YBCO precursor pellets were prepared for use in coarsening experiments. Er-211 was added to some precursor pellets in order to distinguish excess 211 phase added before melting from the Y-211 phase formed via peritectic melting of the 123 phase. Samples were heat treated for various lengths of time at a temperature above the peritectic temperature of YBCO materials to induce coarsening of the 211 particles in the barium cuprate liquid. Samples were then analyzed to examine microstructural development of the 211 particles as well as to quantify the coarsening behavior of the 211 phase with and without platinum doping. These procedures are discussed in the following sections.

3.3.1. The use of Er-211 as a marker

Er-211 was used as a marker in the coarsening experiments in order to distinguish 211 phase which was added to the precursor pellet from 211 phase formed during peritectic melting of the 123 phase. The Er-211 and Y-211 phases form a solid solution of (Er,Y)-211 when they are held together above the peritectic temperature in the presence of barium cuprate liquid.[105,114] It was assumed that (Er,Y)-211 exhibits the same coarsening behavior as Y-211 since the ionic radii of Y and Er are very similar (Y^{3+} = 0.89 Å, Er^{3+} = 0.88 Å).[105] The peritectic temperature of Er-123 is slightly lower than that of Y-123, but it was assumed that this difference did not significantly affect the coarsening characteristics of the Y-211 + Er-211 phase mixture since the temperature at which the experiments were performed was almost 100 °C higher than either peritectic temperature. It was assumed that the diffusivity of Y^{3+} and Er^{3+} within the barium cuprate liquid are comparable. This assumption was also made by other researchers performing experiments using Er-211.[105,114]

Erbium and yttrium materials can clearly be distinguished from each other using backscattered scanning electron microscopy. Er-211 will appear as a light colored phase using backscattered electron imaging, Y-211 will appear as a darker phase, and (Er,Y)-211 will have a color somewhere in between, depending on the ratio of Er to Y. This fact allows the location of the Er-211 phase to be tracked, even after extensive coarsening and mixing with the Y-211 phase has occurred.

3.3.2. Sample preparation

Three types of samples were produced for use in the coarsening experiments. Undoped stoichiometric samples were composed of 100% 123 phase. Undoped excess Er-211 samples were produced by mixing 80 wt.% 123 powder with 20 wt.% Er-211 powder. Pt-doped samples were produced by adding 1 wt.% Pt powder to the 123 + Er-211 powder mixture. The 123 powder was purchased from Seattle Specialty Ceramics (now Praxair Specialty Ceramics). The Er-211 powder was produced by mixing Er_2O_3, $BaCO_3$ and CuO with a mortar and pestle, isopressing the powder, calcining it at 950 °C in a MgO crucible in air for 18 hours and then breaking up the pellet into powder form. This process was repeated three times to ensure complete reaction of the materials. The final Er-211 powder had an average particle size of 2.5 microns. All powder was examined by X-ray powder diffraction and found to be phase pure.

All types of powder combinations were mixed with a mortar and pestle until homogeneity was achieved. The powder mixtures were then filled into rubber tubes with inside diameters of approximately 2 mm. The rubber tubes were sealed and isostatically pressed under 40,000 lbs of pressure to produce compacted rods. The rods were sectioned into pellets approximately 4 mm in length. The pellets were then sintered at 950 °C for 10

hours in order to densify the samples. These samples were then used as precursors for the coarsening experiments.

3.3.3. Heat treatment

The coarsening experiments were performed in an electrically heated furnace. A schematic of the furnace construction is shown in figure 3.2. The heat source in the furnace consisted of two Kanthal® wire coils connected to variable voltage controllers. The temperature profile in the furnace was varied by changing the spacing and diameter of the Kanthal® coils. The maximum temperature in the hot zone was controlled by varying the voltage across the Kanthal® coils. The sample holder consisted of a platinum basket lined with single crystal MgO slices. It has been shown that MgO does not react with the liquid formed during melt processing of 123 materials.[35] The platinum basket was attached to a thermocouple which was lowered into and raised out of the furnace during the coarsening experiments. The tip of the thermocouple was approximately 1 mm from the sample to ensure that temperature measurements were as accurate as possible.

The heat treatment of the coarsening samples was performed by lowering the thermocouple, basket and sample into the furnace until a temperature of 1094°C was reached. This temperature was used because it was a representative temperature in the 211 + Liquid two phase region (see figure 2.2). The coarsening samples were held at 1094 °C for 10 minutes, 15 minutes, 30 minutes, 60 minutes and 120 minutes and then quenched in water. Quenching was performed to preserve the high-temperature microstructure of the 211 phase and barium cuprate liquid. The pellets were then mounted in epoxy, polished and examined using backscattered electron imaging. EDX and electron probe microanalysis were used to analyze sample composition. A number of samples were also placed in distilled water in an ultrasonic bath. This procedure

dissolved the quenched liquid phase so that the individual 211 particles could be collected and examined.

3.3.4. 211 particle size analysis

Analysis of the 211 particle size distribution was performed on the backscattered SEM images of polished cross-sections of the coarsened samples. Particle size distribution cannot be determined simply by measuring the size of the particle cross-sections observed in the micrographs. It can be seen from figure 3.3 that a small observed cross-section may result from a small particle sectioned through the center or a large particle sectioned near the surface. Schwartz-Saltykov diameter analysis was used to determine the actual particle size distribution from the SEM micrographs.[115] The number of cross-sections within different radius intervals were counted and tabulated. The number of actual particles with radii within each radius interval was then calculated according to equation 3.4:

$$(N_v)_j = \frac{1}{\Delta}\left[\alpha_i (N_A)_i - \alpha_{i+1}(N_A)_{i+1} - \alpha_{i+2}(N_A)_{i+2} - \quad \ldots \quad - \alpha_k (N_A)_k\right] \qquad (3.4)$$

where N_v is the number of actual particles with radii within the given radius interval. i and j assume integer values from 1 to k, where k equals the total number of radius intervals. The index j represents the radius interval and is a constant within each calculation. i varies from $i=j$ through $i+1$, $i+2$ etc., up to $i=k$. N_A is the number of cross-sections within each radius interval. Δ is defined as the ratio of the maximum radius to the total number of groups, k. α_i is a statistical coefficient representing the relationship between cross-section radius and actual particle radius. A chart containing these coefficients can be found in reference [115]. The calculation described by equation 3.4

was repeated for each radius interval to determine the number of actual particles with radii within each radius interval.

Equation 3.4 is derived from an examination of spherical particles.[115] 211 particles coarsening in barium cuprate liquid are not spherical, however. Scheil and Wurst's analysis for prolate particles was therefore used to modify equation 3.4 to take into account the non-spherical shape of the 211 particles.[115] This modification is as follows:

$$(N_v)_j = \frac{1}{k(q)\Delta}\sum_{i=j}^{k}\alpha(i,j)(N_A)_i \qquad (3.5)$$

where $k(q)$ is the shape factor for a prolate spheroid and q is the ratio of the minor to major axis. A graph relating $k(q)$ to q can be found in reference [115]. q for the 211 particles examined in the coarsening experiments was determined by measuring the maximum aspect ratio of the 211 particles in each sample from the SEM micrographs of the cross-sectioned samples. The modified 211 particle size distribution was then calculated using equation 3.5.

3.3.5. Liquid viscosity experiment

A simple experiment was also performed to examine the effect of Pt-doping on the viscosity of barium cuprate liquid in YBCO samples raised above the peritectic temperature. A doped and undoped sample were placed on a porous MgO setter and raised above the peritectic temperature of YBCO, causing the 123 phase to decompose to form the 211 phase and barium cuprate liquid. The porosity in the MgO setter resulted in the barium cuprate liquid being wicked into the setter through capillary action. Increased viscosity of the barium cuprate liquid will result in a smaller wicking distance of liquid into the porous setter. The liquid wicking distance was measured for doped and undoped

samples after removal from the furnace in order to determine whether Pt-doping increases or decreases the viscosity of the barium cuprate liquid.

3.4. Results and discussion

Scanning electron microscopy, EDX and electron microprobe analysis were performed on polished cross-sections and extracted 211 particles in coarsened samples. The results were used to examine the microstructural evolution of 211 particles, as well as their coarsening behavior, with and without the use of platinum as a dopant.

3.4.1. Microstructural evolution of 211 particles

Figure 3.4 a) shows a backscattered SEM micrograph of a polished cross-section of an uncoarsened precursor sample containing 80 wt.% 123 and 20 wt.% Er-211. The white spots in figure 3.4 are Er-211 particles surrounded by the gray 123 matrix. The black areas in figure 3.4 a) are pores in the polycrystalline 123 + 211 precursor. Figures 3.4 b) and c) show backscattered SEM micrographs of polished cross-sections of samples that underwent coarsening for 10 and 60 minutes at 1094 °C, respectively. It can be seen that the 211 particles contain white Er-211 centers and gray Y-211 outsides. This figure reveals that the initial Er-211 added to the samples acts as a nucleation site for the Y-211 phase formed via the peritectic decomposition of the 123 phase. This conclusion was supported by work performed by Varanasi et al.[104-105] A small percentage of 211 particles in figures 3.4 b) and c) show no Er-211 in the center but this is likely due to the fact that only particles sectioned somewhere near their centers will show the presence of the Er-211 phase.

Comparison of figures 3.4 b) and c) shows that after small periods of coarsening, the 211 particles have a relatively pure Er-211 center with a relatively pure Y-211 outside. Particles which coarsen in the barium cuprate liquid for a longer period of time, however, exhibit three layers of 211 phase. The center of the particles are still made up of Er-211, the next layer consists of relatively pure Y-211 and the outside layer, which has a light gray color, consists of (Er,Y)-211. This microstructural development can be explained as shown in figure 3.5. The uncoarsened samples below the peritectic temperature are composed of Er-211 particles in a Y-123 matrix. When the samples are heated to a temperature above the peritectic temperature, the Y-123 decomposes to form Y-211 and liquid. During coarsening, the large particles grow at the expense of the smaller particles, as discussed in section 3.2. After short periods of coarsening, the Y-211 on the outside of the smaller particles is transferred to the outside of the larger particles, preserving the original dual-layer appearance of the particles. After longer periods of coarsening, the insides of the smaller particles begin to dissolve along with the outsides of somewhat larger particles. The Er-211 phase from the center of the small particles mixes with the Y-211 phase dissolving from the other particles and grows as (Er,Y)-211 phase on the outside of the largest particles.

The fact that original 211 particles act as nucleation sites for 211 phase formed from the decomposition of the 123 phase is an important result because it allows the initial 211 particle size in the semi-solid melt to be controlled. Figure 3.6 shows an SEM picture of 211 particles extracted from a coarsened sample containing 20 wt.% initial Er-211 and 80 wt.% 123 phase. Figure 3.7 shows an SEM picture of 211 particles extracted from a coarsened sample containing 100% 123 phase. The differences in magnification between the micrographs in figures 3.6 and 3.7 should be noted. Comparison of figures 3.6 and 3.7 shows that the 211 particles formed from the Er-211 + 123 sample are much smaller than the 211 particles formed from the 100% 123 sample. This can be understood by examining the nucleation of the Y-211 phase formed by the decomposition of the 123 phase. The Y-211 phase forms via heterogeneous nucleation on the Er-211 particles for

the samples containing excess original Er-211. The Y-211 phase forming from the 100% 123 samples must undergo homogenous nucleation. The number of 211 particles nucleated via homogeneous nucleation is less than the number of Er-211 heterogeneous nucleation sites in the excess 211 samples. This causes fewer particles of larger size to form in the 100% 123 samples while the number of 211 particles in the excess 211 samples is larger and the particles are smaller. Thus, the addition of excess, small 211 particles is a good method for keeping the 211 particle size in the samples low.

Figure 3.8 shows a backscattered SEM micrograph of a polished cross-section of a Pt-doped excess Er-211 sample which underwent coarsening for 10 minutes at 1094 °C. Comparing figure 3.8 with the corresponding figure of an undoped sample (figure 3.4 b)) shows that the aspect ratio of 211 particles in the Pt doped sample is much larger than for the un-doped sample. This result is supported by similar observations by other researchers.[11,33,38,92,104-105] This increase in aspect ratio of the 211 particles results in an increased surface area to volume ratio. It is therefore concluded that the presence of Pt atoms in the melt decreases γ, the relative interfacial energy of the 211 particles in the barium cuprate liquid. Equation 3.3 shows that coarsening rate is proportional to γ. It is concluded that the decrease in 211 particle coarsening rate in Pt-doped samples is therefore a result of decreased interfacial energy. This conclusion is supported by work performed by others.[104-105,108]

Polished cross-sections of 211 particles in Pt-doped samples were also examined using EDX. No platinum was found in the center of any 211 particles in the doped samples. It is therefore concluded that the platinum powder added to the doped samples does not act as a nucleation site for 211 particles formed via the peritectic decomposition of the 123 phase. An additional $Ba_{10}Cu_4Pt_3O_{20}$ phase was found to form in Pt-doped samples, as shown in figure 3.9. Other Pt phases have been found by Izumi et al.[93] and Varanasi et al.[38] It has been shown that the surface energy of a material within a melt can be affected significantly by the presence of a small amount of a sparingly soluble material in the

liquid. Results show that this is likely to be the case in Pt-doped samples of YBCO. Decreased 211 particle surface energies result in a decreased driving force for coarsening. Changes in 211 particle surface energy also explain the change in aspect ratio of the particles. Lowering the surface energy of the end faces of the particles relative to the long faces causes an increase in aspect ratio.

3.4.2. 211 particle coarsening with and without Pt-doping

Figures 3.10 a) through 3.10 d) show microstructures of 80 wt.% 123 + 20 wt.% Er-211 samples which have undergone coarsening at 1094 °C for various lengths of time. Figures 3.11 a) through 3.11 e) show microstructures of 80 wt.% 123 + 20 wt.% Er-211 samples doped with 1 wt.% Pt which have undergone coarsening at 1094 °C for various lengths of time. It can be seen that a significant amount of coarsening of the 211 particles has taken place in the undoped samples. The platinum doped samples exhibit a much smaller change in 211 particle size with time. It can be seen that the decrease in coarsening in Pt-doped samples has kept the 211 particle size lower and the number of 211 particles higher with time compared to undoped samples.

Figures 3.12 and 3.13 show the results of particle distribution analyses for undoped and Pt-doped samples, respectively. It can be seen that the particle size distribution flattens out much more quickly with time for the undoped samples than for the Pt-doped samples. Figure 3.14 compares the total number of 211 particles per m^3 with time for doped and undoped samples. It can be seen that the total number of 211 particles present in both samples after initial coarsening is lower than the number of excess Er-211 particles added to the precursor. This result supports the theory presented in section 3.4.1 that the excess Er-211 particles act as heterogeneous nucleation sites for 211 phase formed from the peritectic decomposition of 123. Additionally, the fact that the total number of 211 particles present in the Pt-doped samples after initial coarsening is less than the number

of excess 211 particles added to the precursor also shows that the platinum powder did not act as a nucleation site for 211 particles. If this had been the case, the total number of 211 particles would have increased after the samples were raised above the peritectic temperature.

Figure 3.14 shows that the total number of particles per m^3 decreases more quickly with time for the undoped samples than for the doped samples. This decrease in coarsening rate with platinum doping can also be seen in figure 3.15, where average particle size vs. time is plotted for doped and undoped samples. The coarsening rate constant, k, can be estimated from the coarsening data by plotting $r_i^3 - r^3$ vs. time, as shown in figure 3.16. The fact that the coarsening curves in figure 3.16 are both linear show that the coarsening of 211 particles does indeed agree with the expected $t^{1/3}$ relationship predicted by the LSW theory. This is supported by additional research performed by other researchers.[104,107-108,116] Figure 3.16 shows that $k = 3.0 \times 10^{-19}$ m^3/s for undoped samples held at 1094 °C and $k = 1.7 \times 10^{-20}$ m^3/s for samples doped with 1 wt.% Pt. This data shows quantitatively that the coarsening rate of 211 particles decreases significantly for Pt-doped samples.

The theory that the addition of platinum decreases coarsening due to a decrease in liquid viscosity was not supported by the experiments conducted here. More barium cuprate was wicked into the porous MgO setter in Pt-doped samples than in undoped samples. It is also concluded that decreased solubility of yttrium in the barium cuprate liquid is not a likely cause of decreased coarsening in Pt-doped samples. Results presented in chapter 5, as well as results from other researchers,[63] have shown that 123 crystal growth rate increases with the addition of platinum to the precursor samples. This would not be the case if yttrium solubility in the liquid is reduced through the addition of platinum since yttrium diffusivity was shown to be a critical variable in the growth rate of 123 crystals (see chapter 2).

3.5. Conclusions

It has been shown that the use of Er-211 is a good way of "labeling" the initial 211 phase present during coarsening. It was found that excess 211 particles added to the 123 phase act as nucleation sites for additional 211 phase formed via the peritectic decomposition of 123 at temperatures above 1000 °C. 211 particles formed via homogenous nucleation and growth in samples composed of 100 % 123 phase were found to be larger than particles formed via heterogeneous nucleation in excess 211 samples. Quantitative evaluation of 211 particle growth with time was also performed and the results agree with expected coarsening relationships. Results show that the addition of excess 211 particles is an effective means of keeping 211 particle size as low as possible during the processing of YBCO materials. Experiments involving the addition of platinum show that platinum doping decreases the coarsening rate of 211 particles in semisolid melts of barium cuprate. k, the coarsening rate constant, was found to be 3.0×10^{-19} m^3/s for undoped samples and 1.7×10^{-20} m^3/s for Pt-doped samples at 1094 °C. It was found that the interfacial energy of 211 particles in barium cuprate liquid decreases with the addition of a platinum dopant. It was concluded that the decreased coarsening rate in platinum doped samples results from this decrease in interfacial energy. It was found that platinum powder added as a dopant does not act as a nucleation site for 211 particles.

It will be shown in chapter 5 that the increase in 211 particle aspect ratio also explains the increase in growth rate of 123 crystals in Pt-doped YBCO samples. It will be shown in chapter 6 that the dissolution rate of 211 particles depends mainly on the small radius of the particles rather than their length. Faster 211 particle dissolution provides increased flux of yttrium to the 123 surface. The smaller 211 particle size in Pt-doped samples decreases the diffusion distances between the particles and the 123 interface. This was shown to be a critical variable in the growth rate of 123 crystals (see chapter 5).

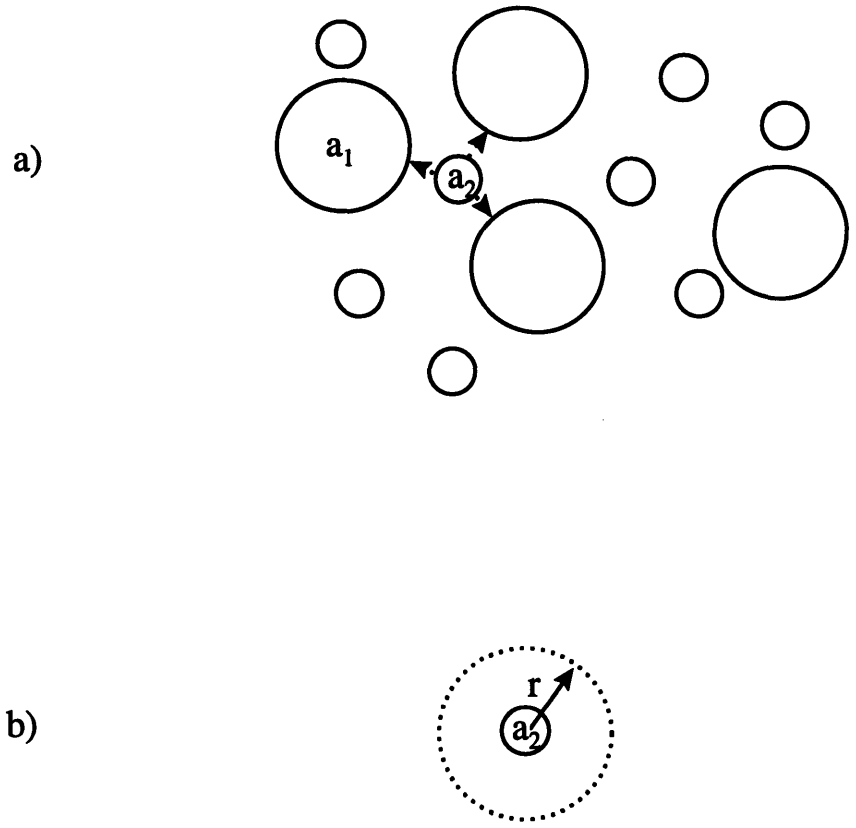

Figure 3.1. a) Schematic showing coarsening of particles with radius a_1 and a_2 in liquid. b) Schematic of diffusion field of radius r around a particle of radius a_1.[109-110]

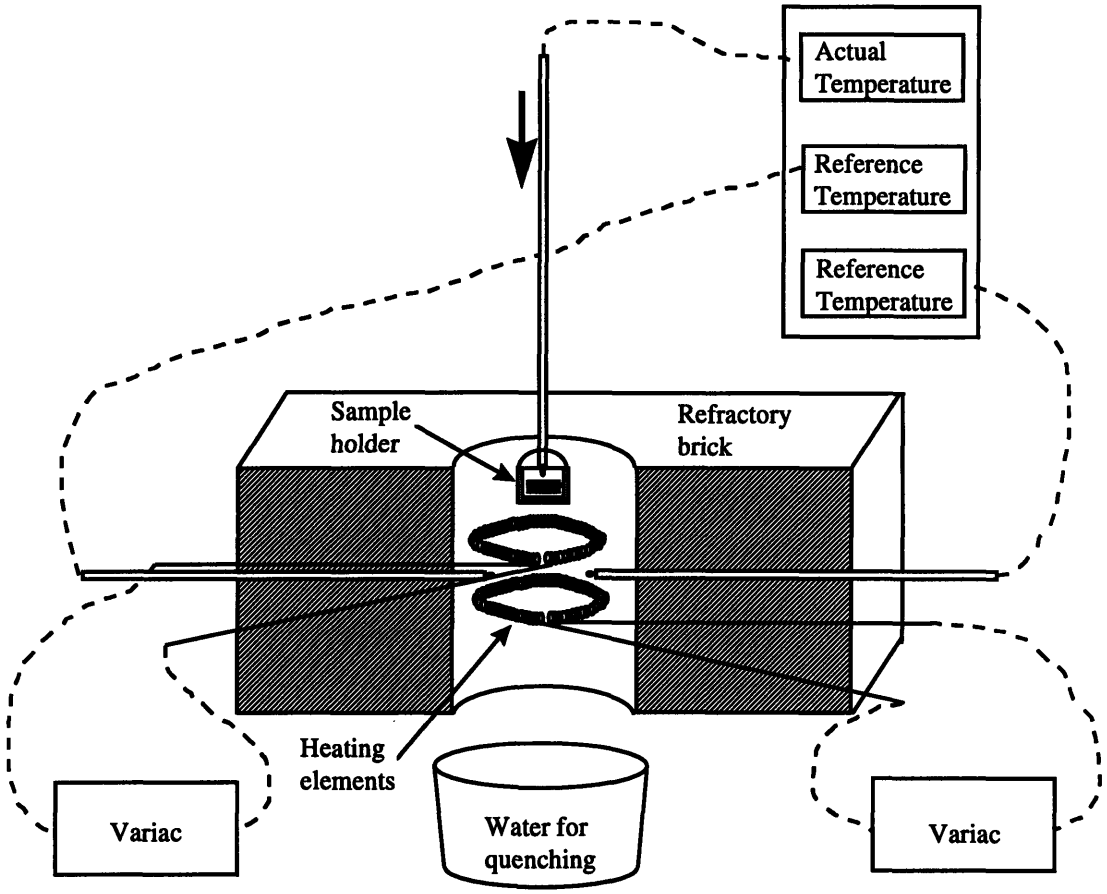

Figure 3.2. Schematic diagram of the furnace construction used for coarsening experiments.

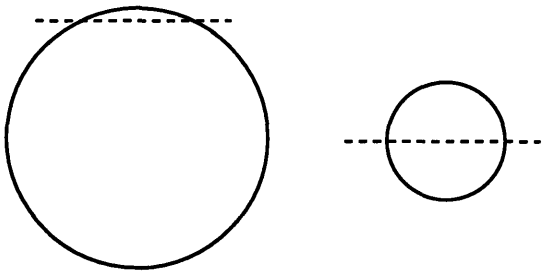

Figure 3.3. Schematic diagram of the sectioning of spheres. Both cross-sections will have the same radius.

a)

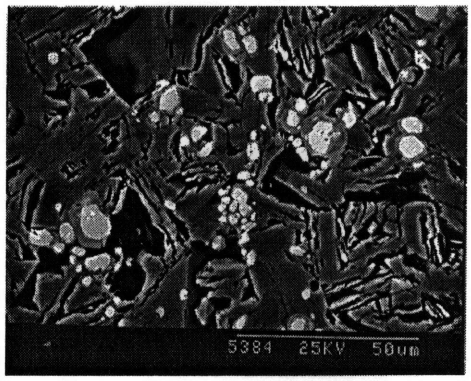

b)

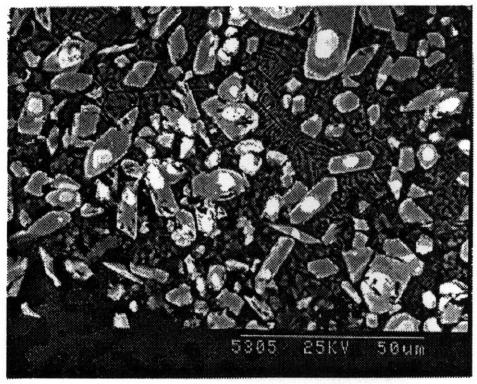

c)

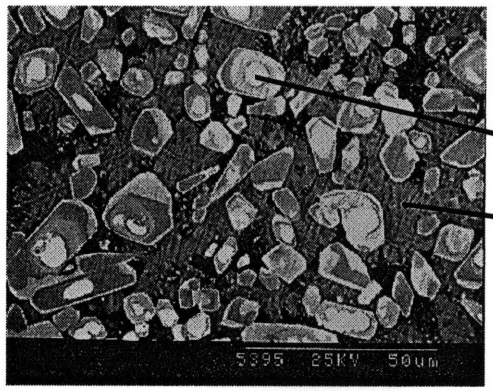

Figure 3.4. Microstructural evolution of 211 particles. a) backscattered SEM micrograph of a polished cross section of an uncoarsened precursor sample containing 80 wt.% 123 and 20 wt.% Er-211. b) backscattered SEM micrograph of a polished cross-section of sample after coarsening at 1094 °C for 10 minutes. c) backscattered SEM micrograph of sample after coarsening at 1094 °C for 60 minutes.

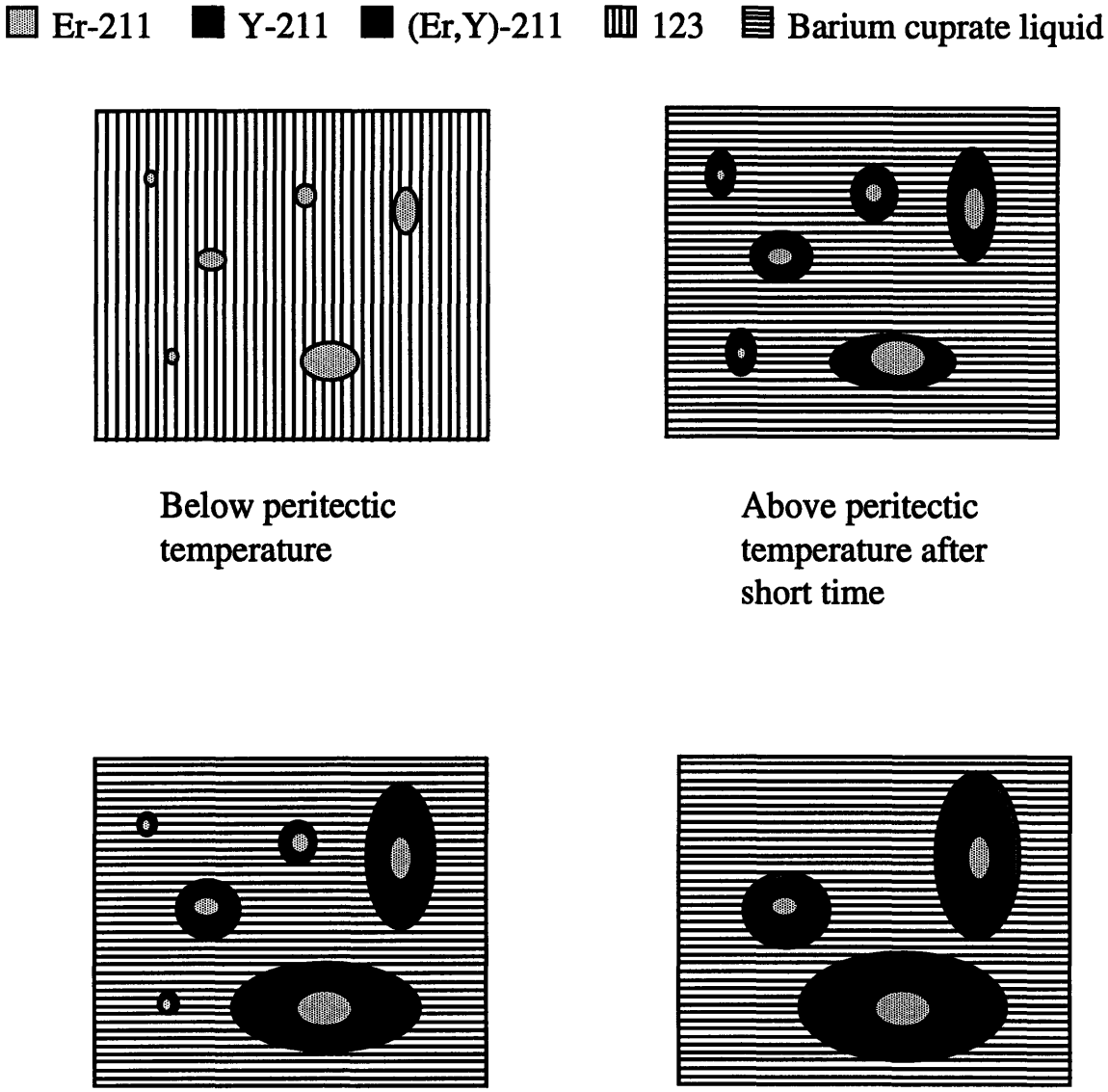

Figure 3.5. Schematic diagram showing evolution of 211 particle microstructure in coarsening samples.

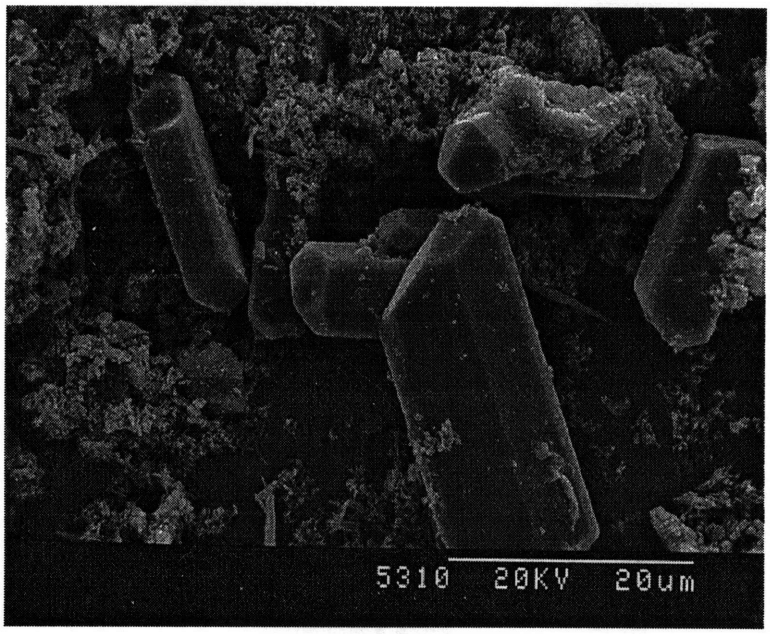

Figure 3.6. SEM picture of 211 particles extracted from a sample containing 20 wt.% initial Er-211 and 80 wt.% 123 phase after coarsening for 30 min.

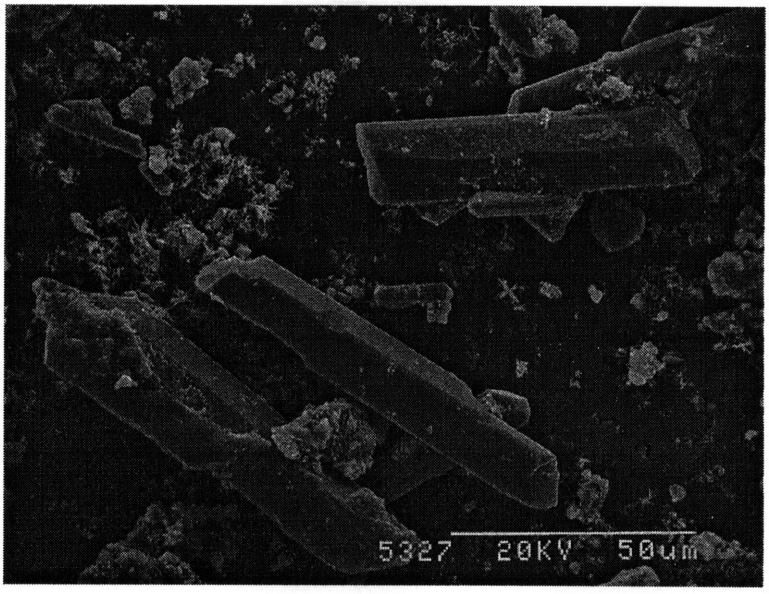

Figure 3.7. SEM picture of 211 particles extracted from a sample containing 100% 123 phase after coarsening for 30 min.

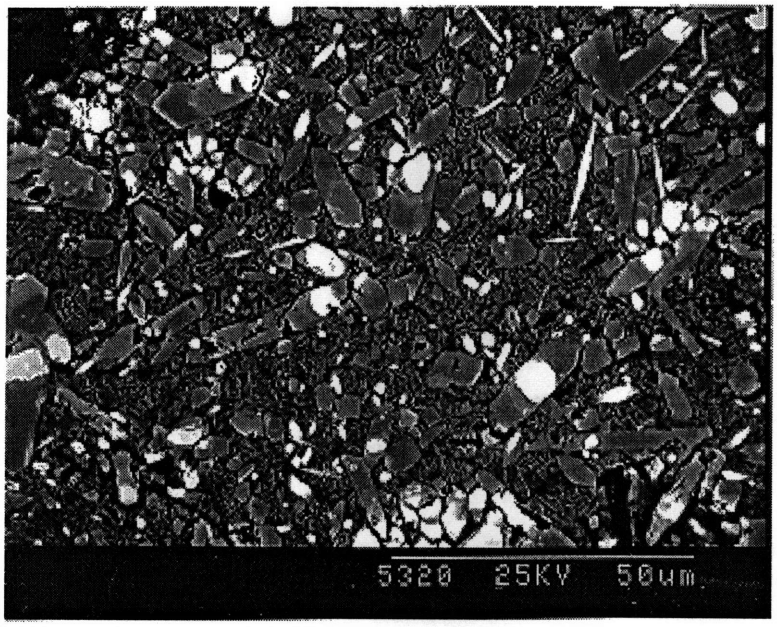

Figure 3.8. Backscattered SEM micrograph of a polished cross-section of a Pt-doped excess Er-211 sample after coarsening at 1094 °C for 10 minutes.

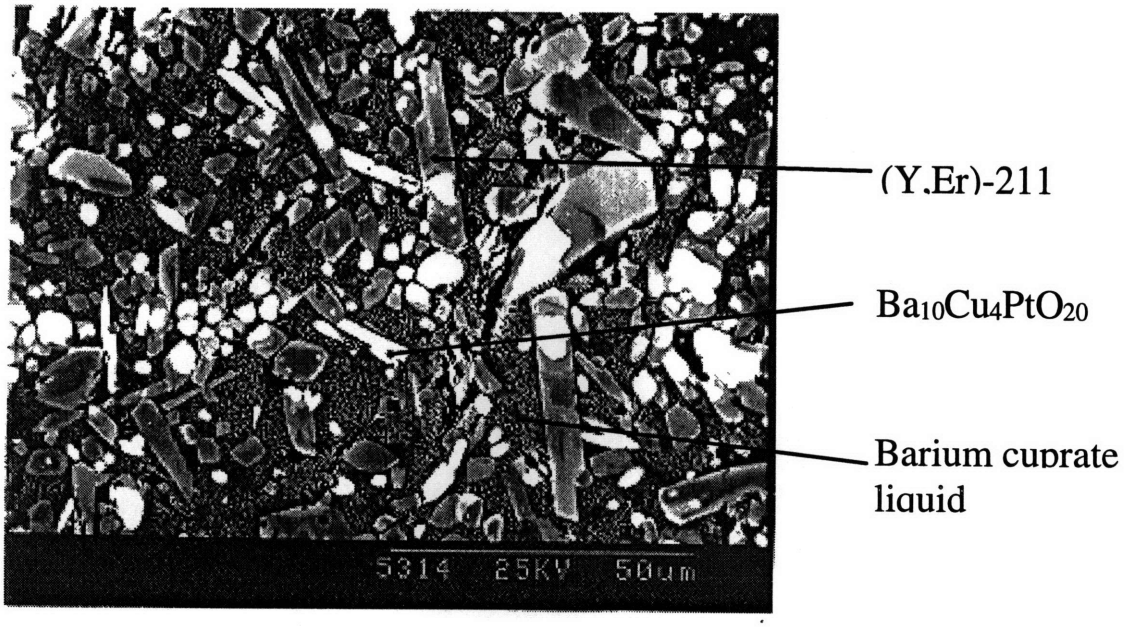

Figure 3.9. Backscattered SEM micrograph of a polished cross-section of a Pt-doped excess Er-211 sample showing the microstructure and composition of phases.

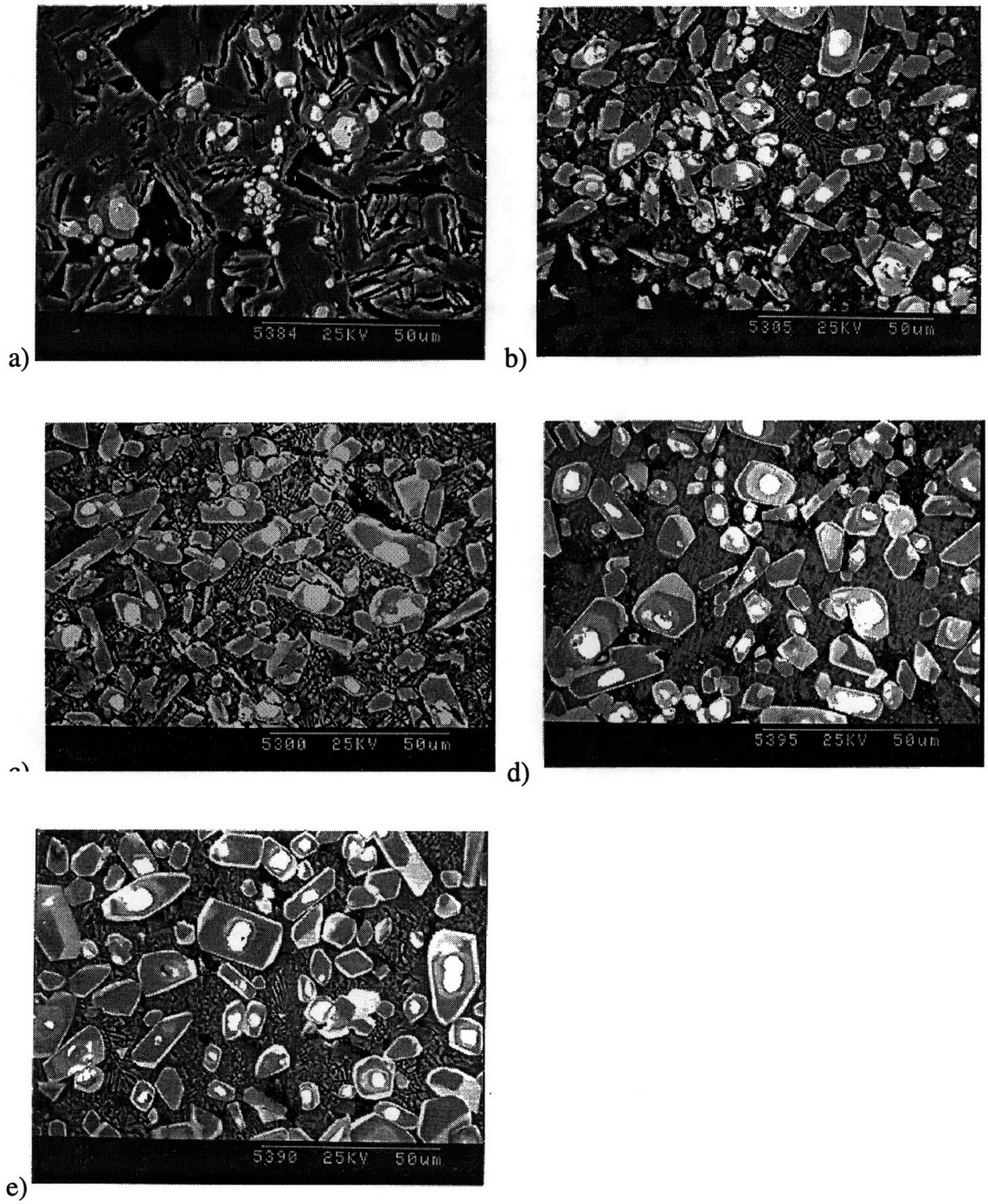

Figure 3.10. Backscattered SEM micrographs of polished cross-sections of 80 wt.% 123 + 20 wt.% Er-211 samples which have undergone coarsening at 1094 °C for a) 10 minutes, b) 15 minutes, c) 30 minutes and d) 60 minutes.

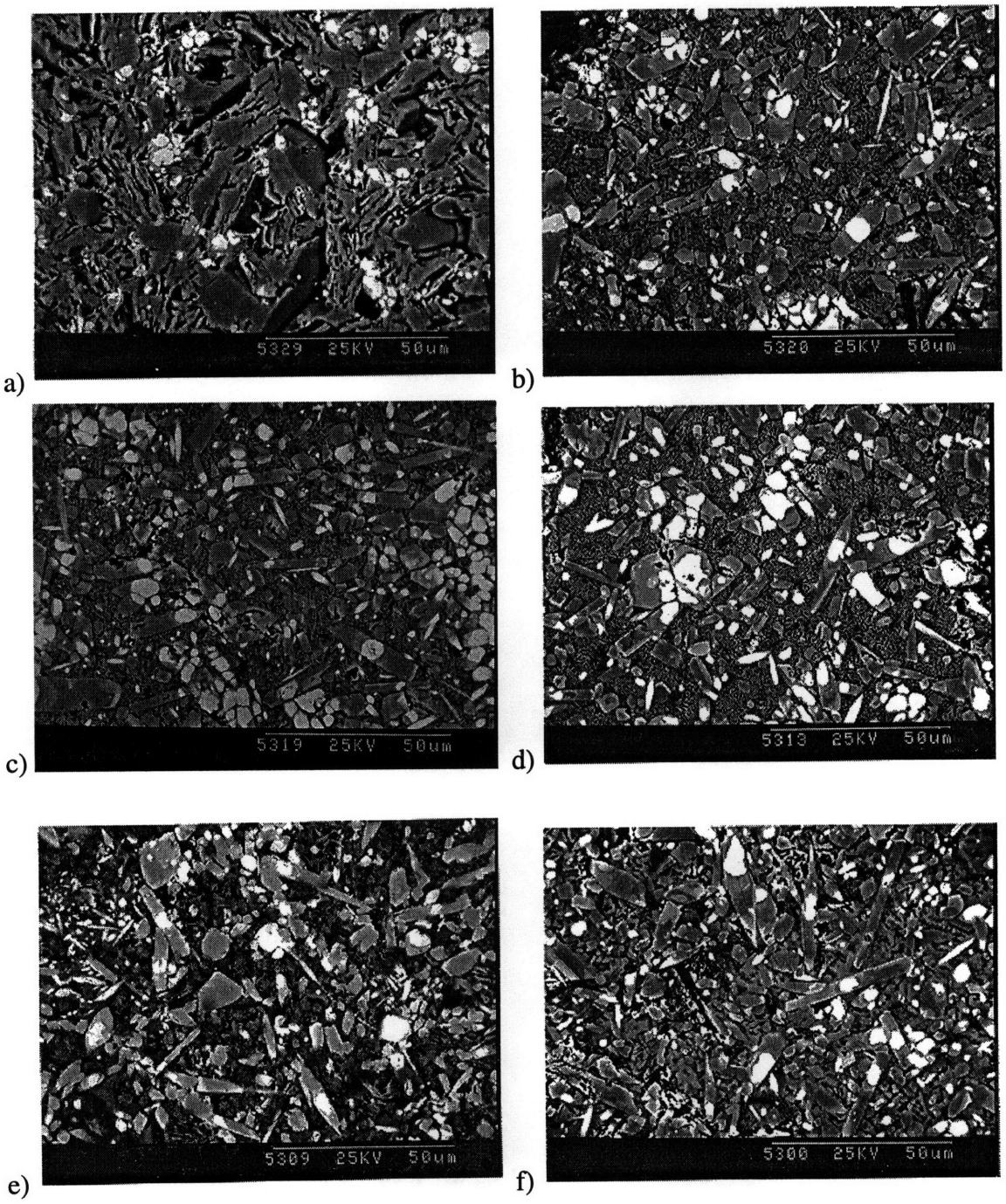

Figure 3.11. Backscattered SEM micrographs of polished cross-sections of Pt-doped 80 wt.% 123 + 20 wt.% Er-211 samples which have undergone coarsening at 1094 °C for a) 10 minutes, b) 15 minutes, c) 30 minutes, d) 60 minutes and e) 120 minutes.

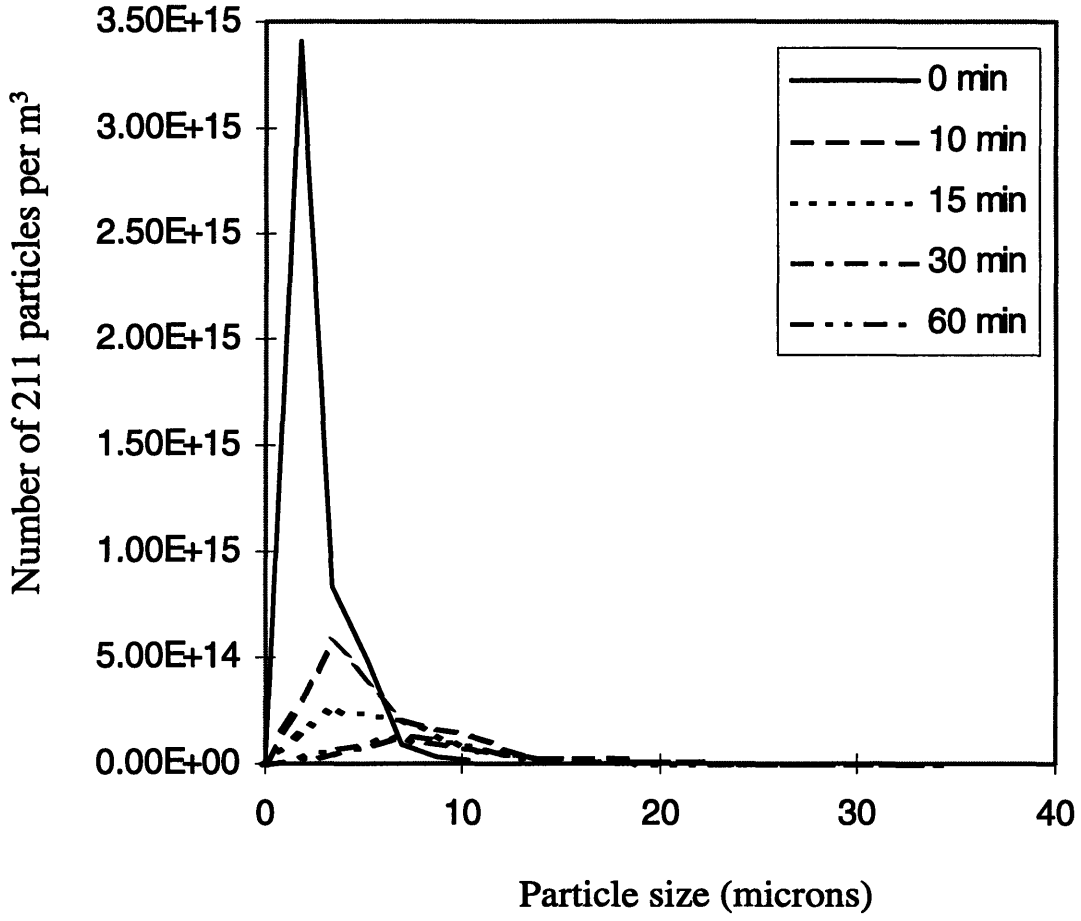

Figure 3.12. 211 particle size distribution vs. coarsening time at 1094 °C for samples composed of 20 wt.% Er-211 and 80 wt.% 123.

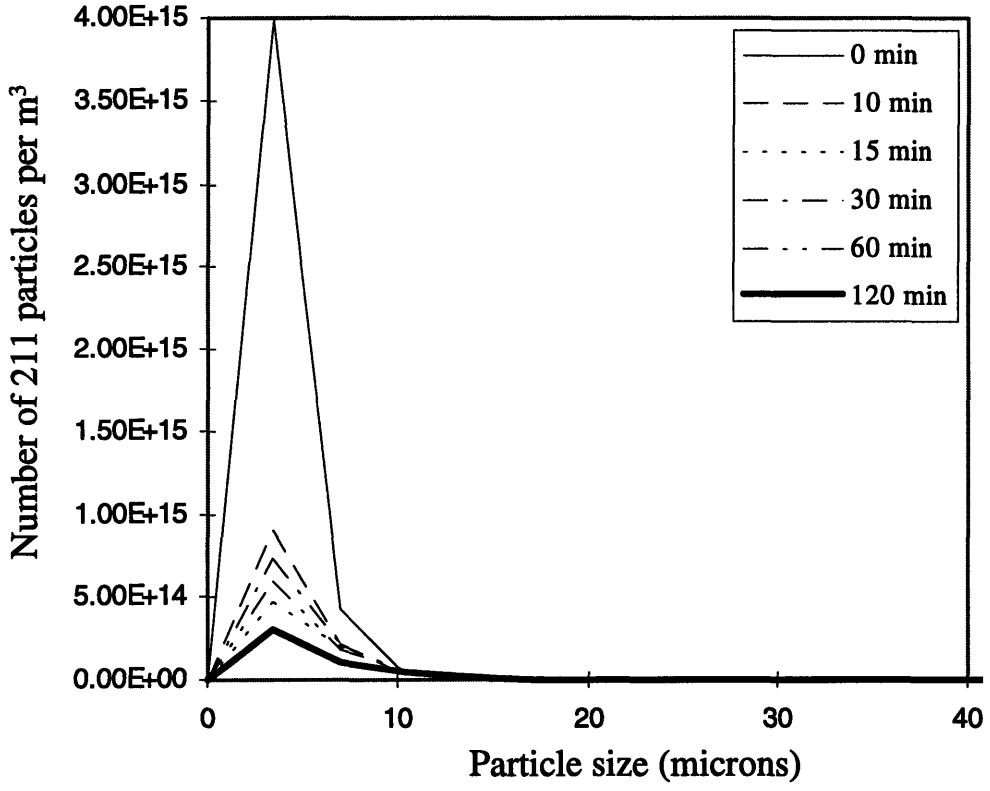

Figure 3.13. 211 particle size distribution vs. coarsening time at 1094 °C for Pt-doped samples composed of 20 wt.% Er-211 and 80 wt.% 123.

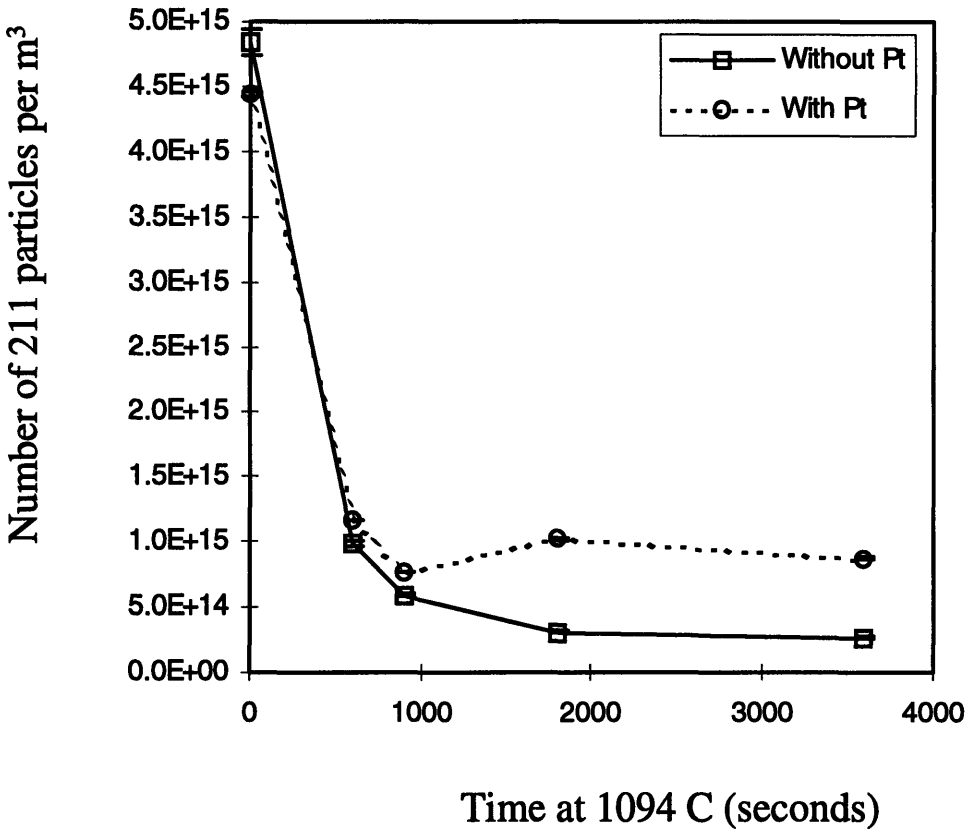

Figure 3.14. Total number of 211 particles per m^3 vs. time at 1094 °C for Pt-doped and undoped samples composed of 20 wt.% Er-211 and 80 wt.% 123.

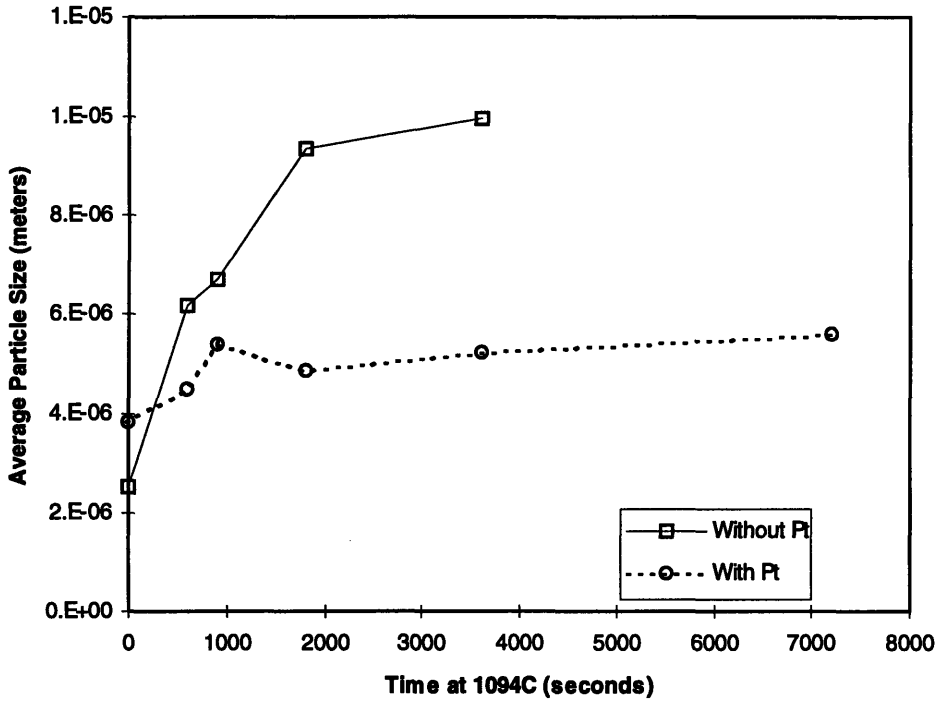

Figure 3.15. Average 211 particle size vs. time at 1094 °C for Pt-doped and undoped samples composed of 20 wt.% Er-211 and 80 wt.% 123.

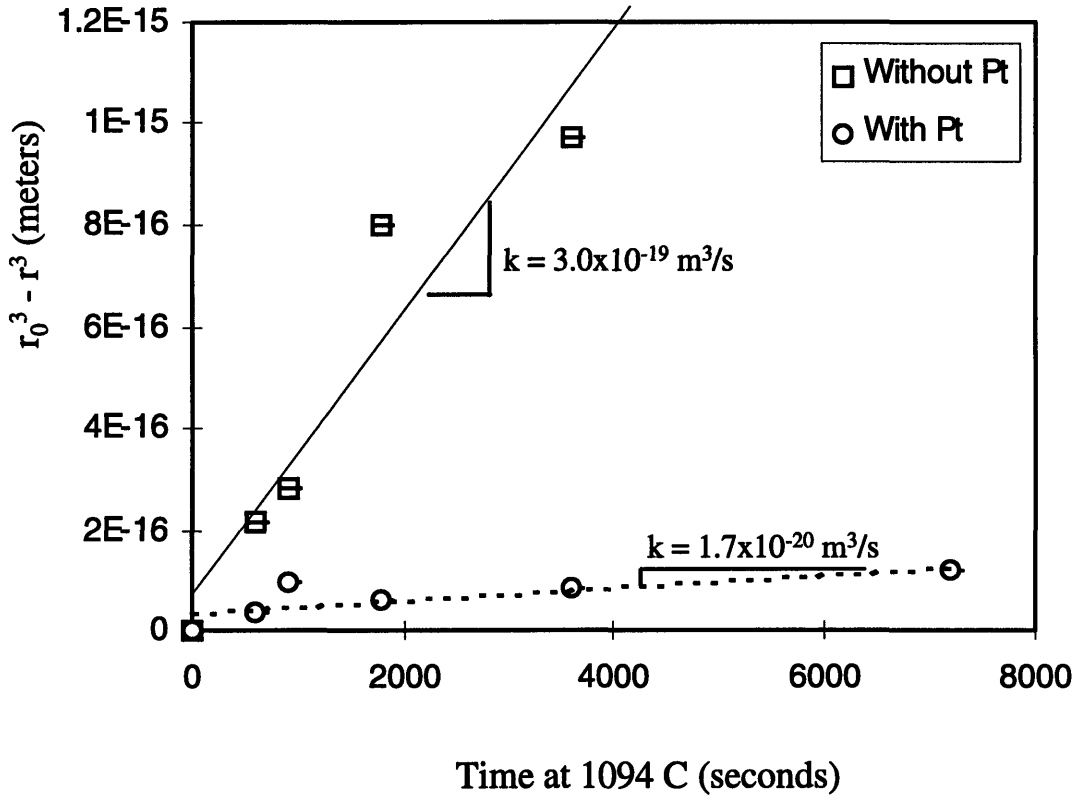

Figure 3.16. $r_i^3 - r^3$ vs. time at 1094 °C for Pt-doped and undoped samples composed of 20 wt.% Er-211 and 80 wt.% 123. k, the coarsening rate constant, was calculated from the slope of the curves.

Chapter 4

Laser Heated Floating Zone (LHFZ) growth of YBCO single crystals

4.1. Introduction

Most industrial applications of bulk HTSC materials require large amounts of high quality YBCO material. As discussed in chapter 2, single crystals exhibit the best superconducting properties of bulk HTSC materials. Experiments were, therefore, undertaken to produce long YBCO single crystal fibers using laser heated floating zone (LHFZ) growth. Polycrystalline precursor fibers were produced by extrusion and melt-processed using LHFZ growth. Factors limiting growth of high quality single crystals, such as surface roughness, irregular cross-sections and porosity in the precursor fibers, and liquid migration and uneven hot zones during LHFZ processing, were identified. These problems were minimized or eliminated and the precursor fiber production and LHFZ growth processes were optimized in an effort to produce single crystal samples in excess of 10 cm in length. Secondary nucleation was found to limit the length of single crystal fibers which can be produced continuously. The process of secondary nucleation in LHFZ crystals was examined and the driving force for nucleation was investigated.

4.2. Experimental procedure

LHFZ growth of single crystals of various YBCO materials was performed using polycrystalline precursor fibers produced by extrusion. Fiber production and LHFZ growth are detailed in the following sections.

4.2.1. Precursor fiber preparation

Fibers composed of the 123, 211 and Nd-211 phases were produced for use as feed rods in the LHFZ growth process. The Nd-211 powder was used to label the 211 particles, as with the Er-211 phase used in the coarsening experiments described in chapter 3. The 123 powder used in the fiber production process was the same type of powder used to produce the coarsening samples described in chapter 3. The 211 powder, in spray dried form, was also purchased from Seattle Specialty Ceramics (now Praxair Specialty Ceramics). The Nd-211 powder was produced by mixing Nd_2O_3, $BaCO_3$ and CuO and processing it using the same method used to produce the Er-211 powder used in the coarsening samples described in chapter 3. The Nd-211 powder was examined using X-ray diffraction and found to be phase pure. Two different powder combinations were used to produce the LHFZ precursor fibers. Excess 211 fibers were produced by mixing 80 wt.% 123 powder with 20 wt.% 211 powder. Excess Nd-211 samples were produced by mixing 80 wt.% 123 powder with 20 wt.% Nd-211 powder.

The basic precursor production process is described in figure 4.1. The powders were weighed and mixed using a mortar and pestle until homogeneity was achieved. The binder solution was produced by dissolving 2 g of Poly(vinyl butyral) (PVB) binder and 1 g of dibutyl phthalate (DBP) plasticizer in 10 ml of octanol. The binder solution was then mixed with the powder and additional octanol to form a slurry. A paste was produced by heating the slurry and allowing the octanol to evaporate. The viscosity of the paste was controlled by monitoring the evaporation of the octanol. The paste was then filled into a stainless steel extrusion die and the chamber was evacuated using a vacuum pump. Long fibers, approximately 350 μm in diameter, were then extruded, dried with a heat gun and rolled onto a spool. A schematic diagram of the extrusion process can be found in figure 4.2. The long fibers were then cut into 20 cm lengths and arranged on Al_2O_3 rods to keep them straight. The wet fibers were placed in a vacuum furnace at 120

°C for 12 hours to evaporate the remaining octanol. The dry fibers were then heated at 500 °C for 10 hours to burn out the binder and plasticizer. Finally, the fibers were sintered at 960 °C for 10 hours to increase their density.

4.2.2. Solidification procedure

The LHFZ processing set-up consisted of a 100 Watt CO_2 laser with dual beam heating optics and a controlled atmosphere growth chamber. A schematic diagram of the LHFZ set-up is shown in figure 4.3. Two polycrystalline precursor fibers, described in the previous section, were mounted in chucks with two axes of rotation and two axes of triangulation. The chucks were mounted on the upper and lower pulling heads of the crystal grower after aligning the fibers in the chucks. The two precursor fibers were then connected by heating the ends of the filaments with the laser beams and joining them. The dual laser beams were focused on opposite sides of the precursor fiber, producing a hot zone with a maximum temperature above the YBCO peritectic temperature.

It can be seen from the YBCO phase diagram shown in figure 2.2 that a semisolid zone composed of the 211 phase and barium cuprate liquid is produced by heating the 123 + 211 samples above the peritectic temperature. Semisolid hot zones of 1 to 2 filament diameters were established by using incident beams with diameters of 900 μm. The temperature of the hot zone was measured with an optical pyrometer and controlled using the laser current source. The precursor fibers were pulled through the hot zone at rates between 0.5 cm/h and 3 cm/h. A standard chamber atmosphere of 100% oxygen at atmospheric pressure was used for precursor materials of the above composition. A polished cross-section of a typical quenched semisolid zone is shown in figure 4.4. The polycrystalline precursor fiber can be seen to the left. A swollen section formed when the barium cuprate liquid in the zone wicks up into the polycrystalline precursor is located between the semisolid zone and the precursor fiber. The interface between the growing

single crystal and the semisolid zone can be seen to the right. The 211 phase in the semisolid zone dissolves in the barium cuprate liquid during solidification and acts as a yttrium source for the growing 123 crystal. The 211 particles which are not completely dissolved are incorporated into the 123 single crystal matrix. Figure 4.5 shows an optical micrograph of a polished cross-section of a typical YBCO single crystal fiber produced by LHFZ growth. After growth, the LHFZ samples were examined using optical microscopy, SEM, four-circle X-ray diffraction and SQUID magnetometry.

4.3. Process optimization

A number of problems were encountered during precursor preparation and LHFZ processing. These included fiber breakage, excess surface roughness, porosity and irregular cross-sections in the precursor fibers. Solidification problems included uneven hot zones, liquid migration and secondary grain nucleation. The following sections detail the changes made in the precursor production and LHFZ growth processes in order to minimize or eliminate these problems.

4.3.1. Optimization of precursor fiber production

Green fibers with lengths in excess of 10 cm are needed in order to produce single crystal 123 fibers at least 10 cm long. These green fibers must have few surface defects to minimize surface nucleation of additional 123 crystals during LHFZ growth. The green fibers must also have uniform cross-sections and low porosity to assure a regular temperature distribution across the zone. Porosity in precursor fibers results in porous 123 single crystals after LHFZ processing, producing inferior superconducting materials. Previous green fiber production techniques produced fibers with some surface roughness, porosity and irregular cross-sections. A number of aspects of the green fiber production

process were changed in order to produce longer green fibers with fewer surface defects and porosity and more uniform cross-sections.

The extrusion step in the precursor production process was previously performed with a syringe from which the needle had been removed. The glass casing of the syringe often cracked under the high extrusion pressures, terminating the extrusion process and contaminating the paste with glass fragments. A stainless steel extrusion die was, therefore, constructed and used in place of the syringe. A Swagelok® fitting was welded to the end of the die to allow various extrusion orifices to be attached to the die. These extrusion orifices consisted of syringe heads from which the needles had been removed. The diameters of the extruded fibers was varied by attaching syringe heads of various gauges to the extrusion die.

The original extrusion process also involved extruding lengths of fiber onto a glass plate. The maximum length of green fibers which were produced in this manner was limited by the length of the glass plate. Fibers also deformed slightly after extrusion onto the plate which resulted in a flat spot along the length of the fiber. Removal of the fibers from the glass plate after the solvent evaporation step was also difficult due to bonding between the fiber and glass plate. This resulted in surface defects and roughness in the green fibers. These problems were minimized by using a heat gun to dry the wet fiber during the extrusion step. The surface of the wet fiber was dried with hot air as it was extruded from the stainless steel die. The dried fiber was still extremely flexible due to the presence of the binder. The long strand of extruded fiber was then rolled onto a take-up spool. The long fiber was unwound and cut into shorter fibers of the desired length after extrusion was complete. The fibers were then be placed directly onto alumina rods for the solvent evaporation, binder burnout and sintering steps since the outside of the fibers was already dry.

Green fibers produced using the original extrusion method occasionally contained large pores which interfered in uniform growth during LHFZ processing. These pores resulted from the incorporation of air during the extrusion process, which was originally performed without the evacuation of the extrusion chamber. Figure 4.6 shows the porous microstructure of a LHFZ processed sample produced before improvements were made in the extrusion process. An additional step designed to reduce pore formation was, therefore, added to the precursor extrusion process. A hole was bored in the side of the extrusion die and connected to a vacuum pump to allow the extrusion chamber to be evacuated. Evacuation of the chamber was performed after the precursor paste was inserted into the die and before extrusion took place.

Improvements made in the precursor production process resulted in significantly improved green fibers. The length of the green fibers was no longer limited by the length of the glass plate. Fibers of nearly unlimited length were produced and rolled onto the take-up spool. Flat spots along the length of the fiber produced by contact with the glass plate were eliminated since the surface of the fiber was dried while suspended in air. Surface roughness and defects produced during removal from the glass plate were also eliminated. The addition of the evacuation step during paste extrusion significantly decreased the amount of porosity in the green fibers. SEM micrographs of green fibers produced using the improved process are shown in figures 4.6 a) and b). It can be seen that the sectioned surface is homogeneous and no pores are visible. LHFZ samples produced from these precursors showed virtually no traces of pre-growth porosity.

4.3.2. LHFZ growth optimization

The LHFZ process was also optimized to grow longer single crystals more reproducibly. The issues of liquid migration, uneven zones, and secondary grain nucleation during LHFZ growth were addressed in an effort to improve the growth process. Examples of

each of these phenomena are shown in figures 4.8 through 4.10, respectively. Zone destabilization due to liquid migration in the zone was reduced by decreasing the maximum temperature in the zone. This decreased the ratio of barium cuprate liquid to 211 solid which retarded the flow of liquid out of the zone (based on the phase rule in the 211 + L region of the YBCO phase diagram shown in figure 2.2). The problem of uneven zones was corrected by changing the position of the beam splitter on the laser set-up until both beams were of equal intensity. The resulting change in the symmetry of the hot zone was observed using the optical pyrometer. The problem of secondary grain nucleation was not completely solved, but nucleation of grains on the surface of the filaments was minimized by eliminating the problem of uneven zones and producing precursor fibers with fewer pores and surface defects.

4.4. Growth rate limitations

The maximum growth rate of YBCO single crystals was found to be approximately 1.5 cm/h. The 123 single crystal interface in samples containing excess 211 changed from a single crystal interface to a polycrystalline interface at pulling rates above this value. Samples containing excess Nd-211 were examined using backscattered scanning electron microscopy in order to obtain visual information on the growth rate dependence of the structure of the 123 single crystal interface. Neodymium doped materials were used to increase the contrast between the 211 phase and the 123 phase during SEM imaging, as was done with Er-211 materials in the previous chapter. The 211 particles in the semi-solid zone and solidified crystal were easily distinguished from the solidified 123 phase. The formation of (Nd, Y)-211 phase mixtures within the 211 particles was also observed, as was seen in the coarsening samples described in chapter 3. Results of experiments involving the addition of Nd-211 instead of Y-211 provide excellent visual information on the structural changes of the 123 interface resulting from variations in growth rate.

Figures 4.11 a) through c) show the change in interface structure with growth rate. It can be seen that a planar single crystal interface is obtained at a growth rate of 1 cm/h, a blocky/faceted interface is obtained at a growth rate of 2 cm/h and a cellular dendritic interface is obtained at a growth rate of 3 cm/h. This correlates with the microstructural changes induced by variations in growth rate observed by Cima et al.[33] and Figueredo et al.,[11] shown in figures 2.10 and 2.11.

It can be seen that the number of 211 particles decreases directly in front of the 123 interface. A diffusion zone which is poor in 211 phase can be seen in front of the 123 interface for samples solidified at all growth rates. This diffusion zone is marked by the arrows in figures 4.11 a) through c). The presence of this zone confirms that 123 growth takes place by dissolution of 211 particles into the undercooled liquid in front of the 123 interface followed by yttrium diffusion across the diffusion zone, as described by the theories developed by Cima et al.[33] and Izumi et al.[10] which were summarized in section 2.4. The presence of this diffusion zone was also observed by Figueredo[11] in crystals produced by LHFZ growth and by Shen[63] in samples produced by electrically heated floating zone growth.

4.5. Secondary nucleation

Many high quality 123 single crystals were produced using the optimized precursor production and LHFZ growth methods. The maximum length of single crystals which were produced continuously was limited to less than 5 cm due to secondary nucleation during growth. These short sections were useful for analysis of superconducting properties and were used for this purpose. Numerous samples were analyzed for a J_c study performed by Sung et al.[31] and for the J_c analysis described in chapter 8. Industrial applications require much longer fibers, however. The dependence of secondary

nucleation on 123 crystal orientation was therefore examined and quantified using four circle X-ray diffraction. The results of the four circle X-ray diffraction study provide evidence for a nucleation model explaining secondary grain nucleation in crystals grown by LHFZ processing.

4.5.1. Crystal orientation determination through the use of four circle X-ray diffraction

Small changes in growth direction were sometimes observed during LHFZ growth. These changes in growth direction resulted in small aberrations observable on the outside of the solidified fiber. Mounting and polishing the fiber revealed that secondary grain nucleation had taken place at this particular place on the fiber, as shown in figure 4.10. This secondary grain nucleation resulted in a grain boundary between the end of one single crystal and the beginning of a second single crystal. Four circle X-ray diffraction was used to examine the orientation of different single crystal YBCO grains in fibers produced by LHFZ growth. The boundaries between the grains were located on the solidified fiber by locating the small aberrations.

The four circle X-ray diffraction apparatus is shown in figure 4.12. Four-circle X-ray diffraction allows the exact orientation of a crystal to be located relative to the sample. The sample was oriented in the X-ray diffractometer as shown in the inset in figure 4.12. The fiber was mounted on a piece of (100) silicon and aligned in the diffractometer using the aligning cross-hairs with the sample in various positions. The (400) peak of the silicon was then located by the diffractometer and the angular values were all zeroed to ensure that the fiber sample was level. It has been shown that the (100)/(010) face is the fast growing face in 123 single crystals solidified using floating zone growth.[11,63] The ab-axis of the crystal, the fast growth direction, was found to grow approximately parallel to the fiber axis.[11] It was, therefore, assumed that the c-axis of the 123 crystal was

nearly perpendicular to the axis of the single crystal fiber when mounting the fiber in the X-ray diffractometer. The (006) peak of the 123 crystal was therefore located approximately by scanning about the χ axis of the diffractometer at the 2-theta value of the 123 (006) peak. The (003) peak of the 123 crystal was also scanned for at the same value of χ. This was done because the 2-theta value of the (006) peak is within 0.1 degrees of the 123 (200) peak and within 1.2 degrees of the 123 (020) peak. It was determined that the original (006) peak was definitely the (006) peak and not the (200) peak or the (020) peak by locating the (003) peak at the same χ value. The exact (006) peak position was then optimized by varying ω. ω determines how much the in-plane angle of the 123 crystal must be changed in order to obtain the maximum peak position. The value of ω, therefore, gives the misorientation of the c-axis of the 123 crystal relative to the normal of the fiber. ω also gives the misorientation of the ab-axis relative to the axis of the single crystal fiber, as shown in figure 4.13, since the ab-axis and the c-axis of the 123 crystal are separated by 90°.

It was found that the misoreintation between the fiber axis and the ab-axis of crystals grown at earlier times during the LHFZ growth process was larger than the misorientation in crystals grown at later points in the process. Figure 4.14 shows the ω peaks of two different single crystal sections in the same fiber. It can be seen that the misorientation of the growth direction was larger for the crystal near the start of solidification (but after single crystal growth had been achieved) than for the crystal near the fiber zone (the end of solidification). Table 4.1 shows that this was the case for all crystals examined using four-circle X-ray diffractometry. A secondary nucleation model is proposed based on this data.

Fiber sample number	crystal location within fiber	measure ω values (degrees)
L15	far from zone	1.94
	near zone	0.27
L33	far from zone	3.00
	near zone	1.85, 2.00, 2.00, 2.00
L55	far from zone	2.30
	near zone	0.62, 0.15, 0.05

Table 4.1. 123 crystal misorientation measured by four-circle X-ray diffraction.

4.5.2. Secondary nucleation model

Figure 4.15 shows a schematic of 123 crystal growth during LHFZ processing. Figueredo[11] showed that mass nucleation and grain selection usually occurs within the first 30 zone lengths during LHFZ growth. Natural grain selection takes place when the fastest growing grain grows and dominates the slower growing grains until only this single grain remains. The grain that remains is oriented such that its ab-axis is more closely aligned with the fiber axis than any other grains nucleated during initial nucleation, allowing it to grow faster than the others. Four-circle X-ray diffraction results have shown, however, that this first grain is not always aligned perfectly with the fiber axis and is often misaligned by a few degrees.

Figure 4.16 shows a model describing secondary nucleation which is believed to take place during subsequent growth of the YBCO fiber. The initial single crystal has a large misorientation relative to the fiber axis (3 degrees, for example). Secondary 123 crystals nucleate on rough spots or fiber imperfections as the fiber is pulled through the hot zone. Any 123 crystal nuclei with ab-axes aligned less favorably relative to the already growing

crystal are quickly stopped as the crystal grows past them. Eventually, however, a 123 crystal with a more favorable orientation than the already growing crystal is nucleated. Such a crystal will grow faster than the already growing crystal. This new crystal will spread as the fiber is pulled through the hot zone, until it has completely dominated the original 123 crystal. Secondary nucleation will then occur along this crystal, until another grain with an even better orientation is nucleated. This process will occur until the ab-axis of the crystal is oriented exactly parallel to the fiber axis.

This model predicts that a continuous single crystal fiber can eventually be grown using LHFZ processing. The fact that 123 single crystals have a maximum growth rate of around 1 cm/h, however, means that it may take more than 10 or 20 hours to form a perfectly aligned crystal. The longest sample grown for this study was processed for 19 hours and contained a 10 cm section with a single grain boundary, with the last crystal approximately 6 cm long. The LHFZ process is a user-controlled process which requires continual monitoring and adjusting of beam position and zone temperature. Significant growth fluctuations can occur if the process is left unmonitored for more than a few minutes. This limits the maximum user-operated growth period to less than 1 day. It has been shown that this is not enough time to grow a single crystal with perfect orientation. Continuous monitoring and feedback of beam position and temperature using a computerized LHFZ system, CCD camera and pyrometer will allow the maximum processing time to be significantly increased. The maximum growth time will then be limited by the length of the crystal growing chamber and the length of the sintered polycrystalline YBCO feed rods which can be produced. The quality of the polycrystalline precursor rods must also be maximized, since surface imperfections, pores, and other flaws destabilize the zone during growth. The use of such high quality precursor fibers, as well as an automated LHFZ growth system, would allow the production of long sections of single crystal fibers without grain boundaries.

4.5. Conclusions

YBCO single crystals with lengths of more than 5 cm were grown reproducibly through the optimization of the precursor fiber production and the LHFZ growth process. The maximum length of 123 single crystals produced by the user-operated LHFZ growth process was found to be limited by the slow growth rate of YBCO materials as well as the problem of secondary grain nucleation. The relationship between 123 crystal growth rate and interface structure was observed in samples containing Nd-211 particles. The maximum growth rate below which single crystal growth takes place was confirmed to be between 1 and 2 cm/h. The 123 single crystal interface changes from a single crystal interface to a dendritic interface at growth rates above these values. The presence of a diffusion zone containing a reduced number of 211 particles in front of the 123 growth interface confirmed the melt-growth models proposed by Cima et al.[33] and Izumi et al.[10] (see chapter 2). A model describing secondary nucleation in YBCO fibers was proposed based on 123 crystal orientation results obtained by four-circle X-ray diffraction. This model suggests that perfectly oriented single crystals can be obtained by using longer processing times, resulting in much longer sections of 123 single crystals. Such results can be obtained through the use of a computerized monitoring and feedback system during LHFZ processing. The use of long, high quality polycrystalline precursor fibers with no pores or surface imperfections is also critical for automated growth of long single crystals by LHFZ growth.

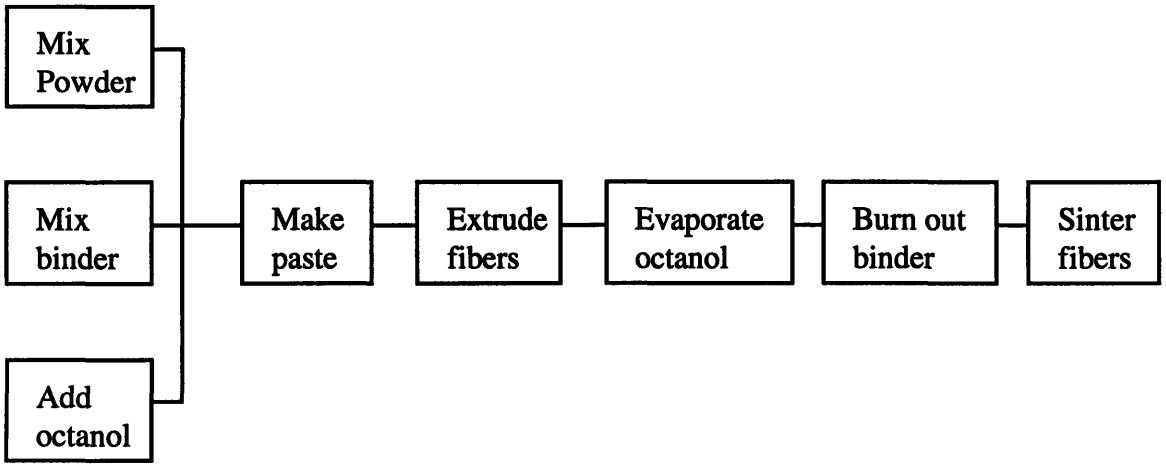

Figure 4.1. Schematic of the basic LHFZ precursor fiber production process.

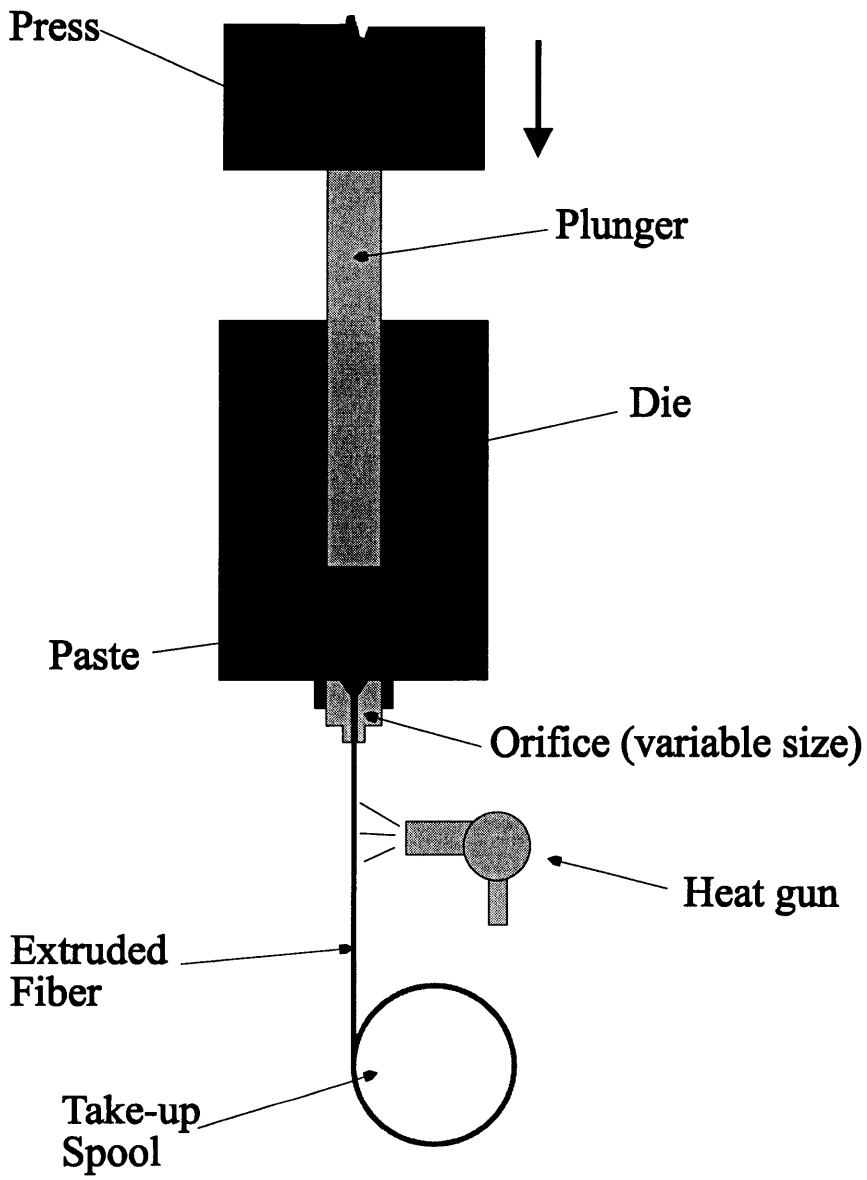

Figure 4.2. Schematic of the extrusion process used in the production of LHFZ precursor fibers.

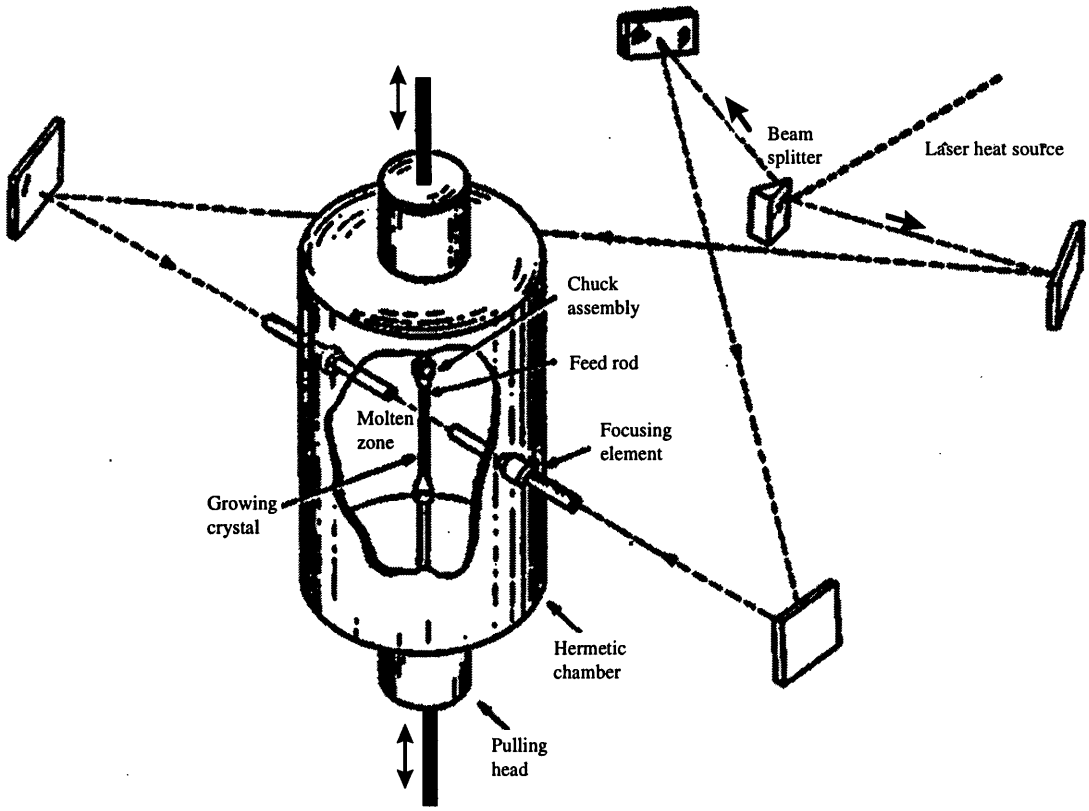

Figure 4.3. Schematic of the LHFZ growth set-up.[11]

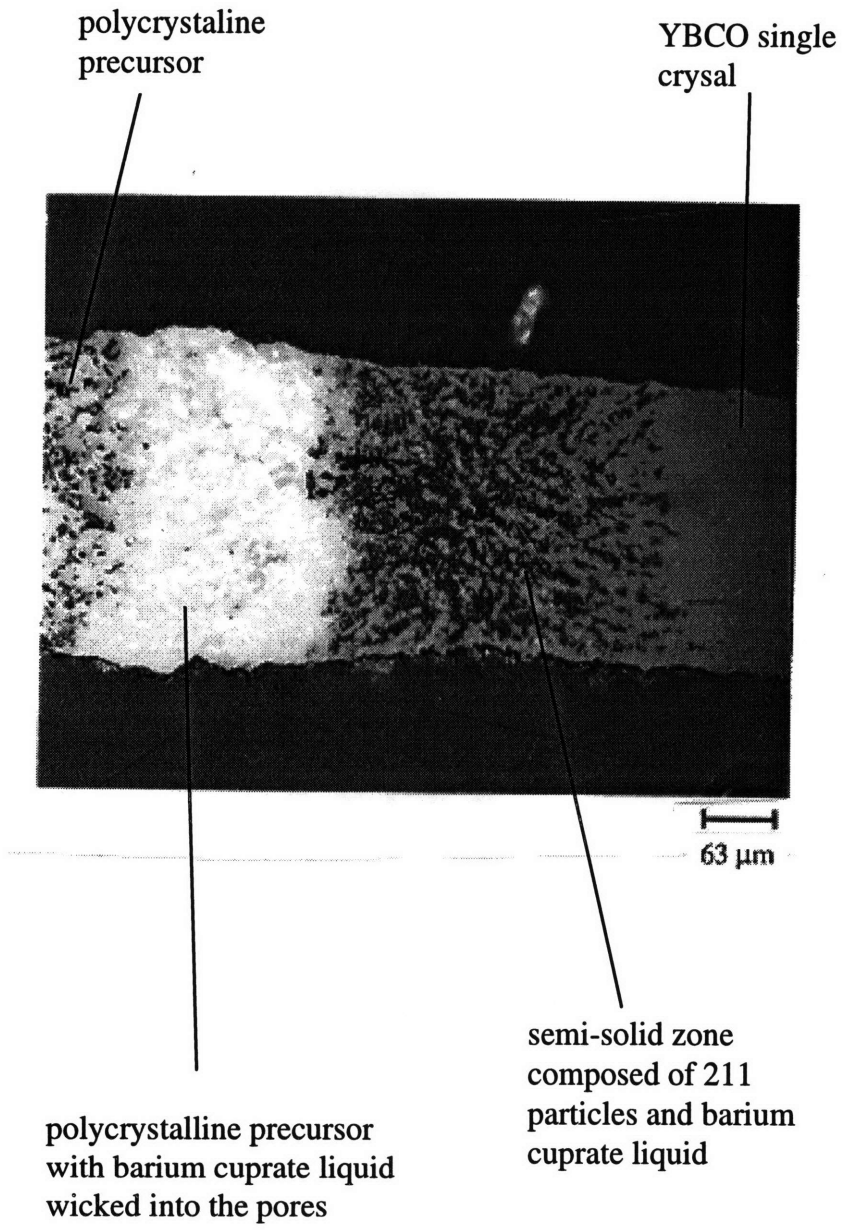

Figure 4.4. Optical micrograph of a polished cross-section of a typical quenched semisolid zone produced by LHFZ growth.

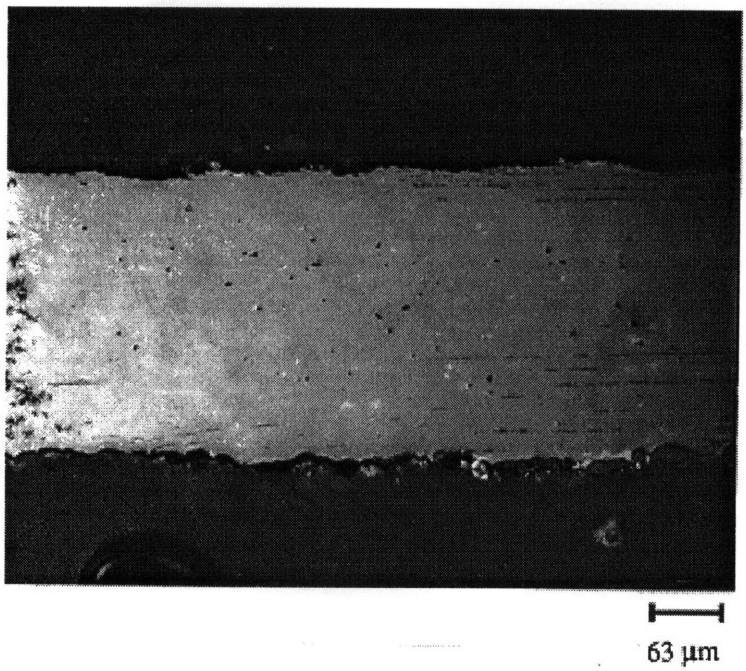

Figure 4.5. Optical micrograph of a polished cross-section of a typical YBCO single crystal fiber produced by LHFZ growth.

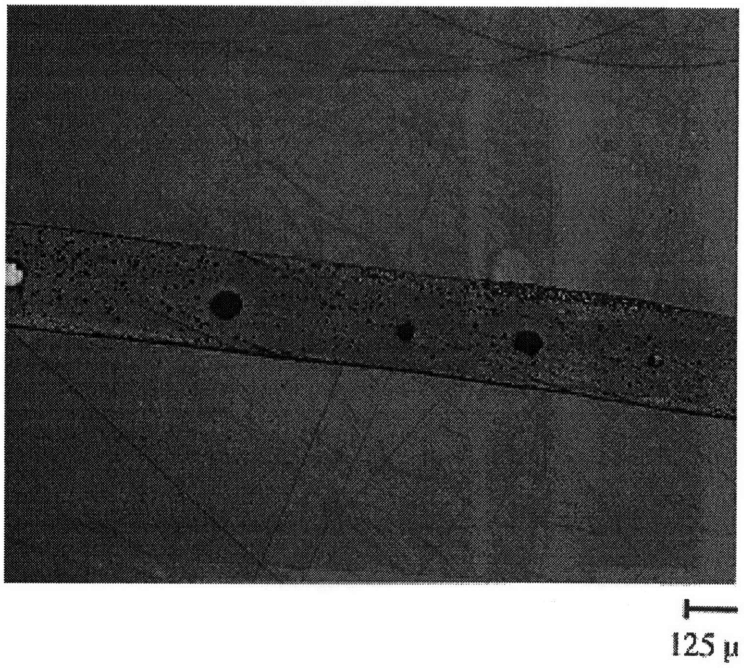

Figure 4.6. Optical micrograph of a polished cross-section of a fiber produced by LHFZ growth showing a porous microstructure before improvements were made in the extrusion process.

a)

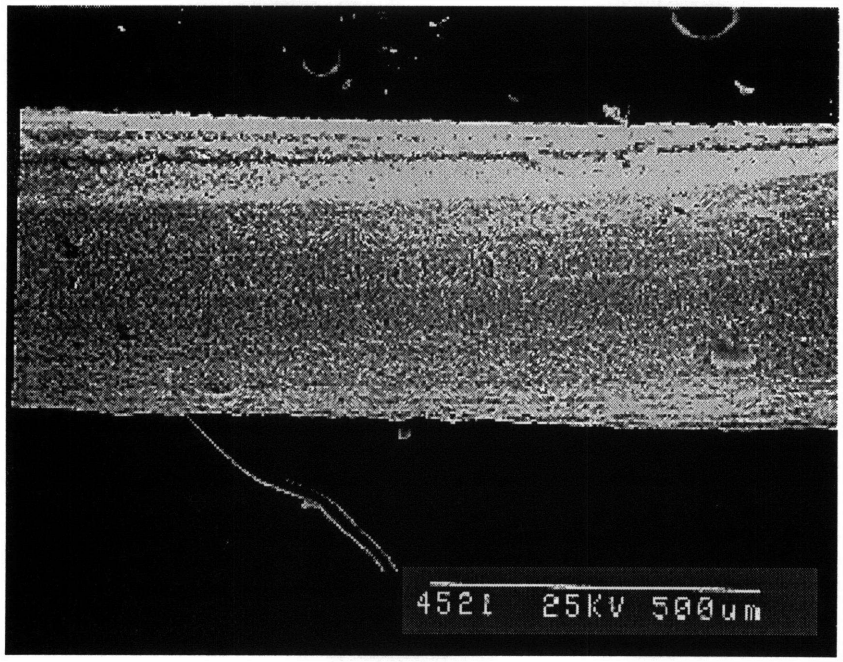

b)

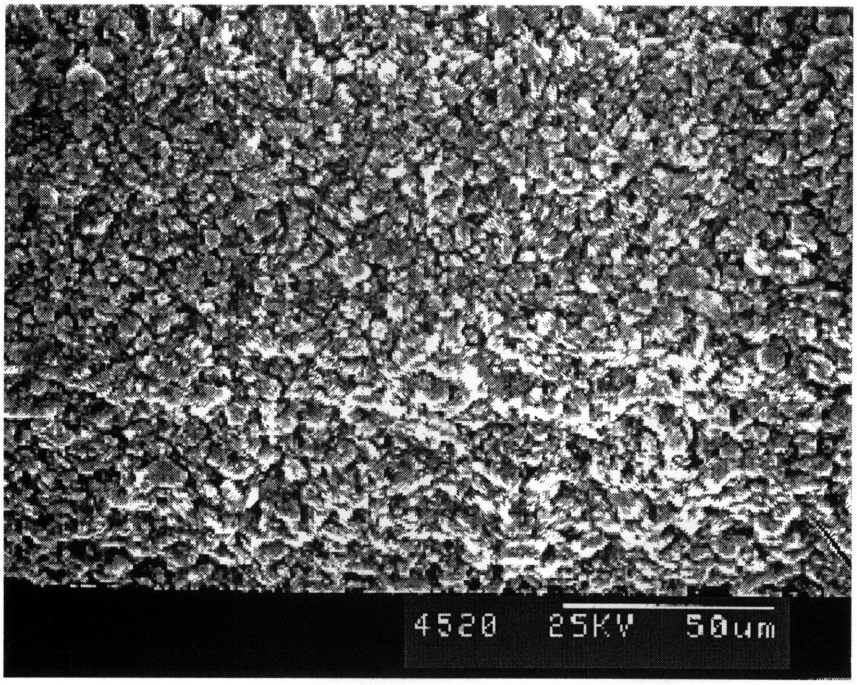

Figure 4.7. a) Low and b) high magnification SEM micrographs of sectioned LHFZ precursor fibers after extrusion.

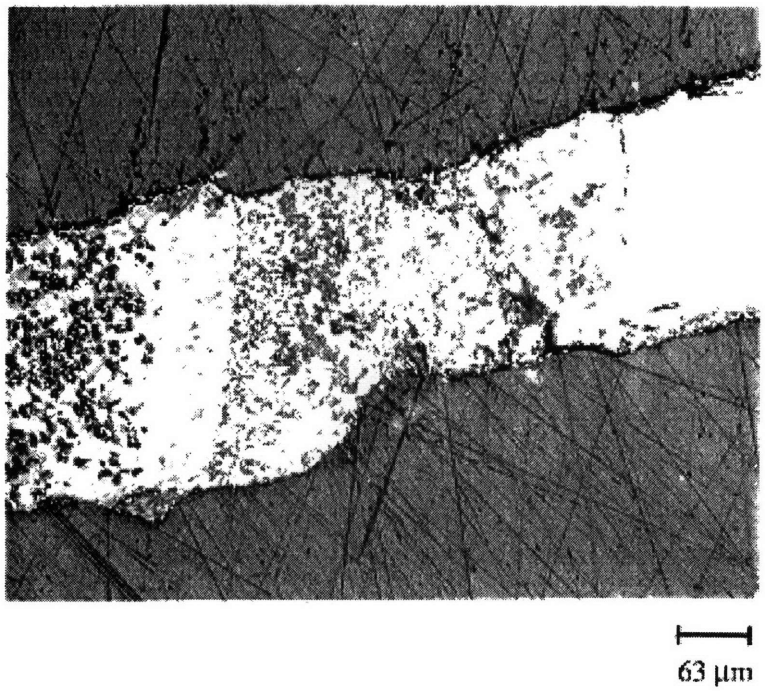

Figure 4.8. Optical micrograph of a polished cross-section of a LHFZ sample showing liquid migration out of the semi-solid zone.

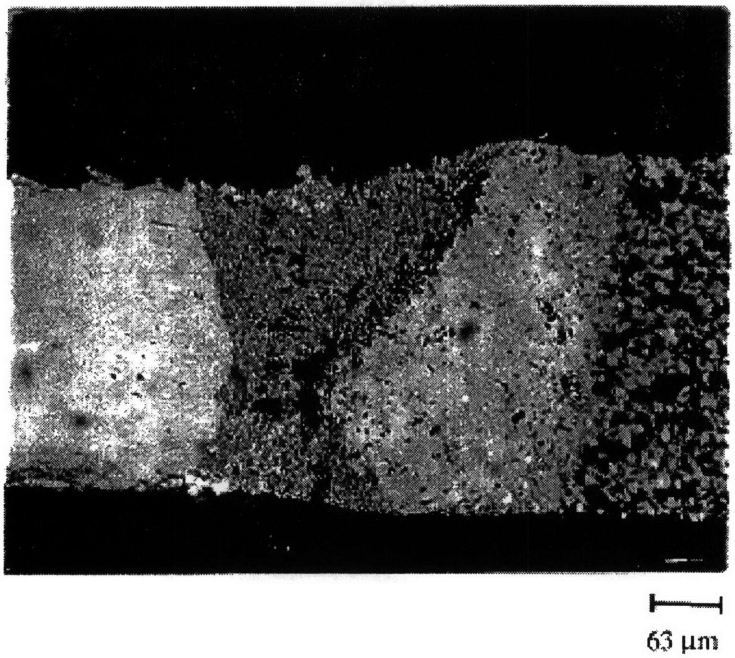

Figure 4.9. Optical micrograph of a polished cross-section of a LHFZ sample showing uneven heating in the semi-solid zone.

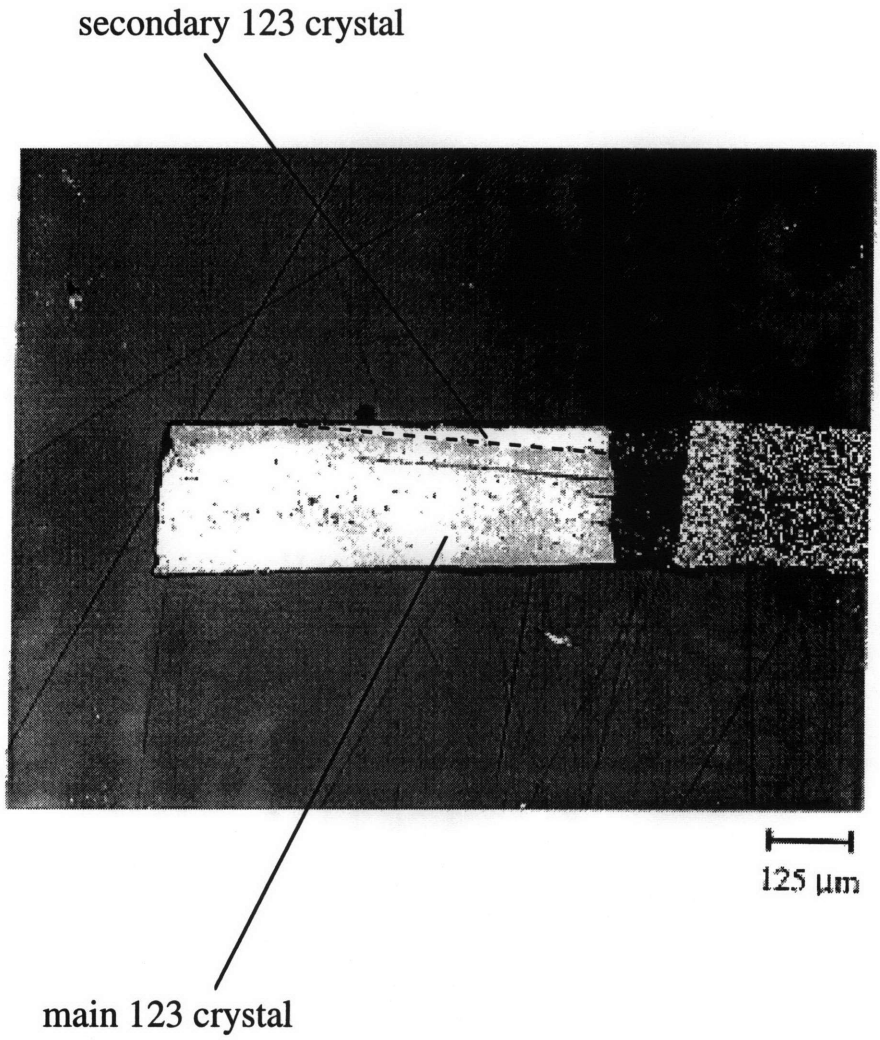

Figure 4.10. Optical micrograph of a polished cross-section of a LHFZ sample showing secondary grain nucleation on the surface of the fiber.

a)

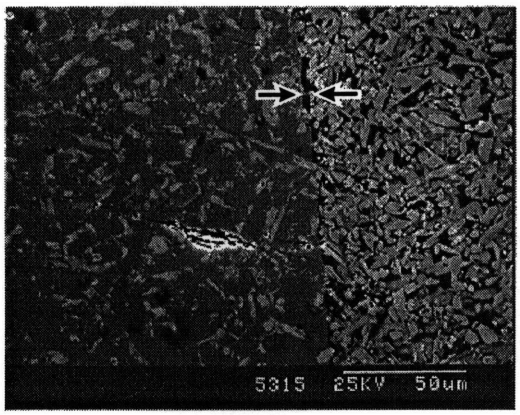

b)

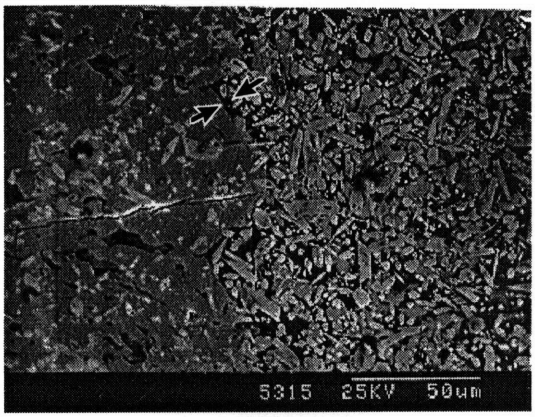

c)

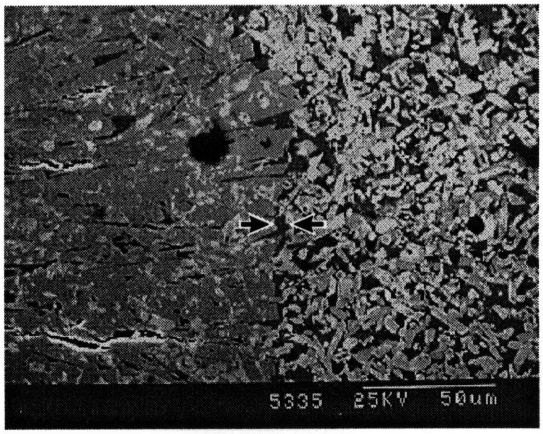

Figure 4.11. Backscattered SEM micrographs of excess Nd-211 LHFZ samples grown at rates of a) 1 cm/h, b) 2cm/h and c) 3 cm/h. It can be seen that the structure of the 123 interface deteriorates with increasing growth rate. A diffusion zone which is poor in 211 phase can be seen in front of the 123 interface for samples solidified at all growth rates. This diffusion zone is marked by the arrows in figures a) through c).

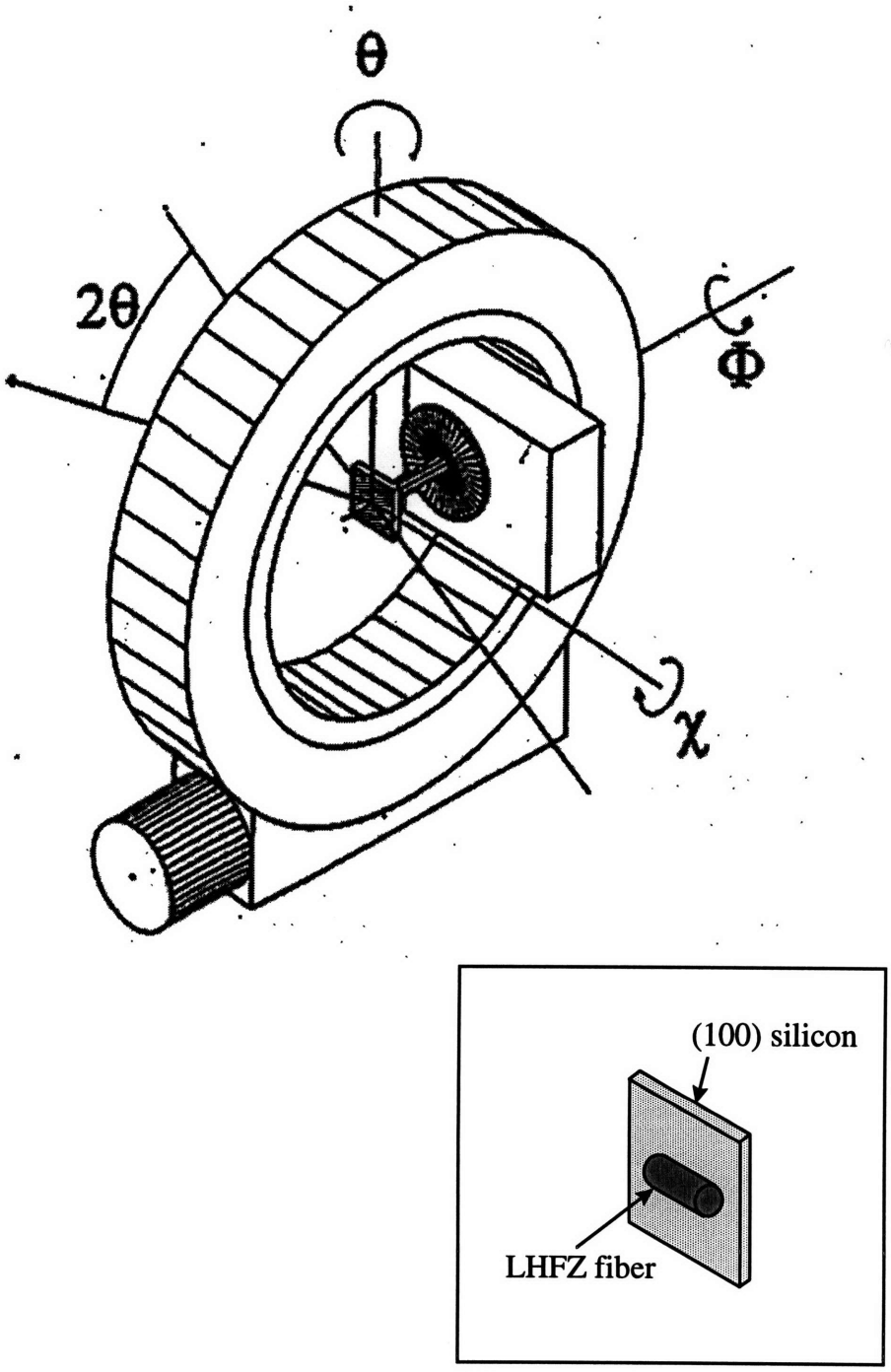

Figure 4.12. Schematic of four-circle X-ray diffraction set-up.[117] LHFZ fiber samples were oriented in the X-ray diffractometer as shown in the inset.

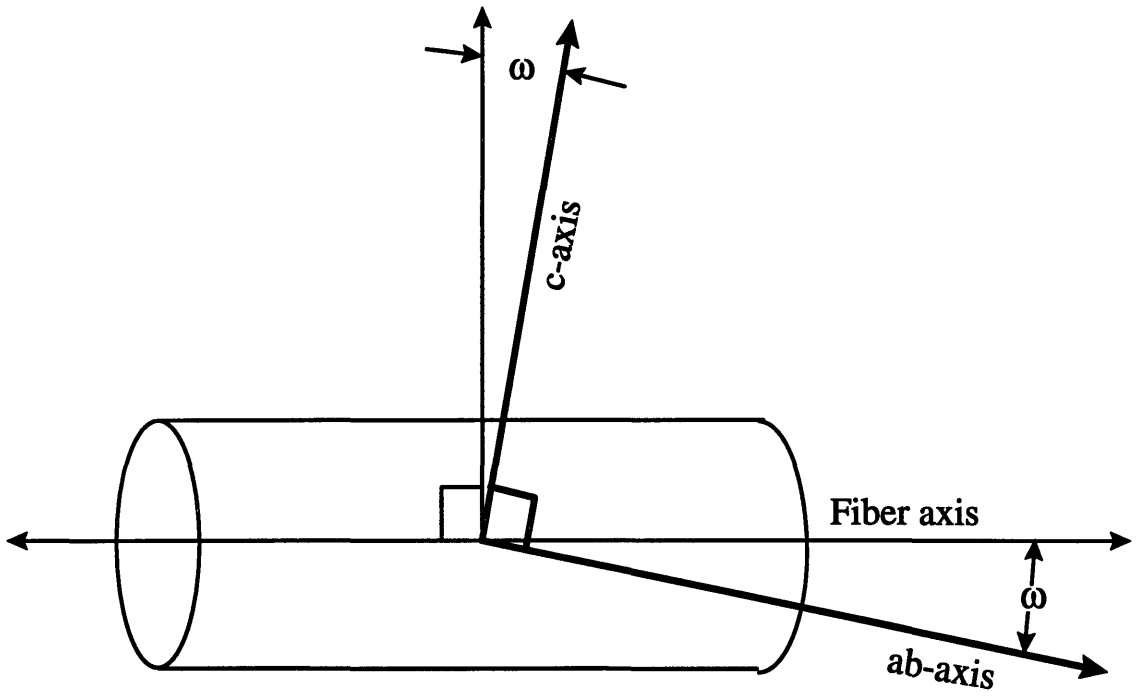

Figure 4.13. Schematic diagram of the c-axis and ab-axis of the 123 crystal relative to the LHFZ fiber axis. ω gives the misorientation of the ab-axis relative to the axis of the single crystal fiber

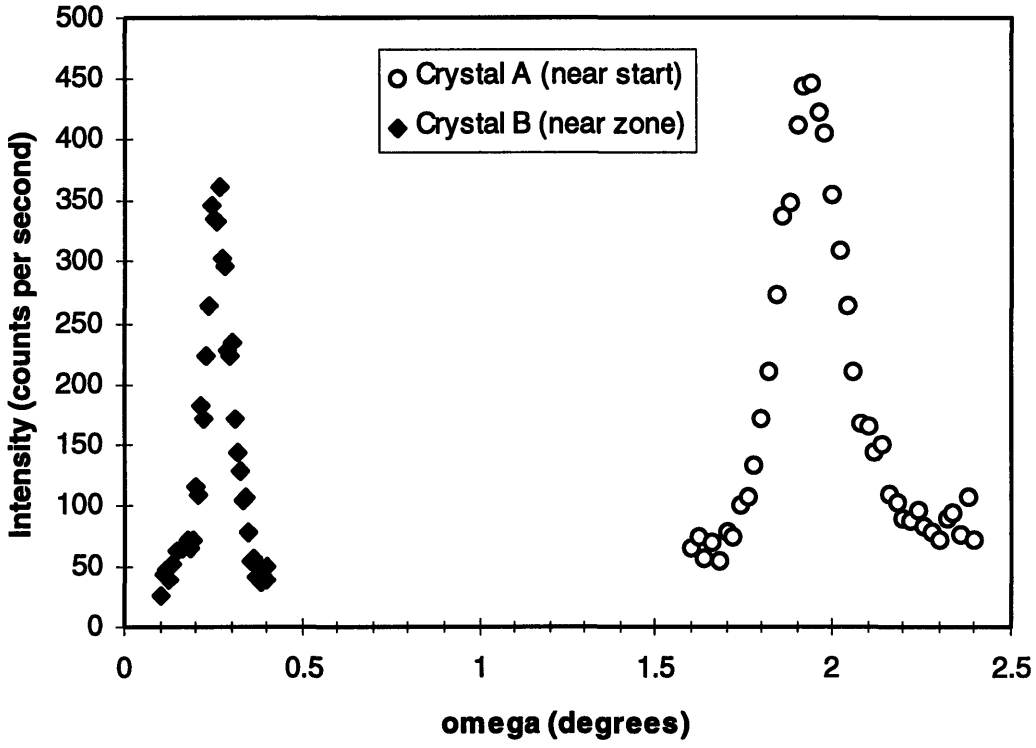

Figure 4.14. ω peaks obtained by four circle diffraction of two single crystals in a LHFZ fiber.

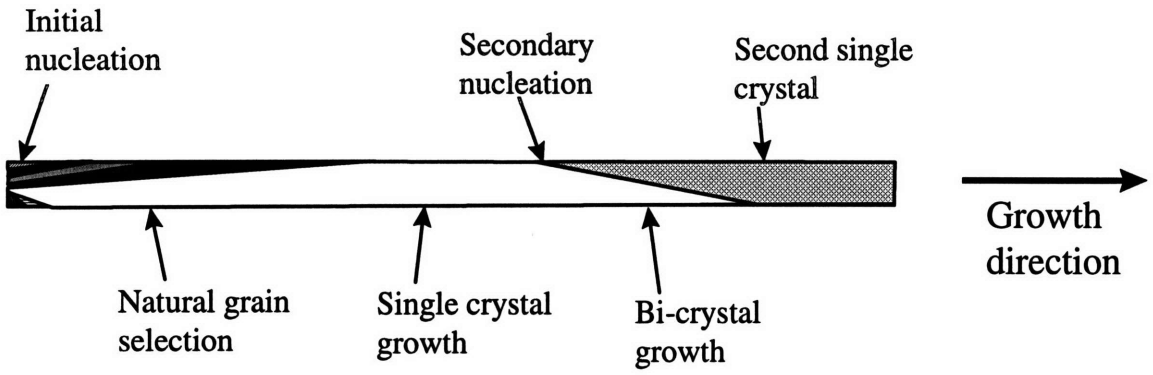

Figure 4.15. Schematic of 123 crystal growth during LHFZ processing.

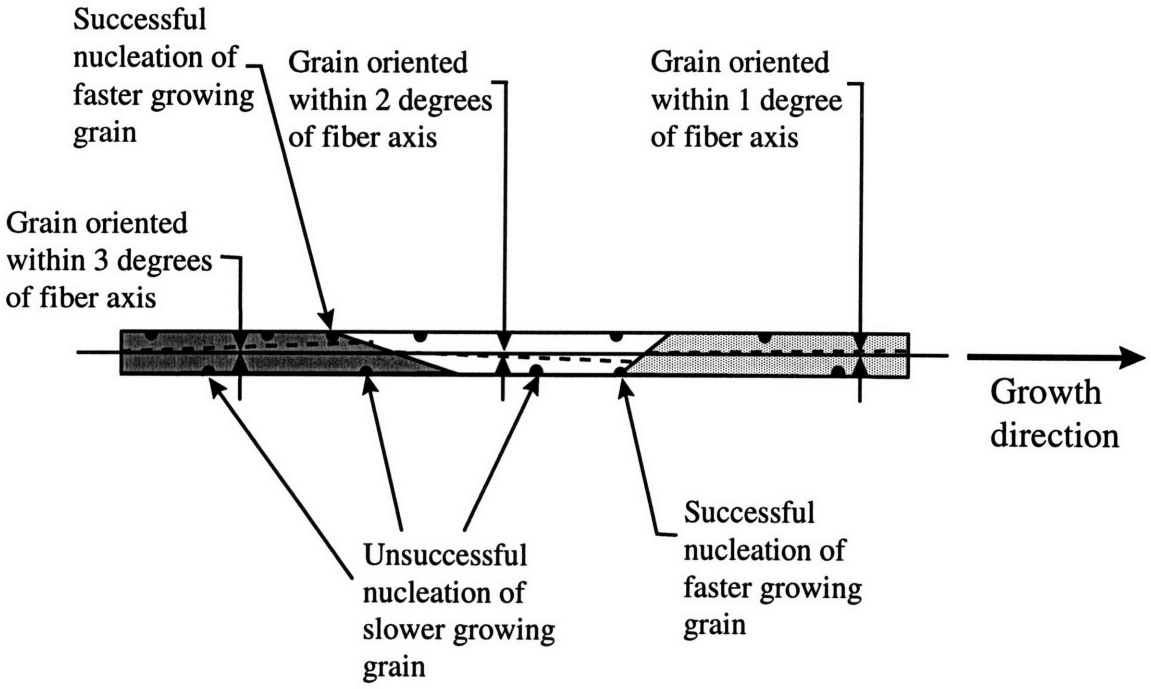

Figure 4.16. Schematic of model describing secondary nucleation which is believed to take place during subsequent growth of the YBCO fiber.

Chapter 5

Seeded growth of YBCO single crystals

5.1. Introduction

Seeded growth is a second method for producing large single crystals of YBCO superconducting material. The effects of variations in processing parameters on crystal growth were, therefore, investigated in this study. The dependence of growth rate on variations in 211 particle characteristics such as volume fraction, particle size and decreased coarsening rate through platinum doping, was investigated. The dependence of growth rate on undercooling was also investigated. Observations were made on YBCO crystal habit and growth interface morphology as a function of 211 particle characteristics and undercooling. 123 crystal habit was examined and related to expected shapes based on periodic bond chain (PBC) analysis. Changes in 123 interface morphology were related to variations in processing parameters. The relationship between growth rate, R, and undercooling, ΔT, was examined for the different growth mechanisms of 123 single crystals.

5.2. Experimental procedure

Seeded growth of YBCO single crystals was performed using single crystal Nd-123 seeds and YBCO precursor pellets of various compositions. Seed and precursor pellet production, as well as the seeded growth process, are described in the following sections.

5.2.1. Nd-123 seed preparation

Single crystal Nd-123 seeds were produced by melt-growth. Nd-123 was chosen as a seed material because it has a crystal structure and unit cell size very similar to that of Y-123. Additionally, Nd-123 has a peritectic temperature of 1090 °C in air (see figure 2.3), which is 90 °C higher than the peritectic temperature of Y-123 (see figure 2.2). Therefore, Nd-123 crystals remain solid at temperatures between the Y-123 peritectic temperature and the Nd-123 peritectic temperature. This is the temperature range in which seeded growth of Y-123 was performed.

Commercial Nd-123 powder (PSC, Inc.), produced using spray pyrolysis, was used to produce the Nd-123 seed crystals. The powder was examined by X-ray powder diffraction and found to be phase pure. The Nd-123 powder was weighed and pressed into 3 g pellets using a 0.5 inch diameter die under 5000 lbs of uniaxial pressure. The pressed pellets were sintered on a polycrystalline MgO plate for 18 hours at 950 °C in air to densify them. They were then placed onto a thin slab of single crystal MgO for heat treatment. Previous work has shown that MgO does not react with the liquid formed during melt processing of 123 materials.[35] Additionally, since the MgO plates used in these experiments were single crystals, no pores or cracks were present to wick the liquid out of the semi-solid melt. The Nd-123 pellet and MgO substrate were placed into a quartz-lined tube furnace and heated in air to 1126 °C at a rate of approximately 10 °C/min. The samples were held at this temperature for 1 h to assure complete melting of the YBCO portion of the sample. The samples were then cooled to 860 °C in 76 h. An extremely low cooling rate of less than 2 degrees per hour was used to ensure growth of large crystals. The samples were then cooled to room temperature using a cooling rate of approximately 1 °C/min. The temperature profile used to produce the Nd-123 seeds is shown in figure 5.1. A schematic of the furnace used for Nd-123 seed production, as well as for the seeded growth experiments, is shown in figure 5.2. Large Nd-123 single

crystals, on the order of hundreds of microns in size, were formed as the sample was slowly cooled below the peritectic temperature.

The heat-treated Nd-123 pellets were mounted in epoxy and sectioned perpendicular to their axes. The pellet cross-sections were polished and examined in polarized light under an optical microscope to determine the size of the Nd-123 crystals. The polished samples were then sectioned into 0.3 mm x 0.3 mm squares using a diamond impregnated wire saw. The surrounding epoxy kept the resulting cubes of Nd-123 material together in pellet form. The sectioned pellets were again examined in polarized light under the optical microscope to determine which sections were made up of single crystals and which sections contained grain boundaries. The orientation of the Nd-123 crystals was determined by examining the cracks within the crystals. 123 materials undergo a phase transition from the tetragonal to orthorhombic phase around 500 °C (see figure 2.2). The change in crystal volume causes the material to crack. The preferred cracking planes have been found to be perpendicular to the c-axes of the crystals.[118] Therefore, the Nd-123 crystals exhibiting no cracks can be identified as having their polished surfaces oriented perpendicular to the c-axis, while cubes with many cracks are known to be oriented parallel to the c-axis. Crystals with fewer widely spaced cracks have orientations somewhere in between. Single crystal Nd-123 cubes oriented with polished sections perpendicular to their c-axis were chosen as seed crystals for use in these experiments.

5.2.2. YBCO precursor pellet preparation

Various types of precursor pellets, including stoichiometric 123 samples, excess 211 samples and platinum doped samples, were prepared for use in the seeded growth experiments. The labels and compositions of each type of sample are listed in table 5.1.

Label	Composition	Milled
Stoichiometric 123	100 wt.% 123	no
Excess 211	80 wt.% 123 + 20 wt.% 211	yes
Pt-doped stoichiometric	99 wt.% 123 + 1 wt.% Pt	no
Pt-doped excess 211	79 wt.% 123 + 20 wt.% 211 + 1 wt.% Pt	yes

Table 5.1. Composition of precursor pellets used in seeded growth experiments.

The 123, 211 and platinum powder used to prepare the precursor pellets used in the seeded growth experiments were the same type used to prepare the coarsening samples and LHFZ samples, described in chapters 3 and 4, respectively. Samples labeled as "unmilled" were produced by mixing the unmilled powders with a mortar and pestle until a homogenous mixture was obtained. Samples labeled as "milled" were produced by milling the mixture of 123 and 211 powders in a ball mill with MgO milling media for 24 hours. Some samples were doped with 1 wt.% platinum powder to decrease the coarsening rate of the 211 particles in the semi-solid melt, as described in chapter 3. The Pt-powder was added to the unmilled 123 and 211 powders and the mixture was homogenized using a mortar and pestle. The pellets were pressed and sintered using the same procedure as for the Nd-123 pellets described in section 5.2.1.

5.2.3. Solidification procedure

Seeded growth involves the placement of a higher-melting R-123 seed material, such as Nd-123, on top of a YBCO sample. The YBCO material is then heated above the peritectic temperature to form 211 particles and liquid (see figure 2.2). This semi-solid melt is undercooled to below the peritectic temperature of 1000 °C and held for a given amount of time. The Nd-123 seed acts as a nucleation site for the Y-123 material. The

peritectic reaction which occurs at the 123 solidification interface is described by equation 2.2. The peritectic reaction occurs by dissolution of the high temperature 211 phase into the liquid followed by reprecipitation onto the 123 surface.

Single-crystal Nd-123 seeds with polished faces parallel to their c-axes were placed face-down onto sintered 123 pellets for the seeded growth experiments. The samples were placed onto single crystal MgO substrates and inserted into a quartz-lined tube furnace (see figure 5.2). The samples were then heated in air to 420 °C and then to 1010 °C in 90 minutes. The samples were held at 1010 °C for 1 hour to ensure complete melting. The temperature was then lowered to the desired undercooling temperature and the samples were held at this temperature for the desired growth time. The level of undercooling, ΔT, was varied as one of the processing parameters in the seeded growth experiments. Undercooling was varied between 0 °C and 15 °C. The samples were quenched in de-ionized water after growth to prevent slow cooling and additional growth of 123 material below the desired undercooling temperature. The temperature profile used for the seeded growth experiments is shown in figure 5.3. Three dimensional growth of a 123 single crystal takes place as shown in figure 5.4. The ab- and c-faces of the 123 single crystal grow outward from the seed material to form four ab-pyramids and two c-pyramids within the 123 single crystal. The 123 crystal is continuous, however, and there are no actual physical boundaries between the different pyramids. Only the bottom half of figure 5.4 was observed in the seeded growth samples since the seed is placed on top of the YBCO precursor pellet. The seeded growth samples were then examined using cross-polarized optical microscopy and scanning electron microscopy.

Figure 5.5 shows the top view of a typical YBCO single crystal produced by seeded growth. The assignment of the crystal faces was performed by examining the direction of cracks within the crystal which were observed after polishing the surface of the crystal. The preferred cracking plane in 123 materials is along planes oriented perpendicular to the c-axis of the 123 crystal, as described in section 5.2.1.

5.3. Results and discussion of the dependence of 123 crystal growth rate on variations in processing parameters

An interesting observation made during the analysis of the crystals grown for this study is that the c-axis growth rate is larger than the ab-axis growth rate (see figure 5.5). This observation is in direct contrast to results of directional solidification processes in which the ab-face of the 123 crystal is the fast growing face.[11,63] This difference is due to the fact that the current seeded growth experiments were performed at low undercoolings while the directional solidification experiments were performed in high temperature gradients resulting in large undercoolings. This will be discussed further in section 5.5 which deals with the relationship between growth mechanism and growth rate of 123 single crystals.

The ratio of c-axis to ab-axis on the top surface of the crystals grown for this study ranged from 1.31 to 1.54. The ratio of c-axis to the ab-axis perpendicular to the seed crystal was even larger, with at typical value being 16.67. This high ratio of c-axis length to ab-axis length has also been observed in other 123 crystals produced by seeded growth.[42,119] This is in direct contrast to other crystals produced by melt growth processes, such as flux growth. The growth rate of the c-axis of typical flux grown crystals was shown to be much slower than the ab-axes. Ratios of ab-axis length to c-axis length ranged from 6.67×10^{-4} to 0.05.[120] The cause for this difference in the ratios of c-axis to ab-axis growth rates for crystals produced by seeded growth and those produced by flux growth is not yet understood.

Figure 5.6 shows the dependence of 123 single crystal growth rate on variations in processing parameters. Figure 5.7 shows an expanded version of the data for the stoichiometric samples shown in figure 5.6. The filled symbols represent the ab-axis of the 123 crystal while the hollow symbols represent the c-axis. It can be seen that growth rate depends on sample undercooling, 211 volume fraction, and Pt-doping. Variations in

growth rate with 211 volume fraction and Pt-doping result from changes in 211 particle characteristics within the samples. The following two sections discuss the dependence of 123 crystal growth rate on sample undercooling and 211 particle characteristics.

5.3.1. The dependence of 123 crystal growth rate on undercooling

Figures 5.8 through 5.10 show polished cross-sections of YBCO crystals grown from excess 211 precursors by seeded growth for 2 h at undercoolings of 9 °C, 12 °C and 15 °C, respectively. It can be seen that the growth rate of the 123 crystals increases with undercooling, ΔT. It can be seen from figure 5.6 that this was the case for all samples, as predicted by modern solidification theory. This result fits the YBCO solidification model proposed by Cima et al.,[33] described in section 2.4. This model predicted that growth rate of 123 crystals is heavily dependent on undercooling. Undercooling of the sample was shown to result in an yttrium concentration gradient in front of the 123 interface. This concentration gradient is the driving force for 211 particle dissolution and yttrium diffusion to the 123 interface. The equation relating growth rate to processing variables (equation 2.4 in section 2.4) can be rewritten for seeded growth to reflect the absence of a temperature gradient as:

$$R = \frac{D_L}{l\left(C_{SY} - C_{LP}\right)}\left[\frac{\Delta T_S}{m_{LY}}\right] \qquad (5.1)$$

where R is the growth rate of a planar 123 interface, l is half the distance between the 211 particles in the barium cuprate liquid, D_L is the diffusion coefficient of yttrium in the liquid, C_{SY} is the yttrium content of the 123 phase, C_{LP} is the yttrium content of the liquid, ΔT_S is the constitutional supercooling (undercooling) ahead of the 123 interface and m_{LY} is the slope of the equilibrium 123 liquidus (assumed to be constant).[33] It can be seen from

equation 5.1 that R will increase with ΔT. This is verified by the results shown in figure 5.6. 211 particle dissolution rate and yttrium diffusion rate increase with undercooling, therefore increasing the rate of yttrium transport to the 123 interface and resulting in an increased growth rate of the 123 crystal. It can be seen from figure 5.6 that a two-fold increase in the sample undercooling, ΔT, results in a two-fold increase in growth rate, R. This is in good agreement with results predicted by equation 5.1.

5.3.2. The dependence of 123 crystal growth rate on 211 particle characteristics

It can be seen from figures 5.6 and 5.7 that 123 crystal growth rate depends on 211 volume fraction and Pt-doping. Growth rate increases by almost an order of magnitude with the addition of excess 211 particles and by almost 10% with the addition of platinum. Figures 5.9 and 5.11 show YBCO crystals grown from excess 211 and stoichiometric 123 precursors at an undercooling of 12 °C, respectively. Comparison of figures 5.9 and 5.11 show that excess 211 additions increase 123 single crystal growth rate. Figures 5.8 and 5.12 show YBCO crystals grown from excess 211 precursors without Pt-doping and with Pt-doping at an undercooling of 9 °C, respectively. Comparison of figures 5.8 and 5.12 show that Pt-doping increases 123 single crystal growth rate. These results can be explained by examining the relationship between the addition of excess 211 particles or Pt-doping and the distance between the 211 particles in the semisolid melt.

The distance between 211 particles in the semi-solid melt is dependent on both 211 particle size and 211 particle volume fraction in the melt. Sung et al.[31] quantified the relationship between l, half the distance between 211 particles, d, the 211 particle diameter, and V_f, the volume fraction of 211 particles in the melt, by assuming a simple cubic arrangement of evenly spaced particles in the melt. They found this relationship to be:

$$2l = \left(\frac{\pi d^3}{6V_f}\right)^{\frac{1}{3}} \tag{5.2}$$

Changes in l due to changes in V_f and d are related to variations in growth rate, R, through equation 5.1. It can be seen from equation 5.1 that a decrease in l by a certain amount produces an increase in R by the same amount.

It was shown in chapter 3 that 211 particles which form in stoichiometric samples are much larger than 211 particles in excess 211 samples. This is due to the fact that the 211 phase forms via homogeneous nucleation in stoichiometric samples and heterogeneous nucleation on excess 211 particles in excess 211 samples. The 211 particles in the semi-solid melt of stoichiometric 123 samples processed by seeded growth are therefore much larger than the 211 particles in excess 211 samples. This was found to be true in the samples produced for these experiments. The average 211 particle diameter for the stoichiometric samples was approximately 11 μm while the 211 particles in the excess 211 samples had an average diameter of approximately 1.5 μm. Some of this decrease in particle size can also be attributed to the fact that the excess 211 samples were produced from milled powder, while the stoichiometric samples were not.

The excess 211 samples also contained 20 wt.% excess 211 particles. The phase rule was used to estimate the volume% of 211 particles in the stoichiometric and excess 211 samples above the peritectic temperature from the binary phase diagram shown in figure 2.2. It was found that the stoichiometric samples contained approximately 23 vol.% 211 (V_f = .23) phase above the peritectic temperature while the excess 211 samples contained approximately 43 vol.% (V_f = .43) 211 phase. The values for 211 particle size, d, and 211 particle volume fraction, V_f, were plugged into equation 5.2 and used to calculate the approximate change in interparticle spacing, l, for the excess 211 samples relative to the stoichiometric samples. It was found that l = 7.2 μm for the stoichiometric 123 samples

and l = 0.8 μm for the excess 211 samples. These values correspond to a decrease in l of nearly an order of magnitude between the stoichiometric samples and the excess 211 samples. Equation 5.1. shows that an order of magnitude decrease in l will result in an order of magnitude increase in growth rate, R. The results shown in figure 5.7 show that this is indeed the case for the crystals grown in these experiments. The growth rate of 123 crystals produced from excess 211 samples is approximately an order of magnitude larger than the growth rate of 123 crystals produced from stoichiometric samples.

It was shown in chapter 3 that Pt-doping reduces the coarsening rate of 211 particles in the barium cuprate liquid. The change in 211 particle size with Pt-doping in the samples processed by seeded growth was estimated based on the results given in chapter 3 (see figure 3.17). The seeded growth samples were held at 1030°C for 1 hour and then cooled to an undercooling temperature slightly below the peritectic temperature of 1000 °C and held there for 2 hours. Only an approximate decrease in 211 particle size with Pt-doping can be calculated from the results in chapter 3 because the coarsening experiments were performed at a temperature of 1094 °C, which is significantly above the temperatures used in the seeded growth experiments. This approximation is still useful for estimating the expected increase in growth rate for Pt-doped samples, however. It was estimated from the results in chapter 3 that the addition of a Pt-dopant will reduce the 211 particle size in the seeded growth samples by an average of 25 % throughout the growth process. A 25 % reduction in 211 particle size results in a decrease of 25% in l, half the interparticle spacing, as well (based on equation 5.2). Equation 5.1 shows that this reduction in l corresponds to an increase in growth rate, R, of 25%. Figures 5.6 and 5.7 show that the approximate increase in 123 crystal growth rate with the addition of platinum is approximately 10%. It is likely that the observed 123 growth rate increase is lower than the value approximated from the coarsening results given in chapter 3 because the processing temperature during seeded growth was approximately 90 °C lower than the temperature used in the coarsening experiments. Coarsening is reduced at the lower

temperatures, causing the beneficial value of Pt-doping as a coarsening reduction agent to be reduced as well.

Growth rate of 123 crystals produced from excess 211 precursors may also be affected by 211 particle segregation which was found to occur in these samples. This phenomenon will be discussed in chapter 7.

5.4. Results and discussion of 123 crystal habit and interface morphology

YBCO crystals grown by seeded growth displayed crystal habits similar to those expected by periodic bond chain (PBC) analysis of 123 crystals. The (011) crystal face, which is predicted by PBC analysis but which is very rare in other melt-grown crystals, was also observed. The morphology of the 123 crystal interface was examined and found to be dependent on undercooling, crystal face and growth mechanism. Results of 123 crystal habit and interface morphology are detailed in the following sections.

5.4.1. Habit of 123 crystals grown by seeded growth

One main crystal habit with small variations was observed in the 123 single crystals produced by seeded growth for this study. Figure 5.11 shows a polished cross-section of a typical YBCO crystal grown from a stoichiometric precursor pellet. As described in section 5.2.1, the c-axis of the crystals can be identified by locating the cracks running through the sample. These cracks form parallel to the ab-axis of the crystal. The c-axis of the crystal is therefore perpendicular to the cracks. Figure 5.10 shows the shape of a typical YBCO crystal grown from an excess 211 precursor pellet. Similar shapes were found in Pt-doped crystals. It can be seen that the c-axis of the top surface of the crystal

shown in figure 5.10 is significantly longer than the ab-axis. Some excess 211 samples also produced crystals such as the ones shown in figures 5.13 and 5.14. The additional face shown in these pictures was determined to be the (011) face. This face has only been observed on 123 crystals by one other researcher.[121] Figure 5.15 shows a typical cross-section of a YBCO crystal grown by seeded growth and sectioned perpendicular to the top of the precursor pellet. It can be seen that the second ab-axis of the crystal (running vertically through the sample) is significantly shorter than the other ab-axis and the c-axis of the crystal. This was found to be the case in all crystals grown by seeded growth, independent of precursor composition.

The manifestation of different crystal faces is due to a combination of the appearance of the slowest growth directions of the crystal determined by crystal structure and variations in growth kinetics of these faces due to variations in process parameters during growth. A number of observations in crystal habit of 123 crystals grown by seeded growth can be explained by examining the theoretical slowest growth directions using periodic bond chain (PBC) analysis. The basic theory of periodic bond chain analysis was developed by Hartman and Perdok.[122] This type of crystal habit analysis depends on the concept of a periodic bond chain which is an uninterrupted, periodically repeated sequence of strong bonds in certain crystallographic directions. A strong bond is considered to be a bond between an atom and its nearest neighbor. A periodic bond chain is a row of strongly bonded atoms within a crystal which has the stoichiometric composition of the crystal. A periodic bond chain in a 123 crystal therefore contains yttrium, barium and copper atoms in a ratio of 1:2:3. Periodic bond chains can be oriented in any direction within the crystal, as long as the stoichiometry criterion is met. A detailed explanation of PBC theory can be found elsewhere.[122]

Three categories of crystal faces can be described by examining orientations of the periodic bond chains within a crystal. An F (flat) face contains two or more non-parallel periodic bond chains. An S (stepped) face contains only one PBC, and a K (kinked) face

contains no PBCs. Each of these different faces has a different growth mechanism. A K face is microscopically rough and needs no nucleation to grow. Atoms are incorporated directly onto the face by a continuous mechanism. S faces have no connections between PBCs and grow by a one dimensional mechanism. F faces grow by a two dimensional growth mechanism. This type of growth can occur either by a spiral growth mechanism or layer-by-layer growth. These growth mechanisms are much slower than the others, causing F faces to be the slowest and most visible faces on the crystal. Crystal habit is, therefore, determined exclusively by F faces.[23,122-123]

One of the most referenced PBC analyses done on 123 crystals was performed by Sun et al.[123] They found that the (001), (011), (013), (112),(114) and (100)/(010) faces were F faces for the tetragonal form of 123 crystals. The theoretical crystal habit of the tetragonal 123 crystal was found to be dominated by the (001), (011) and (100)/(010) faces which were found to be the slowest growing faces. This crystal structure is shown in figure 5.16.

Sectioning the structure shown in figure 5.16 perpendicular to one ab-face results in the structure shown in figure 5.17. The correlation between the theoretical tetragonal 123 crystal structure shown in figure 5.17 and the structure observed in the 123 crystals produced by seeded growth for this study (see figures 5.13 and 5.14) is very good. The (001), (100)/(010) and (011) faces present in the theoretical structure are all present in the structure of the crystals produced for this study. This has only been observed once before.[121]

5.4.2. Interface morphology of 123 crystals grown by seeded growth

PBC analysis suggests that F faces of crystals grow by a two dimensional growth mechanism.[23,122-123] This type of growth can occur either by a spiral growth mechanism

or layer-by-layer growth. Many researchers have investigated the interface morphology and growth mechanism of 123 crystals, resulting in many different growth observations and results. Vandewalle et al.[124-125] suggested sympathetic nucleation of c-faces on fast growing spirals on the ab-faces, leading to a terraced structure. This growth mechanism does not seem to be occurring in the crystals produced for this study since the c-face was found to grow faster than the ab-face. Hopper growth was observed by Hong et al.[70] on the c-face of 123 crystals while Sun et al.[72] observed Hopper growth on the ab-faces. A schematic of Hopper growth is shown in figure 5.18 a).[126] Growth steps nucleate on the edges of the crystal and grow inward. Spiral growth was observed on the c-face by Sun et al.[69,72] and Taylor et al.[120] and on the ab-face by Narlikar et al.[127] Growth spirals were observed on all faces by Marella et al.[128] Figure 5.18 b) shows a schematic of spiral growth which produces many spiral growth hillocks such as the one shown in the bottom part of figure 5.18 b).[129]

Experimental observations of the 123/liquid interface of quenched excess 211 samples processed by seeded growth for this study showed that the ab-face of the crystals grew by spiral growth while the c-face grew by two dimensional nucleation in the form of Hopper growth. Figures 5.19 through 5.22 show the different interface morphologies observed in excess 211 crystals produced by seeded growth. Figures 5.19 a) through c) show SEM micrographs of the interface morphology of the c-face of 123 crystals produced at undercoolings of 6 °C, 9 °C and 15 °C, respectively. The flat interface on these c-faces shows that layer by layer growth is likely. No spiral growth hillocks were observed on any c-faces of these crystals. Figure 5.20 shows a higher magnification SEM image of the c-face of an excess 211 crystal grown at and undercooling of 15 °C. It can be seen that growth steps are present on the surface of the crystal. The c-interface appears slightly curved in the low magnification optical micrograph of the c-face shown in figure 5.21. This is due to the fact that the growth steps nucleate on the outer edges of the c-face of the 123 crystals and grow inward. The inside regions of the c-face are therefore lower than the outer regions of the c-face where growth steps have already formed. This is a

typical interface structure for Hopper growth.[130] These observations show that two dimensional growth on the c-faces of the 123 crystals grown from excess 211 precursors occurred via edge nucleation. This is supported by other research which has shown that the two-dimensional nucleation barrier at the edges is approximately 25% lower than on the face.[77,130] Scheel et al.[131] also report observations of edge nucleation on c-faces of 123 crystals.

Figures 5.22 a) through c) show SEM micrographs of the interface morphology of the ab-face of 123 crystals produced at undercoolings of 6 °C, 9 °C and 15 °C, respectively. Growth hillocks can clearly be seen on the ab-faces of the 123 crystals. It is, therefore, concluded that the ab-faces of the 123 crystals produced from excess 211 samples grow via spiral growth. It can also be seen that the growth hillocks become less pronounced as undercooling is increased. This is due to the fact that growth perturbations in faceted crystals are more stable at low undercoolings than at high undercoolings. This observation lends support to the theory developed by Cima at al.[33] which assumed that the instability of any perturbations in the 123 growth interface resulting from the presence of a supercooled region is stabilized by the high surface energy of the faceted YBCO faces.[33] It can be seen from figures 5.22 a) through c) that this is indeed the case.

5.5. The relationship between growth mechanism and 123 crystal growth rate

The previous section showed that the ab-face of the 123 single crystals produced for this study grew by a spiral growth mechanism while the c-faces grew by two-dimensional Hopper growth. It was shown in section 5.3 that the c-axis growth rate for the 123 crystals produced for this study was always larger than the ab-axis growth rate (see figure 5.5). This observation is in direct contrast to results of directional solidification processes using large temperature gradients (such as floating zone growth) in which the ab-face of

the 123 crystal is the fast growing face.[11,63] This difference is due to the fact that the current seeded growth experiments were performed at low undercoolings while the directional solidification experiments were performed in high temperature gradients resulting in large undercoolings. Equation 5.3 relates growth rate by a spiral growth mechanism, R_{spiral}, to undercooling, ΔT, by:[110]

$$R_{spiral} = fva_0\left[1-\exp\left(-\frac{\Delta G}{kT}\right)\right] \tag{5.3}$$

where a_0 is the distance advanced by the interface in a unit kinetic process, k is Boltzmann's constant, T is temperature, ΔG is the free energy chance accompanying crystallization and is given by:

$$\Delta G = \Delta H - T\Delta S \tag{5.4}$$

where ΔH and ΔS are the enthalpy and entropy of crystallization, respectively. v in equation 5.3 is the frequency factor for transport at the crystal liquid interface and is given by:

$$\nu = \frac{kT}{3\pi a_0^3 \eta} \tag{5.5}$$

where η is the viscosity of the liquid. f in equation 5.3 is given by:

$$f \approx \frac{\Delta T}{2\pi T_P} \tag{5.6}$$

where T_P is the peritectic temperature of the 123 phase.

Equation 5.7 relates growth rate by a two-dimensional (Hopper) growth mechanism, R_{2D}, to undercooling, ΔT, by: [110]

$$R_{2D} = A\nu \exp\left(-\frac{B}{T\Delta T}\right) \tag{5.7}$$

where A and B are constants.

The difference in the dependence of growth rate, R, on undercooling, ΔT, for both growth mechanisms results in the relationship shown in figure 5.23. It can be seen that the growth rate vs. undercooling curves for spiral and Hopper growth cross at a particular undercooling. This correlates well with the experimental observations made in this study, as well as those of other studies. [11,63] At low undercoolings (such as those used in the current study), the c-face, which grows by a two-dimensional Hopper growth mechanism, is found to grow faster than the ab-face, which grows by a spiral growth mechanism. The LHFZ experiments described in chapter 4, as well as directional solidification experiments described elsewhere,[11,63] resulted in the production of YBCO crystals for which the ab-face was the fast growth face. These experiments were performed at higher undercoolings ($\Delta T > 17$ °C). This change from the c-face as the fast growth face at low undercoolings to the ab-face as the fast growth face at high undercoolings can be explained by examining the relationship of the growth curves plotted in figure 5.23. The intersection point in figure 5.23 was estimated by comparing the relationship of fast growth face to undercooling for seeded growth and floating zone growth experiments. [11,63] Thus, differences in the relationship between growth rate, R, and undercooling, ΔT, for the different growth mechanisms of 123 single crystals can account for the fact that the c-face is the fast growth face at low undercoolings while the ab-face is the fast growth face at high undercoolings.

5.6. Conclusions

It has been shown that growth rate of 123 crystals produced by seeded growth was dependent on undercooling, ΔT, and 211 particle spacing. Growth rates increased with increasing undercooling. The addition of excess 211 phase and platinum dopant decreased the 211 particle spacing, therefore increasing the growth rate of the 123 crystals. These results support the 123 solidification model proposed by Cima et al.[33] 123 crystal habit was shown to be similar to that predicted by PBC analysis. The presence of the (001), (100)/(010) and (110) 123 crystal faces were observed in samples produced by seeded growth. The presence of spiral growth hillocks on the ab-faces and Hopper morphologies on the c-faces of the 123 crystals were shown. The presence of these growth mechanisms are in agreement with PBC theory which states that F faces of faceted crystals grow by two dimensional growth mechanisms. It was shown that differences in the relationship between growth rate, R, and undercooling, ΔT, for the different growth mechanisms of 123 single crystals can account for the fact that the c-face is the fast growth face at low undercoolings while the ab-face is the fast growth face at high undercoolings. Future work should include an examination of why the vertical ab-face of the 123 crystal grows more slowly than the horizontal ab-face of 123 crystals produced by seeded growth.

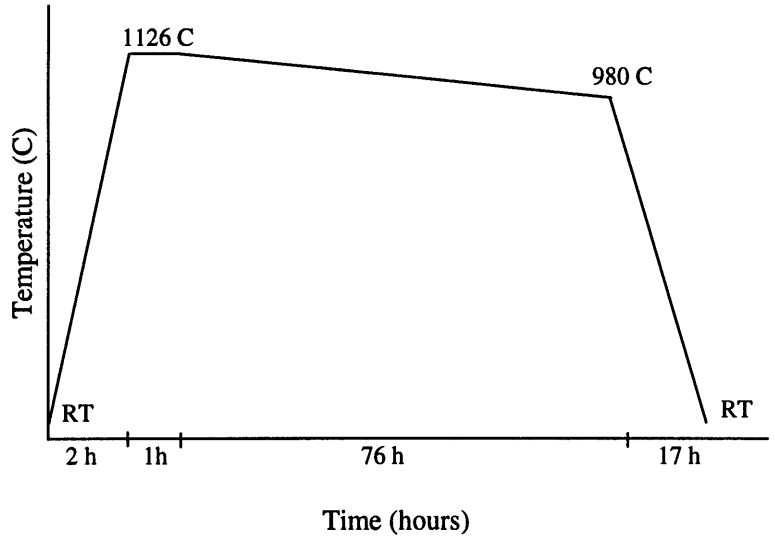

Figure 5.1. Temperature profile used in the production of single crystal Nd-123 seed crystals.

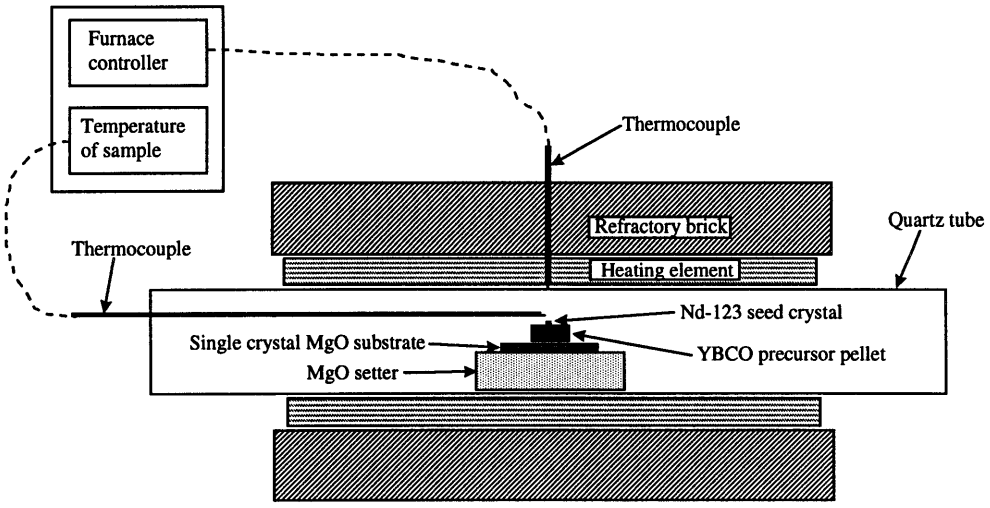

Figure 5.2. Schematic of the furnace used for Nd-123 seed production as well as for the seeded growth experiments.

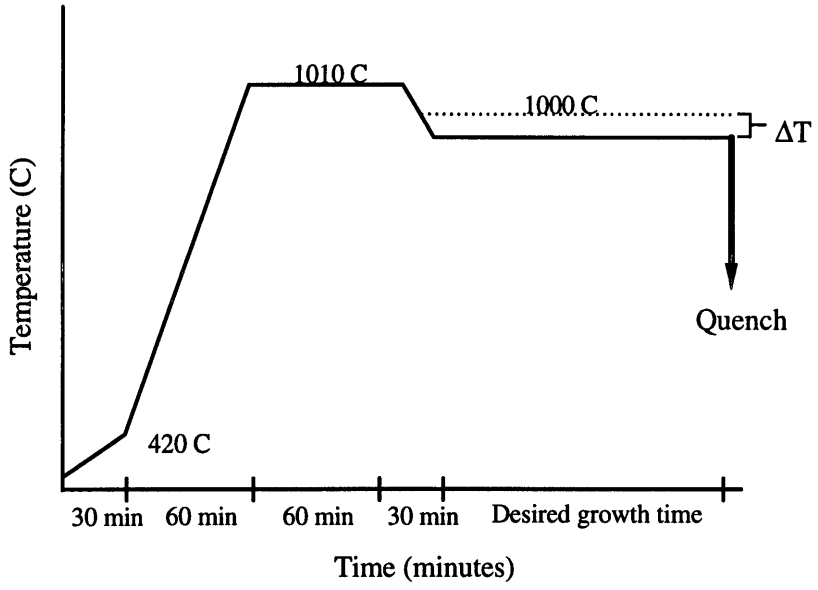

Figure 5.3. Temperature profile used for seeded growth of YBCO single crystals.

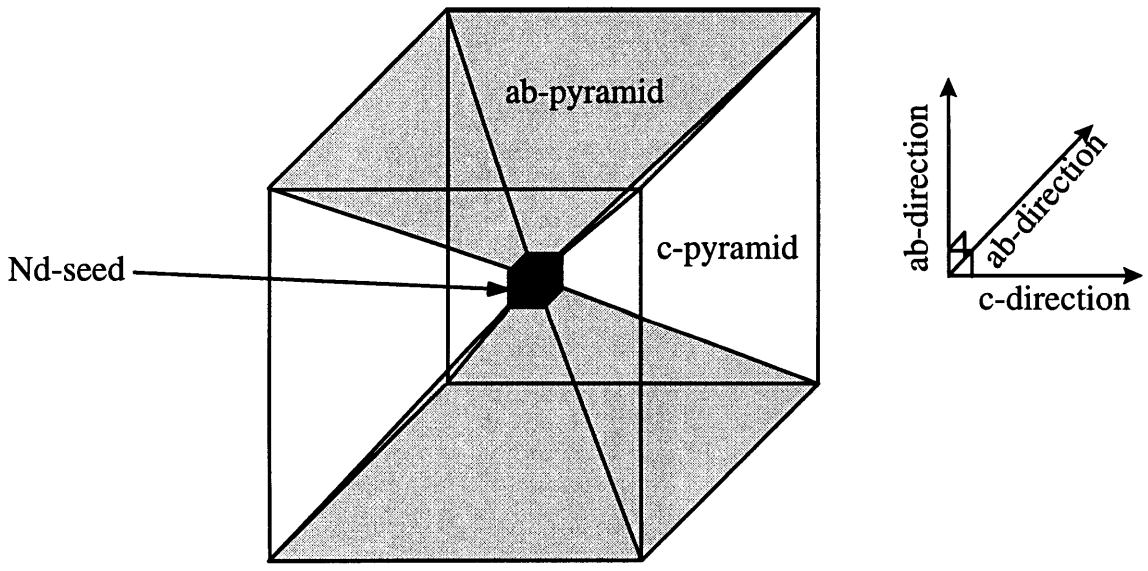

Figure 5.4. Schematic of three dimensional growth of a 123 single crystal from a Nd-123 seed.

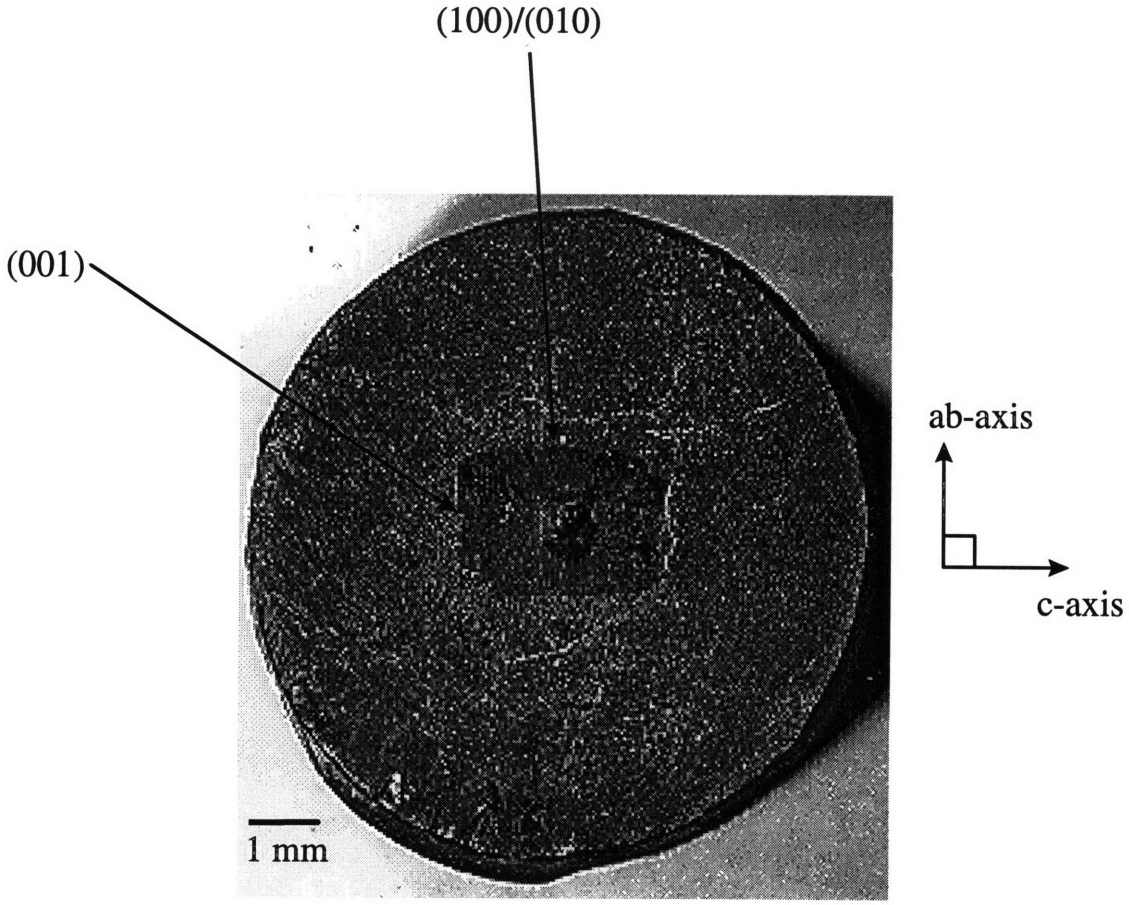

Figure 5.5. Top view of a typical YBCO single crystal produced by seeded growth using a Nd-123 seed crystal. The c-face (001) and ab-face (100)/(010) are marked as shown. It can be seen that the c-axis grows faster than the ab-axis.

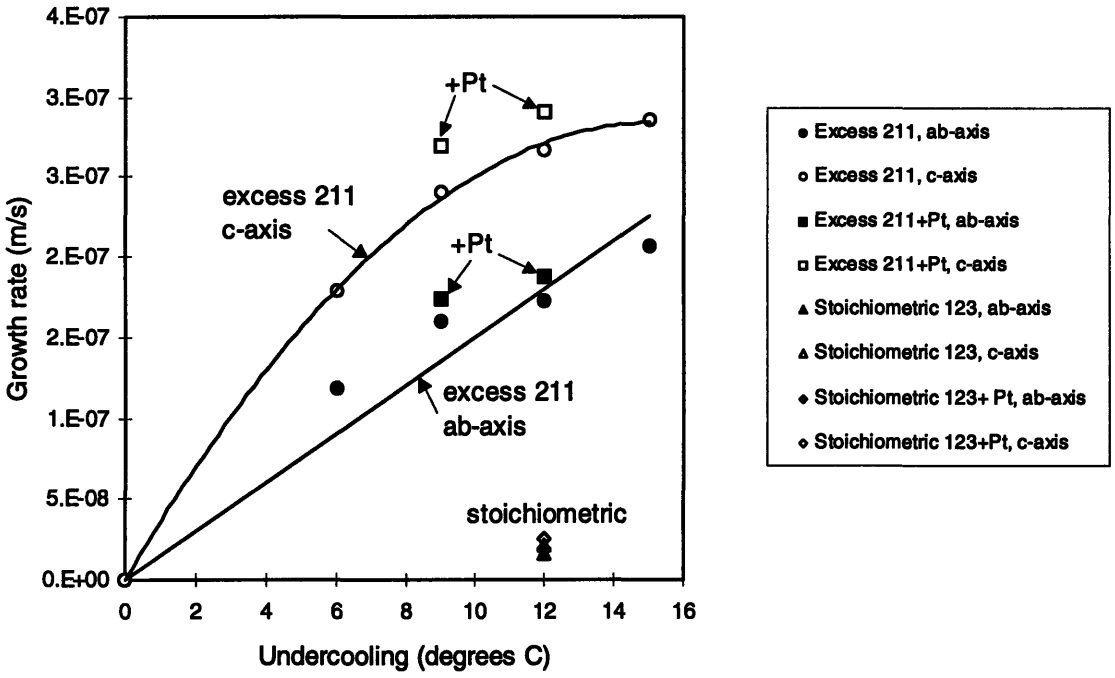

Figure 5.6. The dependence of 123 single crystal growth rate on variations in processing parameters.

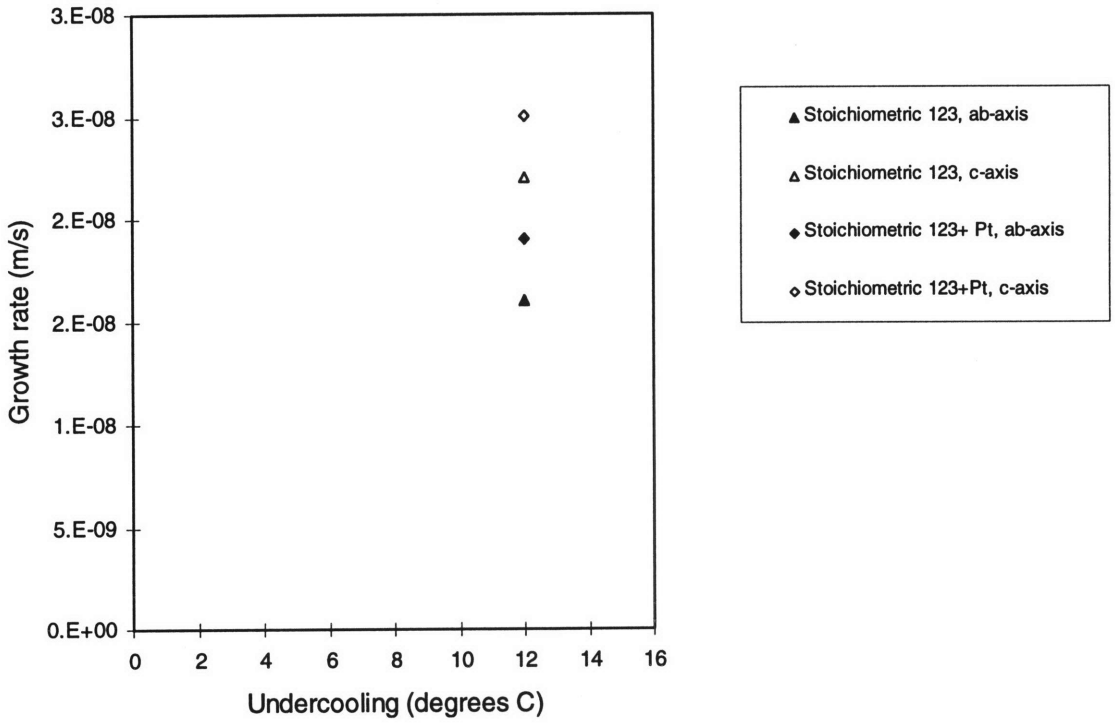

Figure 5.7. The dependence of 123 single crystal growth rate on variations in processing parameters for undoped and pt-doped stoichiometric samples.

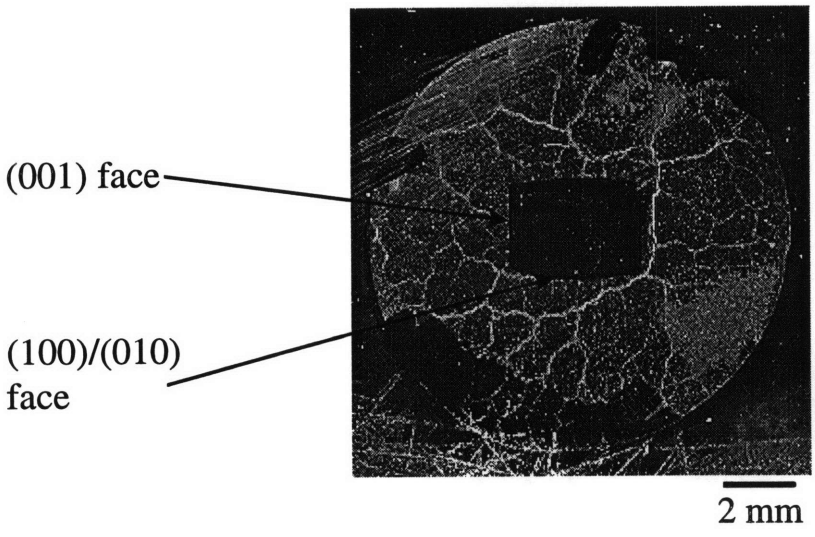

Figure 5.8. Optical micrograph of a polished cross-section of the top surface of a 123 single crystal produced from an excess 211 precursor by seeded growth for 2 h at an undercooling of 9 °C. The c-face (001) and ab-face (100)/(010) are marked as shown

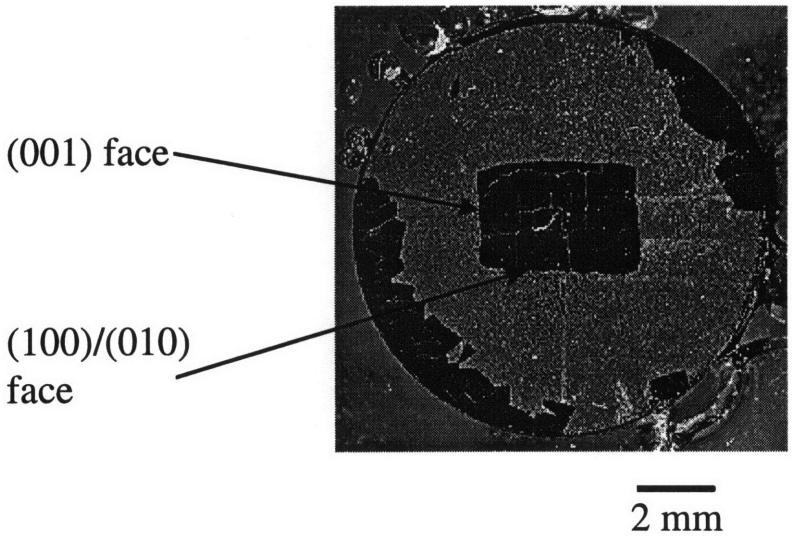

Figure 5.9. Optical micrograph of a polished cross-section of the top surface of a 123 single crystal produced from an excess 211 precursor by seeded growth for 2 h at an undercooling of 12 °C. The c-face (001) and ab-face (100)/(010) are marked as shown.

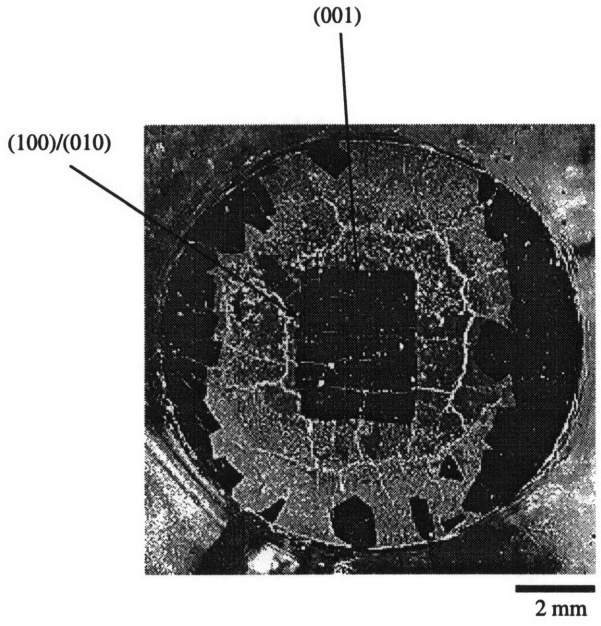

Figure 5.10. Optical micrograph of a polished cross-section of the top surface of a 123 single crystal produced from an excess 211 precursor by seeded growth for 2 h at an undercooling of 15 °C. The c-face (001) and ab-face (100)/(010) are marked as shown.

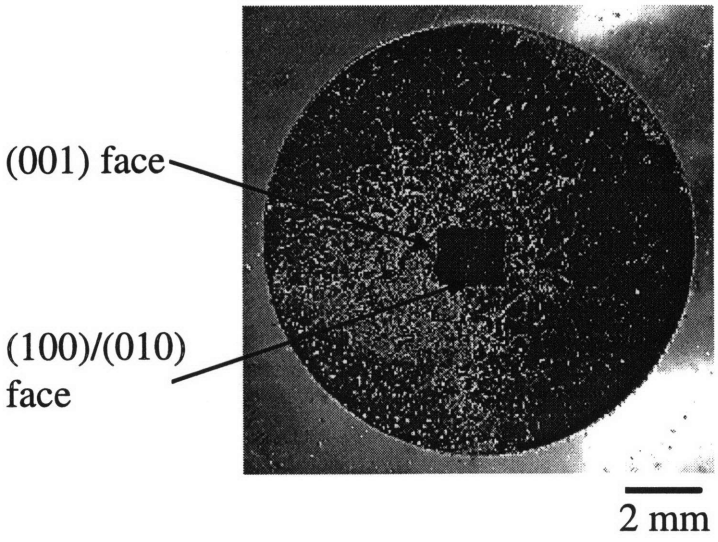

Figure 5.11. Optical micrograph of a polished cross-section of the top surface of a 123 single crystal produced from a stoichiometric 123 precursor by seeded growth for 2 h at an undercooling of 12 °C. The c-face (001) and ab-face (100)/(010) are marked as shown.

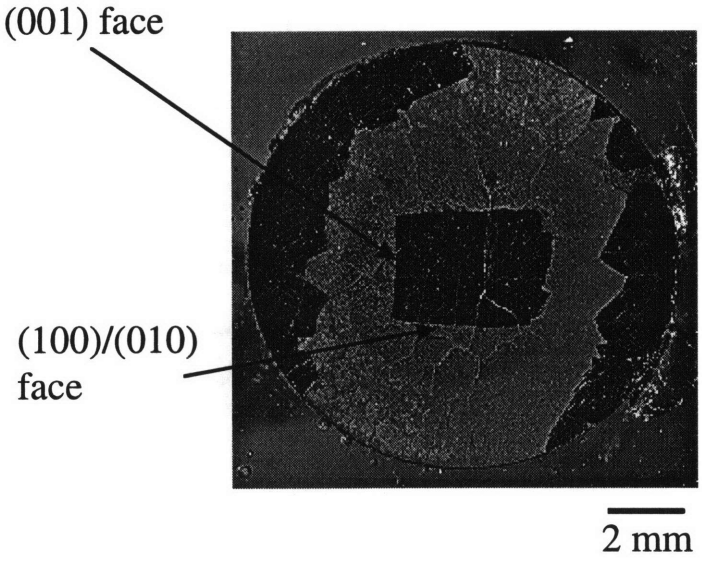

Figure 5.12. Optical micrograph of a polished cross-section of the top surface of a 123 single crystal produced from a Pt-doped excess 211 precursor by seeded growth for 2 h at an undercooling of 9 °C. The c-face (001) and ab-face (100)/(010) are marked as shown.

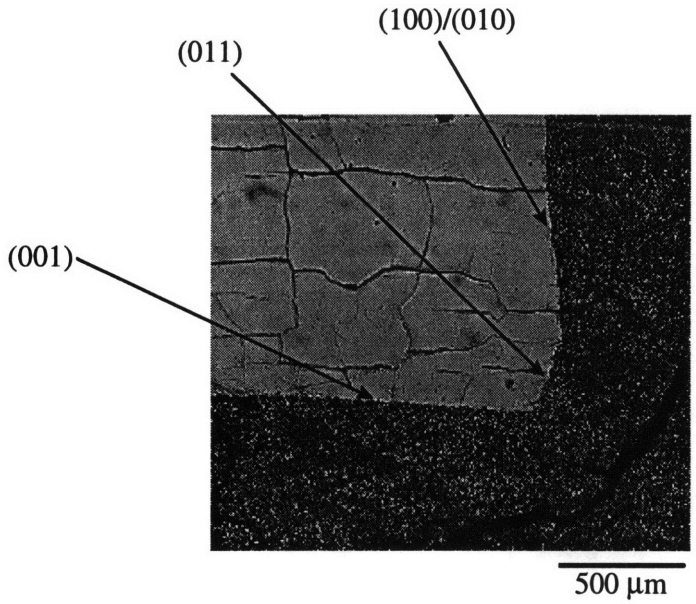

Figure 5.13. Optical micrograph of a polished cross-section of the top surface of a 123 single crystal produced from an excess 211 precursor by seeded growth for 2 h at an undercooling of 6 °C. The c-face (001), ab-face (100)/(010) and (011) face are marked as shown.

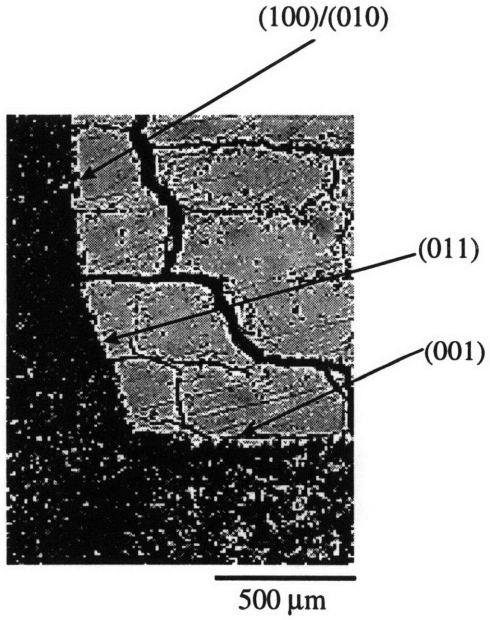

Figure 5.14. Optical micrograph of a polished cross-section of the top surface of a 123 single crystal produced from an excess 211 precursor by seeded growth for 2 h at an undercooling of 12 °C. The c-face (001), ab-face (100)/(010) and (011) face are marked as shown.

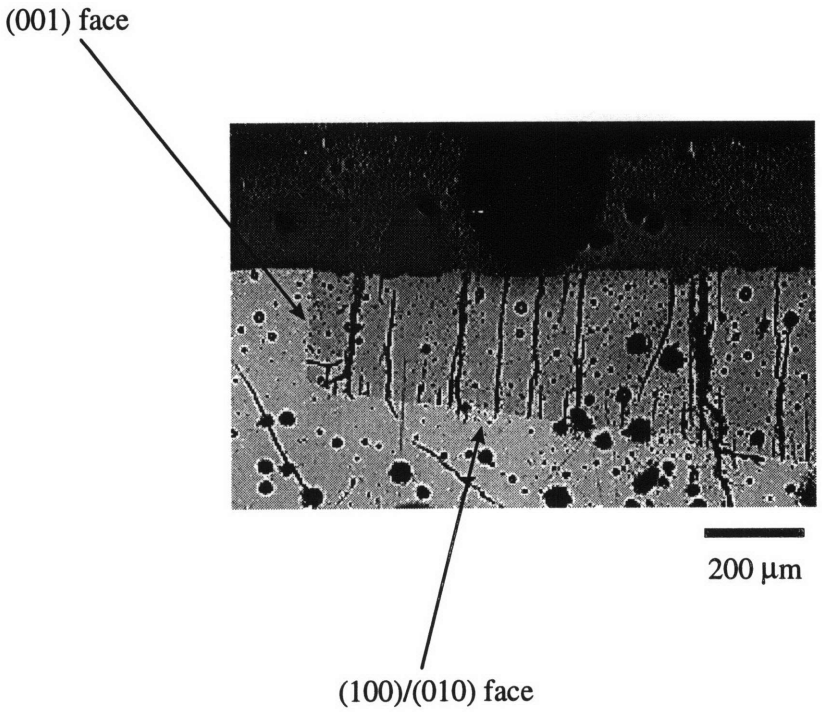

Figure 5.15. Optical micrograph of a polished cross-section of a 123 single crystal sectioned perpendicular to the surface of the sample. The crystal was produced from an excess 211 precursor by seeded growth for 2 h at an undercooling of 15 °C. The c-face (001) and ab-face (100)/(010) are marked as shown.

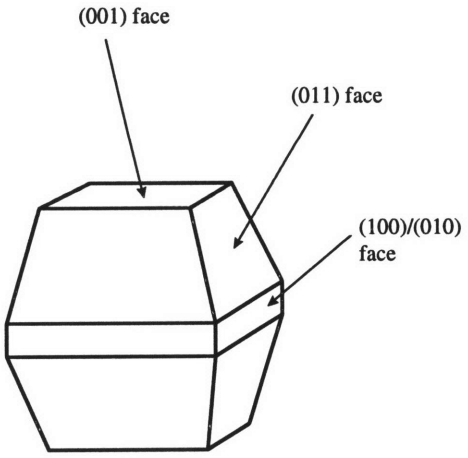

Figure 5.16. Schematic of the theoretical 123 crystal habit calculated by Sun et al.[123] using periodic bond chain (PBC) analysis.

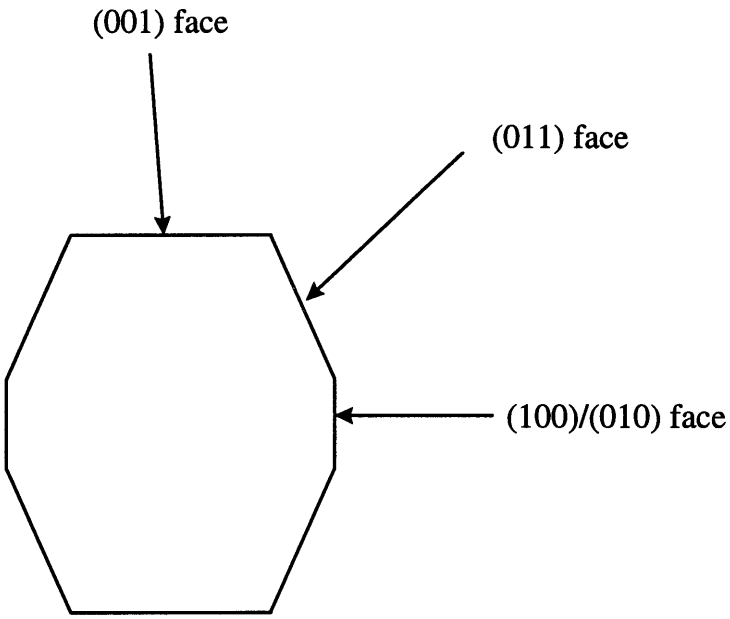

Figure 5.17. Schematic of a section of the theoretical 123 crystal habit shown in figure 5.16. The crystal was sectioned along the c-axis.

a)

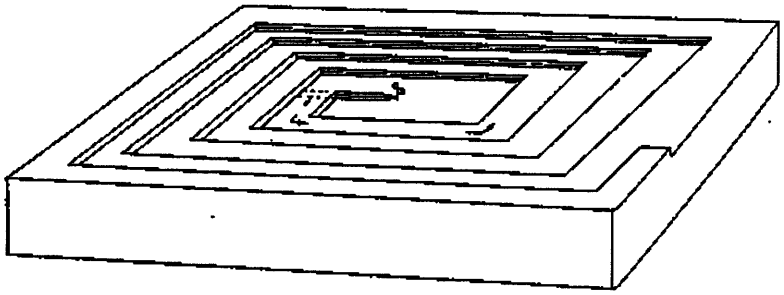

b)

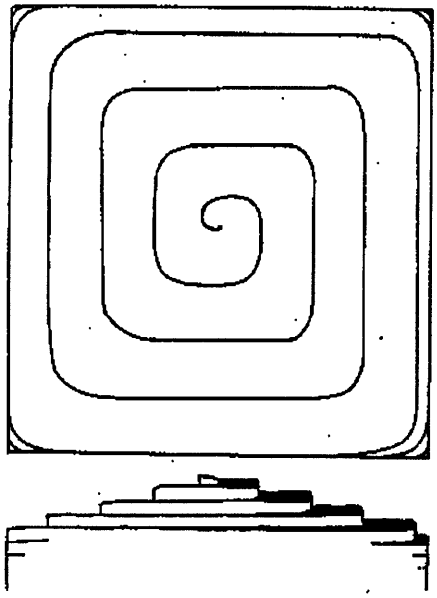

Figure 5.18. a) Schematic of Hopper growth.[126] Growth steps nucleate at the edge of a face and move inward. b) Schematic of spiral growth.[129] Growth spirals shown in the top half of figure b) can nucleate on screw dislocations, causing multiple growth spirals (bottom) to form on the surface of a face.

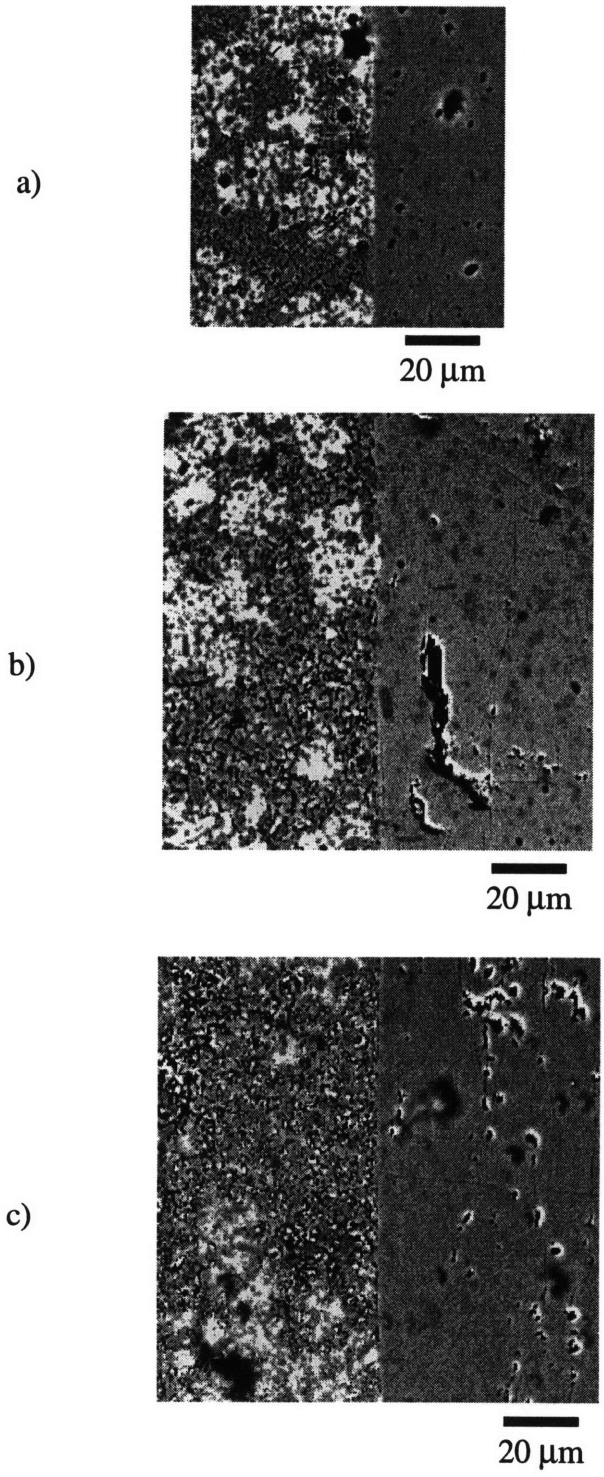

Figure 5.19. SEM micrographs of 123/liquid interface morphologies of the c-face of 123 single crystals produced from an excess 211 precursor by seeded growth for 2 h at undercooling of a) 6 °C, b) 9 °C and c) 15 °C.

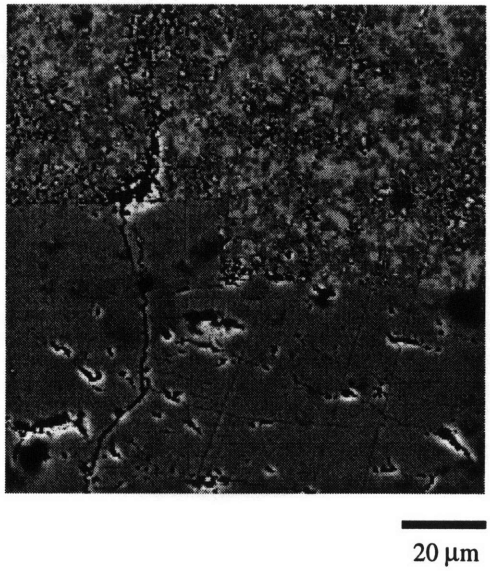

Figure 5.20. Higher magnification SEM micrograph of the c-face of a 123 single crystal produced from an excess 211 precursor by seeded growth for 2 h at undercooling of 15 °C showing the presence of a Hopper growth step.

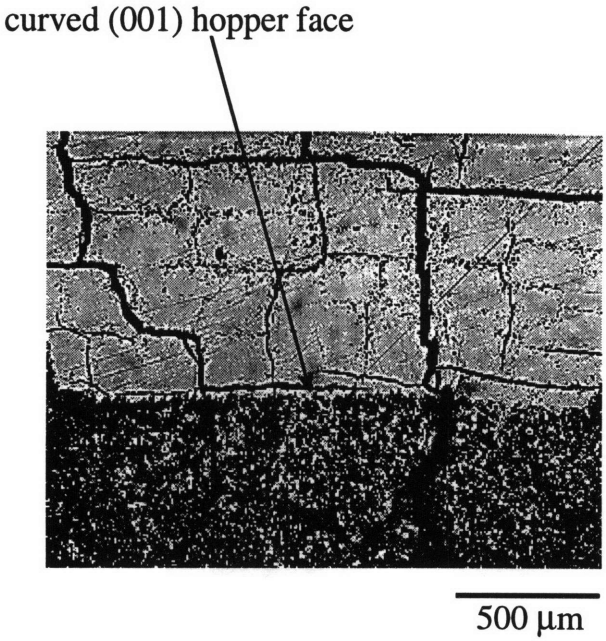

Figure 5.21. Optical micrograph of the c-face of a 123 single crystal produced from an excess 211 precursor by seeded growth for 2 h at undercooling of 12 °C showing the presence of a Hopper microstructure. The curved c-face is due to Hopper steps nucleating on the edges and growing inward.

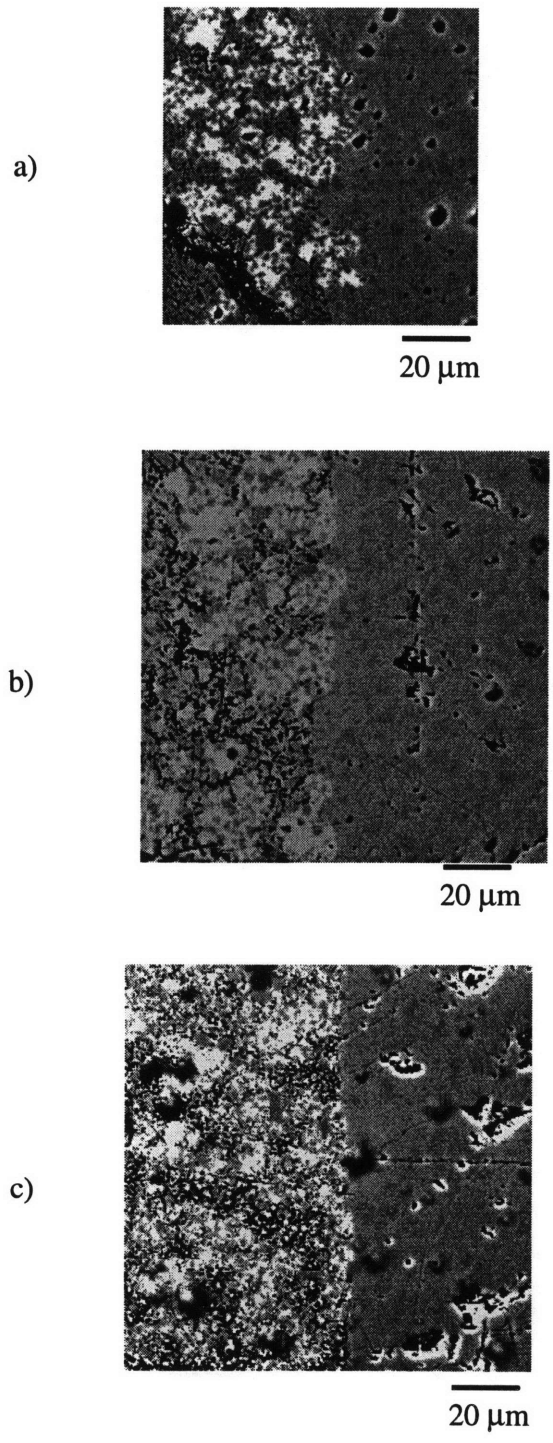

Figure 5.22. SEM micrographs of 123/liquid interface morphologies of the ab-face of 123 single crystals produced from an excess 211 precursor by seeded growth for 2 h at undercooling of a) 6 °C, b) 9 °C and c) 15 °C.

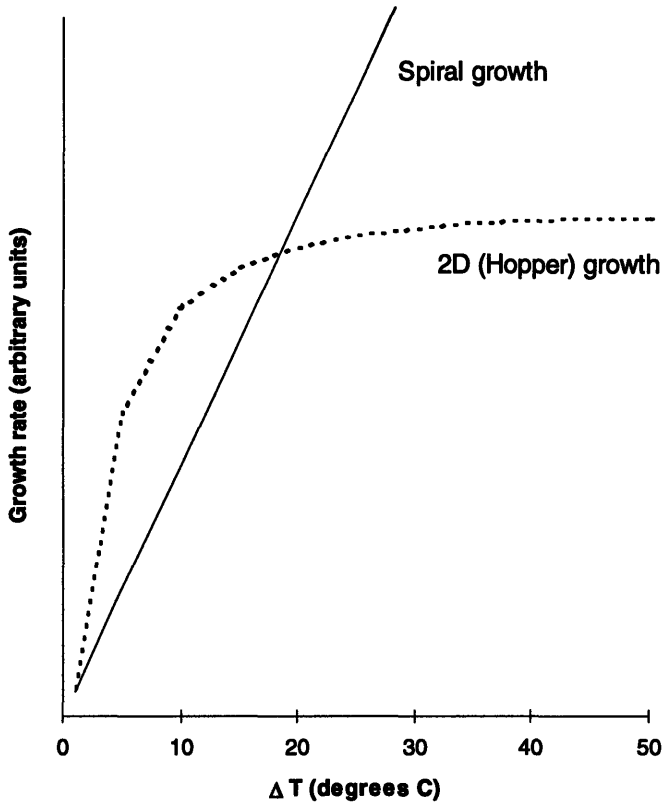

Figure 5.23. Comparison of growth rate, R, vs. undercooling, ΔT, for spiral growth and two-dimensional (Hopper) growth mechanisms. The intersection point was estimated by comparing the relationship of fast growth face to undercooling for seeded growth and floating zone growth experiments.

Chapter 6

The effect of 211 particle dissolution rate on the microstructure of stoichiometric YBCO single crystals produced by seeded growth

6.1. Introduction

Many researchers working on melt growth of YBCO materials have reported seeing inhomogeneous distributions of 211 particles within stoichiometric 123 single crystals.[34-36,38-39] The presence of 211 particles within 123 crystals has been correlated with the enhanced critical current densities in YBCO materials, as discussed in section 2.7.[87,92,94-95,101] 211 particles also act as an yttrium source for the growing 123 crystal during solidification from a melt. Understanding the dissolution of 211 particles in front of the 123 interface and the incorporation and distribution of 211 particles within the 123 crystal during melt growth is, therefore, an important step toward being able to predict the microstructure and enhance the properties of 123 superconducting materials.

6.2. 211 particle segregation and proposed explanations

211 particles segregate along the intersections of the ab-pyramids and c-pyramids of the 123 crystal (see figure 5.4) during three-dimensional growth of 123 single crystals from stoichiometric precursors. This type of 211 particle segregation forms planes of 211 particles through the 123 crystal.[34-35] These planes of 211 particles are observed as "X" tracks if the 123 single crystal is sectioned at right angles through the seed (see figure 6.1). Other shapes, such as X's with squares in the center or trapezoids, can be formed if the crystal is sectioned along other planes.[35] Figure 6.2 shows various types of 211

patterns which can be observed.[35] Such 211 particle segregation patterns have mainly been observed in crystals grown from the melt either by flux growth or seeded growth.[15,34-39] Tracks of 211 particles have also been observed in materials produced by directional solidification. Shen et al.[63] observed 211 particle tracks emanating from single crystal points in fiber samples solidified using an electrically heated zone furnace.

Many researchers have explained 211 segregation phenomena using particle pushing theories.[34,36-38,42] Kim et al.[37] and Varanasi et al.[34] suggested that "X" tracks are formed from 211 particles which are pushed to the edges of the growing 123 crystal by growth steps which are formed during spiral growth of 123 faces. This conclusion was based on the work of a number of other researchers who observed growth spirals on the surfaces of melt grown 123 crystals.[20,29,69,128,132] Varanasi et al. assumed that 123 growth in melt-textured processing takes place via step growth on three mutually perpendicular faces of the crystal. They assumed that these steps grow outward to the edges of the crystal. These growth steps push 211 particles toward the edge of the crystal where they are entrapped by two intersecting growth spirals.

A second growth mechanism was proposed by Vandewalle et al.[124-125] and Hannay et al.[132] They observed stacked terraces of 123 plates formed along the c-direction of 123 crystals. This microstructure was explained using the theory that the c-terraces nucleate sympathetically on the fast growing ab-planes of the 123 crystal. Varanasi et al.[34] extended this theory to assume that such terrace growth takes place on all three faces of the 123 crystal. They suggested that 211 particles pushed by the terraces are also trapped at the intersection of these terraces at the edges of the crystal.[34] Varanasi et al. concluded that "X" tracks were more likely to be found in Pt-doped samples containing small 211 particles which can be pushed by the growth steps more easily.[34,38]

These theories do not explain a number of observations. Sun et al.[72] and Hong et al.[70] showed the presence of hopper-like morphologies on the (100)/(010) surfaces of 123

crystals grown by melt growth.[126] It has been shown that these type of morphologies are most common in crystals formed on the surface of a melt, such as in flux growth or seeded growth.[126] Hopper growth morphology was also found on the c-faces of the 123 crystals produced by seeded growth for the current study, as described in chapter 5. As shown in figure 5.18 a), 123 material nucleates on the edges and corners of the crystal. The steps grow inward toward the center of the face during Hopper growth. It has been shown that the two-dimensional nucleation barrier at the edges is approximately 25% lower than on the face.[77,130] 211 particle pushing by growth steps formed on such crystals will, therefore, result in lines of 211 particles along the axes of the 123 crystal instead of at the intersection of the ab- and c-growth pyramids shown in figure 5.4. Additionally, Shang et al. observed multiple growth hillocks produced by numerous screw dislocations on the (100)/(010) faces of 123 crystals produced by melt growth.[133] Sun et al.[72] and Goyal et al.[82] observed the same growth mechanism on (001) faces. Both groups observed the presence of multiple growth hillocks nucleated in random patterns on each face. Multiple spiral growth hillocks were also found on the ab-faces of the of the 123 crystals produced by seeded growth for the current study, as described in chapter 5. The randomly nucleated spiral growth hillocks grow along the face of the crystal until they impinge upon each other. Any pushed 211 particles will therefore end up segregated in a random fashion, instead of in the observed patterns (see figure 6.2). Such evidence shows that 123 crystals produced using melt processing can grow by either spiral or Hopper growth. Particle pushing by neither growth mechanism can explain the formation of "X" tracks of segregated 211 particles in 123 crystals.

This work presents a model of 211 particle segregation in stoichiometric 123 samples which is based on differences in 211 particle dissolution rates in front of the faces, edges and corners of a growing 123 crystal. This model can be used to explain "X" track formation with and without the addition of Pt, as well as for all modes of growth of 123 crystals.

6.3. Background

As described in chapter 5, seeded growth involves the placement of a higher-melting R-123 seed material, such as Nd-123, on top of a 123 sample. The 123 material is then melted to form 211 particles and liquid. This semi-solid melt is undercooled below the peritectic temperature of 1000 °C and held for a given amount of time. The Nd-123 seed acts as a nucleation site for the Y-123 material. The peritectic reaction which occurs at the 123 solidification interface was described by equation 2.2. The peritectic reaction occurs by dissolution of the high temperature 211 phase into the liquid followed by reprecipitation onto the 123 surface. The yttrium-rich 211 particles act as a yttrium source for the growing 123 crystal.[10,33,78]

Section 2.4 describes the solidification model developed by Cima et al.[33] in which the undercooling at the 123 interface is given by:

$$\Delta T_p = \Delta T_G + \Delta T_S + \Delta T_C \tag{6.1}$$

where ΔT_P is the undercooling below the peritectic temperature, ΔT_G is the depression of the integrated temperature resulting from the temperature gradient, ΔT_S is the maximum "constitutional supercooling" ahead of the 123 interface and ΔT_C is the temperature depression resulting from the deviation in solute concentration at the 211 interface from that of the peritectic liquid composition. ΔT_C has been found to be very small. For purposes of simplification it was therefore assumed that $\Delta T_C = 0$. The single crystals produced for this study were grown at a constant undercooling which results in $\Delta T_G = 0$. The model presented here assumes that $\Delta T_G = 0$ and $\Delta T_C = 0$ such that

$$\Delta T_P = \Delta T_S = \Delta T \tag{6.2}$$

where ΔT is the actual undercooling of the sample. The results of this study will be qualitatively the same for growth in a temperature gradient, however.

A schematic of the one dimensional yttrium concentration profile in front of the growing 123 crystal is shown in figure 6.3. C_L^Y is defined to be the yttrium concentration in the liquid and is dependent on distance from the 123 growth interface. $C_L^{\infty Y}$ is the yttrium concentration in the liquid far away from the 123 interface, C_L^{iY} is the yttrium concentration in the liquid in contact with the growing 123 interface and l is the length scale of the yttrium depleted zone, the distance at which the quantity $C_L^Y - C_L^{\infty Y}$ becomes negligible. The distance l is given by half the distance between 211 particles in the semi-solid melt.

ΔC, the difference in yttrium concentration between the liquid far away from the 123 interface and the liquid in contact with the 123 interface, is given by:

$$\Delta C = C_L^{\infty Y} - C_L^{iY} \tag{6.3}$$

ΔC is dependent on ΔT, the level of undercooling in the system, and is determined by the phase diagram, shown in figure 6.4. The yttrium concentration in the liquid far away from the 123 interface at a given undercooling is determined by the extension of the 211 liquidus. The yttrium concentration in the liquid in front of the 123 interface for a given undercooling is given by the 123 liquidus. It can be seen from figure 6.4 that ΔC increases with increasing undercooling.

The three dimensional yttrium concentration gradient in front of the 123 interface, ∇C_{int}, (shown in figure 6.3 for one dimension), is given by:

$$\nabla C_{\text{int}} = \frac{\partial C_L^Y}{\partial X_{int}} + \frac{\partial C_L^Y}{\partial Y_{int}} + \frac{\partial C_L^Y}{\partial Z_{int}} \qquad \text{in 3 dimensions} \qquad (6.4)$$

where X_{int}, Y_{int} and Z_{int} are taken as the distance from the 123 interface in 3 dimensions.

211 particles in the semisolid zone begin to dissolve as the yttrium depleted region in front of the 123 crystal moves through the sample as the crystal grows outward from the seed. The driving force for dissolution of the 211 particles is given by ΔC_{211} , the difference between the yttrium concentration near the 211 particle and the yttrium concentration in the yttrium depleted region in which the particle is sitting. ΔC_{211} is defined as:

$$\Delta C_{211} = C_L^{\infty Y} - C_L^Y \qquad (6.5)$$

J, the flux of yttrium away from the 211 particle during dissolution is given by Fick's first law:

$$J = -D\nabla C_{211} \qquad (6.6)$$

where ∇C_{211} is the three dimensional yttrium concentration gradient around the surface of the 211 particle. ∇C_{211} in three dimensions is given by:

$$\nabla C_{211} = \frac{\partial C_L^Y}{\partial X_{211}} + \frac{\partial C_L^Y}{\partial Y_{211}} + \frac{\partial C_L^Y}{\partial Z_{211}} \qquad \text{in 3 dimensions} \qquad (6.7)$$

where X_{211}, Y_{211} and Z_{211} are taken as the distance from the 211 particle surface in 3 dimensions.

S, the dissolution rate if the 211 particle per unit surface area is given by:

$$S=JV_m \tag{6.8}$$

where V_m is the molar volume of the 211 phase. Particles with large amounts of their surface area in a high yttrium concentration gradient, ∇C_{211}, will dissolve faster than particles with smaller percentages of their surface area in the gradient.

Yttrium diffuses from the dissolving 211 particles to the 123 interface. The driving force for this diffusion is provided by ∇C_{int}, the yttrium concentration gradient in front of the 123 interface of the growing crystal. Yttrium produced by 211 particles dissolving in the liquid in front of the 123 interface diffuses down the yttrium concentration gradient, $\nabla C_{int,}$ (shown in figure 6.3 for one dimension) to the 123 interface. The yttrium at the 123 interface is then used to form a new area of 123 crystal.

The residence time of the 211 particles in the yttrium depleted region, τ, is given by:

$$\tau = \frac{l}{R} \tag{6.9}$$

Thus, the length of time during which the particles are dissolving depends on the growth rate, R, of the 123 crystal. Any 211 particles which dissolve more slowly than the rate at which the crystal is growing remain undissolved at the end of the residence time. These undissolved 211 particles are incorporated into the 123 crystal as the growth interface moves past them.

It is known that the barium cuprate liquid in the semi-solid 211 + liquid melt contains a higher concentration of copper than is present in the 123 phase. Growth of the 123

crystal into the semi-solid melt therefore results in the rejection of copper at the growth interface.[63-64] Figure 6.5 shows that copper rejected from the face of the growing 123 crystal is rejected one-dimensionally into the liquid directly in front of the face. Copper rejected from the 123 crystal at the edge of the crystal can diffuse around the edge in two dimensions. Copper rejected from the 123 crystal at the corner of the crystal can diffuse around the corner in three dimensions. The copper concentration in the liquid in regions in front of a 123 crystal face will therefore be higher than in front of a 123 crystal edge. The copper concentration in the liquid in regions in front of a 123 crystal edge will in turn be higher than in front of a 123 crystal corner. This corresponds to a lower yttrium concentration in the liquid in regions in front of the 123 crystal face than in front of the 123 crystal edge, and a lower yttrium concentration in the liquid in regions in front of the 123 crystal edge than in front of the 123 crystal corner.

This study examines the dissolution rate of the 211 particles in front of these different areas of the 123 crystal. Finite element models and calculations of the dissolution rate of 211 particles in front of the face, edge and corner of the growing 123 crystal are used to explain the formation of "X" tracks of 211 particles trapped within the 123 single crystal during growth of stoichiometric samples.

6.4. Experimental procedure

Stoichiometric 123 samples prepared as described in sections 5.2.1 and 5.2.2 were used in the seeded growth experiments described here. The seeded growth process is described in section 5.2.3. Single-crystal Nd-123 seeds with polished faces parallel to their c-axes were used in these experiments. The samples were heat treated in air at an undercooling of ΔT = 12 °C as shown in figure 5.3. The samples were quenched after 2 hours of growth to prevent slow cooling and additional growth of 123 material below the desired

undercooling temperature. The samples were then mounted in epoxy, polished, and examined using cross-polarized optical microscopy.

123 single crystals with ab-axes of 400 μm in length and c-axes μm of 480 μm in length resulted from 2 hour seeded growth experiments using an undercooling of ΔT=12 °C. The growth rate of the 123 sample was calculated after subtracting the size of the seed and found to be 1.6×10^{-8} m/s for the ab-axis and 2.2×10^{-8} m/s for the c-axis. The average growth rate of the 123 crystal can, therefore, be approximated as 1.9×10^{-8} m/s. An optical micrograph of a corner of a typical stoichiometric sample is shown in figure 6.2. A section of the "X" track of 211 particles can be seen along the dashed line. The lines of 211 particles run from the corners of the section toward the center of the crystal. Figure 6.6 shows an optical micrograph of the quenched liquid in front of the 123 single crystal. Figure 6.7 shows a typical 211 particle extracted from a stoichiometric YBCO sample. It can be seen that the particles have the approximate shape of cylinders with rounded ends. The particle size of the 211 particles in the semi-solid melt for the stoichiometric samples produced for this study ranges from approximately 2 μm to approximately 25 μm in diameter, where particle diameter was taken as the cylinder diameter.

6.5. Modeling of 211 particle dissolution

Figure 6.8 shows six basic ways in which a 211 particle can impinge upon the growing 123 crystal interface. Particles a) and b) are impinging on the face of a 123 crystal. Particle a) is situated parallel to a face of the 123 crystal. Particle b) is situated perpendicular to the 123 crystal face. Any particle moving toward the face of the 123 crystal will have an orientation of either a) or b) or something in between. Particles c) and d) are impinging on an edge of a 123 crystal. Particle c) is situated parallel to the edge of the 123 crystal. Particle d) is situated perpendicular to the 123 crystal edge. Any particle moving toward the edge of the 123 crystal will have an orientation of either c) or

d) or something in between. Particles e) and f) are impinging on the corner of a 123 crystal. Particle e) is situated parallel to the corner of the 123 crystal. Particle f) is situated perpendicular to the 123 crystal corner. Any particle moving toward the corner of the 123 crystal will have an orientation of either e) or f) or something in between. It is theorized here that the "X" tracks of entrapped 211 particles described above result from differences in 211 particle dissolution rates in front of the faces, edges and corners of the growing 123 crystal. This theory was tested and modeled using the finite element modeling program PDEase®[134] produced by Macsyma Inc. Both Cartesian and cylindrical coordinate systems were used to model the geometry of impinging 211 particles with respect to the 123 interface.

The first task in modeling the growth of the 123 crystal and the dissolution of 211 particles involved defining the conditions of the systems to be modeled. The initial conditions and boundary conditions on the system were set as follows:

- The initial yttrium concentration in the semisolid melt was set to be:

$$C_L^Y = C_L^{\infty Y} \tag{6.10}$$

$C_L^{\infty Y}$ was chosen to be 1000 moles/m^3, the yttrium concentration in the liquid in contact with the 211 particles at the peritectic temperature. This value was estimated from the ternary phase diagram published by Mori et al.[135] and also fits very well with the yttrium concentration in the quenched liquid measured by Honjo et al.[35] during similar seeded growth experiments. Although the simulation was designed to produce a yttrium profile at an undercooling temperature slightly below the peritectic temperature, it was assumed that $C_L^{\infty Y}$ does not change significantly with small changes in temperature.

- The yttrium concentration at the surfaces of the 123 crystal was set to be:

$$C_L^Y = C_L^{\infty Y} - \Delta C \tag{6.11}$$

where ΔC is defined in equation 6.3. For this simulation, ΔC was chosen to be 300 moles/m^3. This value was estimated from the ternary phase diagram published by Mori et al.[135] This value was also shown by Shen[63] to be a good approximation for ΔC at an undercooling of 12°C. $C_L^{\gamma Y}$, the yttrium concentration at the 123 interface, given by equation 6.3, is therefore equal to 700 moles/m^3.

- The yttrium concentration at the surfaces of the 211 particles was set to be:

$$C_L^Y = C_L^{\infty Y} \tag{6.12}$$

- The flux of yttrium at the outside edge of the semi-solid melt was set to be 0.

- D, the diffusivity of yttrium in the liquid, is unknown but is expected to be similar to that for a low viscosity liquid. D was therefore chosen to be 6×10^{-11} m^2/s.

- The diameter of the 211 particles was varied between 1 micron and 25 microns. These values were chosen to be representative of small to large particles found in the semi-solid melt.

- The distance of the 211 particles from the corner and edge of the 123 crystal was varied between 0 and 10 microns. These values were chosen in order to examine the dissolution rate of particles directly in front of the 123 interface as well as far away from the interface relative to variations in yttrium concentration.

An yttrium concentration profile away from the 123 crystal was then generated to simulate the yttrium concentration profile in front of the 123 crystal based on the model developed by Cima et al.[33] This model is discussed in section 2.4. The model shows that the driving force for 211 particle dissolution is a concentration gradient of length l which is formed in front of the 123 interface due to constitutional supercooling at this interface. The distance l was shown to be half the distance between 211 particles in the semi-solid melt. A steady state diffusion profile cannot be used to produce such a profile since steady state diffusion allows diffusion to take place in the barium cuprate liquid at distances much larger than a distance l away from the 123 interface. Fick's second law of diffusion was therefore used to produce an yttrium concentration profile of length l for the current model

Fick's second law of diffusion is given by:

$$\frac{\partial C}{\partial t} = D\nabla^2 C \tag{6.13}$$

The initial and boundary conditions given above were entered into the PDEase®[134] program and the program was run for a diffusion time which produced an yttrium concentration profile with a characteristic length, l, of approximately 7 μm. The diffusion time needed to produce a gradient of this length was 0.1 s. The value of 7 μm for l was chosen based on microstructural evaluation conducted on quenched liquid containing 211 particles produced from stoichiometric 123 samples. l was calculated to be 7.2 μm for stoichiometric samples (see section 5.3.2). The value of 7 μm also fits well with calculations of diffusion length conducted by Shen et al.[64]

Particles situated in orientations a) and c) were modeled using Cartesian coordinates. The programming code used to model the dissolution of particles in orientations a) and c) can be found in appendix A. The system was defined in Cartesian coordinates as the top right quarter of a square (the 123 crystal) surrounded by a quarter of a circle (the semi-solid melt). The system definition also included two circular regions describing 211 particles situated parallel to the face and edge of the 123 crystal. One or both of these regions were bracketed out of the program to examine the effects of each particle individually as well as the initial yttrium concentration profile in the liquid. The system was defined in the xy plane, with the z-direction taken to be perpendicular to the modeling plane. These conditions allowed the modeling of cylindrical 211 particles of infinite length dissolving parallel to the face and edge of a 123 crystal. End effects were neglected since the relative rate of dissolution along the radius of cylindrical particles is much higher than that along the length of the cylinder for particles immersed in a concentration gradient parallel to the axis of the cylinder. The dissolution rate along the radius of such an infinite particle is, therefore, equivalent to the dissolution rate along the radius of a 211 particle with finite length.

An expanded view of the relevant section of the initial yttrium concentration profile generated using cartesian coordinates is shown in figure 6.9. The yttrium concentration profile generated in front of the growing 123 crystal corresponds well to theories and observations of solute concentration profiles for crystal growth from a liquid.[136-137] It can be seen from this figure that the yttrium concentration profile in front of the edge of the 123 crystal is significantly different from the yttrium concentration profile in front of the face of the 123 crystal. This difference is important since the dissolution rate of 211 particles in the liquid in front of the 123 crystal is heavily dependent on the yttrium profile in the liquid.

The dissolution rates of 211 particles situated in orientations a) and c) (from figure 6.8) in the yttrium concentration profile shown in figure 6.9 were then examined. This was done

by placing a 211 particle in the liquid at various distances in front of the 123 crystal face and edge. Figure 6.10 shows the resulting yttrium concentration profile for a 1 micron 211 particle dissolving at a distance of 5 microns from the face of the 123 crystal. Figure 6.11 shows the resulting yttrium concentration profiles for a 1 micron 211 particle dissolving at a distance of 5 microns from the edge of the 123 crystal. J, the flux of yttrium away from the dissolving 211 particle was calculated by PDEase®[134] by evaluating Fick's first law around the radius of the particle according to equation 6.6. This calculation was performed for particles located at various distances from the face and corner of the 123 crystal. The yttrium flux away from the dissolving 211 particle was then converted to the 211 dissolution rate according to equation 6.8.

Particles situated in orientations b) and f) were modeled using cylindrical coordinates. The programming code used to model the dissolution of particles in orientations b) and f) can be found in appendix B. The system was defined in cylindrical coordinates as a perpendicular line (the face of the 123 crystal) or a 90° point (the corner of the crystal). The facets of the corner of the 123 crystal could not be modeled in cylindrical coordinates. The 90° point in the two dimensional construction of the system boundaries resulted in a three dimensional cone with an angle of 90°. The dissolution of 211 particles in front of the corner of a 123 crystal was approximated by the dissolution of particles in front of the 90° cone. The yttrium concentration profile in front of the corner of the 123 crystal is shown in figure 6.12.

The system definition for particles b) and f) also included two regions describing 211 particles situated perpendicular to the face and corner of the 123 crystal, as shown in figures 6.13 and 6.14. Each particle orientation was modeled using a separate program file. The system was defined in the Z-R plane, with the z-direction taken to be the horizontal direction and the R-direction taken to be the vertical direction. PDEase®[134] produced three dimensional results by evaluating the system after rotation around the Z-

axis. 211 particles perpendicular to the face and corner of the 123 crystal were drawn in two dimensions as rectangles with rounded ends. The rectangles were oriented parallel to the axis of rotation in cylindrical coordinates. The radius of the particle ends was taken to be the same as the width of the rectangle. Three dimensional analysis of these particles in cylindrical coordinates produced 211 particles shaped like cylinders with rounded ends. The aspect ratio of the cylinders was approximated as 6:1, based on particle analysis found in chapter 3. The particle length was not critical to the dissolution rates, however, since it was found that the particles dissolve much faster in the radial direction than along their axes.

Particles situated in orientations d) and e) could not be modeled using PDEase,®[134] but conclusions on the effect of their orientations were drawn by comparing the results of the modeling of particles situated in the other orientations.

6.6. Results

Figure 6.15 compares the profile of the yttrium concentration away from the edge of the 123 crystal (along the dashed line in figure 6.9) to the profile of the yttrium concentration away from the face of the 123 crystal (along the solid line in figure 6.9). It can be seen that the yttrium concentration profile in front of the edge is much steeper than that in front of the face of the 123 crystal. The trend in yttrium concentration at the corner will be similar to the yttrium concentration in front of the edge of the 123 crystal except that the yttrium concentration profile at the corner will vary in three dimensions instead of only two for the case of the edge of the 123 crystal. 211 particle dissolution takes place within this yttrium concentration gradient. 211 dissolution rates will be highest for combinations of 123 interface structure and 211 particle orientation which allow a large area of the 211 particle to be situated in the yttrium concentration gradient in front of the

123 interface. Larger sections of 211 particles will be in an area of dissolution in front of the 123 crystal face than in front of the 123 crystal edge. Even less 211 particle area will be present in the yttrium gradient in front of the 123 crystal corner. 211 particle dissolution will, therefore, be greater in front of the 123 crystal face than in front of the 123 crystal edge. 211 particle dissolution rates will be even lower in front of the 123 crystal corner.

Figures 6.16 through 6.19 show the calculated average dissolution rates for 1 micron, 3 micron, 10 micron and 25 micron 211 particles dissolving in front of different locations on the 123 crystal. Figures 6.16 through 6.19 show the dissolution rates of particles oriented parallel to the 123 crystal face, perpendicular to the 123 crystal face, parallel to the 123 crystal edge and perpendicular to the 123 crystal corner, respectively. These orientations correspond to a), b), c) and f) in figure 6.8, respectively. As stated above, the average growth rate for a stoichiometric sample produced by seeded growth at an undercooling of approximately ΔT = 12 °C is 1.9×10^{-8} m/s. This growth rate is also marked on figures 6.16 through 6.19 by a horizontal line near the bottom of the diagram. Figures 6.16 through 6.19 show that particle dissolution rates depend strongly on which area of the 123 crystal the 211 particle is impinging upon and the orientation of the 211 particle. Particle dissolution rates also increase dramatically in all cases as the particles get closer to the 123 interface and ∇C_{211} becomes large. It can also be seen that particle dissolution rate depends strongly on particle size.

Figure 6.16 shows a plot of the dissolution rates vs. distance from the 123 interface for 211 particles of various sizes impinging on the face of the 123 crystal in a parallel orientation (orientation a)). It can be seen that the maximum dissolution rate for a 211 particle dissolving in a parallel orientation in front of the 123 crystal face varies between 1.5×10^{-4} m/s for a 1 micron diameter particle and 9.1×10^{-6} m/s for a 25 micron diameter particle. Thus, it can be seen that if the growth rate of the 123 single crystal is less than 9.1×10^{-6} m/s, all particles 25 microns in diameter or smaller dissolving in a parallel

orientation in front of the face of the 123 crystal will completely dissolve by the time the 123 interface sweeps past them. As stated above, the average growth rate for a stoichiometric sample produced by seeded growth at an undercooling of approximately $\Delta T = 12$ °C is 1.9×10^{-8} m/s. Thus, no 211 particles which started out smaller than 25 microns in size and which are oriented parallel to the 123 face will be trapped by the growing face of the 123 crystal. Figure 6.17 shows a plot of the dissolution rates vs. distance from the 123 interface for 211 particles of various sizes impinging on the face of the 123 crystal in a perpendicular orientation (orientation b)). Comparison of figure 6.16 and figure 6.17 shows that the maximum dissolution rates for 211 particles impinging on the 123 face in a perpendicular orientation is smaller than the dissolution rates for 211 particles impinging on the 123 face in a parallel orientation. Figure 6.17 shows, however, that the dissolution rate for all particle sizes of perpendicular 211 particles in front of the 123 interface are larger than the growth rate of the 123 crystal. All 211 particles with radii of 25 microns or less dissolving in front of the face of the 123 interface will, therefore, completely dissolve by the time the 123 interface sweeps past them.

Figure 6.18 shows a plot of the dissolution rates vs. distance from the 123 interface for 211 particles of various sizes impinging on the edge of the 123 crystal in a parallel orientation (orientation c)). It can be seen from figure 6.18 that the maximum dissolution rates for 211 particles dissolving in a parallel orientation in front of an edge of the 123 crystal are smaller than the dissolution rates for particles in front of the 123 crystal face. As discussed above, the average growth rate for a stoichiometric sample produced by seeded growth at an undercooling of approximately $\Delta T = 12$ °C is 1.9×10^{-8} m/s. The dissolution rates of 1, 3 and 10 micron particles dissolving in a parallel orientation in front of the 123 edge is therefore large enough that the particles will dissolve completely before being passed by the growing 123 crystal interface. The dissolution rate of a 25 micron particle dissolving in a parallel orientation in front of the 123 edge is lower than the growth rate of the 123 crystal, however. Particles 25 microns or larger which are dissolving in a parallel orientation in front of 123 crystal edges will not be completely

dissolved by the time the edge of the growing 123 crystal sweeps past them. As a result, the undissolved part of the 25 micron particle will be engulfed by the edge of the 123 crystal. Thus, the critical trapping size for 211 particles oriented parallel to the edge of the 123 crystal is approximately 25 μm.

Figure 6.19 shows a plot of the dissolution rates vs. distance from the 123 interface for 211 particles of various sizes impinging on the corner of the 123 crystal in a perpendicular orientation (orientation f)). It can be seen from figure 6.19 that the dissolution rates for only the 1 micron and 3 micron particles oriented perpendicular to the 123 crystal corner are larger than the growth rate of the 123 crystal. 211 particles larger than 3 microns which are dissolving in a perpendicular orientation in front of 123 crystal corners will therefore not be completely dissolved by the time the corner of the growing 123 crystal sweeps past them. Thus, the critical trapping size for 211 particles oriented perpendicular to the corner of the 123 crystal is approximately 3 μm.

It can be seen from a comparison of particles e) and f) in figure 6.8 that particles oriented in position f) relative to the 123 crystal corner will have a smaller surface area in contact with the yttrium concentration gradient in front of the corner of the 123 crystal than a particle oriented in position e). The dissolution rate of particles oriented in position e) will, therefore, be higher than the dissolution rate of particles oriented in position f). The smallest particle which can be engulfed by the 123 crystal corner is therefore a 3 micron particle oriented perpendicular to the 123 corner.

It can be seen from a comparison of particles c) and d) in figure 6.8 that particles oriented in position d) (perpendicular to the 123 crystal edge) will have a smaller surface area in contact with the yttrium concentration gradient than a particle oriented in position c) (parallel to the 123 crystal edge). The dissolution rate of particles oriented in position d) will therefore be significantly lower than the dissolution rate of particles oriented in position c). It was shown in figure 6.18 that the critical trapping size for 211 particles

oriented parallel to the edge of the 123 crystal (orientation c)) is approximately 25 μm. Even smaller particles will remain undissolved when oriented perpendicular to the 123 crystal edge (orientation d)). The critical trapping size for 211 particles oriented perpendicular to the 123 crystal edge will be between the critical trapping size for particles oriented parallel to the 123 crystal edge (25 μm) and perpendicular to the crystal corner (3μm). It is therefore estimated that the critical trapping size for 211 particles in oriented perpendicular to the 123 crystal edge is approximately 15 μm.

Entrapment of undissolved particles along the edges and corners of the 123 crystal during melt growth will cause 211 segregation along the intersection of the ab and c growth pyramids shown in figure 5.4. These trapped 211 particles will appear as "X" tracks and other patterns when the 123 crystal is sectioned in various directions. This theory of particle segregation is valid for all growth mechanisms.

The areas of the YBCO crystal containing entrapped yttrium-rich 211 particles will have a larger overall yttrium concentration unless the excess yttrium from the 211 particles is exactly compensated by the entrapment of a barium and copper rich phase within the YBCO crystal as well. It will be shown in chapter 7 that conservation of mass does indeed occur in this manner. The basic mechanism of this conservation of mass is linked to barium cuprate liquid entrapment between 123 platelets formed within the 123 crystal. It was shown in chapter 2 that platelets form in the 123 crystals when a 211 particle intersects the growth front. As discussed above, undissolved 211 particles will impinge on the 123 crystal at the edge and corner in stoichiometric samples and become entrapped within the crystal. 211 particles generally intersect the 123 interface asymmetrically, resulting in unequal growth rates around the 211 particles due to anisotropy in the growth rates along different crystallographic directions. The result is a platelet structure in the 123 crystal, with platelet gaps separating the 123 platelets. The mechanism of platelet formation is shown in figure 2.12. It will be shown in chapter 7 that barium- and copper-

rich liquid becomes trapped within these platelet gaps, resulting in an increased overall concentration of barium and copper in the region of the platelet gap. The presence of trapped barium- and copper-rich liquid between platelet gaps is linked to the presence of 211 particles since platelet gaps are only formed when 211 particles impinge on the 123 growth interface. The overall mass balance is preserved in this manner. This phenomenon will be discussed further in chapter 7.

6.7. Conclusions

It has been shown that 211 segregation in stoichiometric 123 samples is not a result of particle pushing. Finite element models and calculations presented here show that that the entrapment of particles in stoichiometric 123 samples produced by melt growth is a result of differences in 211 particle dissolution rates in front of the 123 crystal face compared to the edge and corner. Large 211 particles in front of the edge and corner of a 123 crystal do not dissolve completely if the particle dissolution rate is lower than the growth rate of the 123 crystal. Larger particles are trapped at the corners than at the edges of the 123 crystal. The critical entrapment size of 211 particles varies according to 211 particle orientation relative to the edge and corner of the 123 crystal. Particles incorporated at the corners and edges of 123 crystals during melt growth form planes of 211 particles which appear as "X" tracks and other patterns when the 123 crystal is sectioned in various directions. Mass is conserved via barium cuprate liquid entrapment within platelet gaps formed by the impingement of trapped 211 particles on the 123 growth front. This theory of particle segregation is valid for all growth mechanisms.

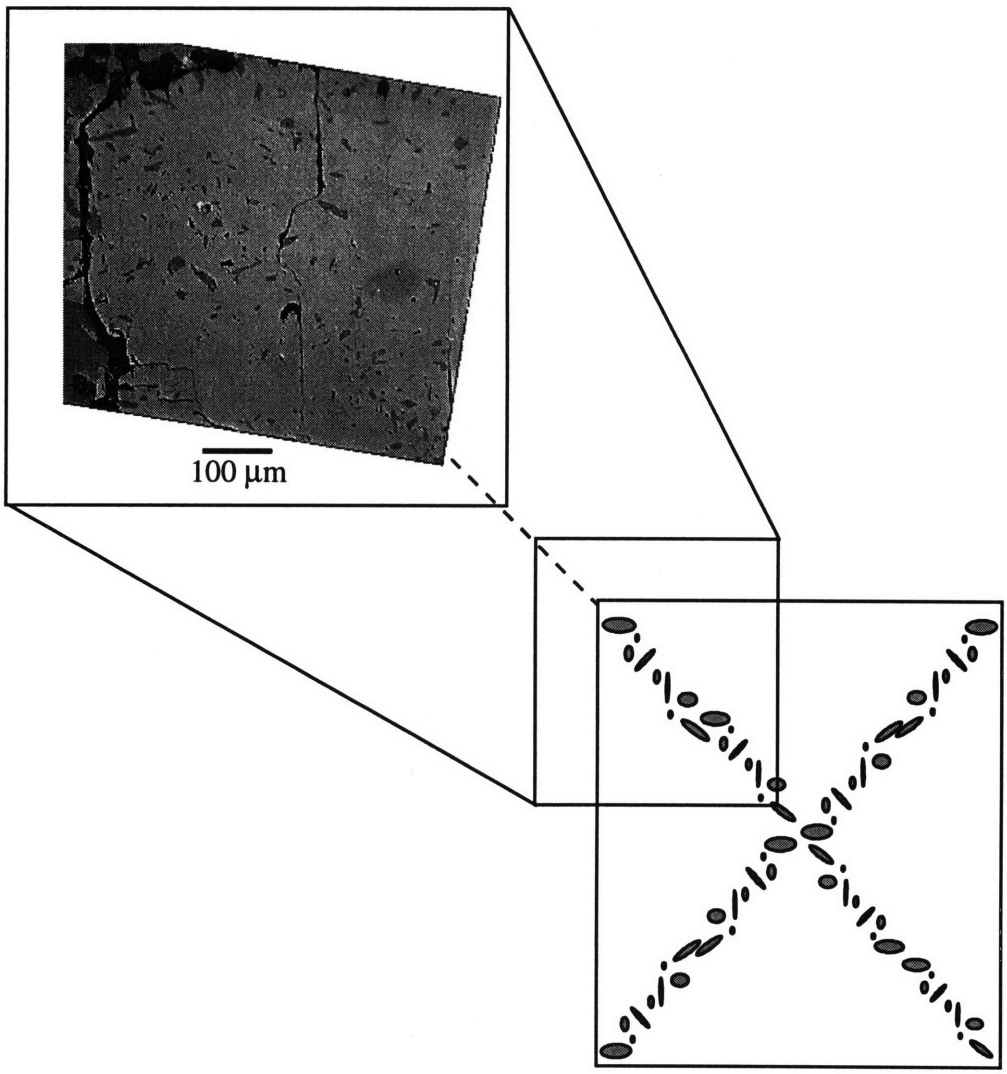

Figure 6.1. Optical micrograph and schematic showing "X" tracks of 211 particles trapped within 123 single crystal.

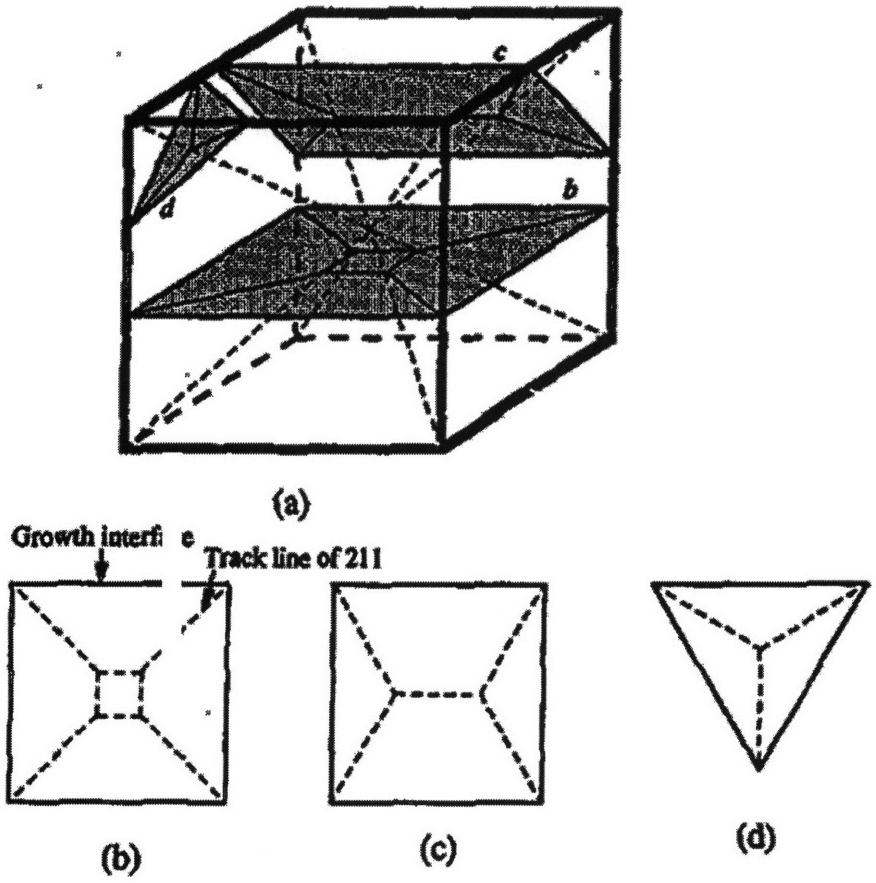

Figure 6.2. Schematic of different 211 segregation patterns which can be observed in stoichiometric samples.[35]

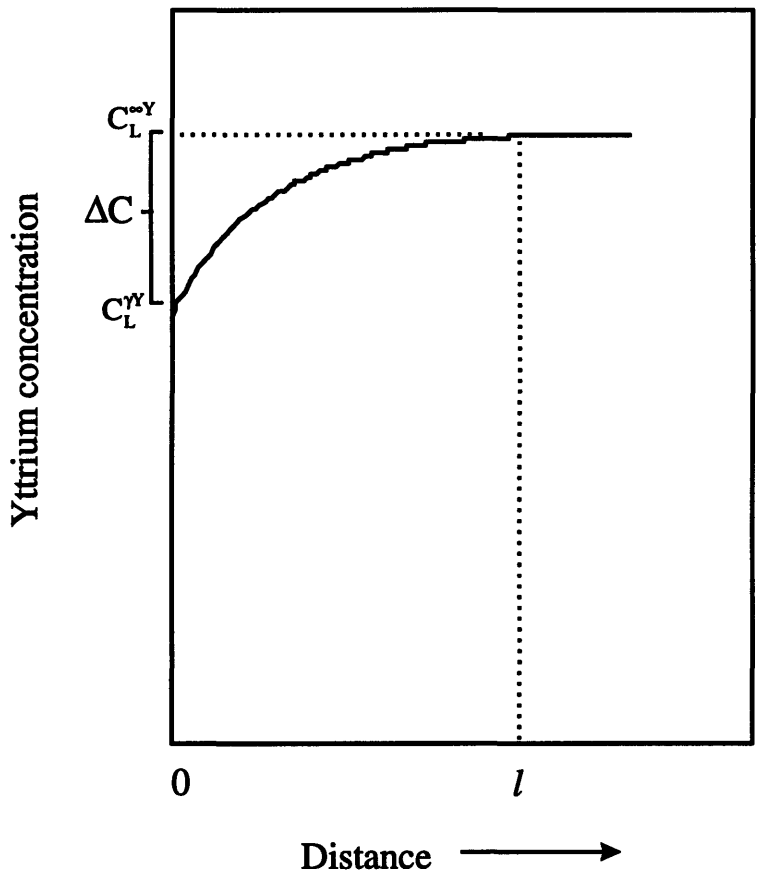

Figure 6.3. Profile of yttrium concentration, C_L^Y, in front of growing 123 crystal. $C_L^{\infty Y}$ is the yttrium concentration in the liquid far away from the 123 interface, $C_L^{\gamma Y}$ is the yttrium concentration in the liquid in contact with the growing 123 interface and l is the length scale of the yttrium depleted zone.

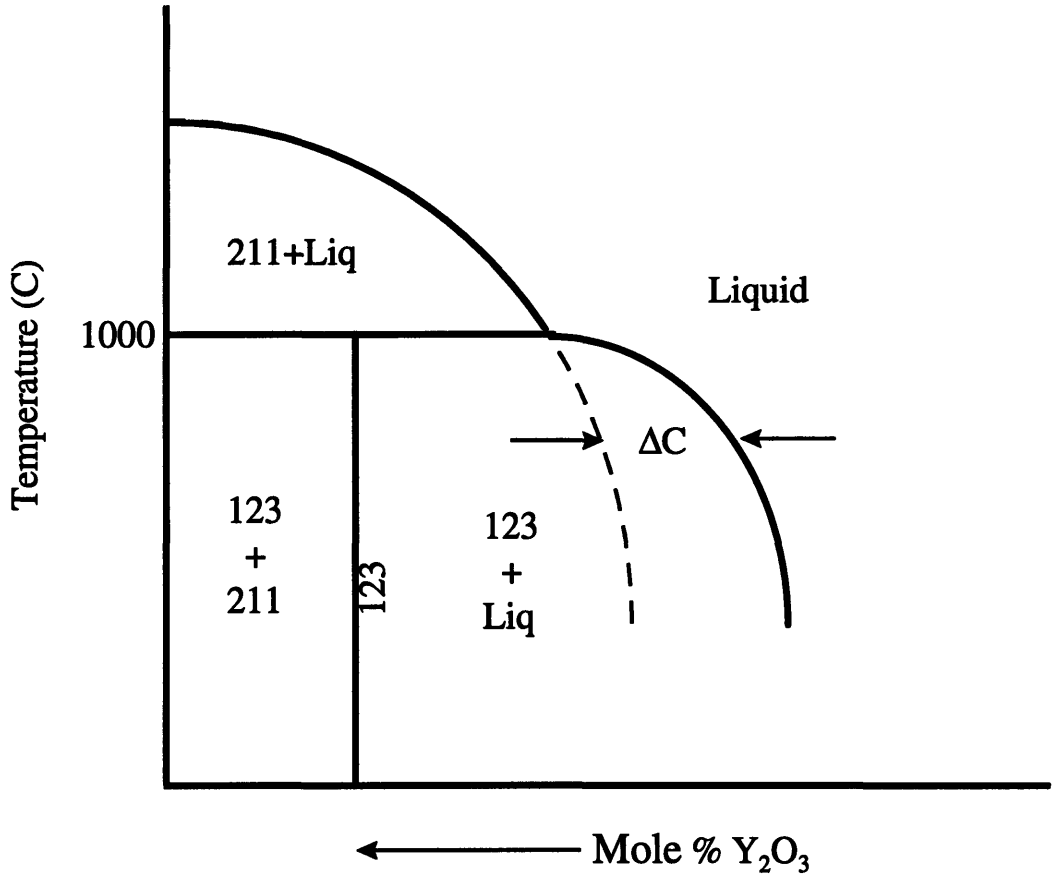

Figure 6.4. Binary phase diagram of the 123 / 211 system showing extension of the 211 liquidus and ΔC.

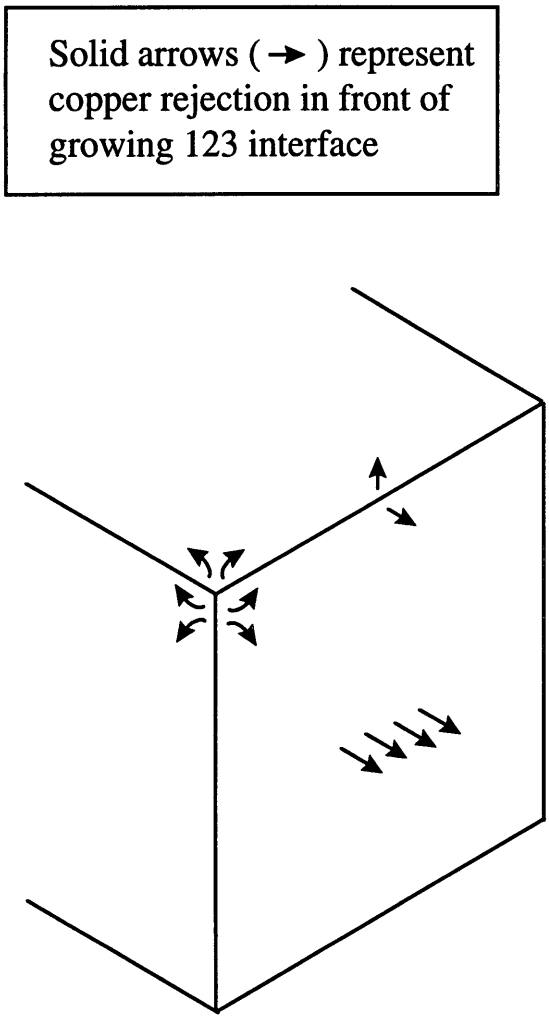

Figure 6.5. Schematic showing copper rejection and diffusion into the liquid in front of the face, edge and corner of the growing 123 crystal.

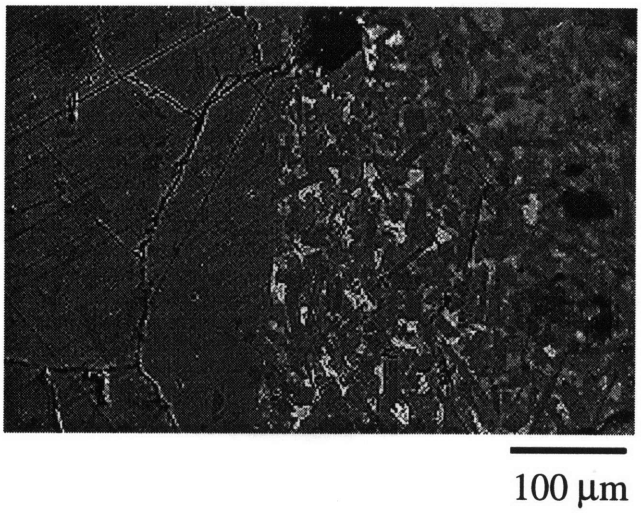

Figure 6.6. Optical micrograph of the quenched liquid in front of the 123 single crystal.

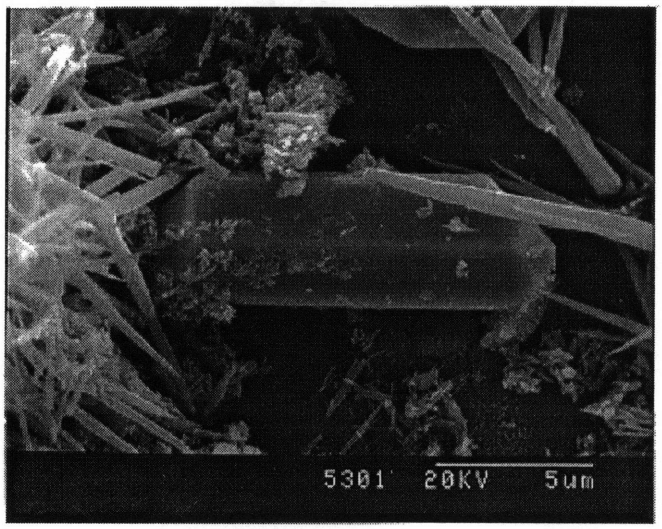

Figure 6.7. SEM micrograph of a typical 211 particle extracted from a stoichiometric YBCO sample.

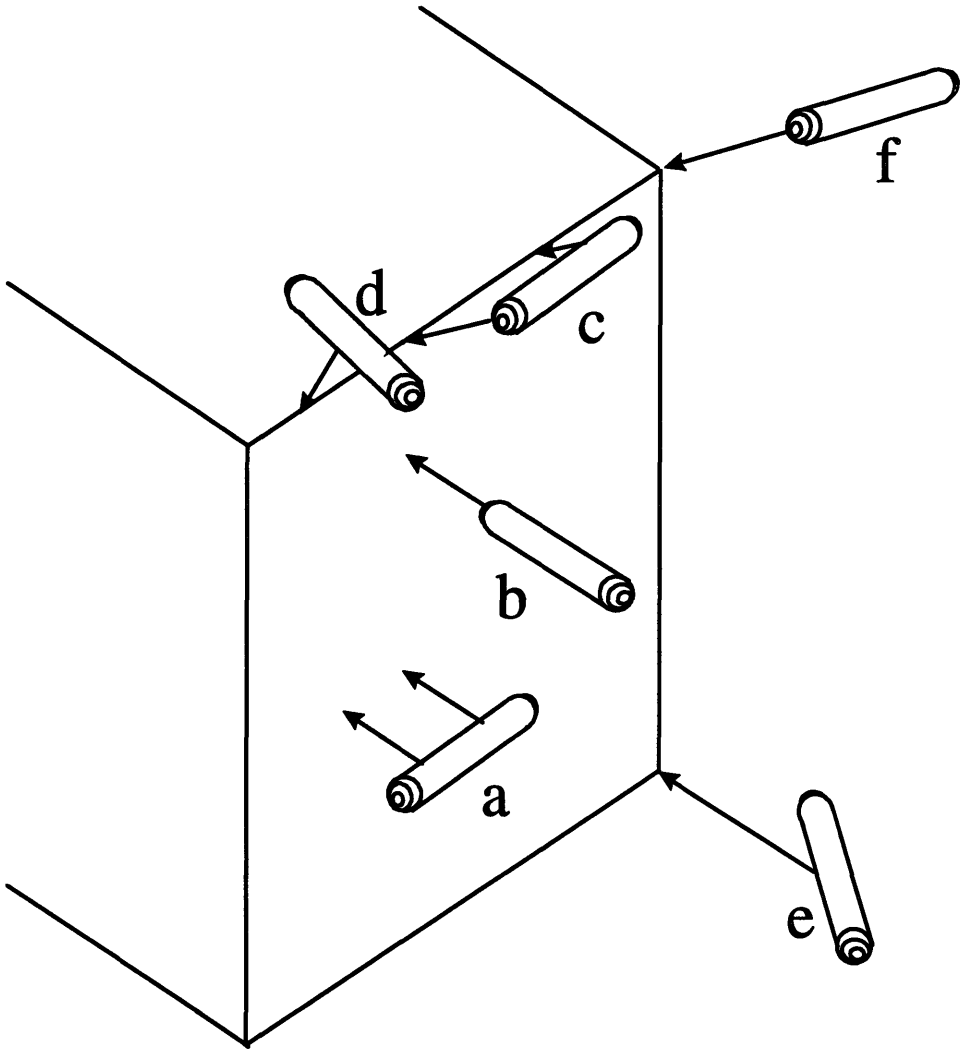

Figure 6.8. Schematic of 6 different ways in which 211 particles can impinge upon a 123 crystal.

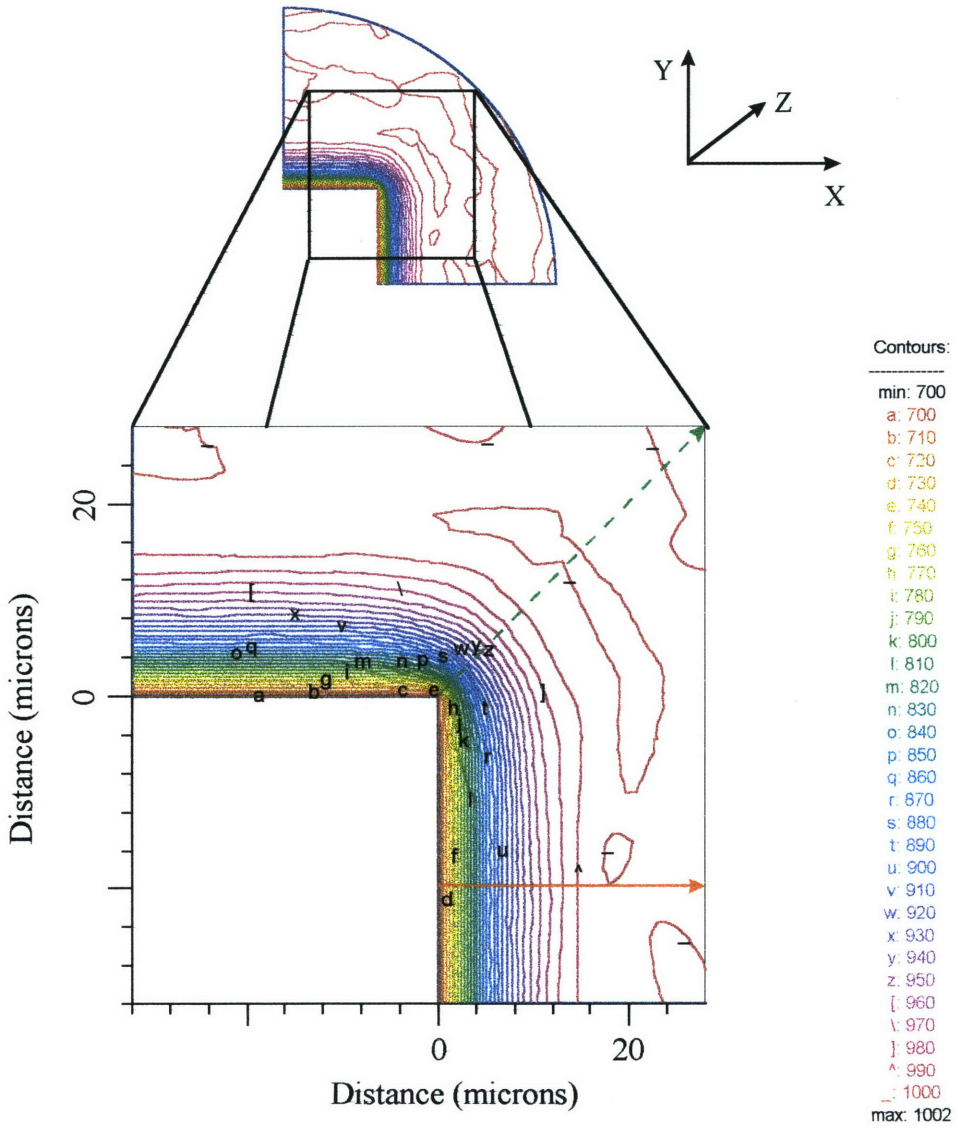

Figure 6.9. FEM diagram showing the yttrium concentration in front of a growing 123 crystal for $\Delta C = 300$ moles/m^3. (generated by PDEase ®[134])

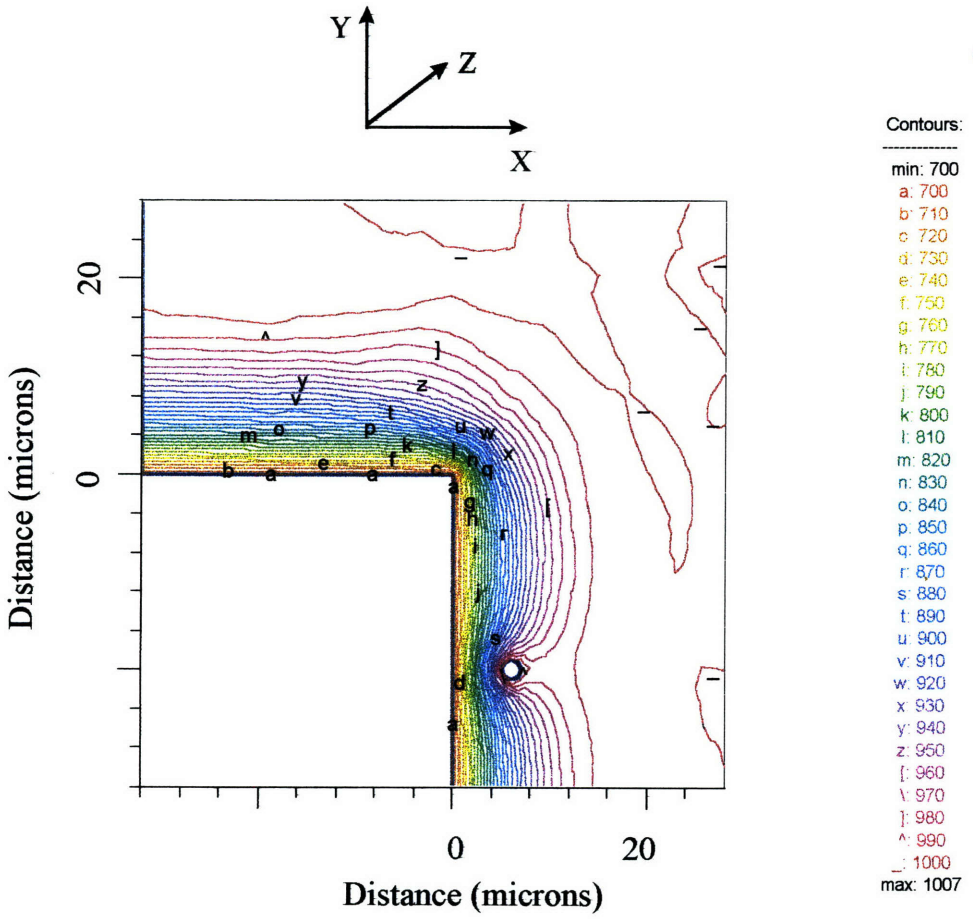

Figure 6.10. FEM diagram showing a 1 micron 211 particle oriented parallel to the 123 crystal face (position a) in figure 6.8) dissolving in front of a growing 123 crystal for $\Delta C = 300$ moles/m^3. (generated by PDEase®[134])

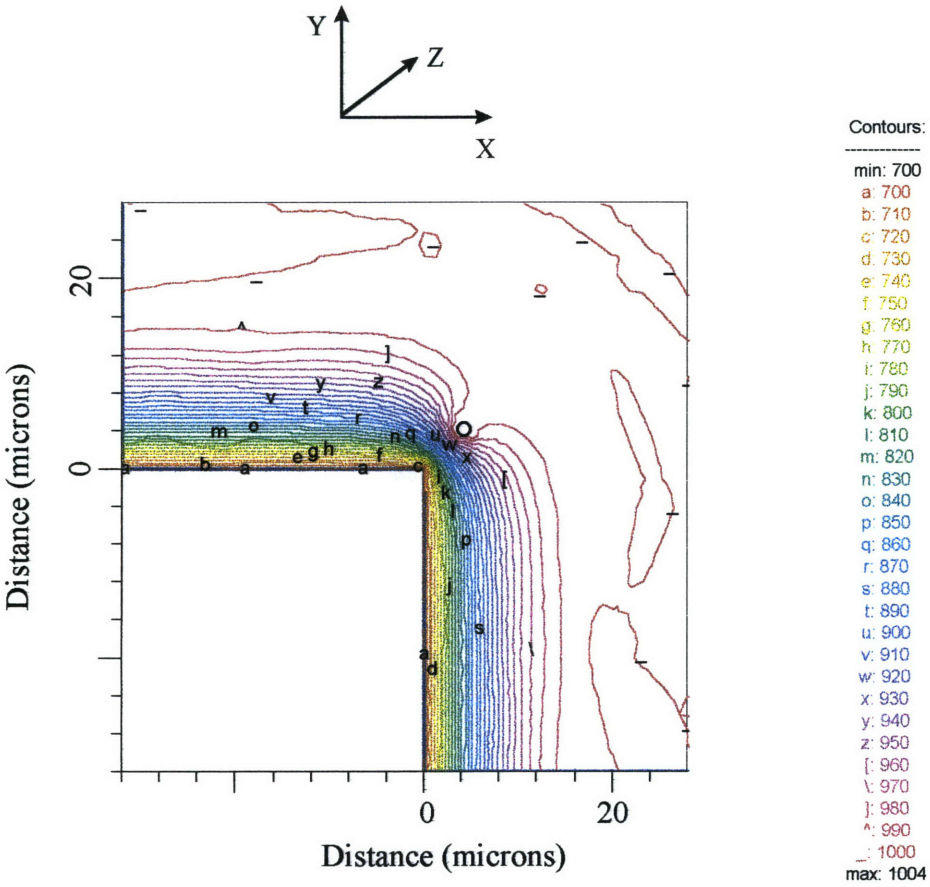

Figure 6.11. FEM diagram showing a 1 micron 211 particle oriented parallel to the 123 crystal edge (position c) in figure 6.8) dissolving in front of a growing 123 crystal for $\Delta C = 300$ moles/m^3. (generated by PDEase®[134])

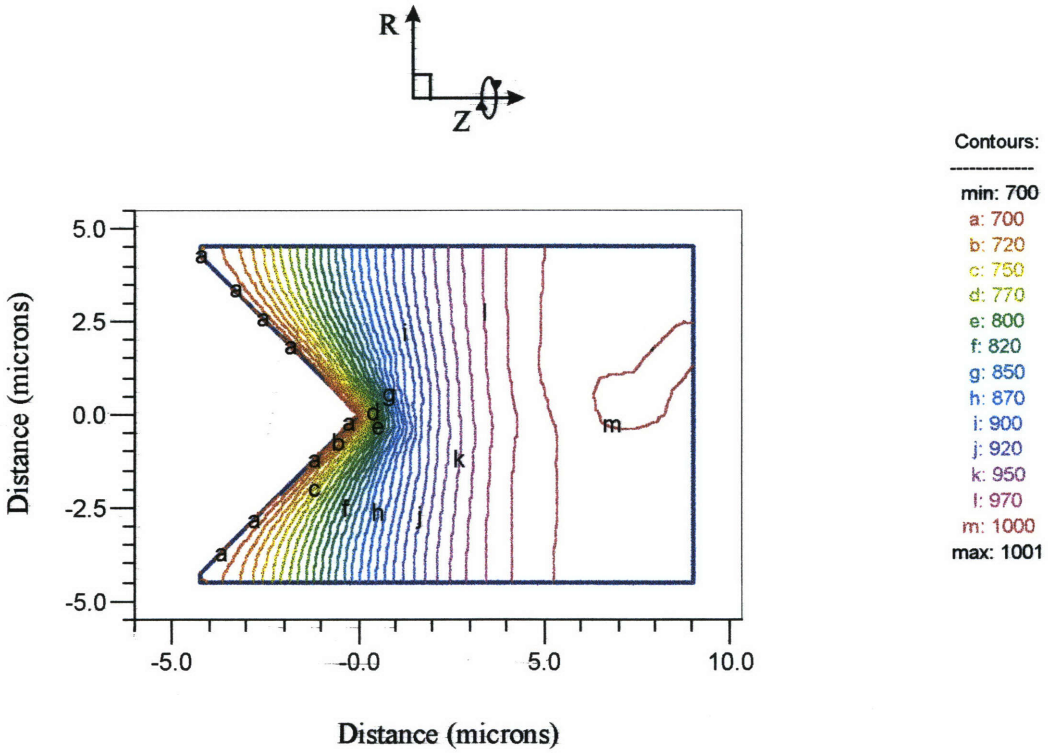

Figure 6.12. FEM diagram showing the yttrium concentration in front of the corner of a growing 123 crystal for $\Delta C = 300$ moles/m^3. (generated by PDEase®[134])

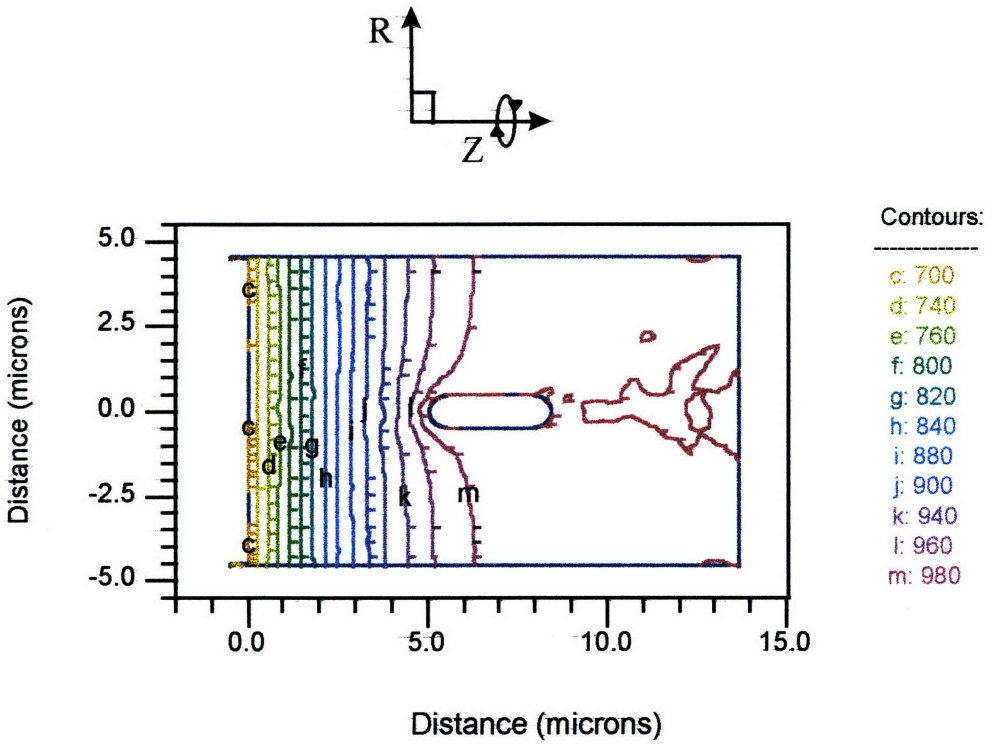

Figure 6.13. FEM diagram showing a 1 micron 211 particle oriented perpendicular to the 123 crystal face (position b) in figure 6.8) dissolving in front of a growing 123 crystal for $\Delta C = 300$ moles/m^3. (generated by PDEase®[134])

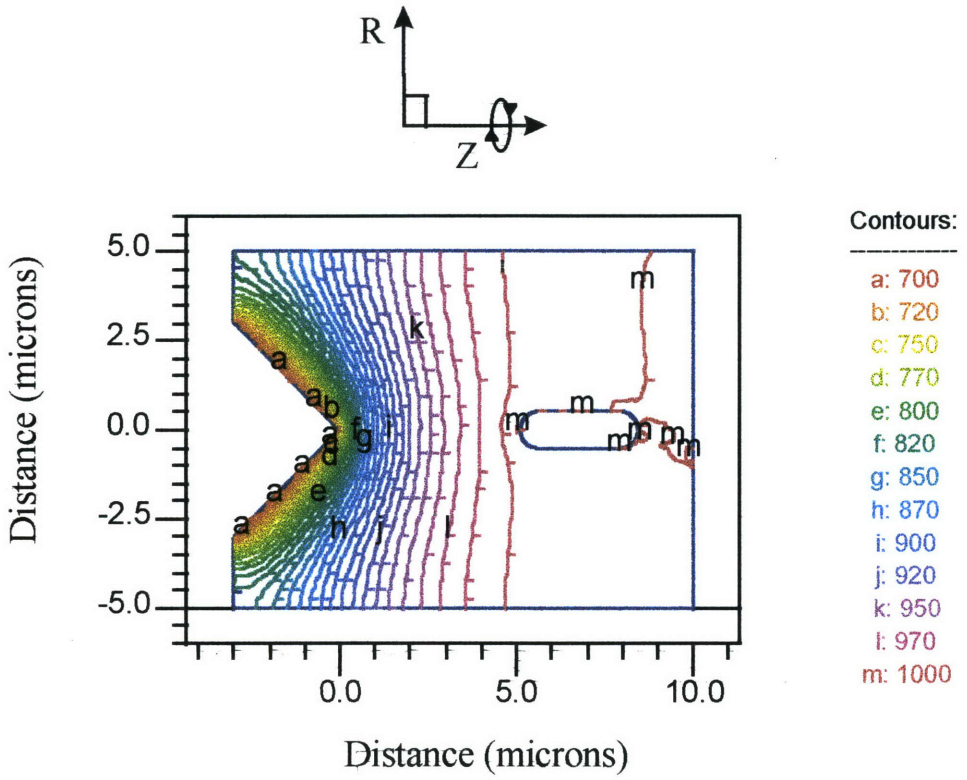

Figure 6.14. FEM diagram showing a 1 micron 211 particle oriented perpendicular to the 123 crystal corner (position f) in figure 6.8) dissolving in front of a growing 123 crystal for $\Delta C = 300$ moles/m^3. (generated by PDEase®[134])

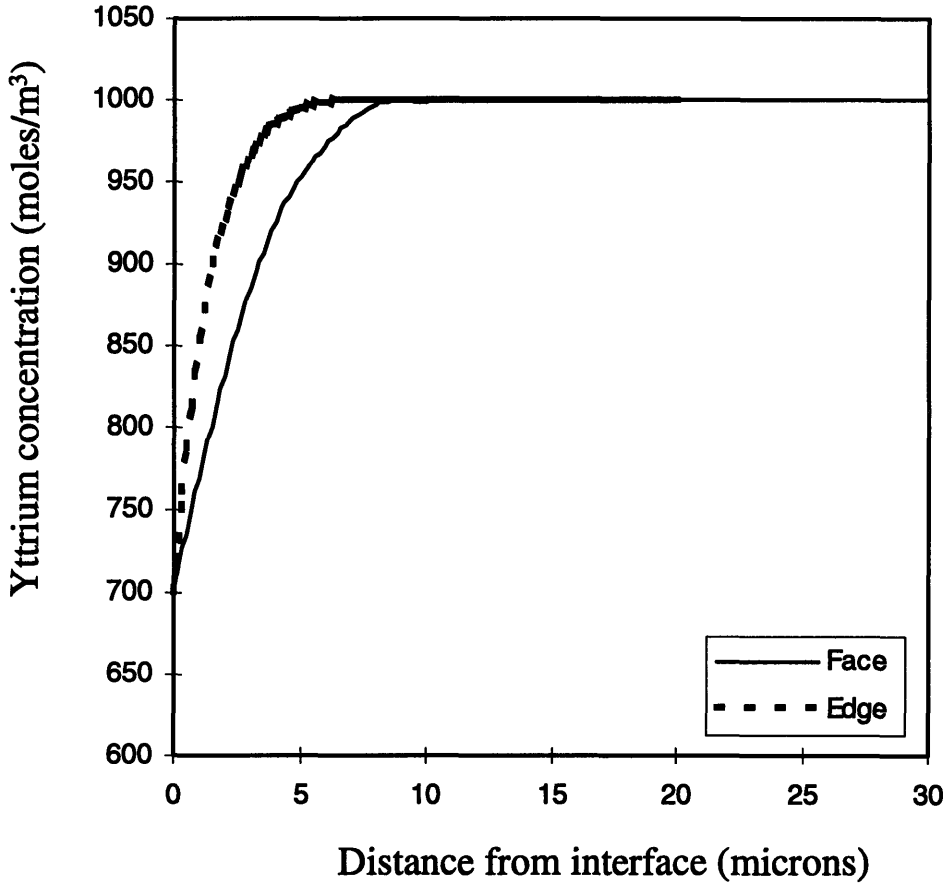

Figure 6.15. Yttrium concentration in front of the face and edge of the growing 123 crystal for $\Delta C = 300$ moles/m^3 (along dashed red line and solid green line in figure 6.9, respectively).

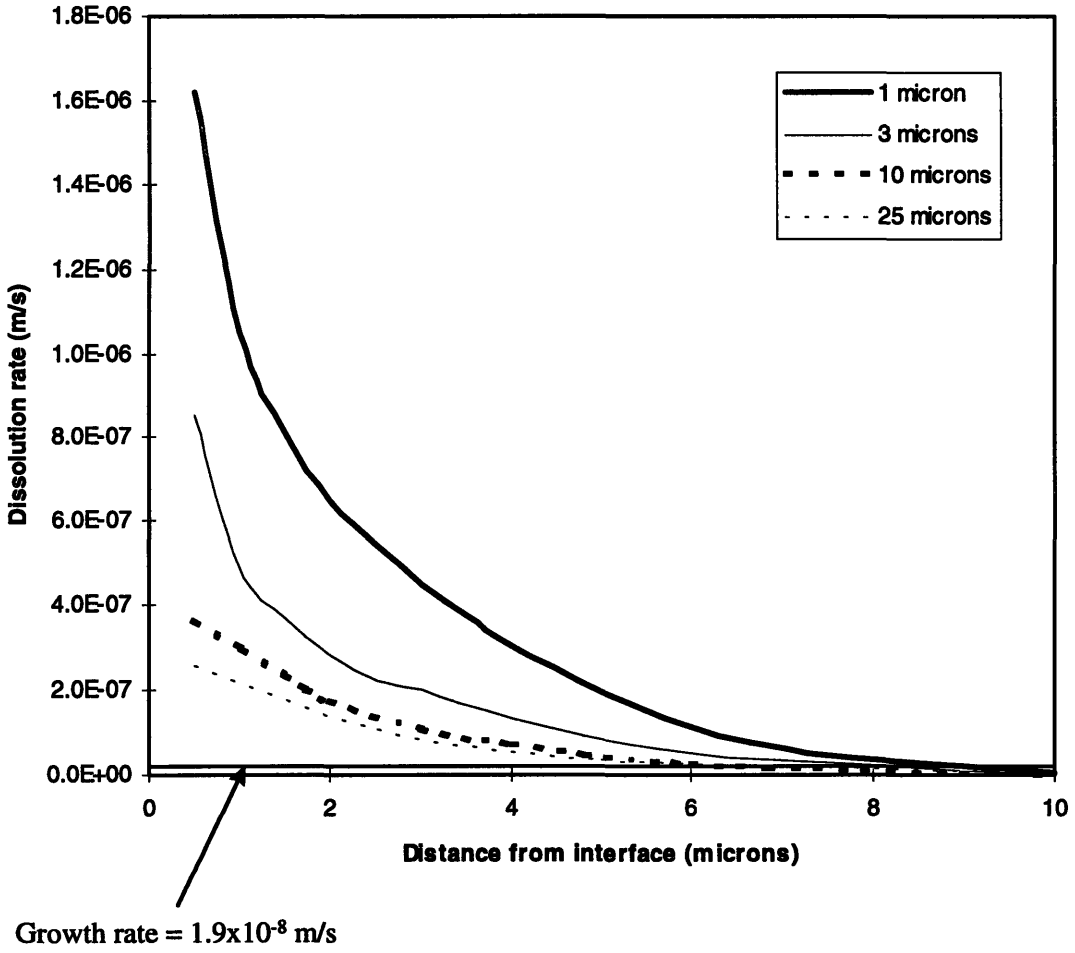

Figure 6.16. 211 particle dissolution rate for various diameter 211 particles oriented parallel to the 123 crystal face (position a) in figure 6.8) in front of a growing 123 crystal for $\Delta C = 300$ moles/m^3.

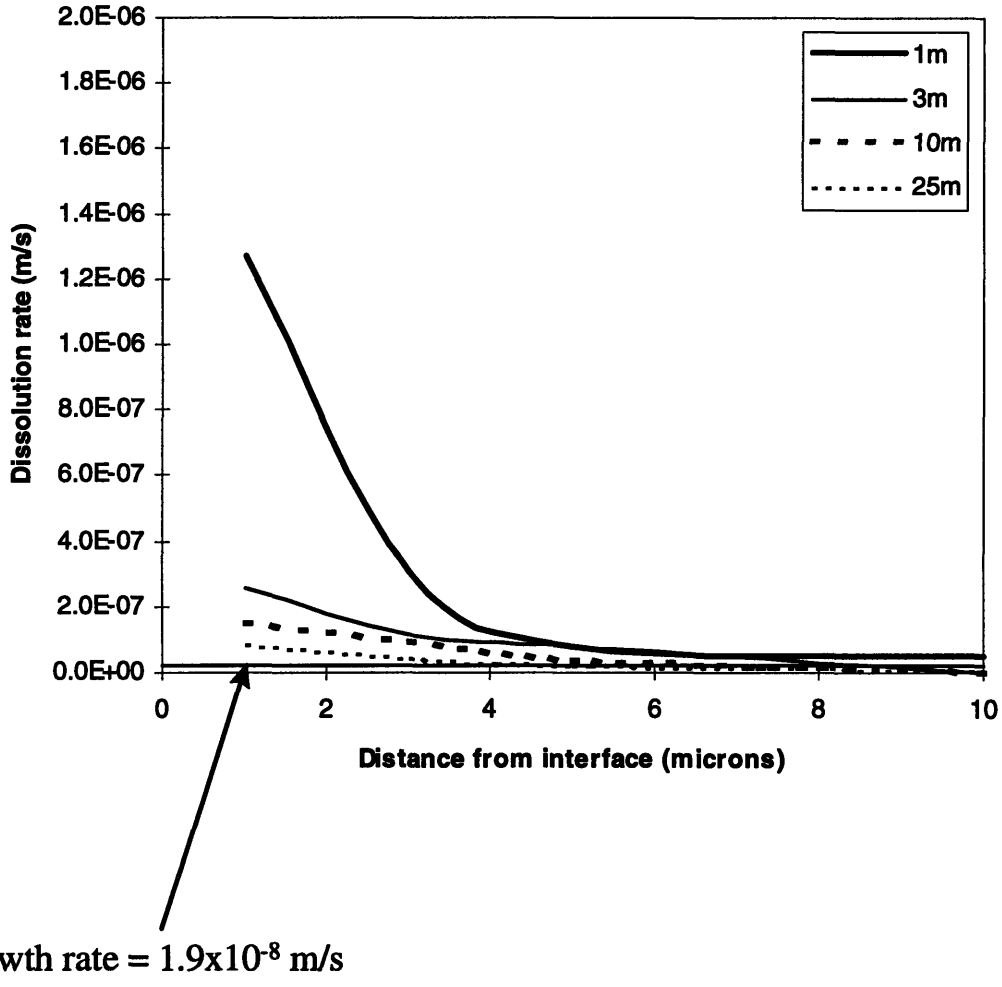

Figure 6.17. 211 particle dissolution rate for various diameter 211 particles oriented perpendicular to the 123 crystal face (position b) in figure 6.8) in front of a growing 123 crystal for $\Delta C = 300$ moles/m^3.

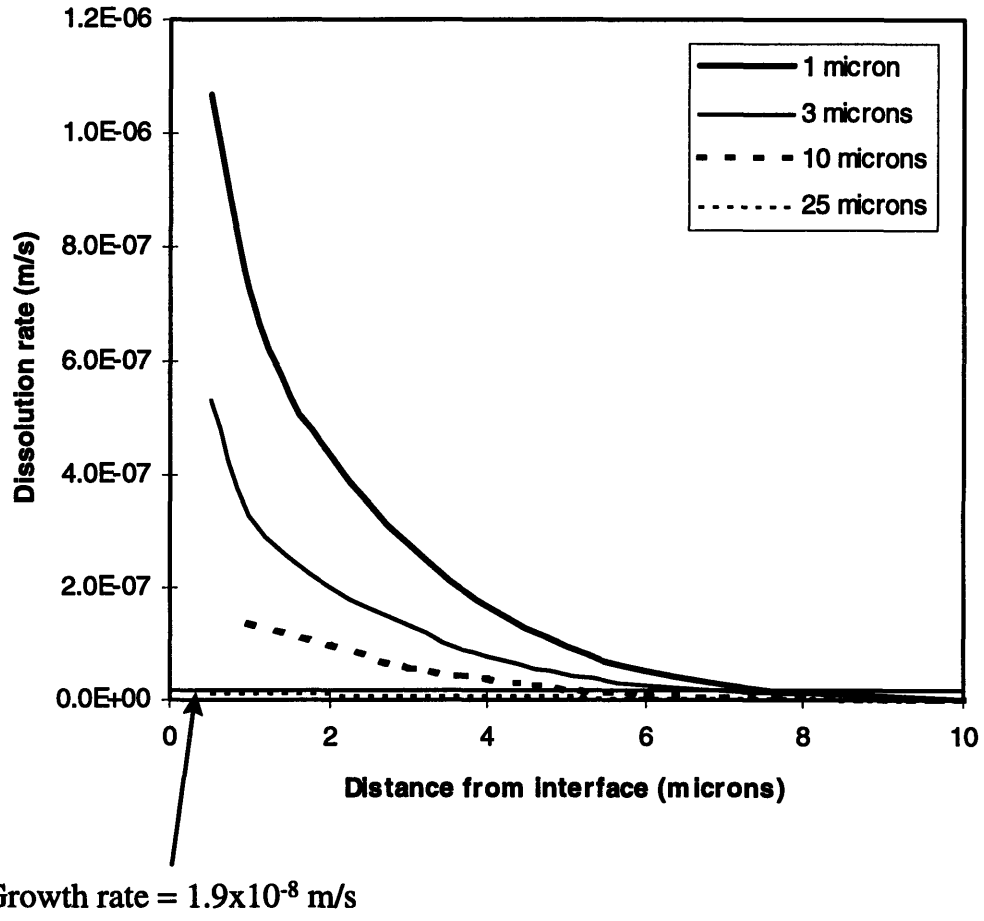

Figure 6.18. 211 particle dissolution rate for various diameter 211 particles oriented parallel to the 123 crystal edge (position c) in figure 6.8) in front of a growing 123 crystal for $\Delta C = 300$ moles/m^3.

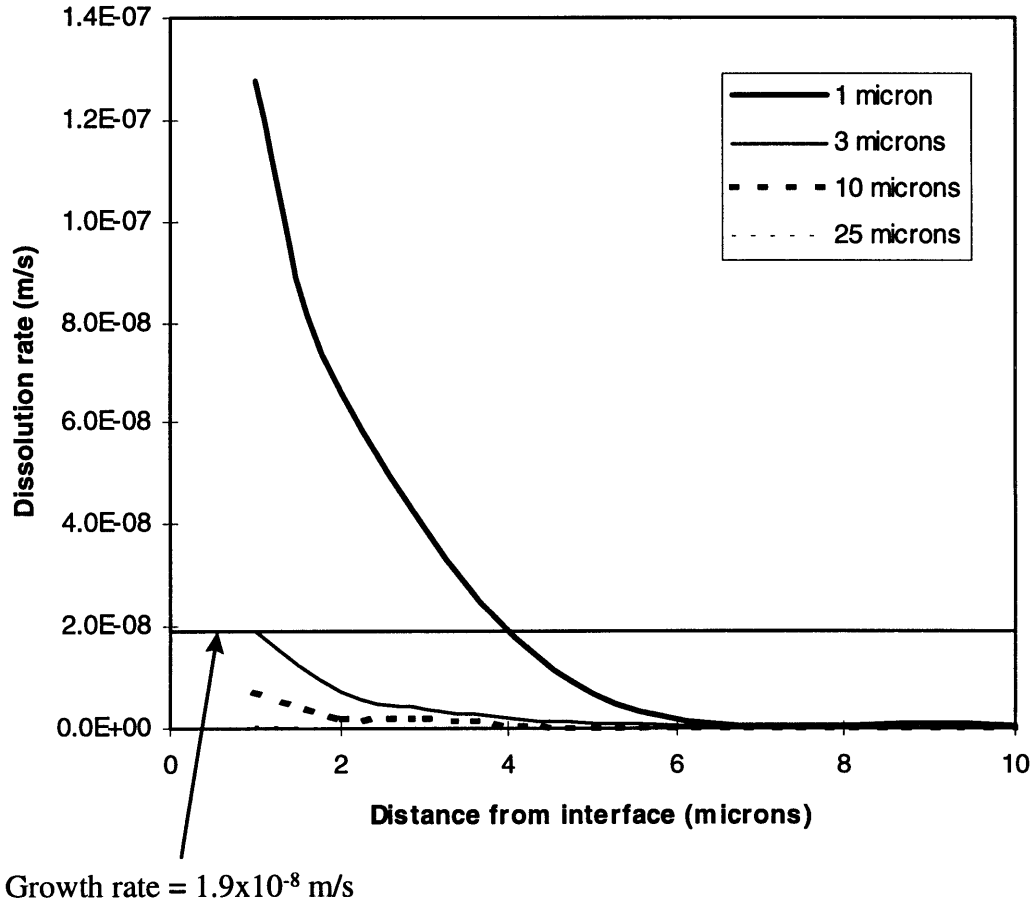

Figure 6.19. 211 particle dissolution rate for various diameter 211 particles oriented perpendicular to the 123 crystal corner (position f) in figure 6.8) in front of a growing 123 crystal for $\Delta C = 300$ moles/m^3.

Chapter 7

The effect of excess 211 particles on the microstructure of YBCO single crystals produced by seeded growth

7.1. Introduction

Many researchers working on melt growth of YBCO materials have also reported seeing inhomogeneous distributions of 211 particles within single crystals prepared from samples containing excess 211 phase.[35-37,39-43] As discussed in chapter 2, the presence of 211 particles within 123 crystals has been correlated with the enhanced critical current densities in YBCO materials.[87,92,94-95,101] 211 segregation within excess 211 samples, therefore, causes significant inhomogeneities in superconducting properties of the materials. This was shown to be true by Endo et al.[42]

The segregation of 211 particles within excess 211 samples is not as simple as the "X" track segregation taking place in stoichiometric samples, discussed in the previous chapter. Numerous researchers have been working on this problem and have arrived at various explanations for the cause of 211 particle segregation in excess 211 samples. These explanations include mismatch between the 123 and 211 crystal structure,[39,41] wetting angle,[43] particle pushing,[36-37,42] and variations in 211 particle dissolution rates.[35] Experimental data obtained during the present study will be presented here and used to evaluate the validity of each of these theories. It was shown in the previous chapter that 211 segregation in stoichiometric 123 samples resulted from variations in 211 particle dissolution rates at different locations on the 123 crystal surface. It is theorized that variations in 211 particle dissolution rates at the different faces of the 123 crystal play a role in 211 particle segregation in excess 211 samples as well. A driving

force for the differences in 211 particle dissolution at different faces based on barium cuprate liquid trapping within the 123 platelet structure is proposed.

7.2. 211 particle segregation and proposed explanations

211 particles segregate within the ab-pyramids and c-pyramids of the 123 single crystal (see figure 5.4) during three-dimensional growth of 123 single crystals from excess 211 precursors.[35] This type of segregation is more complicated to explain than 211 segregation in stoichiometric 123 samples. 211 particles only segregate along the interfaces between the growth pyramids in stoichiometric samples, whereas 211 particles segregate throughout the entire crystal in excess 211 samples. More 211 particles can be found within the four ab-pyramids relative to the c-pyramids in excess 211 samples. It has also been observed that the number of 211 particles within each pyramid increases with distance from the seed.[35] Sectioning the 123 single crystal at right angles to the seed produces the 211 segregation microstructure shown in figure 7.1. Other shapes such as the ones shown in figure 7.2 can be observed when the YBCO crystal is sectioned along other planes.[35] Researchers have also found pockets of low density and high density regions of 211 particles within the YBCO single crystal.[31,36-37,3,41] It has been theorized that these pockets form when barium cuprate liquid flows into a pore or when 211 particles are trapped in a crack in the precursor material.[36-37,39,41] As with the 211 particle segregation occurring in stoichiometric samples, excess 211 particle segregation patterns have most often been observed in crystals grown from melts, either by flux growth or seeded growth.[15,34-36,38-39]

A number of theories have been developed by other researchers to explain 211 particle segregation in excess 211 YBCO materials. Jee et al.[43] suggested that differences in the dihedral angle between the 123 interface and the 211 particles varied with 123 crystal

axis. This theory was based on the observation that the ab-face of the 123 crystal has more morphological perturbations than the c-face. Jee et al. suggested that the flatter c-face of the crystal produced a wetting angle of 0° with the 211 particles impinging upon it. This allowed a liquid film to remain between the 211 particle and the 123 interface, allowing 211 dissolution and yttrium transport to occur across the liquid to the 123 crystal. Jee et al. theorized that concavities in the ab-face of the 123 crystal produce a wetting angle between the 123 interface and 211 particle of more than 0°. They supposed that a dihedral angle of greater than 0° will cause the 211 particle to impinge and touch the 123 interface, without a liquid layer in between. This 211 particle will not dissolve due to the absence of the liquid layer through which yttrium transport occurs. Jee et al. therefore supposed that 211 trapping is greater on the a-face of the crystal than the c-face of the crystal.[54]

This theory is not consistent with 211 particle dissolution theory discussed in chapter 6. It was shown that 211 particles dissolve differently based on the topology of the interface with which they are impinging. It was shown in chapter 6 that 211 particle dissolution was faster in front of a flat interface than at an edge or corner. The opposite will be true for a concave surface. This concept is summarized in figure 7.3. It can be seen that 211 particle dissolution is faster in front of a concave surface than in front of a flat surface and slower in front of a convex surface. 211 particles in front of an ab-face such as the one shown in figure 7.3 a) will have an average dissolution rate which is the same as 211 particles in front of the c-face shown in figure 7.3 b). No extra 211 particles will be entrapped by the ab-face due to an increased number of morphological perturbations. It is therefore concluded that 211 segregation in excess 211 samples is not a result of variations in dihedral angle.

Vandewalle et al.[39] and Cloots et al.[41] proposed that 211 particle segregation occurs due to differences in lattice mismatch between 211 particles and the different faces of the 123 crystal. This theory was developed based on the results of Pellerin et al.[138] who

showed that elongated 211 particles are sometimes incorporated into 123 crystals in preferred orientations. Vandewalle and Cloots suggested that the 211 particles are incorporated into the 123 crystal in preferred orientations in order to minimize strain at the 211/123 interface. They calculated that better lattice matching was achieved between the b-axis of the 211 particles and the ab-axis of the 123 phase relative to the c-axis of the 123 phase. Many other authors have observed 211 segregation in samples with no preferred 211 particle orientation, however.[35-37,42-43] Random 211 particle orientation within the 123 phase does not minimize any strain whatsoever. The lattice mismatch theory cannot explain 211 segregation in these cases. Furthermore, any strain in the 123 crystal arising from the incorporation of a 211 particle is produced after the 211 particle is already incorporated into the crystal. Lattice mismatch is, therefore, not the driving force for 211 particle segregation in excess 211 systems. There is therefore no driving force for different 211 particle concentrations along different 123 axes. The preferred orientation of 211 particles observed by Pellerin et al.[138] can be explained based on the 211 dissolution modeling performed in chapter 6. It was shown that 211 particles impinging perpendicular to the 123 interface dissolve more slowly than 211 particles impinging parallel to the 123 face. This is also be true for samples containing excess 211 particles which become trapped within the 123 crystal. 211 particles oriented perpendicular to the 123 interface are more likely to become entrapped within the 123 crystal than 123 particles oriented parallel to the 123 interface, which dissolve faster. This phenomenon results in a slightly oriented distribution of 211 particles trapped within the 123 crystal.

Endo et al.[42] and others[36,37] have proposed that 211 particle segregation takes place via particle pushing. They suggested that the interfacial energy of the ab-face of the 123 crystal is lower than that of the c-face. The c-face of the 123 crystal will therefore push more 211 particles than the ab-face, based on the Uhlmann Chalmers Jackson (UCJ) particle pushing/trapping theory.[139-141] Endo et al. suggested that the critical particle size for trapping is different at different faces because of the following relationship:[142-143]

$$R^* \propto \frac{\Delta\sigma_0}{\eta \cdot (r^*)^n} \tag{7.1}$$

where R^* is the critical growth rate, $\Delta\sigma_0$ is the 123/211 interfacial energy, η is the melt viscosity and n is an exponent ranging from 1 to 2. Endo et al. also theorized that the volume fraction of trapped 211 particles will increase with undercooling, ΔT, since growth rate, R, of 123 materials increases with undercooling (see chapters 2 and 5). They suggested that 211 particles are pushed at low ΔT and entrapped at high ΔT, as shown in figure 7.4.[42] 211 particles which are initially pushed by the 123 interface will build up in front of the interface. Endo et al. assumed that the number of particles becoming entrapped within the 123 crystal will gradually increase as a greater number of particles build up in front of the interface. They used this assumption to explain the increase in 211 particle volume fraction with distance along the axes of the 123 crystal from the center of the crystal to the edge. Endo et al. performed their particle pushing experiments only on Pt-doped samples and suggested that 211 particle segregation is unlikely in undoped materials because the particles are too large and above the critical pushing size.[42]

211 particle segregation in excess 211 samples is not due to the 211 particle pushing mechanism proposed by Endo et al.[42] The main argument against this mechanism is that the UCJ particle pushing theory was derived based on one particle, or at most a small number of particles, being pushed by a faceted interface. Excess 211 samples containing 20 wt.% excess 211 materials will have an approximate volume fraction of 43 vol.% 211 phase within the barium cuprate liquid. A large number of 211 particles must therefore be pushed by the 123 interface. Additionally, the large volume fraction of 211 particles within the semi-solid melt causes the pushed 211 particles to impinge on other 211 particles further out in the melt, as shown in figure 7.5. The means that the 123 interface must not push 1 or 2 particles or even a single layer of 211 particles, but rather many layers of 211 particles stretching out into the semi-solid melt. This situation is far beyond

any assumptions which can be made in order to apply the UCJ particle pushing theory to 211 particles in the YBCO system.

Experiments performed by Jee et al.[43] also support the idea that 211 particle segregation is not due to particle pushing. Jee et al. grew 123 crystals containing excess 211 particles using the infusion growth process. As described in chapter 2, infusion growth is performed by infiltrating a sintered mass of 211 particles with a Ba-Cu-O glass melt. Jee et al. observed 211 particle segregation in crystals grown using this method. It is impossible for 211 particle pushing to be the cause for 211 particle segregation in the crystals produced by Jee et al. because the 211 particles in the melt were sintered together and were therefore unable to be pushed. 211 particles dissolving in front of the interface are not able to move through a sample composed of a rigid mass of sintered 211 particles.[43] Results obtained in the current study will be used to further evaluate the feasibility of 211 particle segregation resulting from the particle pushing mechanism proposed by Endo et al.[42]

A fourth 211 segregation model based on differences in 211 particle dissolution rates was proposed by Honjo et al.[35] Honjo et al. found differences in copper concentration in front of the ab-face and c-face. The copper concentration in front of the ab-face was higher than that in front of the c-face. Honjo et al. theorized that copper diffused through the liquid from the ab-face to the c-face during initial growth of the 123 crystal when the crystal faces were shorter than the diffusion length of copper in the liquid. Excess 211 particles dissolve in front of the copper rich c-face in order to keep the yttrium concentration constant in front of the interface. Fewer 211 particles are likely dissolve in front of the ab-face in order to compensate for the decrease in copper concentration in front of this face. This phenomenon results in a decreased number of 211 particles entrapped along the c-axis of the solidified 123 crystal relative to the ab-axis. Copper transport through the liquid decreases as the length of the 123 crystal increases during subsequent growth. The slow decrease in the amount of copper transported to the c-face

slowly decreases the dissolution of the particles in front of this face, resulting in an increase in trapped particles along the c-axis of the 123 crystal with increasing growth.[35]

Results obtained during this research show that 211 particle segregation in excess 211 samples is caused by differences in 211 particle dissolution in front of different faces of the 123 crystal. Observations show that solute transport around the 123 crystal corner is not the cause of these differences in 211 particle dissolution rate, however. The validity of the 211 dissolution theory, as well as the assumption of diffusion around the corner of the 123 crystal as the driving force for differences in 211 dissolution rate, will be discussed based on the results obtained in the current study.

7.3. Experimental procedure

YBCO samples containing 20 wt.% excess 211 were prepared as described in section 5.2.2 and used in the seeded growth experiments described here. The seeded growth process is described in section 5.2.3. Single-crystal Nd-123 seeds with polished faces parallel to their c-axes were used in these experiments. The samples were heat treated in air at undercoolings of ΔT = 6 °C, 9 °C, 12 °C and 15 °C, as shown in figure 5.3. The samples were quenched after 2 hours of growth to prevent slow cooling and additional growth of 123 material below the desired undercooling temperature. An additional sample grown at an undercooling of 12 °C was not quenched after 2 h of growth, but allowed to cool slowly by turning off the furnace. This slower cooling allowed all of the remaining semi-solid 211 + liquid phase to solidify to form the 123 phase with 211 inclusions. This experiment was performed in order to examine the microstructure of grain boundaries between different 123 crystals which formed during cooling. The samples were then mounted in epoxy, polished, and examined using scanning electron

microscopy (SEM), energy dispersive X-ray analysis (EDX), and cross-polarized optical microscopy.

211 particle segregation within the YBCO crystals produced by seeded growth was analyzed using optical micrographs taken along the ab-axis and c-axis at various intervals, as shown in figure 7.6. Points 0_{ab} and 0_c correspond to start of growth of the 123 crystal along the ab-axis and c-axis, respectively. Points X_{ab} and X_c correspond to the end of growth of the 123 crystal along the ab-axis and c-axis, respectively. The optical micrographs taken along the axes were converted to black and white images and digitized. The fraction of black and white pixels was then calculated to obtain the area fraction of 211 particles and 123 phase, respectively. 211 particle volume fraction is equal to 211 particle cross-section area fraction calculated using this method because the 211 particles are dispersed randomly within the 123 matrix and the sectional areas analyzed were also chosen at random.[115]

SEM analysis was performed on the 123 crystal/liquid interfaces as described in chapter 5. EDX analysis was also performed on the YBCO samples to examine the composition of the 123 + 211 crystal.

7.4. Results and discussion

The results of 211 particle segregation in excess 211 samples produced by seeded growth will be detailed in the following sections. The validity of the particle pushing theory vs. the incomplete 211 dissolution theory will be assessed based on this data. The driving force for differences in 211 particle entrapment along the different faces of the 123 crystal will also be examined.

7.4.1. 211 particle pushing vs. incomplete 211 particle dissolution

The results of the area fraction calculations for 211 particles dispersed throughout the 123 crystals produced from excess 211 precursors by seeded growth at various undercoolings are shown in figures 7.7 through 7.9. Figure 7.7 shows a typical relationship for the 211 volume fraction vs. distance from the center of the 123 crystal along the ab-axis and the c-axis. The data shown in figure 7.7 was obtained from a crystal produced at an undercooling of 15 °C. It can be seen that the volume fraction of 211 particles along the c-axis was less than the volume fraction along the ab-axis. This was true for all crystals. Figure 7.8 shows the 211 volume fraction along the ab-axis vs. distance from the center of the crystal for excess 211 samples produced at undercoolings of 6 °C, 9 °C, 12 °C and 15 °C. It can be seen that the volume fraction of 211 particles along the ab-axis decreases as the sample undercooling is increased. 211 volume fraction also increases with distance along the ab-axis. Figures 7.10 a) and b) show the magnitude of this increase for a crystal produced at an undercooling of 6°C. The photo in figure a) was taken at point 0_{ab} (shown in figure 7.6) and the photo in figure b) was taken at point X_{ab}.

The data shown in figure 7.8 directly contradicts the particle pushing theory proposed by Endo et al.[42] It can be seen from figure 7.8 that the volume fraction of 211 particles trapped along the ab-axes of the 123 crystals *decreases* with increasing undercooling. It was shown in chapters 2 and 5 that the growth rate of the 123 crystals *increases* with increasing undercooling. Endo et al. theorized that 211 particle volume fraction trapped within the 123 crystal will increase with increasing undercooling because the critical radius for 211 particle pushing decreases with increased growth rates at higher undercoolings (see equation 7.1 and figure 7.4).[42] This was not found to be the case. This data therefore provides additional evidence against particle pushing.

It can also be seen from figure 7.8 that the volume fraction of 211 particles trapped at nearly all points along the ab-axis within the 123 crystal is above the 20 wt.% (20.6 vol.%) excess 211 which was added to the precursor pellet. The particle pushing theory proposed by Endo et al.[42] suggests that particles are pushed ahead of the 123 interface during initial growth and are then increasingly entrapped within the 123 crystal as larger numbers of 211 particles build up in front of the interface and can no longer be pushed. This assumption requires that the initial volume fraction of 211 particles along the ab-axis be lower than the 20.6 vol.% which was added to the precursor material because some of these particles are pushed by the ab-face during initial growth. It can be seen from figure 7.8 that this is not the case. The initial volume fraction of 211 particles along the ab-axis is either equal to or greater than the 20.6 vol.% excess 211 phase added to the precursor pellet. This shows that none of the excess 211 particles can be pushed ahead of the ab-face since they are all incorporated into the 123 crystal. Additionally, the average volume fraction of 211 particles along the ab-axis is greater than the 20.6 vol.% excess added to the precursor. The only way that this can result is from incomplete 211 particle dissolution in front of the ab-face of the 123 crystal.

A number of other observations which refute the particle pushing theory were made during seeded growth experiments on excess 211 samples. Figures 7.11 a) and b) show SEM micrographs of typical ab- and c-interfaces between the 123 crystal and the semisolid melt. It can be seen that there is no layer of excess 211 particles which has built up in front of either interface as Endo et al. suggested would be the case for 211 segregation via particle pushing (see figure 7.4).[42] This provides additional evidence against particle pushing.

Figures 7.12 a) and b) show two optical micrographs of the same grain boundary within an unquenched excess 211 sample grown at ΔT= 12 °C and allowed to cool slowly. This slow cooling allowed all of the remaining semi-solid 211 + liquid phase to solidify to form the 123 phase with 211 inclusions. This grain boundary was created when two

different 123 crystals oriented in different directions impinged upon each other. The orientations of the two crystals are marked as shown in figure 7.12. Two different figures were necessary to show the grain boundary as well as the 211 particles trapped within each 123 crystal. 211 particle pushing theory states that 211 particles are pushed in front of the 123 grain boundary, resulting in a layer of excess 211 particles in front of the interface. This layer of pushed particles will, therefore, be present at the grain boundary if two 123 interfaces grow toward each other and impinge upon each other. It can be seen from figures 7.12 a) and b) that this is not the case. No excess 211 particles are found at the grain boundary between the 123 crystals growing in different orientations.

Endo et al. performed the particle pushing experiments detailed in reference [42] only on Pt-doped samples and suggested that 211 particle segregation is unlikely in undoped materials because the particles are too large and are above the critical pushing size.[42] Experiments performed as part of this study showed that 211 particle segregation does indeed occur in undoped excess 211 samples. This observation provides additional evidence against the particle pushing theory.

7.4.2. Driving force for incomplete 211 particle dissolution

It was shown in the previous sections that the only valid explanation for 211 segregation in excess 211 samples involves differences in 211 particle dissolution rates in front of the ab- and c-faces of the 123 crystal. Possible driving forces for 211 segregation, including copper diffusion around the corner of the 123 crystal and platelet formation, are therefore evaluated in this section. It may also seem that 211 particle coarsening may play a role in the increasing slopes on the 211 volume fraction vs. distance plots shown in figures 7.7 through 7.9. It has been shown by Endo at al.,[42] however, that 211 particle segregation takes place in Pt-doped samples. Examination of Pt-doped excess 211 samples produced for the growth rate study described in chapter 5 showed that this was also the case in the

crystals produced for this work. It was shown in chapter 3 that Pt-doping severely limits the amount of 211 particle coarsening which takes place in the semi-solid melt. The fact that 211 particle segregation occurs in both Pt-doped and undoped excess 211 samples shows that changes in 211 particle dissolution rates as a result of changes in 211 particle size with time due to coarsening is not the driving force for 211 particle segregation in excess 211 samples.

Honjo et al.[35] suggested that differences in 211 dissolution rates at the ab- and c-faces of the 123 crystal occur due to copper diffusion around the corner of the crystal. This diffusion becomes limited and eventually stops as the size of the 123 crystal becomes larger than the diffusion length of the copper in the liquid.[35] A number of observations made during the current study show that this assumption is not very likely. Figure 7.13 shows a typical interface of the c- and ab-growth pyramids within the 123 single crystal. The region of the c-pyramid contains a much smaller volume fraction of 211 particles than the ab-region. It can be seen that the interface between these two regions is very sharp and abrupt. This was found to be the case along all interfaces between the c-pyramids and ab-pyramids in all crystals. Copper diffusion around the corner of the 123 crystal will result in a diffuse difference in 211 particle concentration from the ab-face to the c-face. This was not observed in any crystals examined for this study.

Diffusion of solute around the corner would also cause the 211 particle volume fraction along the ab-axis to decrease as the 211 volume fraction along the c-axis increases. Comparison of figures 7.8 and 7.9 shows that this is not the case. Comparison of figures 7.8 and 7.9 also shows that after a certain growth distance, the volume fraction of 211 particles on *both* 123 crystal axes is greater than 20.6 vol.%. This makes diffusion around the corner even less likely.

Any possible mechanisms explaining differences in 211 dissolution rates on different faces of 123 crystals grown from excess 211 samples must explain two basic facts. First

of all, mass must be conserved. The semi-solid melt out of which the 123 crystal is growing consists of yttrium rich 211 particles and barium- and copper-rich liquid. As discussed in chapter 5, the baseline composition for the excess 211 samples consists of 20 wt.% (or 20.6 vol.%) 211 phase and 80 wt.% (or 79.4 vol.%) 123 phase. This composition is made up of 23.1 atomic% yttrium, 31.7 atomic% barium and 45.2 atomic% copper. YBCO crystals containing an increased volume fraction of 211 particles due to 211 particle segregation will contain a higher percentage of yttrium relative to the precursor material, since 211 particles are rich in yttrium. The yttrium concentration in the 123 phase cannot be changed since the 123 phase is a line compound. Crystals made up of only excess 211 particles and 123 matrix will therefore have a significantly increased yttrium concentration if the overall yttrium concentration in the YBCO crystal (211 particles + 123 matrix) is measured. As a result, the overall copper concentration will also be significantly reduced. The overall composition of the solidified 123 crystal containing the segregated 211 particles should have an yttrium concentration significantly greater than 23 atomic % and a copper concentration significantly less than 45.2 atomic %, since more than a total of 20.6 volume% 211 particles are trapped within the crystal. The overall yttrium and copper concentrations within the sample will also vary with distance, since 211 particle segregation increases with distance from the center of the crystal.

Figure 7.14 compares the overall yttrium concentration measured by EDX along the ab- and c-axes of a YBCO crystal containing segregated 211 particles which was grown at an undercooling of 12 °C. The overall yttrium concentration in the excess 211 precursor pellets is shown as a dashed line in figure 7.14. Figure 7.15 shows the overall copper concentration measured along the ab- and c-axes of the same crystal. The overall copper concentration in the excess 211 precursor pellets is shown as a dashed line in figure 7.15. It can be seen from figure 7.14 that the overall yttrium concentration in the 123 crystal is not higher than the yttrium concentration in the YBCO precursor pellet, as would be expected from massive 211 particle segregation. Figure 7.14 also shows that overall

yttrium concentration in the 123 crystal does not vary significantly with distance. It can be seen from figure 7.15 that the overall copper concentration in the 123 crystal is not significantly lower than the copper concentration in the YBCO precursor pellet, as would be expected from massive 211 particle segregation. Figure 7.15 also shows that overall copper concentration in the 123 crystal does not vary significantly with distance. Figures 7.14 and 7.15 show that the overall yttrium and copper concentrations within the solidified YBCO crystal are approximately the same those in the precursor pellet, even though the solidified YBCO single crystal contains a higher volume fraction of 211 particles than the precursor pellet. This fact suggests that a phase containing excess copper must be present within the YBCO crystal to compositionally balance the excess yttrium in the segregated 211 particles and preserve mass balance. This is indeed the case, as is described below.

211 particle segregation always occurs such that there are less 211 particles trapped by the c-face than the ab-face of the 123 crystal. Any proposed dissolution mechanism must also explain why 211 particle dissolution rates are lower in front of the ab-face than in front of the c-face of the 123 crystal. One possible mechanism which explains both of these pieces of data is based on excess barium cuprate liquid entrapment between 123 growth platelets. TEM studies performed by T. H. Sung on other excess 211 crystals produced in the MIT Ceramics Processing Research Laboratory by the same seeded growth process showed the presence of a platelet structure within the 123 crystals. The platelets contained a barium cuprate second phase layer.[31] Researchers have shown that this barium cuprate phase is trapped by platelets formed within the 123 crystal during solidification from the melt. Platelet formation and trapping of barium cuprate liquid with 123 crystals solidified from barium cuprate melts has been observed by many researchers.[20,44,68,76,82,87,102,124-125,144-145] It has also been shown that barium cuprate liquid trapped between 123 growth platelets is preferentially oriented along the ab-axis of the 123 crystal.[20,44,68,76,82,87,102,124-125,144-145] This liquid trapping phenomenon was thoroughly analyzed by Goyal et al.[82] Figures 7.16 a) through c)[82] show how barium

cuprate liquid is trapped behind 211 particles. Figure a) shows the asymmetric intersection of a 123 platelet gap at the growth front with a 211 particle in the semi-solid melt. Figure 7.16 b) shows how liquid within the platelet gap can be trapped by a second 211 particle intersecting the 123 interface. This particle can, in turn, produce another platelet gap and trap more liquid, shown in figure 7.16 c). Goyal et al.,[82] as well as other authors,[124-125] have shown that the liquid phase is preferentially segregated along the ab-axis of the 123 crystals, as shown in figure 7.16.[82] This was also found to be the case in TEM studies conducted by Sung et al.[31] on other excess 211 crystals produced in the MIT Ceramics Processing Research Laboratory by the same seeded growth process.

It is theorized that 211 particle segregation in excess 211 samples is a result of liquid trapping during melt growth. Sung et al. found that ion milling the surface of the single crystal samples preferentially etched away material from the platelets, making them more visible using optical microscopy. Figure 7.17 shows an optical micrograph (taken by T.H. Sung) of the platelet structure of an ion milled excess 211 crystal produced by S. Honjo in the MIT Ceramics Processing Research Laboratory by the same seeded growth process. The sample orientation is shown as marked in figure 7.17. It can be seen that the number of platelets increases along the ab-direction in this sample. This increase in platelet concentration along the ab-axis mirrors the increase in 211 particle concentration along the ab-axis of the crystal, as shown in figure 7.8. Figures 7.18 a) and b) show higher magnification SEM micrographs (taken by T.H. Sung) of high and low 211 particle concentrations within the crystal. It can be seen that a small number of platelets are present in the low 211 density region shown in figure 7.18 a). A large number of platelets are present in the high 211 density region shown in figure 7.18 b). These figures show that the presence of segregated or depleted regions of 211 particles are directly linked to the trapped barium cuprate liquid between the 123 platelets.

Figure 7.19 shows two optical micrographs (taken by T. H. Sung) of the same region of solidified crystal The photo in figure 7.19 a) was taken after 1 h of ion milling and the

photo in figure 7.19 b) was taken after 100 h of ion milling. Figure 7.19 a) shows a region of a 123 crystal which contains high and low density regions of 211 particles. As discussed above, such regions can occur when 211 particles are trapped in a crack or when barium cuprate liquid flows into a pore in the YBCO precursor material. Figure 7.19 b) shows that the high density 211 region contains a high density of barium cuprate layers trapped between 123 platelets. The low density 211 region contains a low density of platelets. This figure also shows that the presence of segregated or depleted regions of 211 particles are directly linked to the trapped barium cuprate liquid between the 123 platelets.

It is known that the barium cuprate liquid in the semi-solid 211 + liquid melt contains a higher concentration of copper than is present in the 123 phase. Growth of the 123 crystal into the semi-solid melt therefore results in the rejection of copper at the growth interface.[63,64] Figure 7.20 shows a schematic of copper rejection in front of the growth interface for an interface composed of platelets (figure 7.20 a)) and a flat interface (figure 7.20 b)). It can be seen that the copper rejection from growth interfaces on either side of the platelets results in excess copper being rejected into the platelet gaps. The liquid inside the platelet gaps is therefore copper rich (yttrium poor) relative to the liquid in front of a flat interface. The liquid in front of the platelet gaps is copper poor (yttrium rich) relative to the liquid in front of a flat interface, due to the absence of copper rejection in the regions directly in front of the platelet gaps. It was shown in chapter 6 that the driving force for 211 particle dissolution is the yttrium concentration gradient around the 211 particle in front of the 123 interface. Entrapment of copper-rich (yttrium poor) liquid between the 123 growth platelets results in a relative increase in yttrium concentration in front of the interface in the region of the platelet gap, as shown in figure 7.21. $\left(C_L^{Y'}\right)_{inside}$ is the yttrium concentration of the liquid inside the platelet gap shown in figure 7.20 a). $\left(C_L^{Y'}\right)_{outside}$ is the yttrium concentration of the liquid in front of (outside) the platelet gap. 211 particles within the yttrium rich liquid in front of the platelet gaps,

$\left(C_L^{Y}\right)_{outside}$, will therefore dissolve much more slowly than 211 particles in front of flat regions of the 123 interface (regions without platelet gaps). This results in a greater volume fraction of 211 particles being incorporated into the 123 crystal in regions of the 123 crystal composed of platelet gaps.

As discussed above, 211 particle segregation always occurs such that there are less 211 particles trapped by the c-face than the ab-face of the 123 crystal. Any proposed dissolution mechanism must explain why 211 particle dissolution rates are lower in front of the ab-face than in front of the c-face of the 123 crystal. Figure 7.22 shows that copper rejection at the 123 interface and liquid trapping mechanisms vary according to 123 crystal face. Figure 7.22 shows a schematic of the platelet structure at the ab-face and c-face of the growing crystal. It is known that 123 platelets form in an orientation parallel to the ab-axis of the 123 crystal.[82] As shown in figure 7.22 , structural differences in platelet formation at the ab- and c-interfaces, caused by this preferred orientation of the platelets, results in a lower copper concentration in the liquid in front of the ab-face than in front of the c-face (the yttrium concentration in front of the ab-face is therefore higher than in front of the c-face). As previously discussed, the driving force for 211 particle dissolution is the yttrium concentration gradient around the 211 particle in front of the 123 interface. 211 particle dissolution will therefore be lower in front of the ab-face of the 123 crystal than in front of the c-face of the crystal. This difference in 211 particle dissolution rates will result in a greater number of 211 particles being trapped by the ab-face of the 123 crystal than the c-face. This was found to be true for all crystals.

The increase in 211 particle entrapment with growth distance can also be explained by the liquid entrapment theory. It has been shown by Schmitz et al.[68] as well as by Goyal et al.[82] that platelet formation and liquid trapping in the 123 crystal is directly related to the impingement of 211 particles upon the 123 interface. This is described by figures 2.12 and 7.18. As discussed above, the yttrium concentration in front of the 123 interface in

the region of the platelet will be increased relative to regions without platelets since the liquid trapped within the platelet gap is yttrium poor. 211 particle dissolution will therefore decrease in front of the 123 interface around the region of the platelet gap. This decrease in 211 particle dissolution will result in an increased number of 211 particles which remain undissolved in front of the platelet gaps. These undissolved 211 particles will be trapped in the 123 crystal during subsequent growth. Each of these 211 particles creates a new platelet gap with the potential to trap additional yttrium-poor liquid. The increased number of trapped 211 particles causes the amount of liquid trapped between an increased number of platelet gaps to increase as well. This increase in liquid trapping will increase the number of yttrium rich regions in front of the 123 interface, thereby producing an increased number of regions with decreased 211 dissolution rates. An even greater number of 211 particles will therefore be trapped during subsequent crystal growth. This cycle of increasing platelet formation, increasing liquid entrapment, decreased 211 dissolution rate and increased 211 entrapment is a positive feedback process. The relative density of 211 particles trapped within the 123 crystal will therefore increase as the growth distance from the seed increases.

This feedback loop of platelet formation, liquid entrapment and 211 particle entrapment is shown in figure 7.23. Region a) is a region of the 123 crystal near the seed, in other words near the start of 123 growth. 211 particles impinging on the 123 crystal at point a) are trapped and form a trapped liquid region at point b). This trapped liquid reduces the 211 particle dissolution in front of the 123 interface, resulting in an increase in trapped particles at point c). These particles cause the formation of platelets which trap liquid at point d). This increase in trapped liquid at point d) in turn decreases the 211 dissolution rate in front of the 123 interface near the platelet gaps, resulting in more 211 particles trapped at point e). This cycle repeats itself along points f) through h).

The increase in 211 particle entrapment with distance, shown in figures 7.7 through 7.9, can be explained by this mechanism. The fact that excess 211 particles are not present in

stoichiometric 123 samples also explains why this type of 211 segregation does not occur in stoichiometric YBCO samples. All 211 particles in front of the 123 crystal face are dissolved in stoichiometric 123 samples. Excess 211 particles must remain undissolved in front of the 123 interface in order to impinge upon the 123 crystal, starting the cycle of platelet gap formation, liquid entrapment and, eventually, increased 211 entrapment. This process can only occur in samples containing excess 211 phase.

7.5. Conclusions

211 particle segregation within 123 crystals formed from excess 211 precursors was examined and quantified. It was shown that 211 particle entrapment is greater along the ab-axis than along the c-axis of the 123 crystal. 211 particle entrapment increases with growth distance from the center of the 123 crystal. A number of 211 particle segregation theories were investigated in order to explain this phenomenon. It was found that a difference in the 211 dissolution rates in front of the ab- and c-faces of the 123 crystal is the only 211 segregation mechanism which explains all of the data produced in this investigation and found in the literature. It was shown that it is unlikely that 211 particle segregation in excess 211 samples occurs as a result of particle pushing, differences in 211/123 wetting angle or differences in lattice mismatch between 211 particles and the different faces of the 123 crystal. A theory involving barium cuprate liquid entrapment during 123 crystal growth was proposed as a driving force for differences in 211 dissolution rates in front of the ab- and c-faces of the 123 crystal. This liquid entrapment theory can explain all of the data produced in this investigation and found in the literature. It can also explain why bulk 211 segregation in this form is only observed in excess 211 samples. Future work done in this area should include a study on the kinetics of platelet formation and liquid trapping on the various faces of 123 crystals in order to be able to quantify and predict the 211 particle segregation and dissolution phenomenon more accurately.

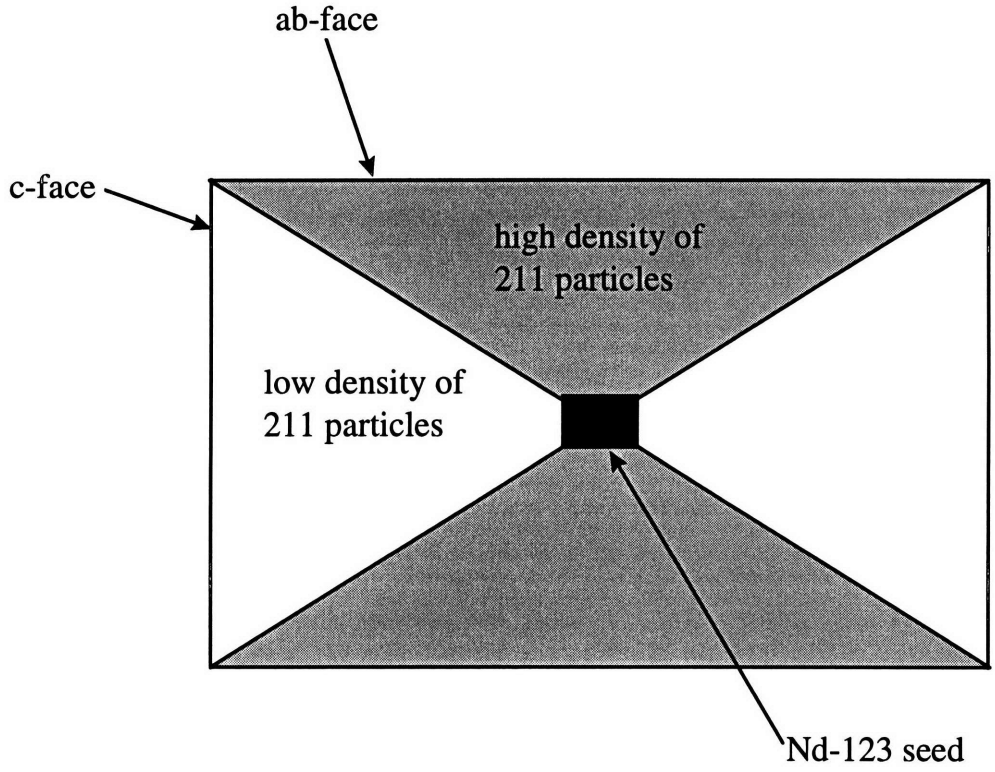

Figure 7.1. Schematic of 211 particle segregation in a cross-section of a YBCO single crystal produced from an excess 211 precursor.

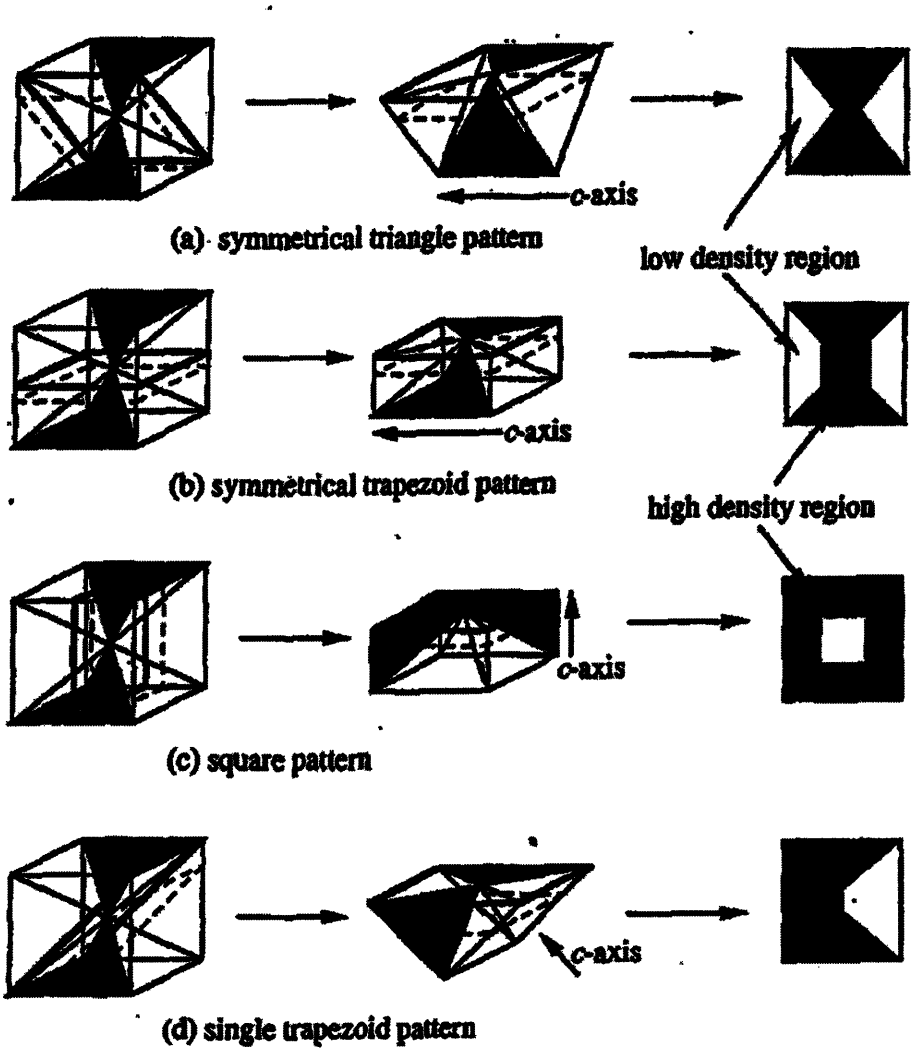

Figure 7.2. Schematic diagrams of various 211 segregation patterns which can be observed in excess 211 samples. Patterns a) through d) can be observed by sectioning the YBCO single crystal along various planes.[35]

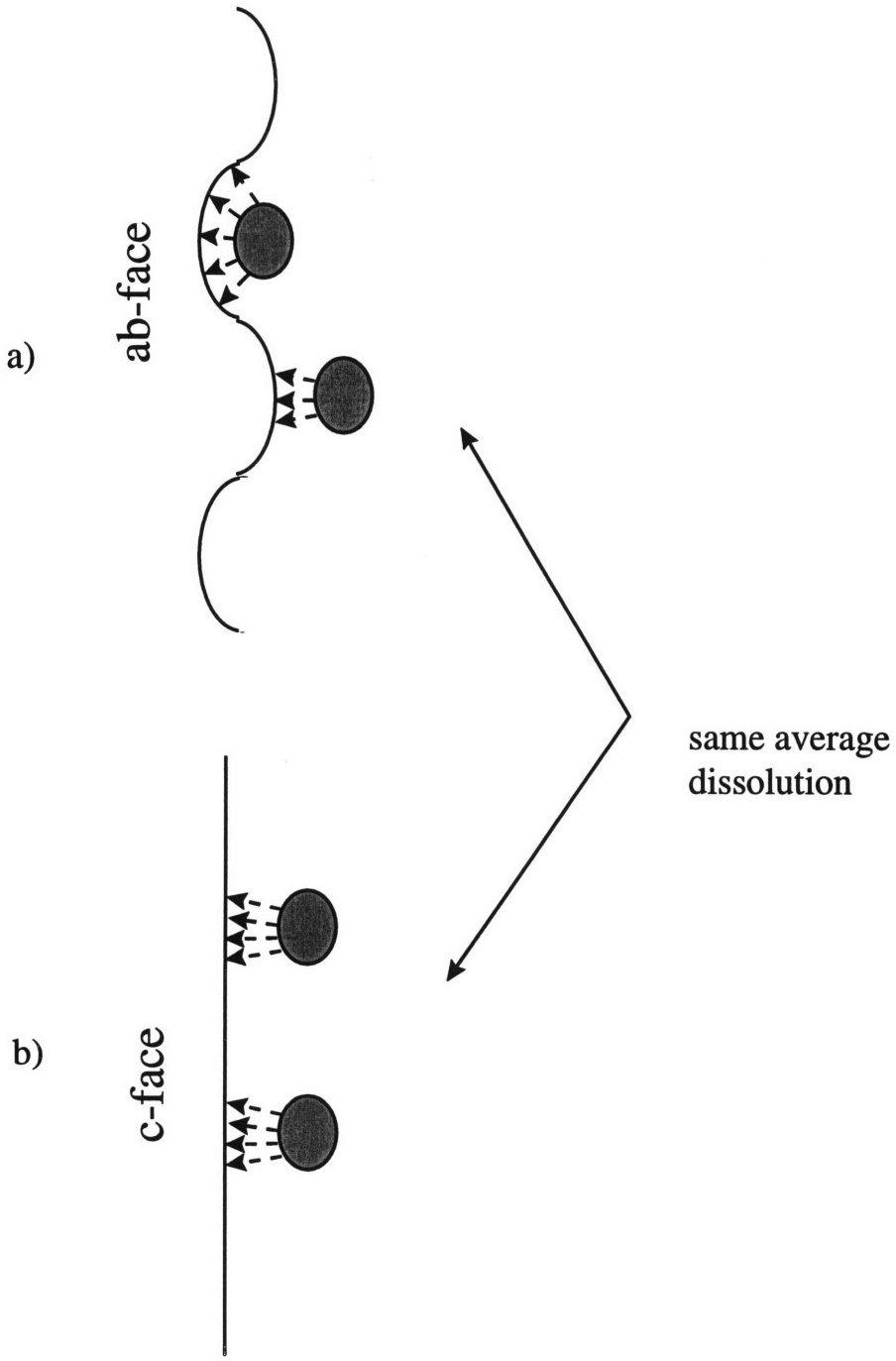

Figure 7.3. Schematic diagrams of 211 particles dissolving in front of a) a curved ab-face and b) a flat c-face of a 123 single crystal. The average dissolution will be the same for both cases.

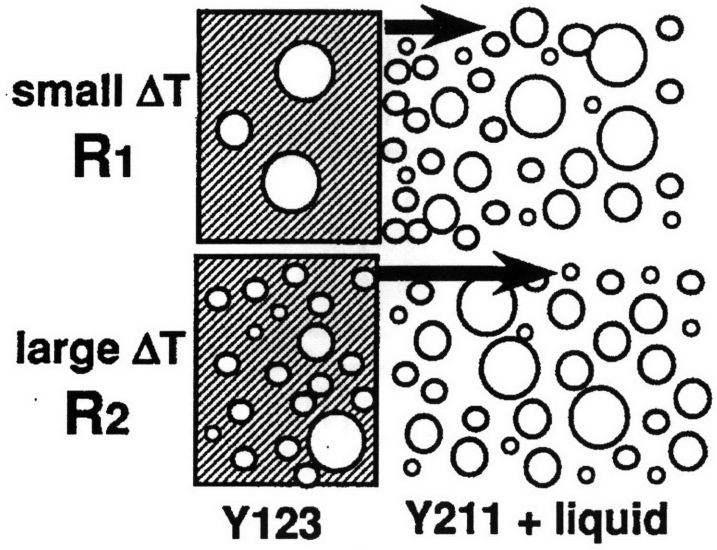

Figure 7.4. Particle pushing theory proposed by Endo et al.[42] suggests that 211 particles should be pushed at low 123 crystal growth rates produced by low undercoolings and entrapped at high 123 crystal growth rates produced by high undercoolings.

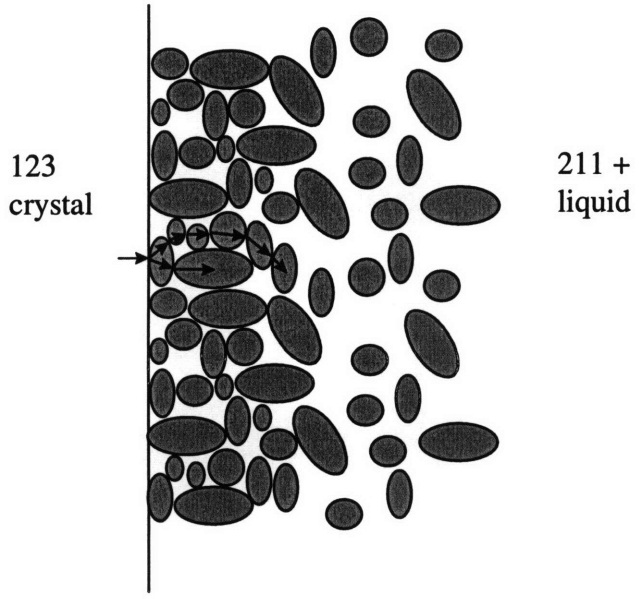

Figure 7.5. Schematic of 211 particle pushing in front of the 123 crystal interface after a period of 123 crystal growth. Many layers of 211 particles must be pushed by the 123 interface.

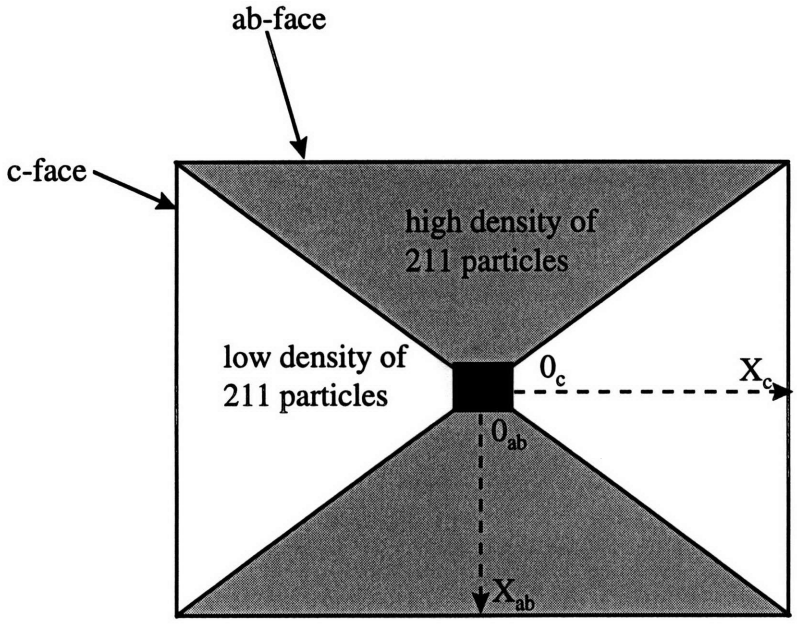

Figure 7.6. Schematic of an excess 211 crystal section showing the location of 211 volume fraction analysis performed along the ab-axis and c-axis of the YBCO crystals.

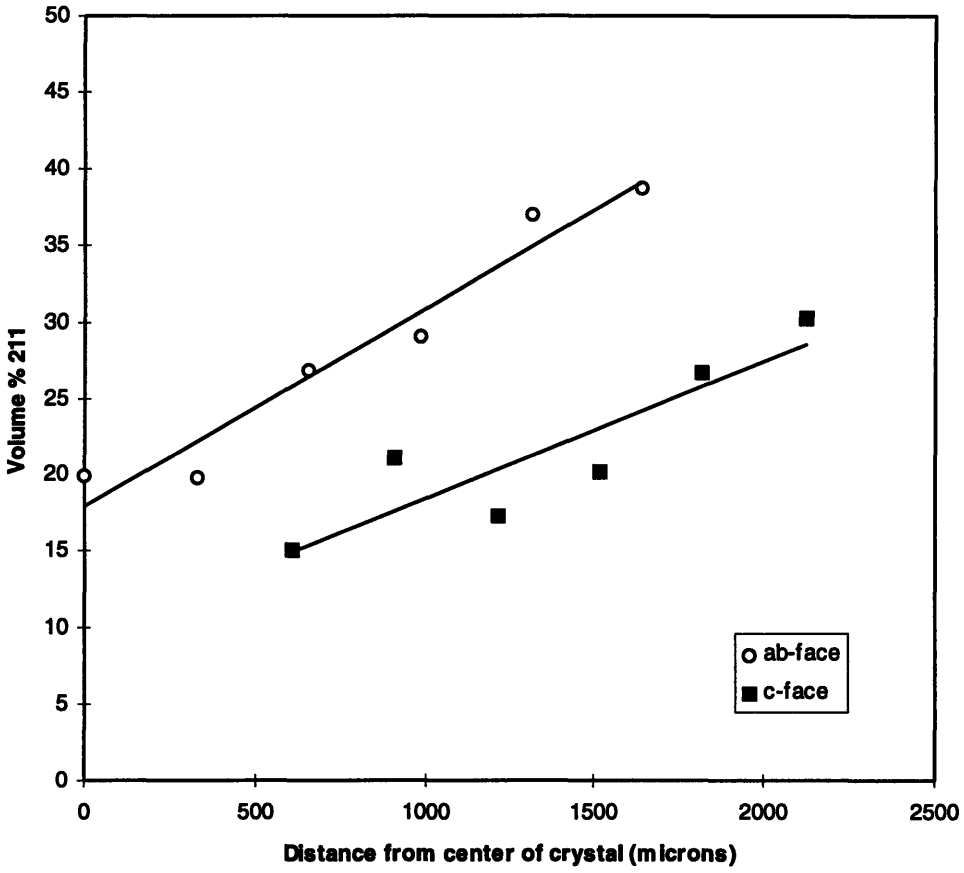

Figure 7.7. Volume fraction of 211 particles vs. distance along the ab-axis and c-axis within a 123 crystal produced at an undercooling of 15 °C.

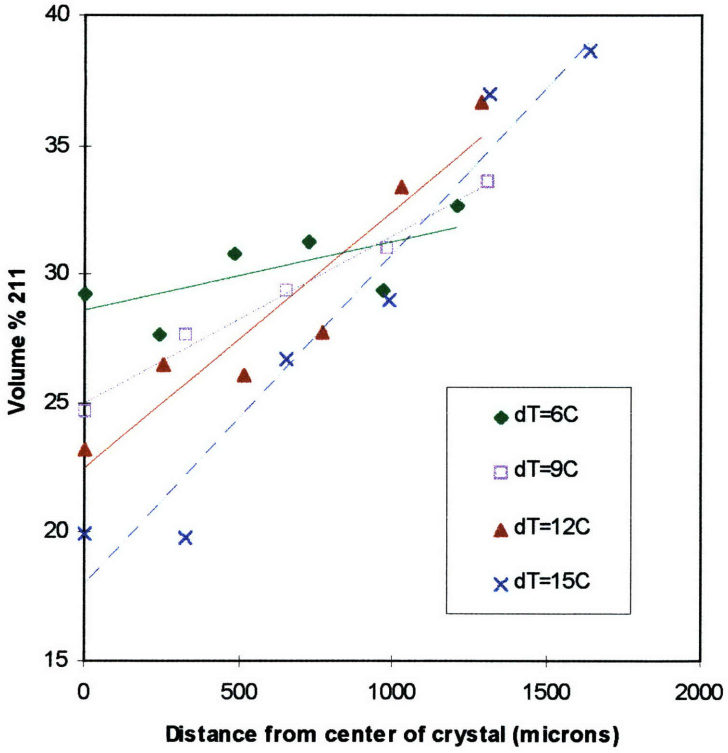

Figure 7.8. Volume fraction of 211 particles vs. distance along the ab-axis within 123 crystals produced at various undercoolings.

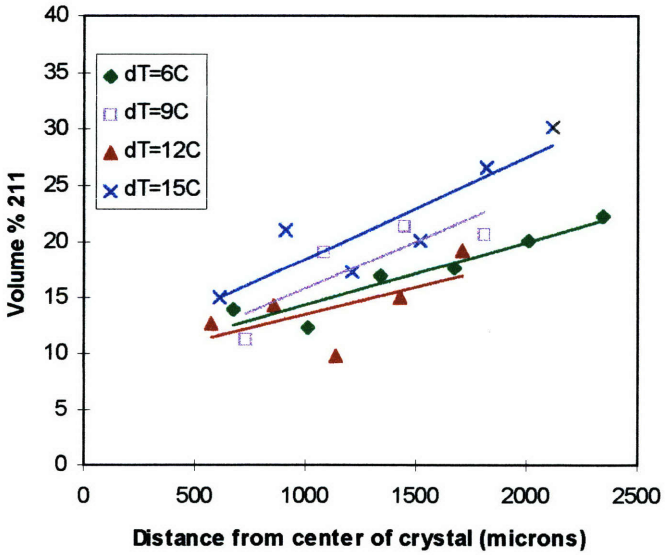

Figure 7.9. Volume fraction of 211 particles vs. distance along the c-axis within 123 crystals produced at various undercoolings.

a)

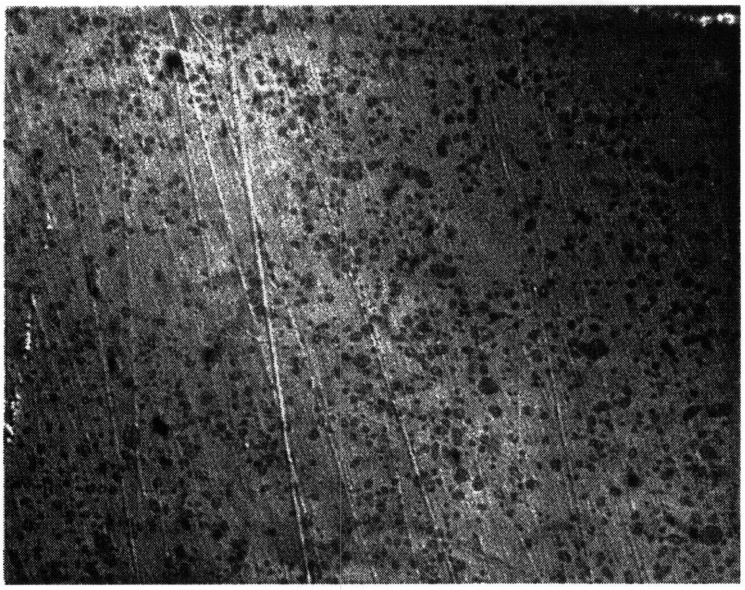

10 μm

b)

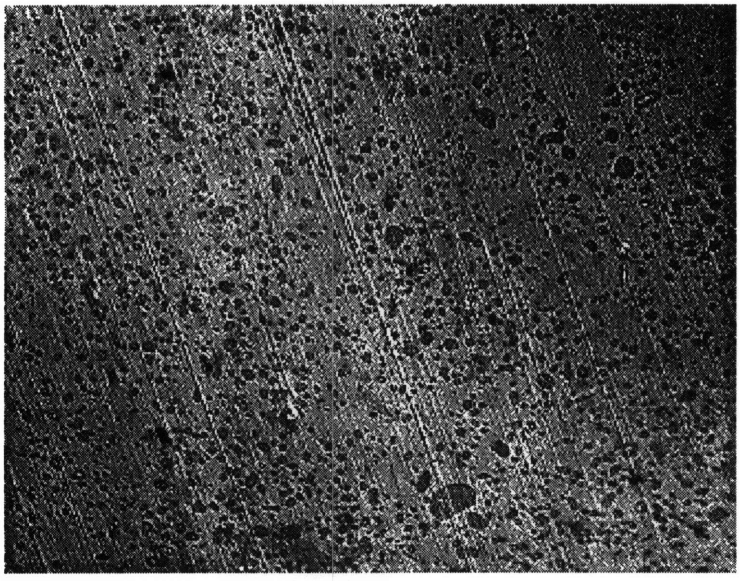

10 μm

Figure 7.10. Optical micrographs of 211 particles trapped within the 123 crystal for an excess 211 sample produced at an undercooling of 6°C. Photo a) was taken at point 0_{ab} (shown in figure 7.6). Photo b) was taken at point X_{ab}.

a)

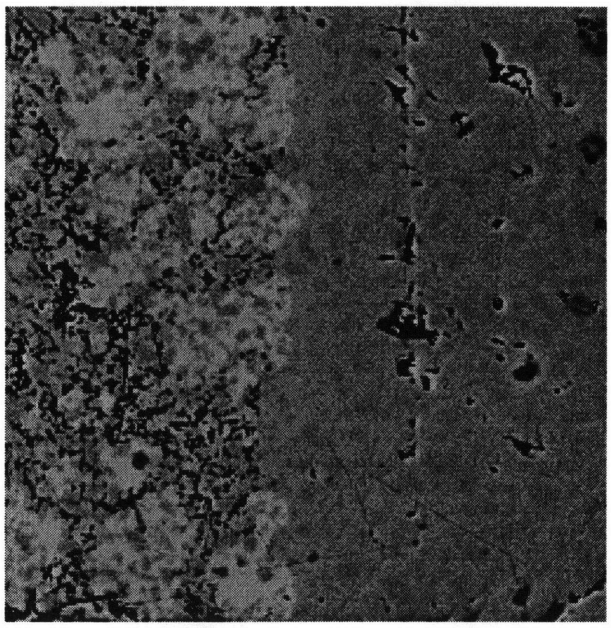

20 μm

b)

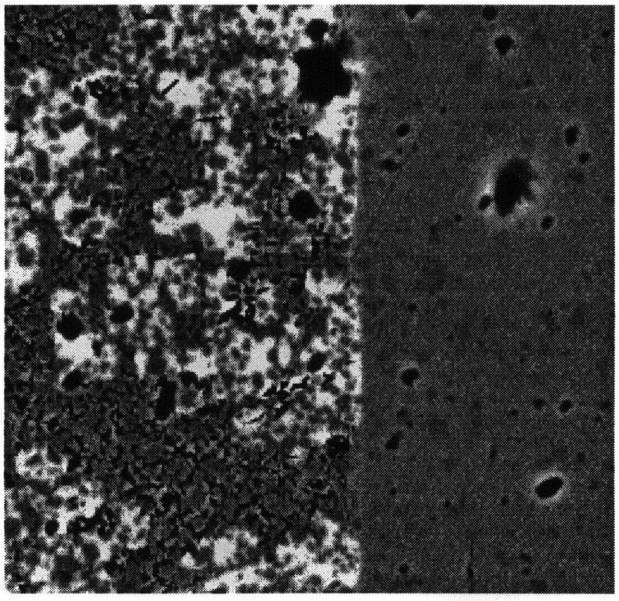

20 μm

Figure 7.11. SEM micrographs of typical 123 / semi-solid liquid interfaces for the a) ab-face and b) c-face of the 123 crystal. It can be seen that no region of pushed particles is evident in front of either interface.

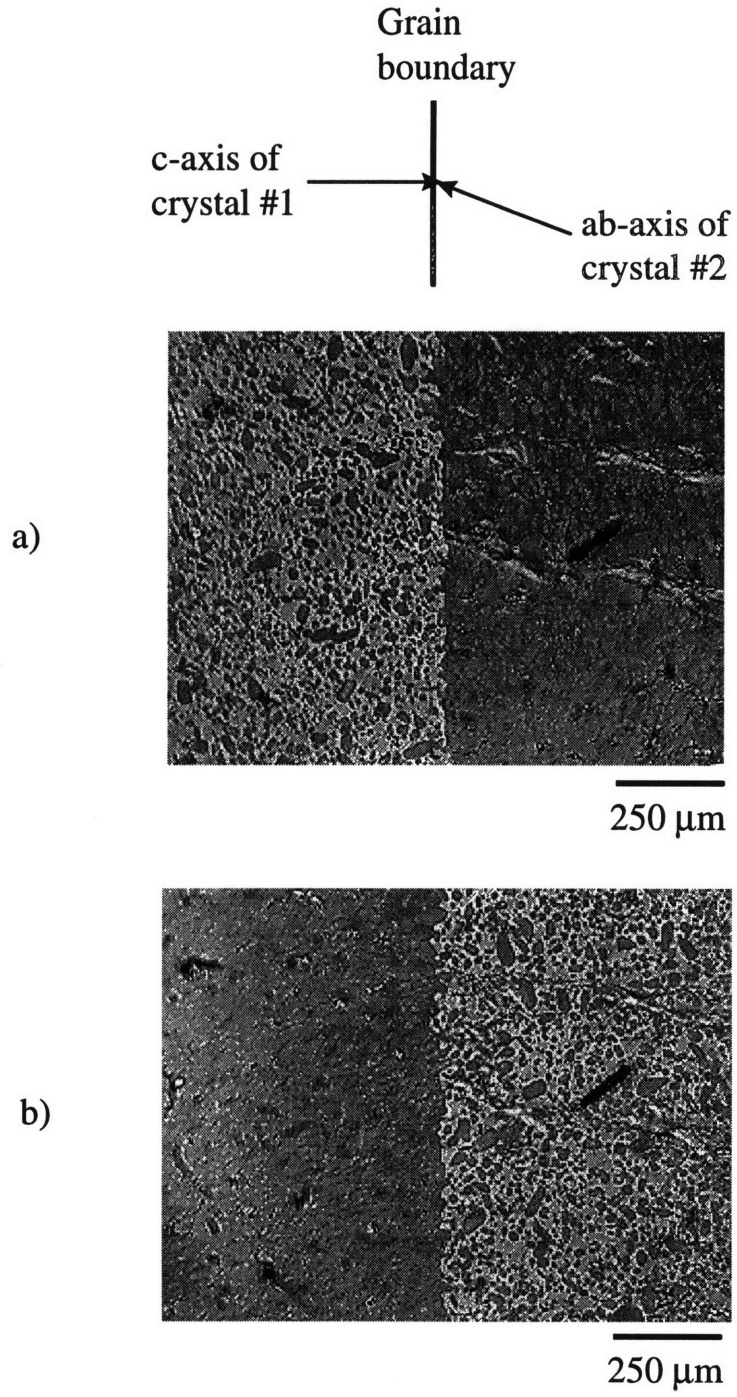

Figure 7.12. Cross-polarized optical micrographs of the same grain boundary within an unquenched excess 211 sample grown at an undercooling of 12 °C. It can be seen that no layer of pushed 211 particles is present at the grain boundary in either grain.

a)

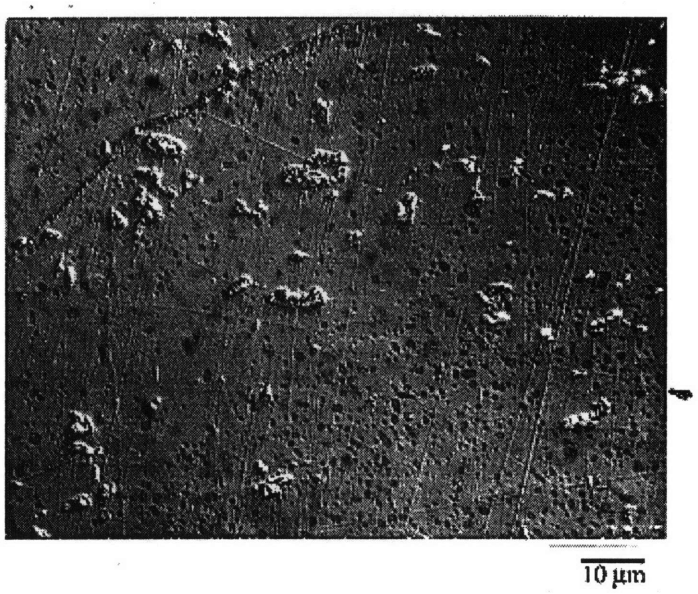

b)

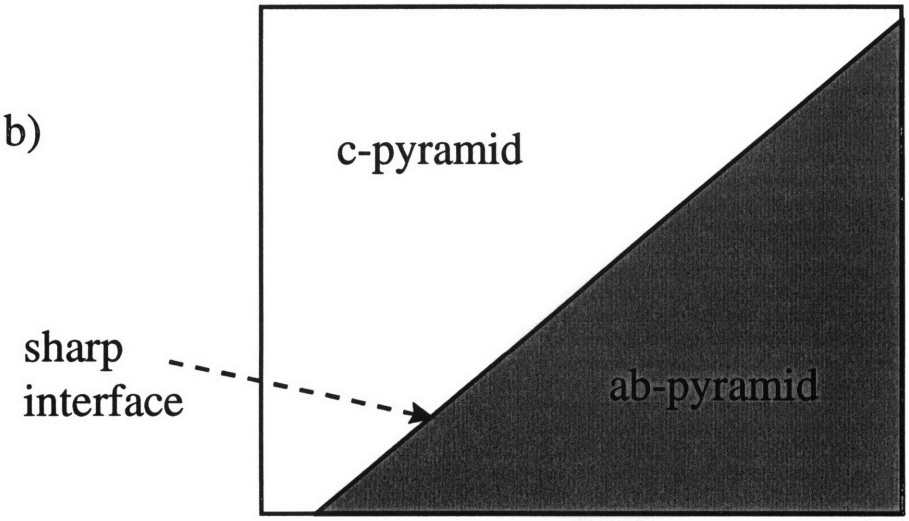

Figure 7.13. a) Optical micrograph and b) schematic of the interface between the ab-pyramid and c-pyramid in a typical excess 211 crystal. It can be seen that the interface between regions of high 211 particle volume fraction and low 211 particle volume fraction is very sharp.

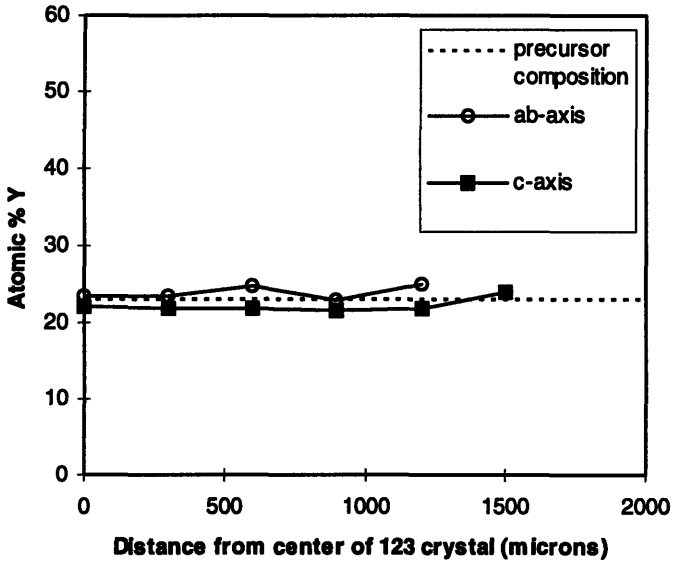

Figure 7.14. Yttrium concentration along the ab- and c-axes of an excess 211 crystal solidified at an undercooling of 12 °C compared with the yttrium concentration in the precursor pellet.

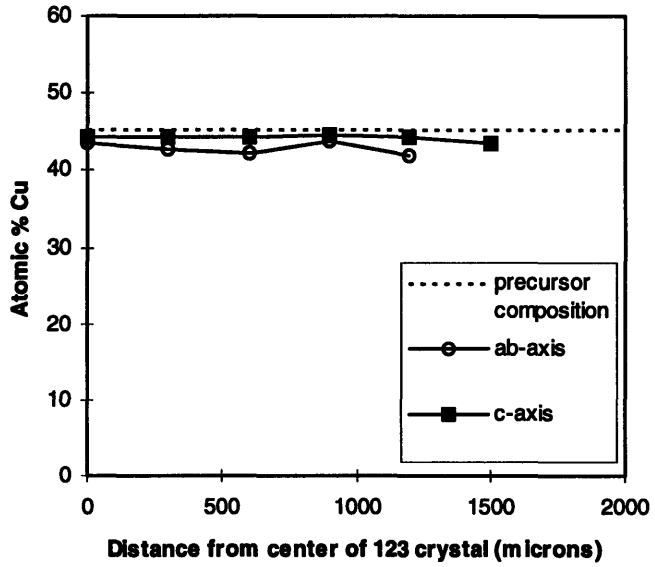

Figure 7.15. Copper concentration along the ab- and c-axes of an excess 211 crystal solidified at an undercooling of 12 °C compared with the copper concentration in the precursor pellet.

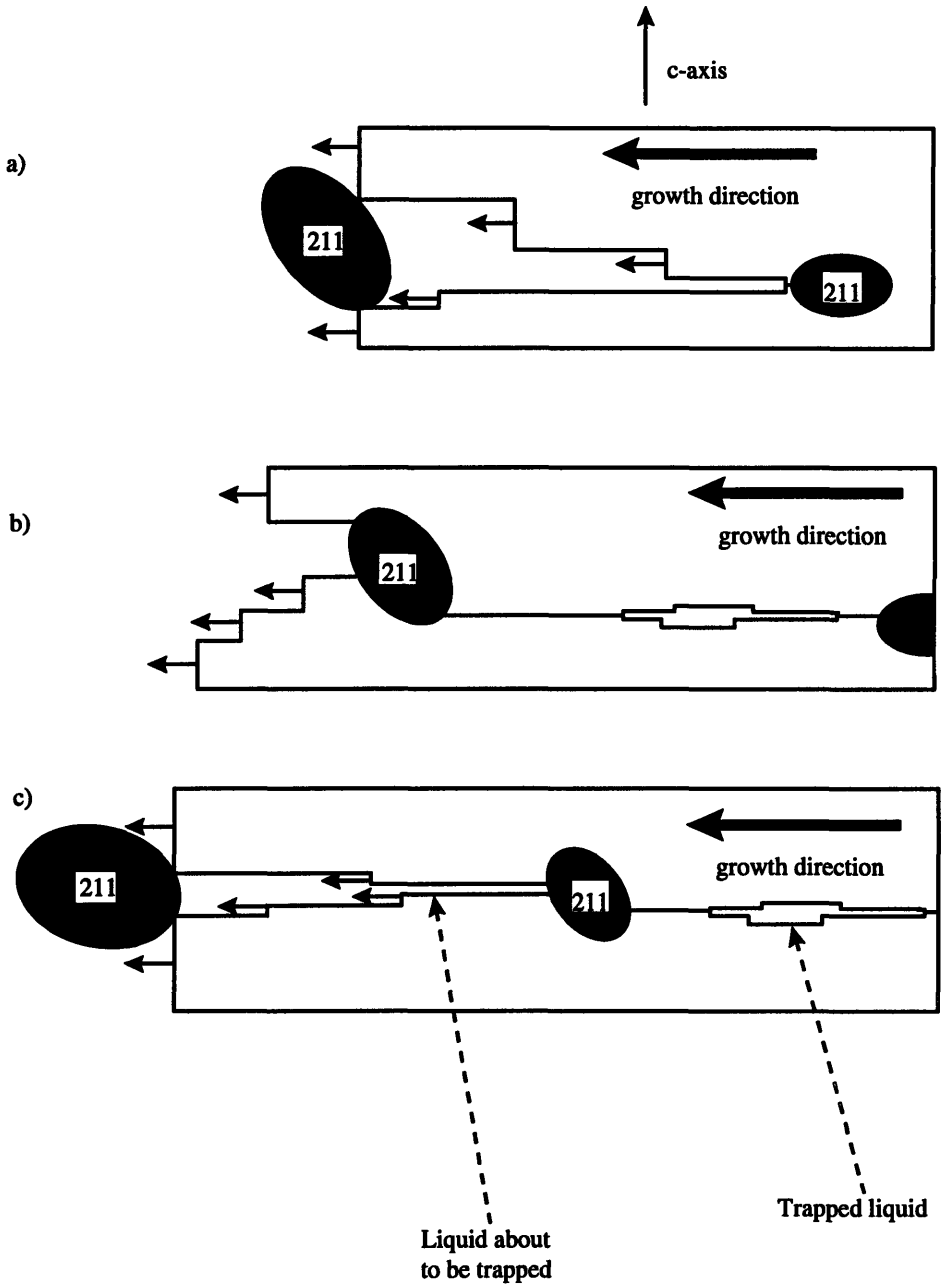

Figure 7.16 Schematic showing the process by which barium cuprate liquid is trapped behind 211 particles. Figure a) shows the asymmetric intersection of a 123 platelet gap at the growth front with a 211 particle in the semi-solid melt. Figure b) shows how liquid within the platelet gap can be trapped by a second 211 particle intersecting the 123 interface. This particle can, in turn, produce another platelet gap and trap more liquid, shown in figure c).[82]

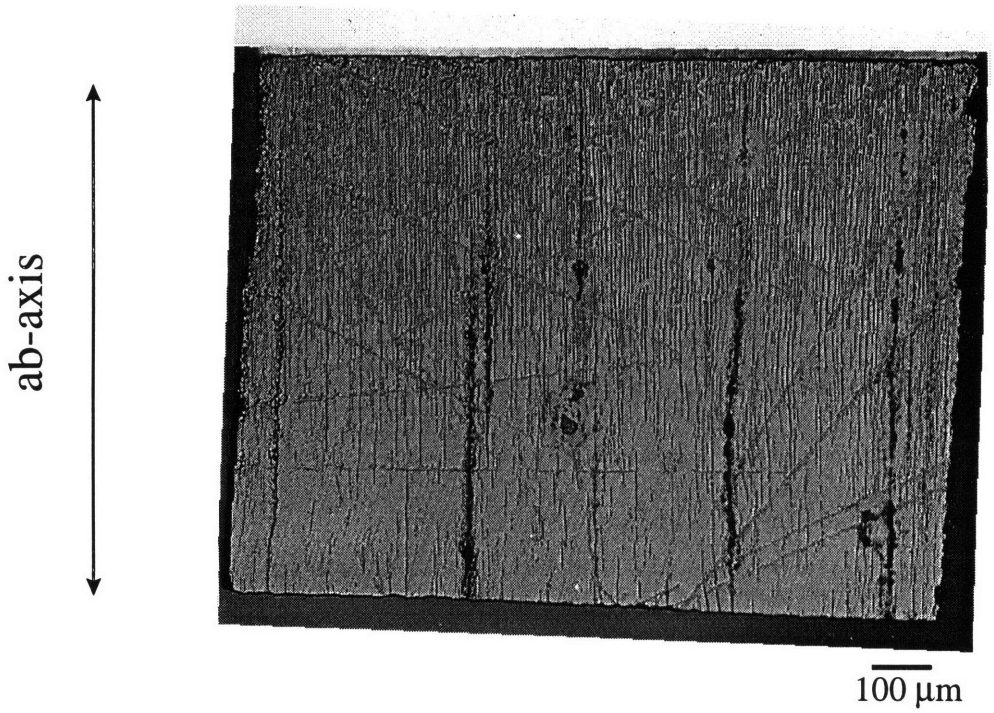

Figure 7.17. Optical micrograph (taken by T. H. Sung) of an ion milled seeded growth sample containing segregated 211 particles. The dark lines in the micrograph are platelet gaps.

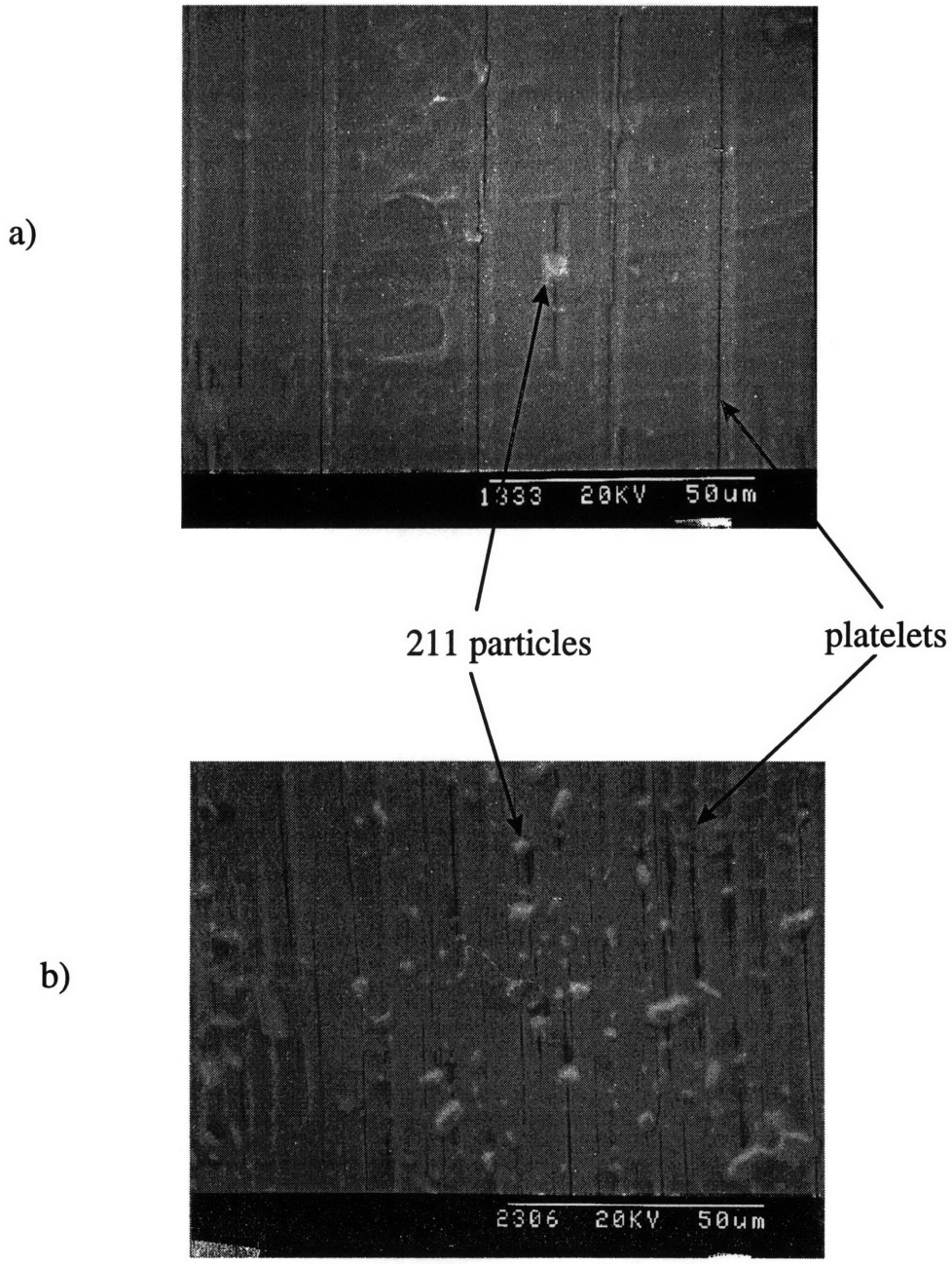

Figure 7.18. SEM micrographs (taken by T. H. Sung) of two different regions of an ion milled YBCO single crystal sample produced by seeded growth. Figure a) shows a low concentration of 123 platelet gaps in a low 211 density region of the crystal. Figure b) shows a high concentration of 123 platelet gaps in a high 211 density region of the crystal.

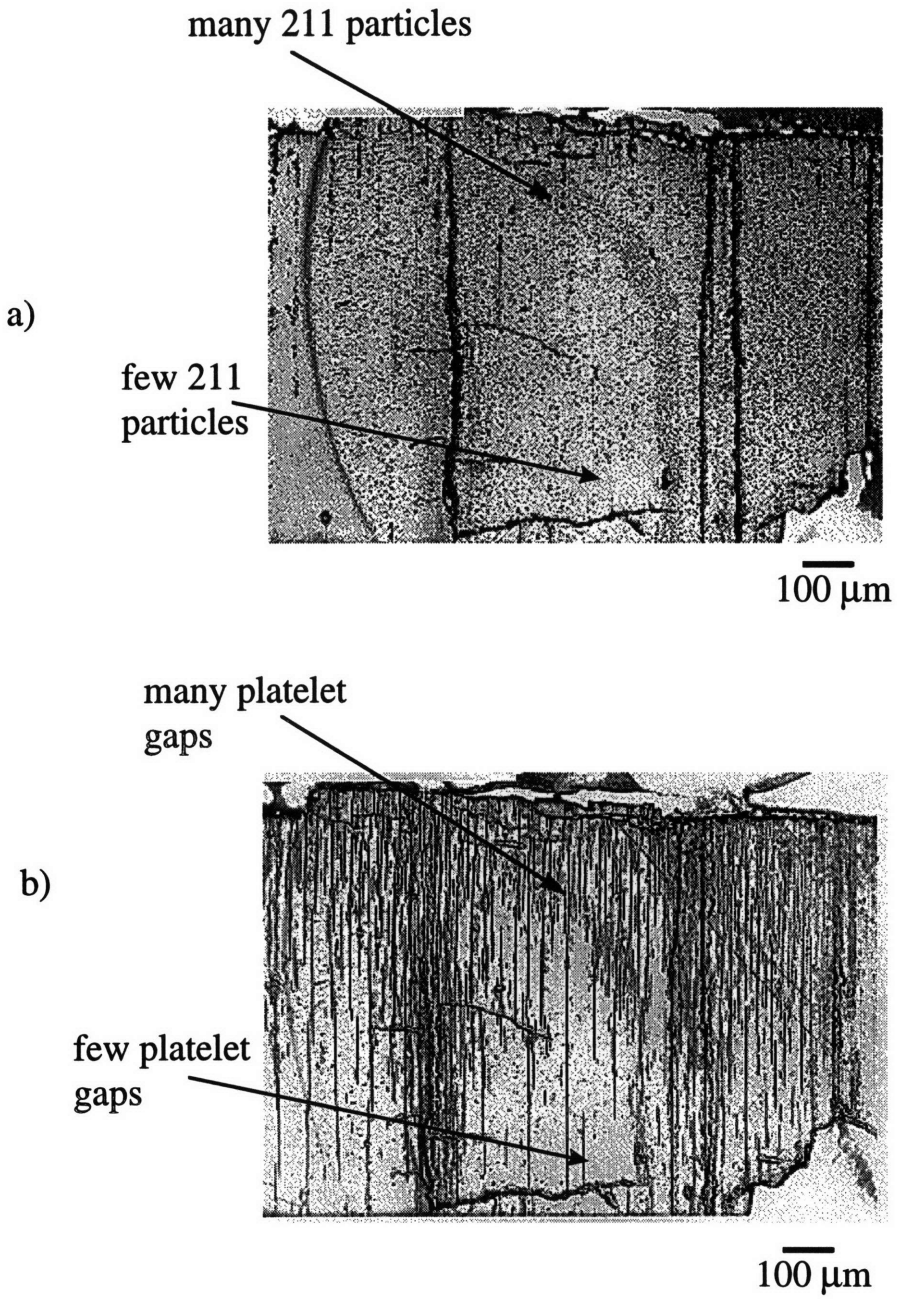

Figure 7.19. Optical micrographs (taken by T. H. Sung) of the same region of a 123 single crystal produced by seeded growth. The photo in figure a) was taken after 1 h of ion milling. The photo in figure b) was taken after 100 h of ion milling.

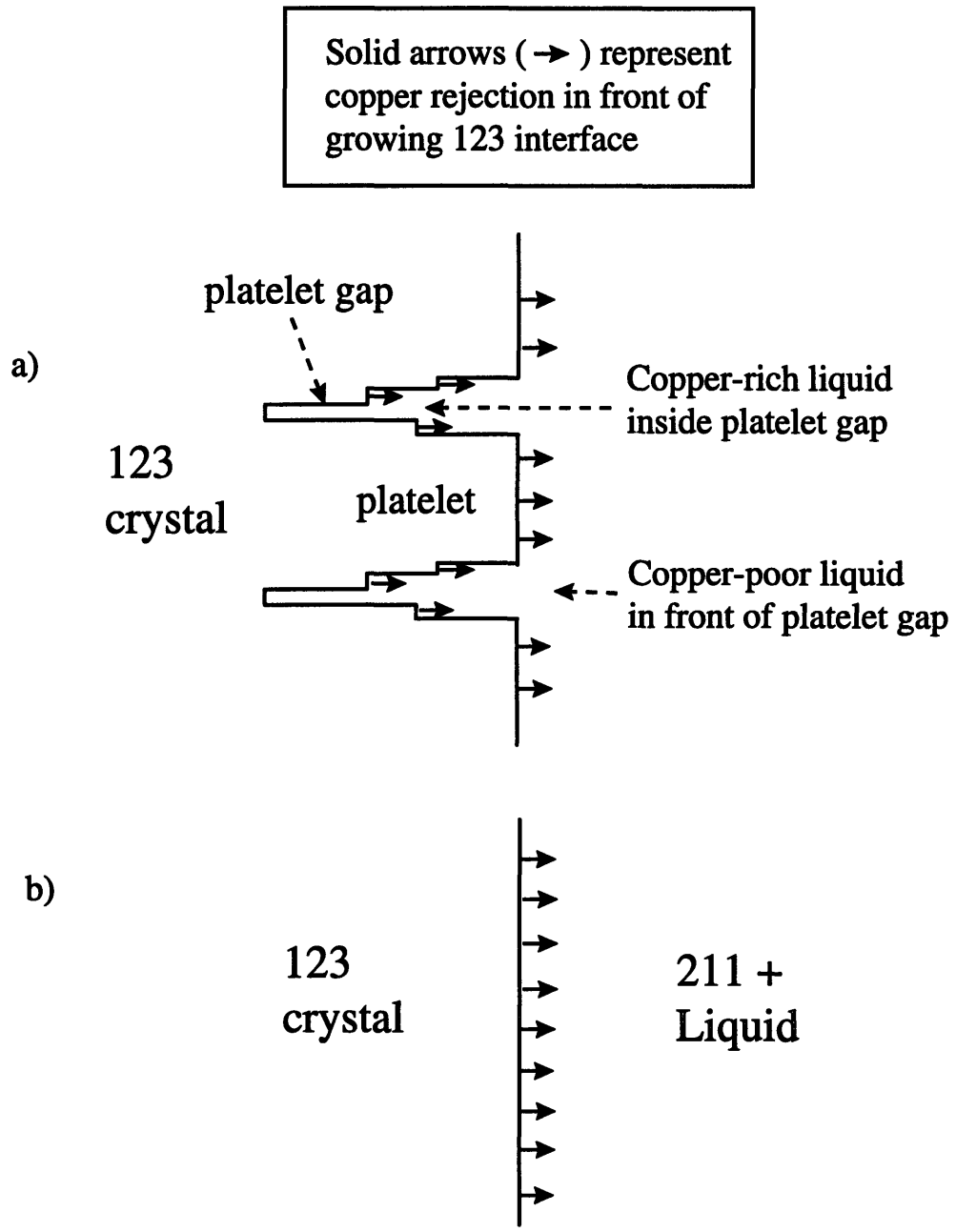

Figure 7.20. Schematic of copper rejection in front of a) an interface composed of platelets and b) a flat interface. The liquid inside the platelet gaps is copper rich (yttrium poor) relative to the liquid in front of a flat interface. The liquid in front of the platelet gaps is copper poor (yttrium rich) relative to the liquid in front of a flat interface.

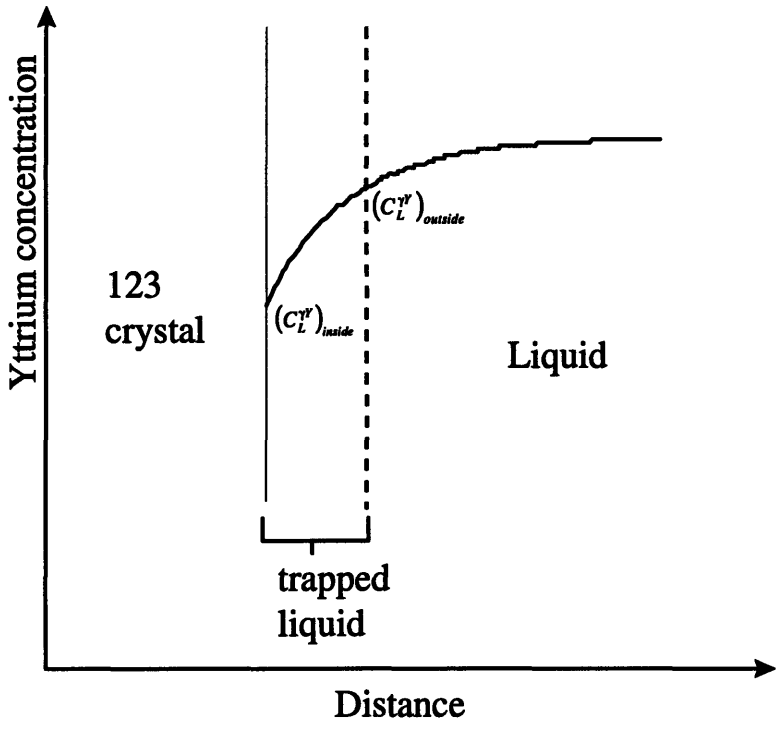

Figure 7.21. Schematic of the yttrium concentration profile in front of an interface composed of platelets. The high yttrium concentration in front of the platelet gap, $(C_L^{Y})_{outside}$, results in decreased 211 particle dissolution in these regions.

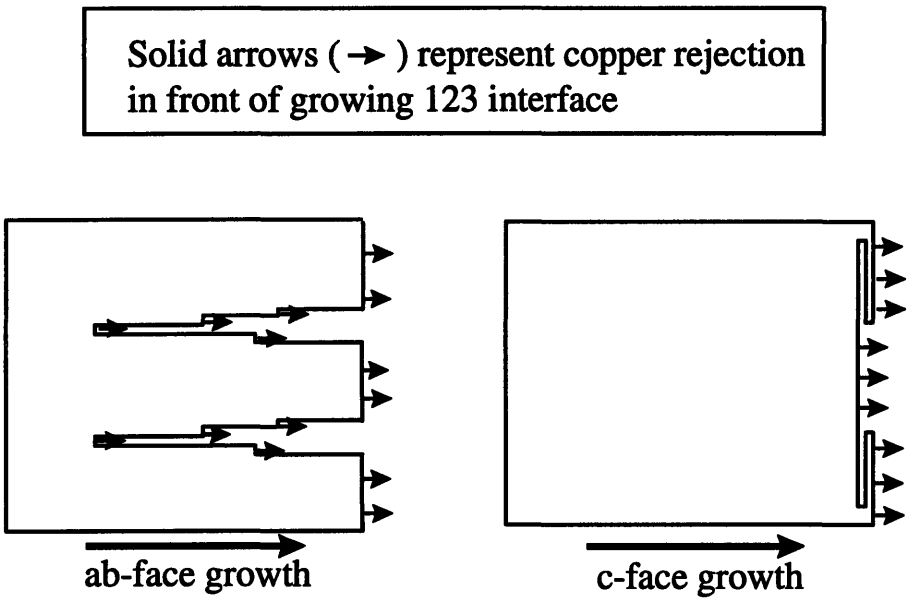

Figure 7.22. Schematic of platelet structure at the ab-face and c-face of a growing crystal. Structural differences cause the copper concentration in the liquid to be lower in front of the ab-face than in front of the c-face. The yttrium concentration is therefore higher in front of the ab-face than in front of the c-face.

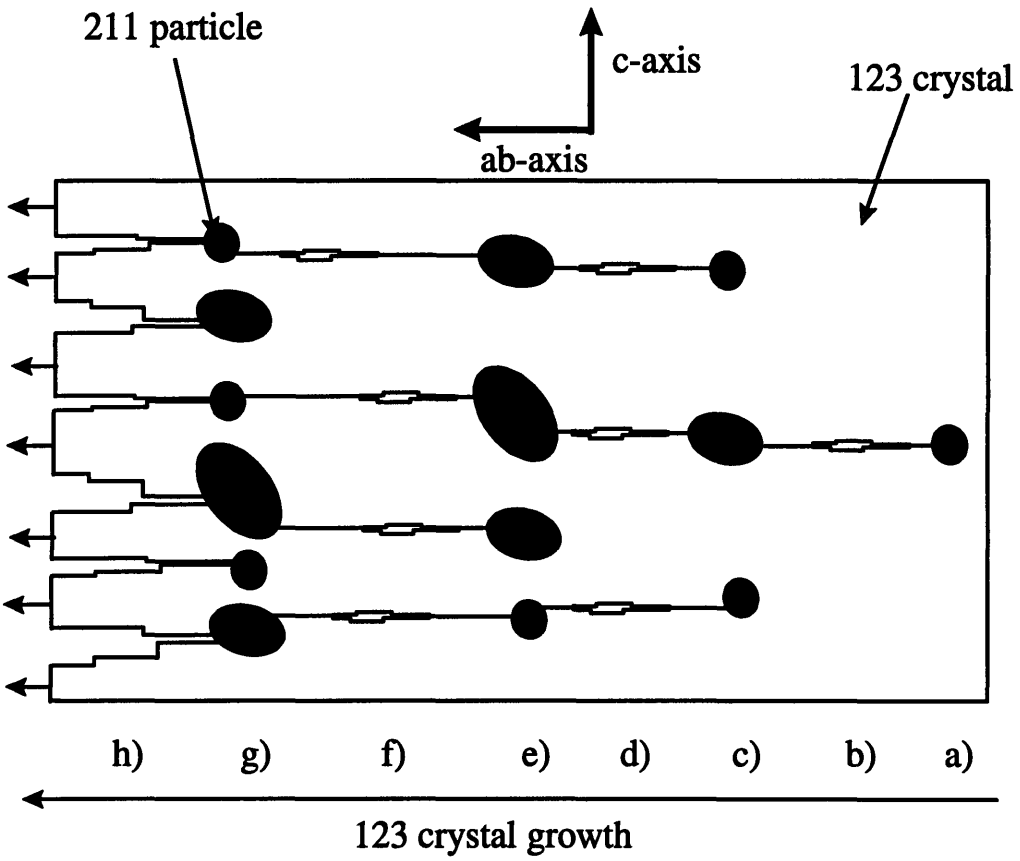

Figure 7.23. Schematic of 211 particle segregation and barium cuprate liquid entrapment in excess 211 samples. 211 particles impinging on the 123 crystal at point a) are trapped and form a trapped liquid region at point b). This trapped liquid reduces the 211 particle dissolution in front of the 123 interface resulting in an increase in trapped particles at point c). These particles cause the formation of platelets which trap liquid at point d). This cycle repeats itself along points e) through h).

Chapter 8

The effect of oxygen annealing on the structure and critical current density of bulk YBCO single crystals

8.1. Introduction

Results presented in chapter 4 show that LHFZ growth can produce large YBCO single crystals. As discussed in chapter 2, most applications of HTSC materials also demand that the critical current density of the material is as high as possible. Many researchers believe that critical current densities in YBCO single crystals can be enhanced through the introduction of flux pinning centers. It has been theorized that microstructural defects within the YBCO crystals can act as flux pinning centers, as discussed in chapter 2. Many observations by other researchers have linked the presence of enhanced flux pinning in YBCO materials to the presence of 211 particles within a single crystal or textured material.[23,88,94-99] Murakami and others used the uniform distribution of very fine 211 particles to significantly enhance J_c values in YBCO materials.[23,94-95] 211 particles are too large to act as flux pinning centers directly, as described in section 2.3.2. Murakami et al. proposed that the interface between the 211 particles and the 123 matrix acts as a pinning center.[94] Wang et al.[100] and Yamaguchi et al.[101] suggested that the stacking faults around the 211 inclusions act as pinning centers.

It has also been found that the 211 inclusions are associated with the presence of the second phase layers. The presence of barium cuprate second phase layers between 123 platelets formed perpendicular to the c-face of the 123 crystal is common in melt-textured YBCO materials.[20,44,68,76,82,87,102,124-125,144-145] The formation of this platelet structure is discussed in chapter 2. Jin et al. has shown that the spacing between the platelets in 123

systems containing 211 inclusions is a strong function of the number of 211 inclusions.[102]

Oxygenation at elevated temperatures has also been shown to increase the superconducting properties of YBCO materials. This is due to the formation of the high T_c superconducting orthorhombic phase from the tetragonal phase with increased oxygenation.[30,146-148] Recent research has shown that defects which may act as flux pinning centers are introduced during annealing in oxygen.[31,149] Sung et al.[31] correlated the formation of these defects with the presence of 211 particles and barium cuprate layers between platelets.

Ahou et al.[149] have reported that the 123 phase is not a thermodynamically stable phase at room temperature. The 123 phase decomposes by reaction 8.1 to form the 124, 211 and $BaCuO_2$ phases during low temperature annealing.[149]

$$YBa_2Cu_3O_{6.76}(s) \rightarrow 1/2\ YBa_2Cu_4O_8(s) + 1/4\ Y_2BaCuO_5(s) + 3/4\ BaCuO_{2.01}(s) \qquad (8.1)$$

The slow kinetics of this reaction at room temperature make the 123 phase metastable.[149] The 124 crystal structure is equivalent to the 123 crystal structure with additional copper and oxygen atoms arranged as shown in figure 8.1.[150] Research by Sung et al.[31] has shown that intergrowth of extra copper-oxygen planes form in the YBCO materials during low temperature annealing.[31] The presence of such intergrowth layers have been confirmed by a number of researchers.[44] These planes of copper-oxygen intergrowth take the form of single 124 stacking faults (among other types of stacking faults) along the ab-axis of the material (see figure 8.2). TEM photos by T. H. Sung[31] of LHFZ fibers show that this reaction occurs near 211 particles and barium cuprate second phase layers(see figure 8.3). Sung et al.[31] suggested that the 211 particles and barium cuprate layers act as a sink for the 211 phase and barium cuprate phase produced by reaction 8.1. Murikami et al. have suggested that oxygen diffusion

rate is larger around the 211 particles.[95] Enhanced oxygen diffusion near the 211 interface will enhance the intergrowth reaction in these regions as well.

A series of experiments were therefore performed to evaluate the effect of sample oxygenation times on crystal structure, flux pinning and critical current density of YBCO materials.

8.2. Experimental procedure

J_c values of single crystal YBCO samples produced by LHFZ growth and annealed in oxygen for various lengths of time were evaluated using SQUID magnetometry. Sample preparation, oxygen annealing, four-circle X-ray analysis and J_c analysis using SQUID magnetometry and Bean's model are presented in this section.

8.2.1. Sample preparation and annealing

YBCO single crystal samples produced by laser heated floating zone growth were prepared for critical current density measurements and structural evaluation using four-circle X-ray diffraction. LHFZ single crystal fibers composed of 80 wt.% 123 phase and 20 wt.% 211 phase solidified at 1cm/h were sectioned into lengths of approximately 4 mm. The diameter of the fibers was approximately 250 μm. Samples were annealed in flowing oxygen at 480 °C for various amounts of time to evaluate the effects of oxygen annealing time on critical current density. Table 8.1 contains details of all single crystals prepared for J_c evaluation.

Label	Sample number	Annealing time
L(A)	L55	10 h
L(B)	L55	40 h
L(C)	L55	100 h
L(D)	L55	200 h
L(E)	L33	10 h
L(F)	L33	100 h
L(G)	L33	200 h

Table 8.1. Details of samples produced for J_c measurements and structural analysis.

8.2.2. SQUID magnetometry

Single crystal samples annealed for various lengths of time were analyzed using a DC SQUID magnetometer (Quantum Design, MPMS). A magnetic field is applied to a superconducting sample by the SQUID magnetometer, which induces a supercurrent to flow in the sample. The flowing supercurrent in turn sets up an internal magnetic field large enough to exactly cancel the applied magnetic field. The induced magnetic field can be measured and converted to critical current density values using Bean's critical state model (see section 8.2.3.). As discussed in chapter 2, critical current densities of YBCO samples vary significantly with the direction of the applied field.[11-12,25,27,56-58] Figure 8.4 from Figueredo[11-12] shows the dependence of magnetization vs. angle for similar fibers produced by LHFZ growth. Maximum magnetization measurements are obtained when the c-axis of the crystal is oriented perpendicular to the applied magnetic field. LHFZ samples grow with the fiber axis parallel to the ab-axis of the 123 crystal. Visual examination of the fiber provides no information about the orientation of the c-axis relative to the fiber radius. Magnetization measurements must therefore be

performed on the fiber for several rotation angles to determine the position of the c-axis (as shown in figure 8.4). Magnetization vs. magnetic field can then be evaluated with the c-axis oriented perpendicular to the applied field.

8.2.3. J_c evaluation using the Bean critical state model

Magnetization hysteresis loops such as the one shown in figure 8.5 were obtained for samples analyzed using SQUID magnetometry. The magnetic hysteresis values were then converted to critical current densities using the Bean critical state model.[151] The Bean critical state model assumes that when a superconducting sample is immersed in a magnetic field, a supercurrent is set up within a certain penetration depth which is just large enough to reduce the internal local field to 0. The critical current density within the penetration depth is then proportional to the induced magnetization of the sample divided by the penetration depth. The penetration depth into the sample increases as the applied magnetic field increases. The critical current density within the entire sample will be proportional to the induced magnetization divided by the sample size if the magnetic field is large enough to penetrate through the entire sample. This assumption allows critical current densities to be calculated from the induced magnetization measurements obtained using SQUID magnetometry.[54,151] J_c is related to magnetization by equation 8.2 for cylindrical samples.

$$J_c = \frac{30\Delta M}{d} \qquad \text{for a cylinder} \tag{8.2}$$

where ΔM is the hysteresis width of the induced magnetic field and d is the diameter of the cylinder. Equation 8.2 was used to calculate J_c values for cylindrical single crystal fibers produced by LHFZ growth.

8.2.4. Structure analysis using four-circle X-ray diffractometry

Single crystal samples produced by LHFZ growth and annealed for various lengths of time in flowing oxygen at 500 °C were examined using four-circle X-ray diffractometry. The basic procedure for sample preparation, alignment and analysis using four-circle X-ray diffractometry is described in chapter 4. The (006) peaks of the annealed LHFZ samples were scanned in order to examine how the c-axis lattice parameter changed with annealing time.

8.3. Results and discussion

The following sections detail the results of J_c measurements and four-circle X-ray diffraction analysis of 123 single crystal fibers produced by LHFZ growth and annealed in oxygen for various lengths of time. Variations in J_c and crystal structure with increased annealing times are related to the introduction of copper-oxygen intergrowth layers formed via the decomposition of the 123 phase during oxygen annealing.

8.3.1. J_c dependence on annealing time

Figure 8.6 shows the results of J_c analysis by SQUID magnetometry for 123 single crystal samples produced by LHFZ growth and annealed at 500 °C in flowing oxygen for various lengths of time. All samples came from the same single crystal fiber. Difference in superconducting properties are therefore a result of post growth processing. It can be seen that the sample annealed for 10 hours has the largest amount of deterioration in J_c with increasing applied field. The sample annealed at for 100 h has a smaller dependence of J_c on applied field. The 200 h sample shows the highest critical current densities at fields above 2 Tesla. All LHFZ samples have J_c values of at least $1x10^5$ A/cm^2 and the sample annealed for 100 hours has a J_c of more than $2x10^5$ A/cm^2. These values are

equal to or better than the highest critical current densities obtained for unradiated bulk YBCO samples (see figure 2.7).

It is theorized that the intergrowth of extra copper-oxygen planes within the annealed YBCO single crystals produced by LHFZ growth acts as pinning centers to increase critical current densities at high applied fields. This is supported by the J_c data shown in figure 8.6. The sample annealed for 10 h has the lowest J_c values at high applied fields. Flux pinning is therefore lower in this sample. J_c values at high applied fields increases with oxygen annealing for 100 h and 200 h. Flux pinning is therefore stronger in these samples. This trend supports the theory by Sung et al.[31] that copper-oxygen intergrowth formed during oxygen annealing enhances flux pinning and therefore, critical current densities at high fields, in YBCO materials.

8.3.2. Variations in 123 crystal structure with annealing time

The volume fraction of 124 phase and other intergrowth produced during annealing of the YBCO fibers was too low to detect using powder or four-circle X-ray diffraction. Significant flux pinning can be induced in YBCO materials with volume fractions of intergrowth significantly below the detection limit of X-ray diffractometry. The effects of oxygen annealing on the c-axis lattice parameter can be observed using four-circle X-ray diffraction, however. Figure 8.7 shows the results of four-circle X-ray diffraction analysis of the (006) peaks of the 123 phase for samples annealed at 500 °C in flowing oxygen for various lengths of time. The intensities of the (006) peaks have been normalized with respect to each other. It can be seen that the (006) peak position shifts to higher values of 2Θ with increased oxygen annealing time. Figure 8.8 shows the change in c-axis lattice parameter with oxygen annealing time calculated from the peak positions shown in figure 8.7. It can be seen that the c-axis lattice parameter increases with oxygenation time. As discussed in chapter 2, the c-axis lattice parameter for $YBa_2Cu_3O_{6.91}$, the oxygenated

orthorhombic phase, is c = 11.82 Å. The c-axis lattice parameter for $YBa_2Cu_3O_{6.06}$, the oxygen deficient tetragonal phase, is c = 11.82 Å.[51] Jorgensen et al.[146] calculated the change in the 123 c-axis lattice parameter with oxygen content. Their results are shown in figure 8.9. It can be seen that the c-axis lattice parameter of pure 123 decreases with increasing oxygen addition. This does not correlate with the data taken from the annealed 123 single crystal fibers examined in this study. The results of c-axis lattice parameter measurements shown in figure 8.8 show that the c-axis of the 123 crystals expands with increased annealing time. It is concluded that the change in c-axis lattice parameter of the annealed superconducting material with increasing oxygenation is not due to increased oxygen content, but rather due to increased stacking faults in the annealed material. These results, as well as the J_c measurements and the theories proposed by Sung et al.[31] and Ahou et al.,[149] all support each other. It is therefore concluded that flux pinning and critical current densities in single crystal YBCO materials can be increased with annealing in oxygen.

8.4. Conclusions

It was shown that YBCO single crystals produced by LHFZ growth exhibit critical current densities of more than $2x10^5$ A/cm^2 at 0 T and 77 K. This value is near the current maximum observed J_c for non-irradiated YBCO bulk single crystals (see figure 2.7). It was also shown that oxygen annealing increases magnetic flux pinning in 123 single crystals at high applied fields. It is concluded that oxygen annealing introduces flux pinning centers into the superconducting material via the decomposition of the 123 phase to form 124 intergrowth and other stacking faults, according to the theories proposed by Sung et al.[31] and Ahou et al.[149] Analysis of the 123 crystal structure using four-circle X-ray diffraction shows that the 123 lattice expands with increasing annealing, which is consistent with the introduction of stacking faults along the ab-planes of the 123 structure.

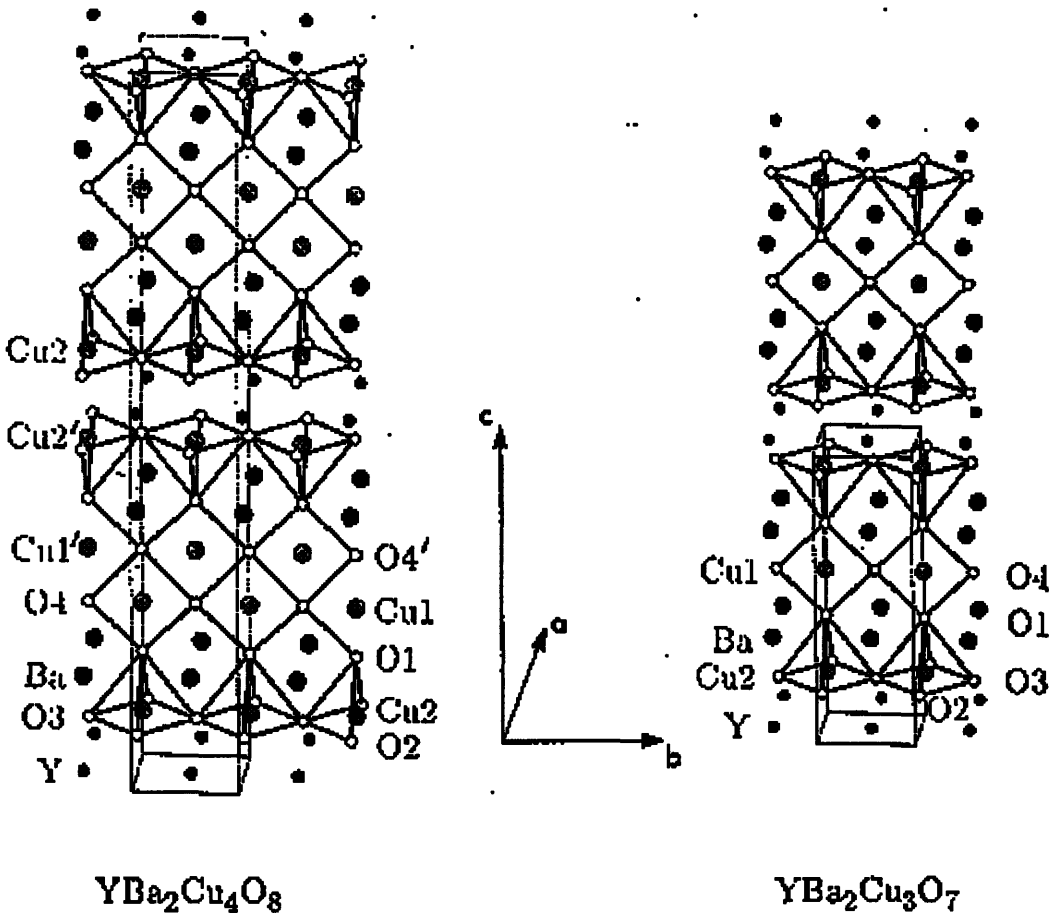

Figure 8.1. Comparison of the crystal structures of the 123 and 124 phase.[150]

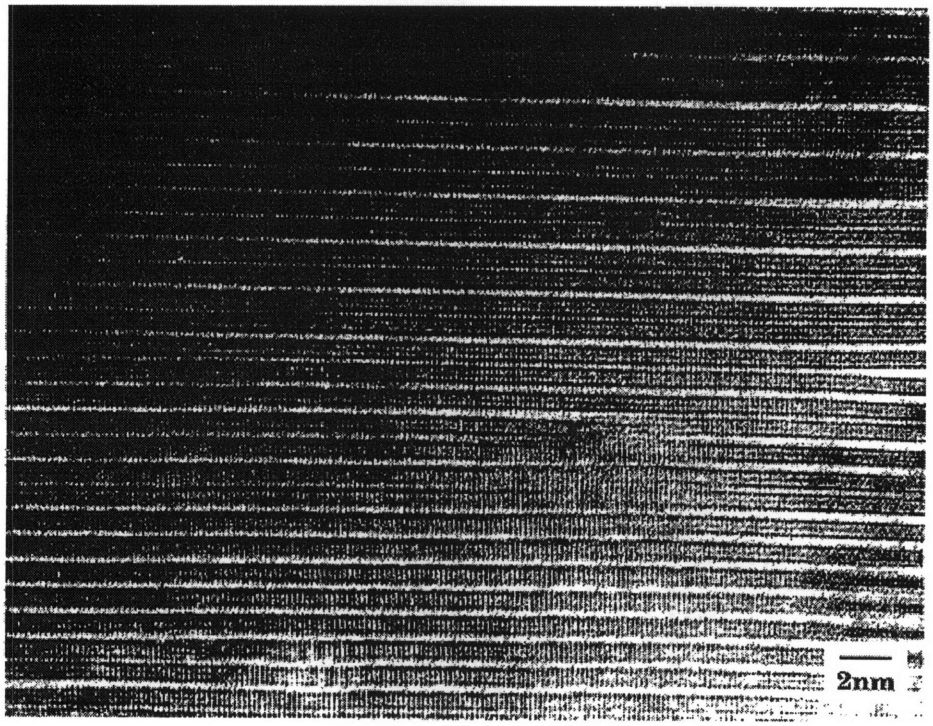

Figure 8.2. TEM micrograph (taken by T. H. Sung) of an annealed LHFZ sample viewed perpendicular to the c-axis showing the presence of stacking faults in the form of extra copper oxide planes.

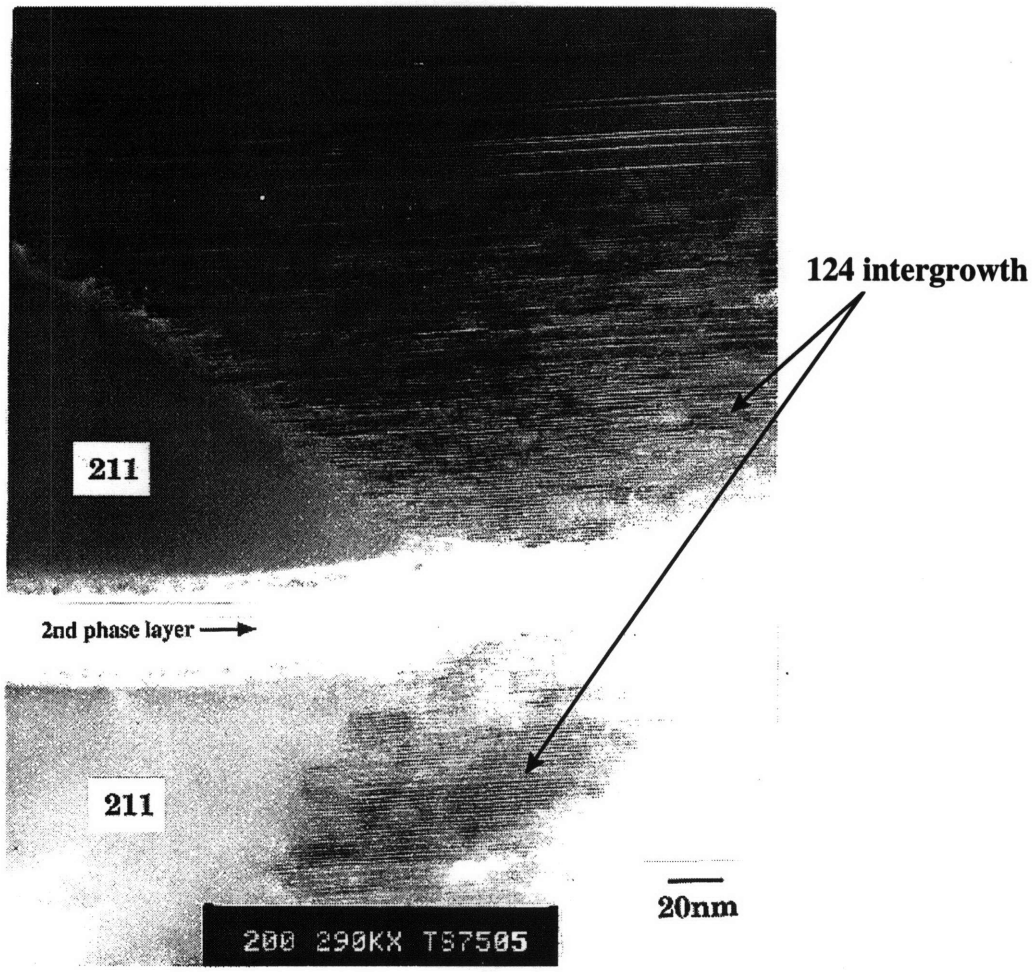

Figure 8.3. TEM micrograph (taken by T. H. Sung) of an annealed LHFZ sample viewed perpendicular to the c-axis. 124 intergrowth can be seen near the 211 particle and barium cuprate second phase layer.

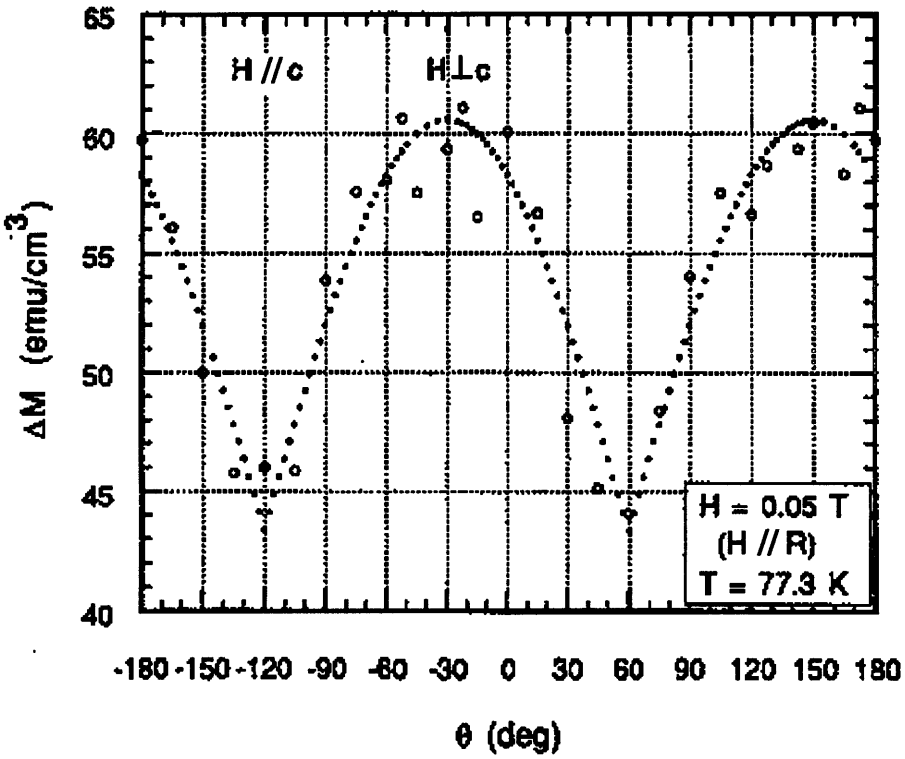

Figure 8.4. The dependence of magnetization vs. angle for LHFZ single crystals.[11-12]

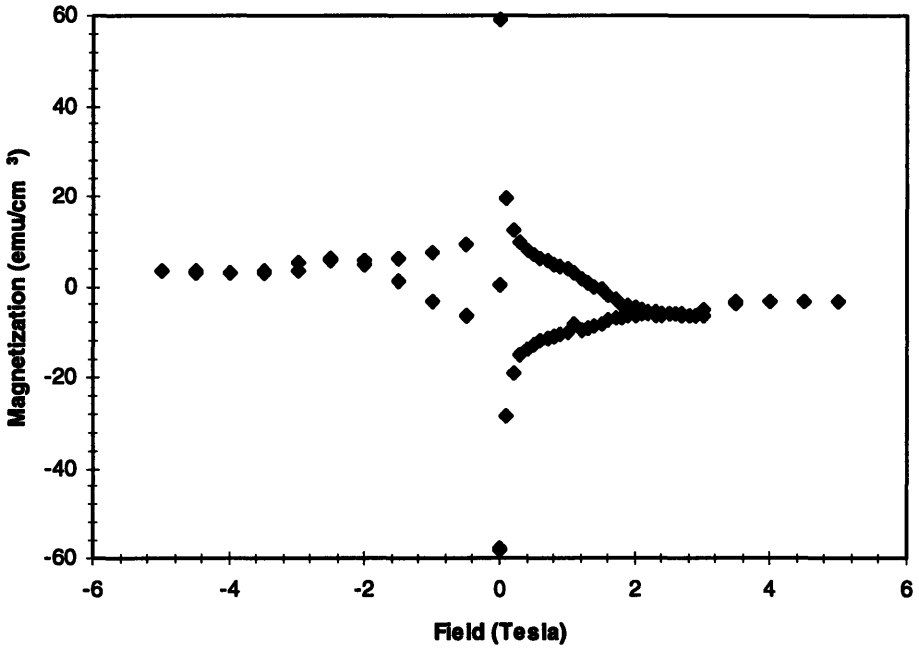

Figure 8.5. Magnetic hysteresis loop obtained by SQUID magnetometry for LHFZ sample L55 annealed for 200 h.

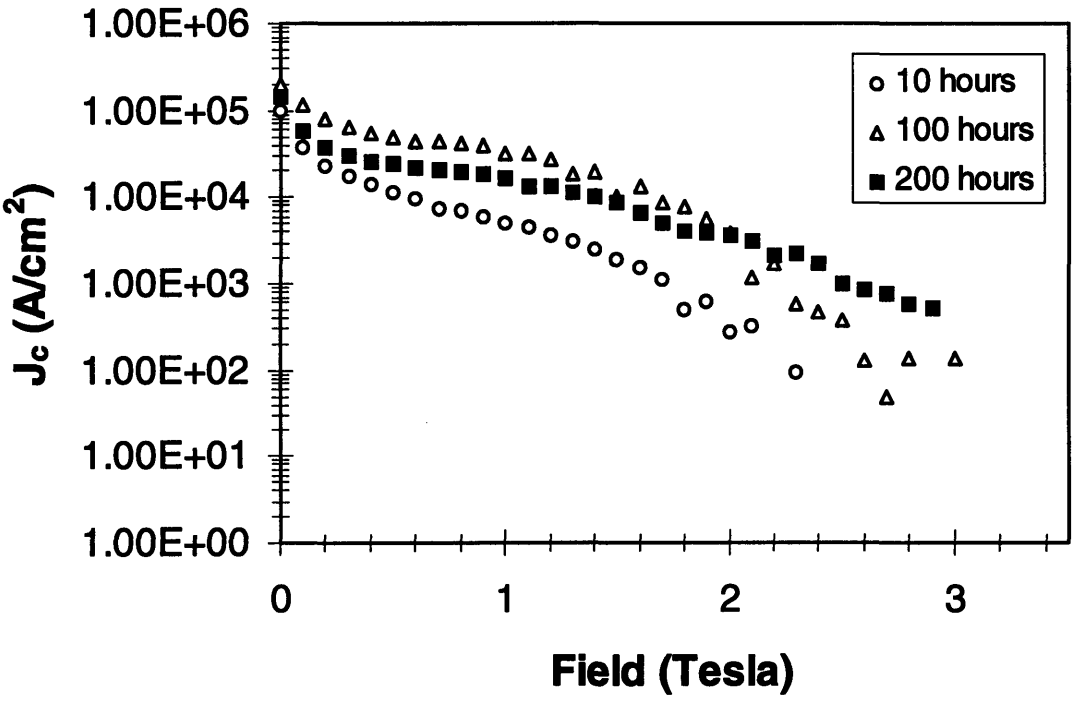

Figure 8.6. J_c vs. applied field for LHFZ samples annealed for various amounts of time.

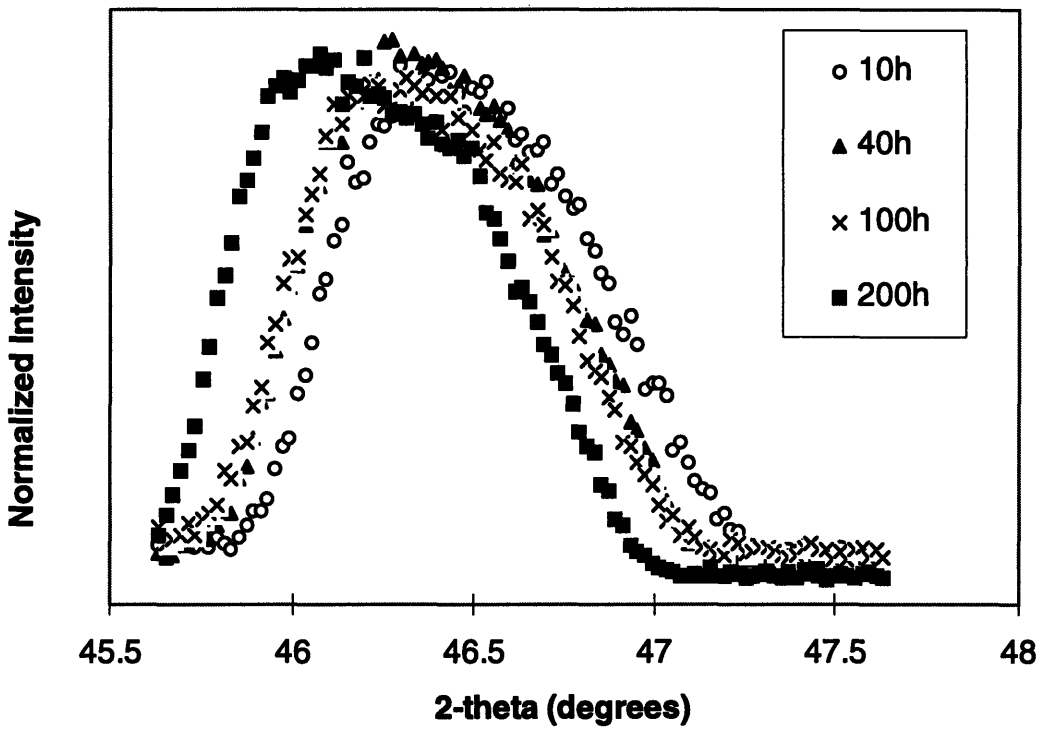

Figure 8.7. Four circle X-ray diffraction data showing 123 (006) peak shifts taking place during oxygen annealing.

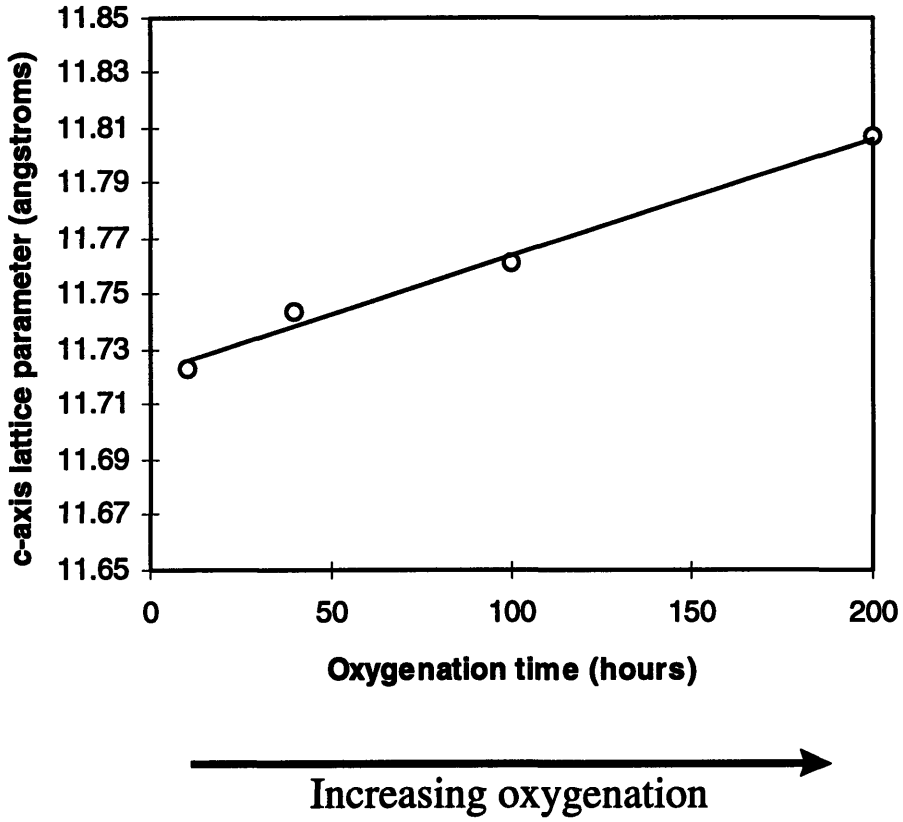

Figure 8.8. Changes in c-axis lattice parameter of the 123 phase taking place during oxygen annealing.

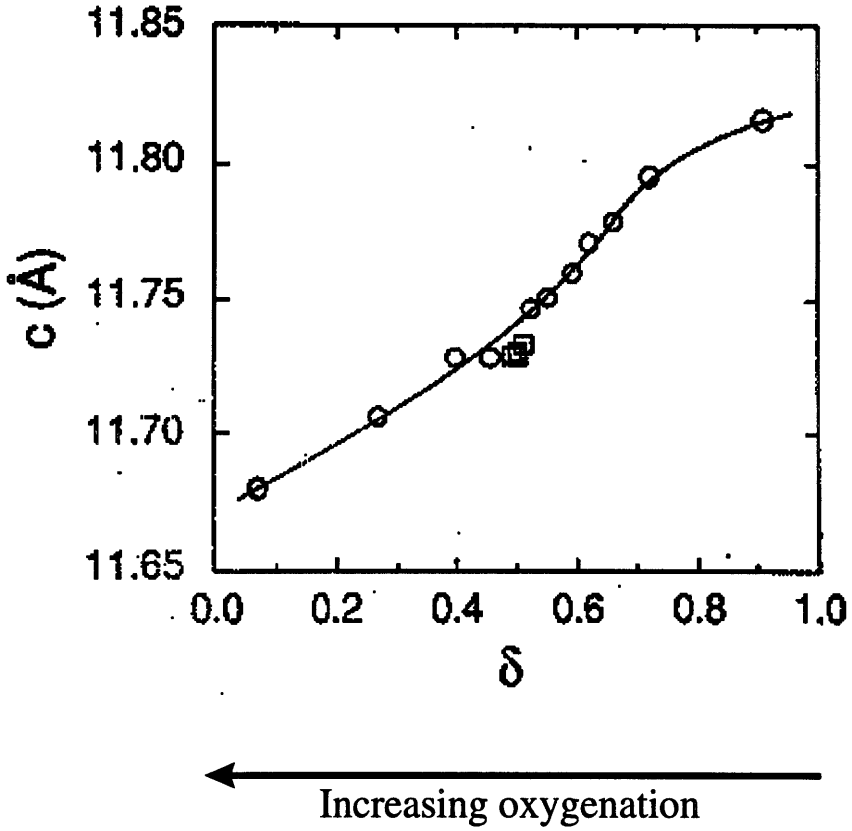

Figure 8.9. Decrease in 123 c-axis lattice parameter due to changes in 123 crystal structure with the incorporation of additional oxygen atoms.[149]

Chapter 9

Conclusions and future work

9.1. Conclusions

The work presented here has dealt with improving and understanding single crystal growth, microstructural development and properties of melt-processed YBCO high temperature superconductors. A number of new results and theories were presented in the areas of single crystal production using LHFZ growth and seeded growth, 211 particle segregation in stoichiometric and excess 211 YBCO materials, coarsening of 211 particle in the semi-solid melt and current transport properties of the superconducting materials.

YBCO single crystals in lengths of more than 5 cm were grown reproducibly through the optimization of the precursor fiber production and the LHFZ growth process. The maximum length of 123 single crystals produced by the user-operated LHFZ growth process was found to be limited by the slow growth rate of YBCO materials as well as the problem of secondary grain nucleation. The maximum growth rate below which single crystal growth takes place was confirmed to be between 1 and 2 cm/h. The 123 single crystal interface deteriorates at growth rates above these values. A model describing secondary nucleation in YBCO fibers was proposed based on 123 crystal orientation results obtained by four-circle X-ray diffraction. This model suggests that perfectly oriented single crystals can be obtained by using longer processing times, resulting in much longer sections of 123 single crystals.

YBCO single crystals produced by LHFZ growth exhibit critical current densities of more than 2×10^5 A/cm^2 at 0 T and 77 K. This value is near the current maximum observed J_c

for non- irradiated YBCO bulk single crystals. It was also shown that oxygen annealing increases magnetic flux pinning in 123 single crystals at high applied fields. It is theorized that oxygen annealing introduces flux pinning centers into the superconducting material via the decomposition of the 123 phase to form 124 intergrowth and other stacking faults, according to the theories proposed by Sung et al.[31] and Ahou et al.[149] Analysis of the 123 crystal structure using four-circle X-ray diffraction shows that the 123 lattice expands with increasing annealing, which is consistent with the introduction of stacking faults along the ab-planes of the 123 structure.

It was shown that growth rate of 123 crystals produced by seeded growth is dependent on undercooling, ΔT, and 211 particle spacing. Growth rates increased with increasing undercooling. The addition of excess 211 phase and platinum dopant decreased the 211 particle spacing and increased the growth rate of the 123 crystals. These results support the 123 solidification model proposed by Cima et al.[33] 123 crystal habit was shown to be similar to that predicted by PBC analysis. The presence of the (001), (100)/(010) and (110) 123 crystal faces were shown in samples produced by seeded growth. The presence of spiral growth hillocks on the ab-faces and hopper morphologies on the c-faces of the 123 crystals were shown. The presence of these growth mechanisms are in agreement with PBC theory which states that F faces of faceted crystals grow by two dimensional growth mechanisms. It was shown that differences in the relationship between growth rate, R, and undercooling, ΔT, for the different growth mechanisms of 123 single crystals can account for the fact that the c-face is the fast growth face at low undercoolings while the ab-face is the fast growth face at high undercoolings.

It was shown that 211 segregation in stoichiometric 123 samples is not a result of particle pushing. Finite element models and calculations presented here show that that the entrapment of particles in stoichiometric 123 samples produced by melt growth is a result of differences in 211 particle dissolution rates in front of the 123 crystal face compared to the edge and corner. Large 211 particles in front of the edge and corner of a 123 crystal

do not dissolve completely if the particle dissolution rate is lower than the growth rate of the 123 crystal. Larger particles are trapped by the corners than by the edges of the 123 crystal. The critical entrapment size of 211 particles varies according to 211 particle orientation relative to the edge and corner of the 123 crystal. Particles incorporated at the corners and edges of 123 crystals during melt growth form planes of 211 particles which appear as "X" tracks and other patterns when the 123 crystal is sectioned in various directions. This theory of particle segregation is valid for all growth mechanisms.

211 particle segregation within 123 crystals formed from excess 211 precursors was examined and quantified. It was shown that 211 particle entrapment is greater along the ab-axis than along the c-axis of the 123 crystal. 211 particle entrapment increases with growth distance from the center of the 123 crystal. A number of 211 particle segregation theories were investigated in order to explain this phenomenon. It was found that variation in 211 dissolution rates in front of the ab and c faces of the 123 crystal is the only 211 segregation mechanism which explains all of the data produced in this investigation and found in the literature. It was shown that it is unlikely that 211 particle segregation in excess 211 samples occurs as a result of particle pushing, differences in 211/123 wetting angle or differences in lattice mismatch between 211 particles and the different faces of the 123 crystal. A theory involving barium cuprate liquid entrapment during 123 crystal growth was proposed as a driving force for differences in 211 dissolution rates in front of the ab and c faces of the 123 crystal. This liquid entrapment theory can explain all of the data produced in this investigation and found in the literature. It can also explain why bulk 211 segregation in this form is only observed in excess 211 samples.

It was shown that the use of Er-211 is a good way of "labeling" the initial 211 phase present during coarsening. It was found that excess 211 particles added to the 123 phase act as nucleation sites for additional 211 phase formed via the peritectic decomposition of 123 at temperatures above 1000 °C. 211 particles formed via homogeneous nucleation

and growth in samples composed of 100 % 123 phase were found to be larger than particles formed via heterogeneous nucleation in excess 211 samples. Quantitative evaluation of 211 particle growth with time was also performed and the results agree with expected coarsening relationships. Results show that the addition of a platinum dopant as well as the addition of excess 211 particles is an effective means of keeping 211 particle size as low as possible during the processing of YBCO materials. k, the coarsening rate constant, was found to be 3.0×10^{-19} m^3/s for undoped samples and 1.7×10^{-20} m^3/s for Pt-doped samples. It was found that the interfacial energy of 211 particles in barium cuprate liquid decreases with the addition of a platinum dopant. It was concluded that the decreased coarsening rate in platinum doped samples results from this decrease in interfacial energy. It was found that platinum powder added as a dopant does not act as a nucleation site for 211 particles.

9.2. Future work

The research presented here raised a number of questions which have yet to be answered and which were beyond the scope of this work. It was shown in chapter 5 that the vertical ab-face of 123 crystals produced by seeded growth grows much more slowly than the ab-axis of the crystal oriented parallel to the surface of the precursor pellet. It was also shown that the ratio of c-axis to ab-axis growth rates is much larger for crystals produced by seeded growth compared to those produced by flux growth. The cause for these phenomena is not yet understood. One possible cause may be differences in oxygen content at the surface of the YBCO melt and within the melt. The surface of the 123 crystal produced by seeded growth is in contact with the air atmosphere in the furnace while the bottom of the 123 crystal is not. The ab-axis growing parallel to the surface of the YBCO precursor pellet therefore grows in the presence of a larger oxygen concentration than the ab-axis growing perpendicular to the surface of the melt. Crystals

grown by flux growth also commonly grow within an oxygen depleted melt. The decreased ratio of c-axis to ab-axis growth rate in flux grown crystals may also be related to this decrease in oxygen content. PBC analysis of the 123 crystal structure by Sun et al.[123] showed that oxygen concentration plays a significant role in the crystal habit of 123 materials. Future work should include an examination of differences in oxygen concentration on the surface of the YBCO melt and within the melt to determine whether oxygen concentration affects the crystal habit of the 123 crystal during melt growth. Solution of this problem will allow much thicker YBCO single crystals to be produced by seeded growth.

Chapter 7 showed that 211 particle segregation in excess 211 YBCO crystals produced by melt growth results from differences in 211 particle dissolution rates in front of the ab and c faces of the 123 crystal. It was shown that decreased 211 particle dissolution in front of the 123 crystal faces is due to barium cuprate liquid entrapment within the platelet structure of the 123 crystal. 123 platelets are known to form parallel to the ab-axes of the 123 crystal and perpendicular to the c-axis. This preferred platelet orientation makes platelet formation easier at the ab-faces of the 123 crystal than at the c-faces. Future work in this area should be aimed at determining the exact difference in platelet formation kinetics at the different 123 faces. Platelet geometry and the link between platelet formation and the quantity and composition of the trapped barium cuprate liquid should also be investigated. Greater knowledge of platelet formation and liquid trapping could lead to the development of processes to reduce 211 segregation in excess 211 materials.

YBCO single crystals were produced using LHFZ processing. Single crystal fiber length was limited to less than 10 cm due to the slow growth rate of YBCO materials as well as the problem of secondary grain nucleation. The LHFZ growth system is currently a user-controlled process which requires continual monitoring and adjusting of beam position and zone temperature. This limits the maximum growth period to less than 1 day. It has

been shown that this is not enough time to grow a single crystal with perfect orientation due to secondary grain nucleation. Continuous monitoring and feedback of beam position and temperature using a computerized LHFZ system, CCD camera and pyrometer will allow the maximum processing time to be significantly increased. The maximum growth time will then be limited by the length of the crystal growing chamber and the length of the sintered polycrystalline YBCO feed rods which can be produced. Future work in the area of LHFZ growth of YBCO materials should include the use of such an automatic monitoring system which will allow much longer periods of growth. Long sections of single crystal fibers without grain boundaries could be produced in this manner. The use of long, high quality polycrystalline precursor fibers with no pores or surface imperfections is also critical for automated growth of long single crystals by LHFZ growth.

Appendix A
PDEase®[134] program for particle dissolution in Cartesian coordinates

Title

"Dissolved Y concentration in front of 123 crystal"

Select

errlim = 0.001 {error limit}

Variables

u(range=0,10000) {moles/m3} {yttrium concentration, C_L^Y }

Definitions

dC=300 {ΔC}

Cinit = 1000 {moles/m^3} {yttrium concentration in the liquid far away from the 123 interface, $C_L^{\infty Y}$ }

Cface=Cinit-dC {yttrium concentration in the liquid in contact with the growing 123 interface, C_L^{YY} }

a=.5e-6 {particle radius}

l=5*a {distance between particle and 123 crystal}

tf=.1 {profile generation time}

D = 6e-11 {m2/s} { diffusivity }

edge1=10e-6+l {position of edge of 211 particle in front of face}

cent1=10e-6+l+a {position of center of 211 particle in front of face}

edge2=10e-6+(l/1.414) {position of edge of 211 particle in front of corner}

cent2=10e-6+((l+a)/1.414) {position of center of 211 particle in front of corner}

flux=D*grad(u) {flux of yttrium away from dissolving 211 particle}

Initial Values

u = Cinit {moles/m3} {yttrium concentration in the liquid far away from the 123 interface, $C_L^{\infty Y}$ }

Equations

div(D*grad(u)) = dt(u) {Fick's second law - generates yttrium profile}

Boundaries

{region 1: semi-solid zone}

start(10e-6,-6e-6)

line to (40e-6,-6e-6)

arc (center=-6e-6,-6e-6) to (-6e-6,40e-6)

line to (-6e-6,10e-6)

value(u)=Cface

line to (10e-6,10e-6)

finish

{region 2: 211 particle in front of corner}

exclude

value(u) = Cinit

start "corner" (edge2,edge2)

arc (center=cent2,cent2) angle=-360

finish

{region 3: 211 particle in front of face}

exclude

value(u) = Cinit

start "face" (edge1,0)

arc (center=cent1,0) angle=-360

finish

Time

0 to tf

Plots

for t=endtime

contour(u) as "Y concentration"

contour(u) as "Expanded Y concentration (moles/m3)"
zoom (-6e-6,-6e-6,30e-6,30e-6)

elevation (u) from (10e-6,0) to (40e-6,0) as " Y concentration away from face (moles/m3)" print*

elevation (u) from (10e-6,10e-6) to (30e-6,30e-6) as " Y concentration away from corner (moles/m3)" print*

elevation(magnitude(flux)) on "face" as "Y flux away from particle in front of face" print*

elevation(magnitude(flux)) on "corner" as "Y flux away from particle in front of face" print*

End

Appendix B
PDEase®[134] program for particle dissolution in cylindrical coordinates

```
Title

    "Dissolved Y concentration in front of 123 crystal"

Select

    errlim = 0.001

Coordinates

    xcylinder("z","r")

Variables

    u(range=0,1000) {moles/m3}

Definitions

    dC=300
    Cinit = 1000 {moles/m3}

    Cface=Cinit-dC
    a=.5e-6
    q=5e-6
    l=5*a
    g=a+q
    b=l-a
    tf=.1
    n=9*a
    w=2*a
    e=9.1*a
    rate = 2e-7 {m/s}
    D = 6e-11 {m2/s}          { diffusivity }


    flux2=D*grad(u)
    dV=(magnitude(flux2))*.000074
```

```
Initial Values

        u = Cinit {moles/m3}
Equations
        div(D*grad(u)) = dt(u)


Boundaries
        region 1
                value(u)=Cface
                start(0,-n)
                line to (0,n)
                natural(u)=0
                line to(-a,n)
                line to(-a,e)
                line to(3*e,e)
                line to (3*e,-e)
                line to(-a,-e)
                line to(-a,-n)
                finish

        exclude
                value(u)=Cinit
                start "particle" (g,a)
                arc (center=g,0) angle=180
                line to (l+a+q,-a)
                arc (center=l+a+q,0) angle=180
                line to(a+q+l/2,a)
                finish

Time

        0 to tf by .1

Plots

        for t=endtime

        contour(u) as "Y concentration"

        elevation(dV) on "particle" as "Y flux away from particle in front of face" print*

End
```

References

1. M. A. Omar, *Elementary Solid State Physics: Principles and Applications*, Adison Wesley, Philippines, 1975.

2. D. Robins, *Introduction to Superconductivity*, IBC Technical Services Ltd., London, 1989.

3. C. P. Poole, Jr., T. Datta, H. A. Farach, *Copper Oxide Superconductors*, Wiley and Sons, Toronto, 1988.

4. M. K. Wu, J. R. Ashburn, C. J. Torng, P. H. Hor, R. L. Meng, L. Gau, Z. J. Huang, Y. Q. Wang and C. W. Chu, Phys Rev. Lett. **58** 908 (1997).

5. S. Honjo and T. Hara, Proceedings of the US-Japan Workshop on high T_c superconductors, K. Salama (ed), 1993, p. 53.

6. F. C. Moon, Nature, **350** 270 (28 March 1991).

7. Z. J. J. Stekly and E. Gregory, in *High Temperature Superconducting Materials Science and Engineering: New Concepts and Technology*, D. Shi (ed), Pergammon, New York, 1994, p. 441.

8. T. Hara, K. Okaniwa and T. Yammamoto, Internal report of the Tokyo Electric Power Company.

9. K. Salama, A. S. Parikh and L. Woolf, Appl. Phys. Lett. **68** 1993 (1996).

10. T. Izumi, Y. Nakamura and Y. Shiohara, J. Mater. Res., **7** 1621 (1992).

11. A. M. Figueredo, Ph.D. Thesis, MIT, 1993.

12. A. M. Figueredo, M. J. Cima, M. C. Flemings, J. S. Haggerty, T. Hara, H. Ishii, T. Ohkuma and S. Hirano, Physica C 241 **92** (1995).

13. Y. A. Jee, S.-J. L. Kang, J. H. Suh and D. Y. Yoon, J. Am. Ceram. Soc. **76** 2701 (1993).

14. W. Ruikun, R. Hongtao, X. Ling, H. Qing, W. Chaoqun and Y. Dingan, Supercond. Sci. Technol. **3** 344 (1990).

15. P. J. McGinn, in *High Temperature Superconducting Materials Science and Engineering: New Concepts and Technology*, D. Shi (ed), Pergammon, New York, 1994, p. 345.

16. D. Dimos, P. Chaudhari, J. Mannhart and F. K. LeGoues, Phys. Rev. Lett. **61** 219 (1988).

17. J. W. Ekin, Advan. Ceram. Mater. **2** 586 (1987).

18. F. W. Gayle and D. L. Kaiser, J. Mater. Res. **6** 908 (1991).

19. J. E. Blendell, C. A. Handwerker, M. D. Waudin and E. R. Fuller, Jr., J. Crystal Growth **89** 93 (1988).

20. M. Marella, B. Molinas, and B. Burtet Fabris, J. Mater. Sci. **29** 3497 (1994).

21. S. Jin, T. H. Tiefel, R. C. Sherwood, M. E. Davis, R. B. von Dover, G. W. Kammlott, R. W. Fastnacht and H. D. Keith, Appl. Phys. Lett. **52** 2074 (1988).

22. M. Murakami, M. Morita, K. Doi and K. Miyamoto, Jpn. J. Appl. Phys. **28** 1184 (1989).

23. H. Fujimoto, M. Murakami, S. Gotoh, N. Koshizuka and S. Tanaka, Adv. Supercond. **2**, 285 (1990).

24. Z. Lian, Z. Pingxiang, J. Ping, W. Keguang, W. Jingrong and W. Xiaozu, Supercond. Sci. Tech. **3** 490 (1990).

25. M. Tachiki and S. Takahashi, Solid State Communications, **72** 1083 (1989).

26. M. Tachiki and S. Takahashi, Solid State Communications, **70** 291 (1989).

27. R. M. Schalk, H. W. Weber, Z. N. Barber, P. Przyslupsky and J. E. Evetts, Physica C **199** 311 (1992).

28. C. Gerber, D. Anselmetti, J. G. Bednorz, J. Mannhart and D. G. Schlom, Nature, **350** (1991).

29. S. Jin, G. W. Kammlott, S. Nakanara, T. H. Tiefel and J. E. Graebner, Science **253** 427 (1991).

30. T. Inada and M. Kuwabara, Physica C **190** 172 (1991).

31. T.-H. Sung, K. Rigby, M. J. Cima, M. C. Flemings, J. S. Haggerty, S. Honjo, H. Shen and J. D. Yoo, "Origin of platelet structure in melt-textured YBCO superconductors" to be submitted.

32. J. Mannhart, D. Anselmetti, J. C. Bednorz, C. Gerber, K. A. Mueller and D. G. Schlom, Supercond. Sci. Technol, **5** S125 (1992).

33. M. J. Cima, M. C. Flemings, A. M. Figueredo, M. Nakade, H. Ishii, H. Brody and J. S. Hagggerty, J. Appl. Phys. **72** 179 (1992).

34. C. Varanasi, M. A. Black and P. J. McGinn, J. Mater. Res., **11** 565 (1996).

35. S. Honjo, M. J. Cima, M. C. Flemings, T. Ohkuma, H. Shen, K. Rigby and T. H. Sung, "Seeded crystal growth of $YBa_2Cu_3O_{6.5}$ in semisolid melts", to be published in the Journal of Materials Research.

36. C.-J. Kim, K.-B. Kim, G.-W. Hong and H.-Y. Lee, Mater. Res. **10** 1605 (1995).

37. C.-J. Kim, S. H. Lai and P. J. McGinn, Mater. Lett. **19** 185 (1994).

38. C. Varanasi and P. J. McGinn, Physica C 207 **79** (1993).

39. N. Vandewalle, M. Ausloos, N. Mineur, R. Cloots, G. W. Hong and C. J. Kim, Supercond. Sci. Technol. **9** 665 (1996).

40. L. Durand, D. Dierickx, P. Regnier and O. Van Der Biest, Supercond. Sci. Technol **9** 290 (1996).

41. R. Cloots, N. Wandewalle and M. Ausloos, J. Crystal Growth **166** 816 (1996).

42. A. Endo, H. S. Chauhen, T. Egi and Y. Shiohara, J. Mater. Res. **11** 795 (1996).

43. Y. A. Jee, H. Ching and S.-J. L. Kang, to be published in the Journal of Materials Research.

44. W. Geya, S. Tiansheng, F. Yaoxian, C. Chuanbing and Y. Hongchuan, Supercond. Sci. Technol. **6** 657 (1993).

45. R. S. Roth, C. J. Rawn, F. Beech, J. D. Whitler and J. O. Andersson in *Ceramic Superconductors II*, M. F. Yan (ed), American Ceramic Society, Westerville, OH, 1988, p. 13.

46. J. D. Whitler and R. S. Roth, *Phase diagrams for High-Tc Superconductors*, Am. Ceram. Soc., Westerville, OH (1991).

47. K. Oka, M. Saito, M. Ito, K. Nakane, K. Murata, Y. Nishihara and H. Unoki, Jpn. J. Appl. Phys., Part 2, **28** L219 (1989).

48. K. Oka and H. Unoki, J. Crystal Growth **99** 922 (1990).

49. R. Beyers and T. M. Shaw, Solid State Physics **42**, H. Ehrenreich and D. Turnbull (eds.), Academic Press, Boston, MA (1989), p. 140.

50. A. W. Williams, G. H. Kwei, R. B. Von Dreele, A. C. Larson, I. D. Reistrick, and D. L. Bish, Phys. Rev. B **37** 7960 (1988).

51. E. D. Specht, C. J. Sparks, A. G. Dhere, J. Brynestad, O. B. Cavin, D. M Kroeger and H. A. Oye, Phys. Rev. B **37** 7426 (1988).

52. S. X. Dou, H. K. Liu, C. C. Sorrell, K.-H. Song, M. H. Apperley, S. J. Guo, K. E. Easterling and W. K. Jones, Materials Forum, **14** 92 (1990).

53. J. D. Livingston in *Encyclopedia of Materials Science and Engineering*, M. B. Bever (ed),Volume 6, Pergammon Press, 1986, p. 4741.

54. S. Sengupta and D. Shi, in *High Temperature Superconducting Materials Science and Engineering: New Concepts and Technology*, D. Shi (ed), Pergammon, New York, 1994, p. 131.

55. B. Raveau, Physics Today, October 1992.

56. G. Jakob, M. Schmitt, T. Kluge, C. Tome-Rosa, P. Wagner, T. Hahn and H. Adrian, Phys. Rev. B **47** 12099 (1993).

57. G. W. Crabtree, J. Z. Liu, A. Umezawa, W. K. Kwok, C. H. Sowers, S. K. Malik, B. W. Veal, D. J. Lam, M. B. Brodsky and J. W. Downey, Phys. Rev. B **36** 4021 (1987).

58. V. Selvamanickam and K. Salama, Appl. Phys. Lett. **57** 1575 (1990).

59. V. S. Bobrov and M. A. Lebyodkin, Physica C **178** 411 (1991).

60. S. Jin and J. E. Graebner, Mat. Sci. Eng. **B7** 243 (1991).

61. K. E. Gray, R. T. Kampwirth, J. M. Murdock, D. W. Capone, Physica C **152** 445 (1988).

62. Y. Zhu, H. Zhang, H. Wang and M. Suenaga, J. Mater. Res. **12** 2507 (1991).

63. H. Shen, Ph.D. Thesis, MIT, 1995.

64. H. Shen, K. Rigby, M. C. Flemings, M. J. Cima and J. S. Haggerty, "Solute Distributions in the Semi-Solid Melt during the Growth of $YBa_2Cu_3O_{6+\delta}$ Single Crystals" to be published in the Journal of Materials Research.

65. H. Shen, M. C. Flemings, M. J. Cima, J. S. Haggerty, S. Honjo, K. Rigby and T.-H. Sung, "Solidification of $YBa_2Cu_3O_{6+\delta}$: Part I, Morphology " to be published in the Journal of Materials Research.

66. R. Boutellier, B. N. Sun, H.J. Scheel and H. Schmid, J. Crystal Growth **96** 465 (1989).

67. C. N. W. Darlington, D. A. O'Connor and C. A. Hollin, J. Cryst. Growth **91** 308 (1988).

68. G. J. Schmitz, J. Laakmann, C. Wolters, S. Rex, W. Gawalek, T. Habisreuther, G. Bruchlos and P. Goernert, J. Mater. Res. **8** 2774 (1993).

69. B. N. Sun, R. Boutellier and H. Schmid, Physica C **175** 189 (1989).

70. W. Hong, S. Shuxia, Y. Zhaohe, W. Zhuo, S. Xiaonong, Z. Huansui, J. Minhua and C. Huanchu, J. Crystal Growth **99** 929 (1990).

71. P. Fischer, Physica C **196** 105 (1992).

72. B. N. Sun and H. Schmid, J. Crystal Growth, **100** 297 (1990).

73. M. A. Rodriguez, B.-J. Chen and R. Snyder, Physica C **195** 185 (1992).

74. K. Oka, K. Nakane, M. Ito, M. Saito and H. Unoki, Jap. J. Appl. Phys. **27** L1065 (1988).

75. M. Maeda, M. Kadoi and T. Ikeda, Jap. J. Appl. Phys. **28** 1417 (1989).

76. K. Salama, V. Selvamanickam, L. Gao and K. Sun, Appl. Phys. Lett. **54** 2352 (1989).

77. A. A. Chernov in *Crystal Growth and Characterization*, R. Ueda dn J. B. Mullin (eds), North-Holland, Amsterdam, 1975, pp. 35-52.

78. T. Izumi and Y. Shiohara, J. Mater. Res., **7** 16 (1992).

79. Y. Yamada and Y. Shiohara, Physica C **217** 182 (1993).

80. Y. Kanamori, Y. Shiohara, Physica C **264** 305 1996.

81. Y. Namikawa, M. Egami and Y. Shiohara, *The 1995 International Workshop on Superconductivity, Co-sponsored by ISTEC and MRS*, Maui, Hawaii, June 18-21, 1995, p. 51.

82. A. Goyal, K. B. Alexander and D. M. Kroeger, Physica C **210** 197 (1993).

83. L.T. Romano, O.F. Shilling and C.R.M. Grovenor, Phisica C **178**, 41 (1991).

84. C.J. Kim, K.B. Kim, K.W. Lee, C.T. Lee, G.W. Hong, I.S. Chang and D.Y. Won, Mater. Lett. **11**, 241 (1991).

85. C. Varanasi, M. A. Black and P. J. McGinn, Supercond. Sci. Technol. **7** 10 1994..

86. P.J. McGinn, W. Chen, N. Zhu, C. Varanasi, L. Tan and D. Balkin, Physica C, **183**, 51 (1991).

87. P. McGinn, W. Chen, N. Zhu, L. Tan, C. Varanasi and S. Sengupta, Appl. Phys. Lett. **59** 120 (1991).

88. J. Shimoyama, J. Kase, S. Kondoh, E. Yanagisawa, T. Matsubara, M. Suzuki and T. Morimoto, Jpn. J. Appl. Phys. **67** 915 (1990)

89. P.J. McGinn, N. Zhu, W. Chen, M. Lanagan and U. Balachandran, Physica C, **167**, 343 (1990)

90. D.F. Lee and K. Salama, Jpn. J. Appl. Phys. **29**, L2017 (1990).

91. D.F. Lee, X. Chaud and K. Salama, Physica C, **181**, 81 (1991).

92. M. P. Delamare, I. Monot, J. Wang, J. Provost and G. Desgardin, Supercond. Sci. Technol. **9** 534 (1996).

93. T. Izumi, Y. Nakamura, T.-H. Sung and Y. Shiohara, J. Mater. Res. **7** 801 (1992).

94. M. Murakami, K. Yamaguchi, H. Fujimoto, H. Nakamura, T. Taguchi, N. Koshizuka and S. Tanaka, Cryogenics **32** 931 (1992).

95. M. Murakami, S. Gotoh, N. Koshizuka, S. Tanaka, T. Matsushita, S. Kambe and K. Kitazawa, Cryogenics **30** 390 (1990).

96. D.F. Lee, X. Chaud and K. Salama, Jpn. J. Appl. Phys., **31**, 2411 (1992).

97. M. Wacenovsky, R. Miletich, H.W. Weber and M. Murakami, Supercond. Sci. Technol., **4**, S184 (1991).

98. S. Gotoh, N. Koshizuka, M. Yoshida, M. Murakami, H. Fujimoto and S. Tanaka, Supercond. Sci. Technol., **4**, S226 (1991).

99. E.H. Lee, S.H. Oh and S.Y. Yoon, Jpn. J. Appl. Phys., **31**, 1318 (1992).

100. Z. L. Wang, A. Goyal and D. M. Kroeger, Phys. Rev. B **47** 5373 (1993).

101. K. Yamaguchi, M. Murakami, H. Fujimoto, S. Gotoh, T. Oyama, Y. Shiohara, N. Koshizuka and S. Tanaka, J. Mater. Res. **6** 1404 (1991).

102. S. Jin, G. W. Kammlott, T. H. Tiefel, T. T. Kodas and T. L. Ward, Physica C **181** 57 (1991).

103. M. P. Delamare, I. Monot, J. Wang and G. Desgardin, J. Electron. Mater. **24** 1739 (1995).

104. C. Varanasi, P. J. McGinn and S. Sengupta, J. Electron. Mater. **23** 1143 (1994).

105. C. Varanasi and P. J. McGinn, J. Electron. Mater. **22** 1251 (1993).

106. N. Ogawa, I. Hirabaiashi and S. Tanaka, Physica C **177** 101 (1991).

107. T. Izumi, Y. Nakamura and Y. Shiohara, J. Mater. Res., **8** 1240 (1993).

108. S. P. Athur, V. Selvamanickam, U. Balachandran and K. Salama, J. Mater. Res. **12** 2976 (1996).

109. Y.-M. Chiang, D. Birnie III and W. D. Kingery, *Physical Ceramics: Principles for Cermaic Science and Engineering*, Wiley and Sons, New York, 1997.

110. W. D. Kingery, H. K. Bowen and D. R. Uhlman, in *Introduction to Ceramics*, John-Wiley, New York, 1976.

111. I. M. Lifshitz, V. V. Slyozov, J. Phys, Chem. Solids **19** 35 (1961).

112. C. Wagner, Z. Elektrochem. **65** 35 (1961).

113. G. W. Greenwood, Acta. Metall. **4** 243 (1956).

114. D. Balkin, C. Varanasi, P. McGinn, *The 1992 International Workshop on Superconductivity, Co-sponsored by ISTEC and MRS*, Honolulu, Hawaii, June 23-26, 1992.

115. E. E. Underwood, *Quantitative Stereology*, Addison-Wesley, Massachusetts, (1970).

116. M. L. Grifith, R. T. Huffman and J. W. Halloran, J. Mater. Res. **9** 1633 (1994).

117. M.-F. Ng, Ph.D. Thesis, MIT, 1995.

118. A. Goyal, P. D. Funkenbusch, D. M. Kroeger and S. J. Burnd, J. Appl. Phys. **71** 2363 (1992).

119. A. Endo, H. S. Chauhan, Y. Nakamura and Y. Shiohara, *The 1995 International Workshop on Superconductivity, Co-sponsored by ISTEC and MRS*, Maui, Hawaii, June 18-21, 1995, p. 59.

120. K. N. R. Taylor, P. S. Cook, T. Puzzer, D. N. Matthews, G. J. Russell and P. Goodman, J. Crystal Growth **88**, 541 (1988).

121. A. A. Zhokhov and G. A. Emel'chenko, J. Crystal Growth **129** 786 (1993).

122. P. Hartman and W. G. Perdok, Acta Cryst. **8** 49 (1955).

123. B. N. Sun, P. Hartman and C. F. Woensdregt, J. Crystal Growth, **100** 605 (1990).

124. N. Vandewalle, R. Cloots, and M. Ausloos, Physica C **235-240** 427 (1995).

125. N. Vandewalle, R. Cloots, and M. Ausloos, J. Mater. Res. **10** 268 (1995).

126. S. Amelinckx, Phil. Mag. **44** 337 (1953).

127. A. V. Narlikar, P. K. Dutta, S. B. Samanta and O. N. Srivastava, J. Crystal Growth **121** 527 (1992).

128. M. Marella, B. Molinas, B. Burtet Fabris, L. Meregalli and P Gerontopolous, J. Mater. Sci. Lett. **13** 1108 (1994).

129. BW. K. Burton, N. Cabrera and F. C. Frank, Phil. Trans. Roy. Soc. A **243** 299 (1951).

130. H. Fredrikson, Jerkont. Ann. **155** 571 (1971).

131. H. J. Scheel and P. Niedermann, J. Crystal Growth **94** 281 (1989).

132. C. Hannay, R. Cloots and M. Ausloos, Solid State Communications **83** 349 (1992).

133. S. X. Shang, H. Wang and X. L. Sheng, J. Crystal Growth, **129** 411 (1993).

134. PDEase®, Macsyma Inc., 20 Academy Street, Arlington, MA, 02174, (1996).

135. N. Mori, H. Hata and K. Ogi, J. Japan Inst. Metals. **56** 648 (1992).

136. W. F. Berg, Proc. Roy. Soc. A **164** 79 (1938).

137. S. P. F. Humphreys-Owen, Proc. Roy. Soc. A **197** 218 (1949).

138. N. Pellerin, P. Odier, P. Simon and D. Chateigner, Physica C **222** 133 (1994).

139. D. R. Uhlmann, B. Chalmers and K. A. Jackson, J. Appl. Phys. **35** 2986 (1964).

140. D. M. Stefanescu and B. K. Dhindaw, in *Metals Handbook* (ASM International, Metals Park, OH, 1988, Vol. 15, p. 142.

141. D. M. Stefanescu, B. K. Dhindaw, S. A. Kacar and A. Moitra, Metal. Trans. A **19** 2847 (1988).

142. D. Shangguan, S. Ahuja and D. M. Stefanescu, Metall. Trans A **23** 669 (1992).

143. J. Poetschke and V. Rogge, J. Cryst. Growth **94** 726 (1989).

145. R. L. Meng, L. Gau, P. Gautier-Picard, D. Rairez, Y.-Y. Sun and C. W. Chu, Physica C **232** 337 (1994).

146. C. A. Bateman, J. Zhang, H. M. Chan and M. P. Harmer, J. Am. Ceram. Soc. **75** 1281 (1992).

147. J. D. Jorgensen, B. W. Veal, A. P. Paulikas, L. J. Nowicki, G. W. Crabtree, H. Claus and W. K. Kwok, Phys Rev. B **41** 1863 (19910).

148. R. J. Cava, A. W. Hewat, E. A. Hewat, B. Battlogg, M. Marezio, K. M. Rabe, J. J. Krajewski, W. F. Peck and L. W. Rupp, Physica C **165** 419 (1990).

149. Z. Ahou and A. Navrosky, J. Mater. Res. **7** 2920 (1992).

149. M. Daeumling, Physica C **184** 13 (1991).

150. R. J. Nelmes, J. S. Loveday, E. Kaldis and J. Karpinski, Physica C **172** 311 (1990).

152. C. P. Bean, Phys. Rev. Lett. **8** 250 (1962).

153. M. C. Flemings, *Solidification Processing*, McGraw-Hill, New York (1974).

154. D. C. Larbalestier, *Advances in Superconductivity IV, Proceedings of the 4th International Symposium on Superconductivity, Sponsored by ISTEC*, H. Hayakawa and N. Koshizuka (eds.), Tokyo, Japan, October 14-17, 1991, p. 20.